INFORMATION TO USERS

This manuscript has been reproduced from the microfilm master. UMI films the text directly from the original or copy submitted. Thus, some thesis and dissertation copies are in typewriter face, while others may be from any type of computer printer.

The quality of this reproduction is dependent upon the quality of the copy submitted. Broken or indistinct print, colored or poor quality illustrations and photographs, print bleedthrough, substandard margins, and improper alignment can adversely affect reproduction.

In the unlikely event that the author did not send UMI a complete manuscript and there are missing pages, these will be noted. Also, if unauthorized copyright material had to be removed, a note will indicate the deletion.

Oversize materials (e.g., maps, drawings, charts) are reproduced by sectioning the original, beginning at the upper left-hand corner and continuing from left to right in equal sections with small overlaps.

ProQuest Information and Learning
300 North Zeeb Road, Ann Arbor, MI 48106-1346 USA
800-521-0600

MECHANISMS OF ELECTROHYDRODYNAMIC (EHD) FLOW AND HEAT TRANSFER IN HORIZONTAL CONVECTIVE BOILING CHANNELS

By

James S. Cotton, B.Eng., M.Eng.

A Thesis

Submitted to the School of Graduate Studies

in Partial Fulfilment of the Requirements

for the Degree

Doctor of Philosophy

McMaster University

Hamilton, Ontario, Canada

MECHANISMS OF ELECTROHYDRODYNAMIC (EHD) FLOW AND HEAT TRANSFER IN BOILING CHANNELS

DOCTOR OF PHILOSOPHY (2000) McMASTER UNIVERSITY
(Mechanical Engineering) Hamilton, Ontario, Canada

TITLE: Mechanisms of Electrohydrodynamic (EHD) Flow and Heat Transfer in Horizontal Convective Boiling Channels

AUTHOR: James S. Cotton, B.Eng., M.Eng., P.Eng.

SUPERVISORS: Dr. M. Shoukri and Dr. J.S. Chang

NUMBER OF PAGES: xvii, 283

Abstract

Experimental and numerical investigations have been conducted to study the mechanisms involved in the electrohydrodynamic (EHD) induced flow and heat transfer augmentation of two-phase systems. The experimental study involved tube-side boiling heat transfer of the environmentally friendly HFC-134a in a single-pass, counter-flow heat exchanger 1.5 m in length, 12.7 mm O.D., 10.92 mm I.D., with a 3.18 mm rod electrode. The electrode position was varied from a concentric geometry to an eccentric geometry offset vertically from the centerline by ±2.73 mm. The applied voltage was 0 kV to 8 kV DC or 0 kV to 24 kV peak to peak AC (60 Hz and 6.6 kHz). Experiments were conducted for inlet qualities of 0% to 60%, mass fluxes from 100 kg/m^{2}s to 500 kg/m^{2}s and heat fluxes of 10 kW/m^2 and 20 kW/m^2. Pressure drop, heat flux, quality and inlet void fraction were measured, the inlet and outlet flow regimes were observed and three different methods of estimating the heat transfer coefficients have been compared.

The EHD flow boiling experimental results show that the overall heat transfer coefficients can be increased up to 250% for an 8.0 kV DC applied voltage and up to approximately 300% for 24 kV (peak to peak) 60 Hz AC voltage in the concentric arrangement without a significant increase in pressure drop. Where the concentric electrode, the pressure drop across the heat exchanger increased 1.8 and 2.6 fold for the DC and 60 Hz AC maximum heat transfer enhancement tests, respectively. The EHD power consumption was less than 3 mW for the DC experiments and less than 0.2 W for the 60 Hz AC experiments. Locally, heat transfer coefficient enhancement in excess of 2000% has been observed. The results suggest that under the parameters investigated, augmentation increased with high electric fields, decreased with increased mass and heat fluxes and both

increased and decreased with increasing quality, depending on the flow pattern. Finally, through the application of a low frequency (60 Hz) AC electric field, unlike any flow patten encountered in previous investigations, an entrained-droplet oscillatory flow regime developed. At the outlet of the test section the flow fluctuation occurred at approximately twice the frequency of the applied voltage as observed from this flow developed.

The onset threshold of EHD flow was studied through dimensional analysis. As is proposed, the influences of EHD induced flow on a system become significant when the Dielectric Rayleigh number is of the same order of magnitude as the square of the liquid Reynolds number, $E_{l\varepsilon} \approx Re_l^2$. Flow visualization experiments have shown that when the proposed dimensionless criterion is satisfied, EHD body forces may have a strong influence on the flow pattern within the channel. The redistribution of the phases is observed at smaller mass flux levels and have been observed to induce a transition from stratified wavy flow to intermittent (plug or slug) or annular flow and in a transition from dispersed-annular flow to a symmetric annular flow. The various flow configurations clearly affect both the heat transfer and the pressure loss in the system.

The evaluation of the electric field plays an essential role in any attempt to determine the effect of the electrical forces on the liquid-vapour interface. Numerical calculations of the electric field distribution in two-phase flow with different vapour-liquid distributions and interfacial geometries in both concentric and eccentric electrode arrangements have been conducted both analytically and numerically using a finite element analysis. The results reveal qualitative evidence regarding the redistribution of phases and provide an estimate of the forces acting on the interface. Through the addition of the interfacial electric force to an established flow regime transition model (the Steiner map), a proposal is made to modify the flow mapping prediction method to account for the presence of the electrode (concentric) and electric field on the transition boundaries between stratified wavy and annular or intermittent flow. The flow regimes encountered in the convective boiling process have been reconstructed in an attempt to explain the pressure drop and heat transfer augmentation

using the proposed EHD flow regime map and local surface temperature measurements.

In addition to the application of a DC voltage by previous investigators, high frequency AC voltages have been investigated to verify the dominant EHD forces, *i.e.* dielectrophoretic (E_{te}) vs. electrophoretic (E_{to}). By applying a voltage frequency of 6.6 kHz, the flow pattern transition and heat transfer coefficient results coincide with those observed for the DC fields. As this frequency is expected to prevent the accumulation of a surface charge density on the liquid-vapour interface, the agreement between the DC and 6.6 kHz AC results suggests the electrophoretic component of the electric body force is not a significant factor in enhancing two-phase convective boiling.

Finally, experiments conducted for the eccentric geometry have provided evidence that through the establishment of the appropriate electric field distribution, a desired change of flow regime will occur to augment the heat transfer rates at significantly lower voltage levels and pressure drop penalties. These results were based on the interpretation of the finite element results of the electric field distribution for the arrangement under investigation. The experiment has shown that when the electrode was positioned eccentrically +2.73 mm from the centerline, a 160% enhancement in heat transfer coefficient was observed under the application of a 2 kV DC voltage while the pressure drop increase was only 1.2 fold.

Through the evaluation of the dimensionless criterion for EHD induced effects, electric field distribution analysis, EHD flow regime transition criterion and local and overall parametric analysis, the present investigation has shown that the developed electric body forces lead to a reduction in the thermal boundary layer thickness, increased convection, enhanced boiling dynamics and interfacial instabilities that can result in a phase redistribution. The consequence of this flow regime transition is the potential for significantly enhanced heat transfer rates at the wall, with only minimal increases in pressure drop.

Acknowledgements

First and foremost I would like to express my gratitude for the leadership and guidance provided to me by my supervisors Dr. M. Shoukri and Dr. J.S. Chang. The breadth and integrity of this research was significantly influenced by your great knowledge base, understanding, flexibility and, Dr. Chang, your unique ability to motivate. I would be remiss if I did not include my adopted supervisor, Dr. R.L. Judd. Your patience, kindness and willingness to review my thesis from cover to cover puts you in a league of your own. I feel extremely lucky to have been your student. You gentlemen are true friends and mentors. I would also like to express my sincere thanks to Dr. P. Wood and Dr. M. Baird for their support and expertise throughout my years of grad school.

To Dr. A. Yabe, Yajima-san and all of my friends in Japan, my three months experience in your care was one of the best experiences during my PhD both professionally and personally. My memories of that time seem not to fade.

Special acknowledgment is extended to Chris Norris, Drazena Brocilo, Dr. Amad Abdul-Razzak, Harland MacKenzie, Dave Novog, Eric Wood and Adrian Clarke for their valuable advise, assistance, technical support and friendship that they extended to me throughout my years at McMaster. I look forward to working with you again. And to all of the friends I have made at McMaster, especially Tony, Shawn, Buck and Matt, thank you for being there.

I would also like to express my appreciation to the departmental technicians, Dave, Jim, Joe, Paul and Ron, for their expert advice, patience, support and sincere friendship. Thanks guys.

This work was made possible by the incredible foresight of several individuals at Long Manufacturing Ltd., the primary sponsor of this project. John Burgers, Tracey Smith-Pollard and Ted Zielinski, I thank you for looking into the future and supporting me through my studies. Partial funding for myself and this project by the following organizations, McMaster University, MITI/AIST, NSERC, OGS and ASHRAE is also gratefully acknowledged.

To my family, my parents, Al and Sharron, Lianne and Ryan. Your support, interest and understanding has made this accomplishment possible. I am proud to be your son and brother, thank you so much.

Finally, to my wife Michelle, without your help this could not have been possible, you are the most incredible woman I have ever met and this thesis is as much yours as it is mine. I cannot express how important your support, encouragement and understanding has been to me over the last four years. You have been my editor, my motivator (I think that is the nicest way to say that) and most importantly my friend. You always remind me that dreams come true, so why stop dreaming. You inspire me and for that I thank you.

TABLE OF CONTENTS

List of Tables

Number **Page**

List of Figures

Figure **Page**

To Michelle

Chapter 1

Introduction

The subject of heat transfer enhancement has developed into an active field of study during the past quarter century in response to demands for more efficient and compact heat exchangers, as well as the need to develop effective devices in reduced gravity environments. Automotive, space, aircraft and refrigeration industries are continuously seeking new methods to improve heat exchanger performance, reduce the heat exchanger size for a given duty, increase cycle efficiency and reduce pumping or compressor requirements. Virtually every heat exchanging device is a potential candidate for enhanced heat transfer.

The evolution of heat transfer enhancement technology in the past half century has been well documented by investigators such as Bergles *et al.* (1983, 1988, 1991) and Webb *et al.* (1980, 1983a, 1983b, 1987, 1994). A variety of methods have been implemented to enhance heat transfer coefficients. Several of these are summarized in various reviews by Bergles and Webb and have been published by Webb (1994) in a recent text. The majority of augmentation techniques focus on the disruption and destabilization of the thermal boundary layer in single-phase applications and increased boiling dynamics or phase redistribution in two-phase applications using heat transfer enhancers, such as swirl flow inserts or tube surface modifications. However, most techniques also result in a significant increase in pressure drop.

Among the many processes that have received considerable attention in the past decade for heat transfer enhancement is a phenomena commonly referred to as *electrohydrodynamics* (*EHD*). One major advantage of this method is an enhancement in heat transfer without a significant change in pressure drop. The electrohydrodynamic technique utilizes an electric field to induce secondary motions. These motions may destabilize or reduce the thickness of the thermal boundary layer near the heat transfer surface, leading to increased turbulence, bulk mixing flow or interfacial vaporization, thereby potentially augmenting heat transfer rates at the wall.

In the last decade, research and assessment of EHD technology suggests the technique has passed its infancy stage and commercialization is certain. The interest in this novel heat exchanger technology has grown rapidly due to the attractive benefits the technique exhibits. Advantages of the EHD technique include:

- Improved system performance, including variable capacity systems (*i.e.* varying voltage levels).
- Improved energy efficiency - heat transfer enhancement.
- Reduced system weight, volume, material and costs.
- Reduced pumping requirements with optimum electrode arrangements - EHD pumping, or simply reduced pressure drops compared with other enhanced systems.
- Broad range of system control and faster flow control.
- Moving components and mechanisms are not required.
- Potential for gravity free applications.

The concept of electrohydrodynamic enhancement of heat transfer rates was first reported in a patent by Chubb (1916). Since then, EHD has been the subject of numerous analytical and experimental investigations. Early work concentrated on the enhancement

of single-phase natural or forced convective heat transfer, using various dielectric fluids such as transformer oil, silicon oil, hexane, aviation fuel and air. Typically, the design consists of a single tube heat exchanger with a coaxial electrode within the heat transfer fluid. Investigations have reported significant enhancement, up to a few thousand percent, with only minor pressure drop penalties. However, enhancement rarely occurs much above the laminar regime, as the induced secondary flow becomes negligible compared to the strength of the turbulent eddies, making the range of applicability limited.

More recently, the focus of electrohydrodynamic research has shifted to applications related to phase change. This is primarily due to the difference in electrical properties of the liquid and vapour phase of dielectric fluids. Thus, an electric field in two-phase applications can contribute additional body forces not normally present in a single-phase flow. Generally, the contributing factors for phase change processes are dominated by the electric field distribution and the difference in the specific dielectric constant of the two phases. Both experimental and theoretical research has shown that these forces may lead to a reduction in the thermal boundary layer thickness, increased convection, enhanced boiling dynamics, interfacial instabilities or phase migration that can result in a flow pattern redistribution. The consequence is the potential augmentation of heat transfer rates at the wall over a wide range of conditions.

Table 1.1 provides a summary of the enhancement obtained in several investigations for shell-side and tube-side flow boiling heat transfer of refrigerants with electrohydrodynamics.

1.1 Scope of Work

To contribute to the international efforts aimed at developing EHD as a heat transfer augmentation technique, a refrigerant test facility was built with accurate measurement and

control systems to collect heat transfer, pressure drop, flow regime and electrical data.

The test facility can be operated to investigate both horizontal evaporation and condensation influenced by an impressed electric field. The electric field is imposed through a rod electrode supplied with a high voltage potential, supported within the grounded

Table 1.1: Previous Work in EHD Enhanced Convective Boiling with Refrigerants.

Source	Heat Transfer Surface	Electrode Geometry	Fluid	Max. η	Comments
Ohadi (1991)	Smooth Tube	Straight Wire	R-123	4.5	Shell-Side Boiling
Ogata & Yabe (1991)	Smooth Tube	Straight Wire	R-11/ ethanol	8.5	Shell-Side Boiling
Cooper (1992)	Finned Tube	Wire Mesh	R-114 & oil	13	Pool Boiling
Ogata *et al.* (1992)	Smooth Tube Bundle	Straight Wire	R-123	8.0[a] 2.5[b]	Shell-Side Boiling [a]5 tube bundle [b]blench scale bundle
Ohadi *et al.* (1992)	Tube	Wire	R-123, R11	4.5 1.7	Shell-Side Boiling
Yabe *et al.* (1992)	Tube & Shell	Wire	R-123, R-134a	3	Forced Convection
Ohadi *et al.* (1993a)	Tube	Wire Mesh	R-123 & oil	5	Shell-Side Boiling
Singh *et al.* (1993)	19 fpi Tube	Mesh Wire	R-123	8.5	Shell-Side Boiling
Yamashita & Yabe (1995)	Smooth Tube	Rolled Punched Plates	R-123	6	Falling film
Cheung *et al.* (1995)	40 fpi Tube Bundle	Straight Wire Mesh Wire	R-134a	35.5	Shell-Side Boiling
Ohadi *et al.* (1995a)	Flat Plate	Perforated Plate	R-123	3	Shell-Side Boiling
Ohadi *et al.* (1995b)	19 fpi Tube	Wire Electrode	R-123	5	Shell-Side Boiling
Salehi *et al.* (1995)	Micro fined	Wire Electrode	R-134a	10	Force Convection
Bryan & Seyed-Yagoobi (1997)	Tube & Shell	Wire	R-134a	6.5	Forced Convection

NA: Not Available, fpi: fins per inch, η: heat transfer ratio

refrigerant tube. The electrode may be arranged in either a concentric or eccentric configuration and experiments are performed for DC and low (60 Hz) and high (6.6 kHz) frequency AC voltage levels.

Both local and overall heat transfer coefficients and overall pressure drops are measured during convective boiling. The intent of the investigation is to measure the necessary parameters in convective vaporization, with and without electric fields, for each frequency and electrode arrangement. The experimental test conditions were selected to cover the range of most refrigeration systems, with emphasis in regions of significant enhancement performance. Time dependent local surface temperatures along the flow channel, pressure drop, heat flux, inlet and outlet flow regime and void fractions are measured in an attempt to analyse how the electric field may redistribute the two-phase mixture near the heat transfer surface and accordingly, affect the heat transfer rate.

The flow pattern behaviour in an electric field is extremely complex as the electrohydrodynamic effects are known to cause the migration of the phases, deformation of the interface and the disruption and collapse of bubbles into smaller discrete bubbles depending on the electric field strength and distribution. Subsequently, the electrohydrodynamic effects caused by non-uniform electric field distributions can be used to explain the enhancement of phase-change heat transfer. To facilitate this understanding, an analysis of the static electric field distributions in a pipe containing various two-phase configurations is carried out where the field is applied in either a concentric or an eccentric electrode arrangement. These results provide a qualitative assessment regarding the direction of phase migration and possible flow pattern transition and are used to determine the net EHD force acting on the flow. The net force is combined with a proposed flow pattern map for an annular geometry to evaluate the local flow regimes along a heated channel where

EHD effects occur. Coupling the EHD flow pattern map with the interpretation of the measured time-averaged and transient surface temperatures, a sequence of convective boiling flow patterns in an annulus is proposed for various flow and electric field conditions.

Existing correlations in the literature for predicting flow boiling and condensation heat transfer coefficients inside horizontal tubes involving electrohydrodynamics presently do not exist. By establishing the sequence of flow regimes encountered, insight can be gained in the interpretation of local heat transfer data to clarify the effect of EHD forces on flow regime augmentation influencing heat exchanger effectiveness and may lead to a methodology for determining more accurate heat transfer coefficients in the foreseeable future.

Finally, the threshold of EHD effects is analysed through dimensional analysis to estimate when the EHD forces become significant compared with other factors inherent to the flow. The results are compared against the flow visualization experiments to determine a criterion to predict when EHD body forces may have a strong influence on the liquid-phase, consequently influencing the flow pattern within the channel.

The fundamental goal of this dissertation is the initiation of a methodology in the development of the EHD technique to the control and enhancement of heat transfer in two-phase systems. In an effort to develop high performance heat exchangers that incorporate the potential benefits of superimposing an electric field on an existing fluid flow it is critical to understand how and when the additional forces influence the flow. As presented in this investigation through dimensional analysis, electric field distribution analysis and a criterion for flow pattern transition, significant information regarding the electrohydrodynamic phenomena applied to convective boiling is revealed.

Chapter 2

Two-Phase Flow and Heat Transfer

The heat transfer and fluid flow processes associated with liquid-vapour phase-change phenomena are among the most complex transport processes encountered in engineering practice. Unlike a more comprehensive review of the various elements of two-phase flow and phase change processes, such as Rohsenow *et al.* (1985), Whalley (1990), Carey (1992) and Collier and Thome (1994), the present chapter attempts to provide an overview of the aspects important to horizontal flow vaporization in a tube without the EHD effect: flow pattern recognition and identification, two-phase pressure drop and the prediction of flow boiling heat transfer coefficients. The following chapters describe the additional complexities associated with the presence of the electrode and the application of electric fields to two-phase mixtures.

2.1 General Definitions and Relations

Before proceeding with the technical aspects of flow vaporization involved in this study, the present section provides definitions of several two-phase flow parameters.

• ***Quality, x,*** is the mass proportion of fluid in the vapour state. At thermodynamic equilibrium, the quality is the amount by which the enthalpy of the system is above the saturation enthalpy as a proportion of the latent heat of vaporization i_{fv}:

$$x_{eq}=\frac{i-i_l}{i_{fv}} \tag{2.1}$$

where x_{eq} is the equilibrium thermodynamic quality, and i and i_l are the enthalpy of the two-phase mixture and the liquid phase at the given saturation temperature and pressure, respectively. In fluid flow, the flow quality can be given by the mass of vapour that flows past a plane as a proportion of the total mass passing that plane:

$$x=\frac{\dot{m}_v}{\dot{m}} \tag{2.2}$$

where $\dot{m}_v$ and $\dot{m}$ are the vapour and total mass flow rates, respectively.

• ***Total Mass Flux*** is given by

$$G=\frac{\dot{m}}{A_x} \tag{2.3}$$

where A_x is the cross sectional area of the tube, $A_x = A_i - A_e$. The subscripts i and e refer to the inside of the test section tube and to the electrode, respectively.

• ***Vapour and Liquid Mass Fluxes G_v and G_l*** through a cross-sectional plane of the tube are:

$$G_v=\frac{\dot{m}x}{A_x}=Gx \tag{2.4}$$

$$G_l=\frac{\dot{m}(1-x)}{A_x}=G(1-x) \tag{2.5}$$

• ***Void Fraction, α*** is the volumetric fraction of vapour, in a flowing two-phase medium is represented as a proportion of the cross sectional area defined by:

$$\alpha=\frac{A_v}{A_x}=1-\frac{A_l}{A_x} \tag{2.6}$$

where A_v and A_l are the cross-sectional areas occupied by vapour and liquid, respectively.

• ***Velocity of the Vapour and Liquid, u_v and u_l*** are the space-averaged velocities each phase would attain based upon the proportion of the cross-sectional area occupied by the phase.

$$u_v=\frac{\dot{V}_v}{A_v}=\frac{\dot{V}_v}{\alpha A} \quad , \quad u_l=\frac{\dot{V}_l}{A_l}=\frac{\dot{V}_l}{(1-\alpha)A} \tag{2.7 a,b}$$

where $\dot{V}_v$ and $\dot{V}_l$ are the vapour and liquid volumetric flow rates, respectively.

• ***Superficial velocity, j_φ*** is the velocity that each phase would attain if it were to flow alone in the tube:

$$j_v=\frac{\dot{V}_v}{A_x} \quad , \quad j_l=\frac{\dot{V}_l}{A_x} \tag{2.8 a,b}$$

or

$$j_v = u_v\alpha \quad , \quad j_l = u_l(1-\alpha) \tag{2.9 a,b}$$

where j_v and j_l are the vapour and liquid superficial velocity, respectively.

• ***Slip ratio S*** is the ratio of vapour to liquid velocities $S= u_v/u_l$ and is related to the quality and void fraction by:

$$\alpha=\frac{x}{x+(1-x)\frac{\rho_v}{\rho_l}S} \tag{2.10}$$

where ρ_v and ρ_l are the respective vapour and liquid mass densities.

• ***Reynolds number, Re_φ***, for each phase φ is given by

$$Re_\varphi=\frac{G_\varphi D_h}{\mu_\varphi} \tag{2.11}$$

where D_h refers to the hydraulic diameter of the tube with an electrode, and μ_φ refers to the dynamic viscosity of the phase φ.

• ***Boiling number, Bo,*** for a heated two phase mixture is:

$$\frac{q''}{Gi_{fv}} \tag{2.12}$$

• ***Convection number, Co***, for a two-phase mixture is:

$$Co = \left(\frac{1-x}{x}\right)^{0.8}\left(\frac{\rho_v}{\rho_l}\right)^{0.5} \tag{2.13}$$

• ***Froude number, Fr_{lo}***, for a two-phase mixture, assuming all flow to be liquid, is:

$$Fr_{lo} = \frac{G^2}{\rho_l^2\, g\, D} \tag{2.14}$$

2.2 Flow Patterns and Transition Models

The difference between the liquid and vapour phase velocities, gravitational forces acting on the flow and the momentum transfer between the phases, creates various distributions of liquid and vapour in a channel commonly known as flow patterns or flow regimes. Collier and Thome (1994) give a comprehensive review of the common classifications of flow regimes observed in horizontal tubes, Figure 2.1a. In horizontal flow, the most common flow patterns are bubble, plug, stratified, stratified wavy, slug, annular-dispersed, annular and mist flow. The description of these flow patterns, adopted and modified to include annular geometries, is summarized in Chapter 5. During vaporization, the flow pattern changes. Figure 2.1b depicts the two-phase flow patterns that may be observed along a horizontal evaporation tube where a low velocity, initially saturated single-phase liquid is subjected to a constant wall heat flux.

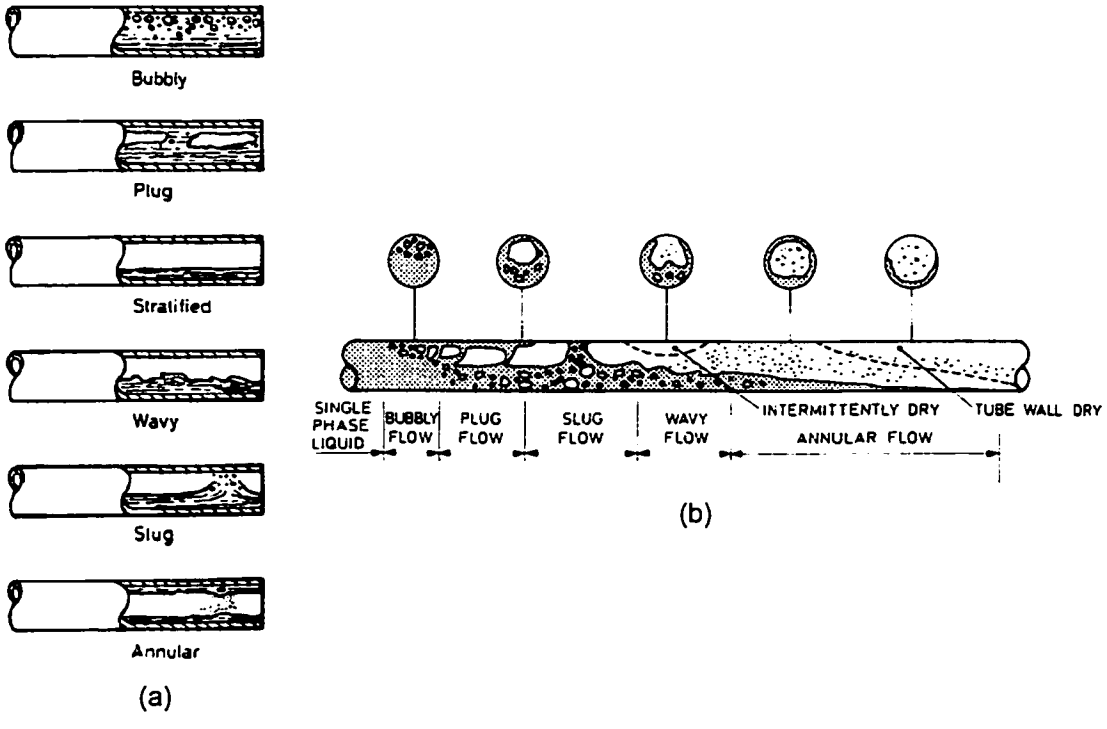

Figure 2.1: a) Flow Patterns in Horizontal Two-Phase Flow in a Tube, b) Example of a Sequence of Flow Patterns in Horizontal Flow Boiling (Collier and Thome, 1994).

The observations of the different flow regimes associated with a particular system depend on the flow conditions. In general, when heat is added to a subcooled liquid, the mechanisms are governed by single-phase forced convection. Bubble flow is initiated at the onset of nucleate boiling. The bubbles appear to grow from nucleation sites and are carried into the mainstream of the flow, tending towards the upper surface due to buoyancy. As the void fraction increases, individual bubbles coalesce to form plugs and then slugs of vapour appear. The void fraction eventually becomes very high and the liquid tends to remain at the bottom of the tube, due to gravity, in a configuration called stratified or wavy-stratified flow. Stratified flow is usually followed by a form of annular flow, characterized by a liquid film flowing along the wall with a vapour core. Although the wall is completely wetted, the liquid tends to collect along the lower portion of the tube forming a non-symmetric liquid annulus due to the force of gravity creating annular dispersed flow.

The different fluid dynamic phenomena associated with each flow pattern requires a prediction of the configuration of the liquid and vapour in the channel. To this end, a variety of empirical flow regime maps have been developed. Typically, the flow patterns are represented as areas on a graph, the coordinates of which are generalized parameters, often containing the superficial velocities of each phase. Reviews of several earlier maps are provided by Spedding and Nguyen (1980) and included as an introductory chapter in most two-phase flow texts (*e.g.*, Carey, 1992). Although flow maps generally developed for flows in circular pipes efforts have been made to develop flow regimes for annular geometries, but they have focussed on high radius ratios in the range of 0.375 to 0.625. Further, as suggested by Osamusali and Chang (1988), the influence of the inner tube is dominant at low superficial velocities. Table 2.1 summarizes some of the most recent models for tubular

geometries relevant to the present investigation.

Table 2.1: Summary of Selected Flow Regime Maps.

Map	Main Parameter	Orientation	Comments
Taitel and Dukler (1976)	$X_{tt}^2 = (dp/dz)_l/(dp/dz)_v$ $F = G_v / [\rho_v(\rho_l - \rho_v)Dg]^{1/2}$ $K = F\,[G_l D/\mu_l]^{1/2}$ $T^2 = (dp/dz)_l/[g(\rho_l - \rho_v)]$	Originally Horizontal	Theoretical-based model based on the transition from stratified flow.
Hashizume (1983)	$X_h = [(1-x)/x]\lambda\psi'$ $Y_h = Gx/\lambda$ $\lambda^2 = (\rho_v/\rho_{wa})(\rho_l/\rho_{wa})$ $\psi' = (\sigma_{wa}/\sigma_l)^{1/4}[(\mu_l/\mu_{wa})(\rho_{wa}/\rho_l)^2]^{1/3}$	Horizontal	Modified Baker (1954) Map.
Klimenko and Fyodorov (1990)	$F_{KF} = 0.074(D/b_{La})^{0.67}\,Fr_v +$ $8[1-\rho_v/\rho_l)^{0.1}]^2\,Fr_l$ $F_{KF} > 1.0$ *Unstratified* $F_{KF} < 1.0$ *Stratifed*	Horizontal	Mechanistic Criterion - for transition from stratified to unstratified flows.
Steiner (1993) VDI Map	$X_{tt}^2 = (dp/dz)_l/(dp/dz)_v$ $F = G_v / [\rho_v(\rho_l - \rho_v)Dg]^{1/2}$ $K = F\,[G_l D/\mu_l]^{1/2}$ $T^2 = (dp/dz)_l/[g(\rho_l - \rho_v)]$	Horizontal and inclined	Modified Taitel and Dukler map, includes angle of inclination (Includes surface tension).
Kattan *et al.* (1998a)	Mass Flux & Quality G, x	Horizontal and inclined	Modified Steiner map valid for both adiabatic and diabatic flows.

The studies referenced in Table 2.1 are concerned with fully developed flow regime structures within an empty round tube without EHD. In order to apply these flow maps to the present investigation, significant modifications to the mechanistic criterion are required. The development of an analytical approach to flow regime transitions in horizontal annular flow, both with and without EHD, is detailed in Chapters 5 and 6.

2.3 Two-Phase Pressure Drop

Being able to predict pressure drop during two-phase flow is essential for the design of thermalhydraulic systems, including the various components of refrigeration and air-conditioning equipment. The total pressure drop is composed of several components: frictional, accelerational, gravitational, interfacial transfer and external forces. The frictional

component, which generally constitutes the largest part of the total pressure drop, results from the shear stress between the flowing fluid and the channel wall and the interfacial drag due to the different velocities of phases. The momentum interactions affect the pressure drop through mechanisms such as mass transfer between the phases for example the effect a droplet entrained into a vapour core resulting in a local reduction in the vapour velocity. The accelerational component results from a change in the momentum of the two-phase mixture due to evaporation in heated channels and/or flashing from a loss in pressure. In heated channels, the accelerational pressure drop may become significant as evaporation changes both the mass and the velocity of each phase. In adiabatic two-phase applications, the accelerational pressure drop is due only to flashing caused by pressure loss and/or vapour expansion. However, as the typical system pressure is several times larger than the pressure drop, this component is normally negligible.

The present work is concerned with the measurement of the pressure drop in a heated channel with external forces. Therefore, both acceleration and friction must be considered, Chapter 6 and 7 present the influences the external forces (EHD). In modelling the frictional pressure drop, two approaches have been followed. These models consider the two-phase flow as either a homogeneous mixture or a separated flow. In the homogeneous mixture model, the two phases have equal velocities are assumed to be in thermodynamic and mechanical equilibrium. In contrast, the separated flow model treats the phases flowing separately at different velocities. The following two sections give a brief overview of the various models used to determine two-phase pressure drop in a tube with emphasis on the frictional component, since this component usually constitutes most of the total pressure drop.

The Homogeneous Model

The homogeneous model is expected to perform well in predicting the pressure drop of low quality two-phase flow with high concentrations of small bubbles, or high quality spray or droplet flows. The homogeneous model treats the two-phase flow as a single fluid with an appropriate homogeneous density ρ_H and homogeneous viscosity μ_H. Accordingly, the frictional pressure gradient of a homogeneous two-phase flow is:

$$\left(\frac{dp}{dz}\right)_f = -f\frac{1}{D}\frac{G^2}{2\rho_H} \tag{2.15}$$

where f is the friction factor, D is the pipe diameter, and G is the two-phase mass flux. The homogeneous density is given by:

$$\frac{1}{\rho_H} = \frac{x}{\rho_v} + \frac{1-x}{\rho_l} \tag{2.16}$$

where x is the quality and ρ_v and ρ_l are the vapour and liquid densities, respectively. The friction factor f is calculated as in the case of single-phase flow. For example, the friction factor according to Blasius (1913) takes the form:

$$f = \frac{C}{Re^n} \tag{2.17}$$

where C and n are empirical constants and depend on the Reynolds number and tube surface conditions. Equation (2.17) requires a model for the dynamic viscosity of the two-phase mixture to be used in calculating the Reynolds number $Re=GD/\mu_H$. Various empirical correlations which satisfy the limiting cases at $x=0$, $\mu_H=\mu_l$ and at $x=1$, $\mu_H=\mu_v$ have been suggested in the literature. The correlation proposed by McAdams (1942) is adopted here:

$$\frac{1}{\mu_H} = \frac{1-x}{\mu_l} + \frac{x}{\mu_v} \tag{2.18}$$

The Separated Flow Models

Separated flow models consider the phases to be divided into two streams, liquid and

vapour. The basic premise is the assumption that each of the two phases attain constant but not necessarily equal velocities. One of the earliest methods for predicting the frictional pressure drop during two-phase flow was developed by Lockhart and Martinelli (1947). This procedure suggests that the frictional pressure drop during two-phase flow can be predicted by correcting the single-phase frictional pressure drop with two-phase multipliers Φ_L^2 and Φ_V^2 defined as:

$$(\frac{dp}{dz})_f = \Phi_L^2 (\frac{dp}{dz})_L \tag{2.19}$$

$$(\frac{dp}{dz})_f = \Phi_V^2 (\frac{dp}{dz})_V \tag{2.20}$$

where $(dp/dz)_L$ is the frictional pressure gradient of the liquid and $(dp/dz)_V$ is the frictional pressure gradient of the vapour if each of the two phases were to flow alone in the channel. These are calculated by:

$$(\frac{dp}{dz})_L = -f_l \frac{1}{D} \frac{(1-x)^2 G^2}{2\rho_l} \tag{2.21}$$

$$(\frac{dp}{dz})_V = -f_v \frac{1}{D} \frac{x^2 G^2}{2\rho_v} \tag{2.22}$$

Lockhart and Martinelli (1947) defined the parameter X as:

$$X = \left[\frac{(dp/dz)_L}{(dp/dz)_V}\right]^{1/2} = \frac{\Phi_V}{\Phi_L} \tag{2.23}$$

Substituting Equations (2.21), (2.22) and (2.17) into Equation (2.23) we obtain:

$$X = \left(\frac{\mu_l}{\mu_v}\right)^{\frac{n}{2}} \left(\frac{1-x}{x}\right)^{\frac{2-n}{2}} \left(\frac{\rho_v}{\rho_l}\right)^{\frac{1}{2}} \tag{2.24}$$

where n in Equation (2.24) has been taken to be either 0.25 or 0.2 for smooth pipes. Lockhart and Martinelli (1947) suggested that Φ_L and Φ_V be expressed solely as a function of X (for two-component flows at low pressure) represented by the relations:

$$\Phi_L^2 = 1 + \frac{C}{X} + \frac{1}{X^2} \tag{2.25}$$

$$\Phi_V^2 = 1 + CX + X^2 \tag{2.26}$$

where C varies between 5 to 20. Chisholm (1973) derived Equations (2.25) and (2.26) and obtained a relation for C as:

$$C = \frac{1}{S}\left(\frac{\rho_l}{\rho_v}\right)^{1/2} + S\left(\frac{\rho_v}{\rho_l}\right)^{1/2} \tag{2.27}$$

where S is the slip ratio, *i.e.* the ratio between the vapour phase velocity to the liquid phase velocity. In general, the value of C depends on whether the flow of each phase considered separately is laminar or turbulent, and on the nature of the flow regime. For turbulent two-phase flows where a strong interaction between the two phases exists, such as homogeneous flow, high values of C are observed. Whalley (1990) showed that in the case of separated flow, where little to no interaction occurs between the phases, C could be as low as 2 for laminar flow and as low as 3.66 for turbulent flow.

Martinelli and Nelson (1948) extended the procedure described above for evaporating steam-water flow. Assuming turbulent flow for both phases, they developed an equation relating Φ_L to X close to the critical pressure and adopted the Lockhart and Martinelli relation for Φ_L and X for atmospheric pressure. Using data presented by Davidson *et al.* (1943), Martinelli and Nelson (1948) were then able to establish correlations for intermediate pressures, between the atmospheric and critical pressures. The correlations were subsequently redefined as a function of Φ^2_{LO}. The two-phase flow multiplier, based on the pressure gradient where the total flow is assumed to be liquid, is given as:

$$\Phi^2_{LO} = \frac{(dp/dz)_L}{(dp/dz)_{LO}} \tag{2.28}$$

where $(dp/dz)_{LO}$ is the frictional pressure drop assuming the total flow to be liquid.

Baroczy (1966) produced a general graphical correlation for Φ^2_{LO} as a function of property index, mass dryness fraction and mass flux. However, the graphical nature of the correlation was difficult to use in thermalhydraulic simulation codes.

Chisholm (1973) transformed Equation (2.25) into a more convenient form by expressing the function in terms of Φ^2_{LO} instead of Φ^2_L. The suggested correlation is:

$$\Phi^2_{LO} = 1 + (\Gamma^2 - 1)[Bx^{(2-n)/2}(1-x)^{(2-n)/2} + x^{2-n}] \tag{2.29}$$

where

$$\Gamma^2 = \left[\frac{(dp/dz)_{VO}}{(dp/dz)_{LO}}\right] = \left(\frac{\rho_l}{\rho_v}\right)\left(\frac{\mu_v}{\mu_l}\right)^n \tag{2.30}$$

$$B = \frac{C\Gamma - 2^{2-n} + 2}{\Gamma^2 - 1} \tag{2.31}$$

Based on Baroczy's correlation, Chisholm suggested a conservative value of B may be determined from the following table:

Table 2.2: Values for the Parameter B in Equation (2.29).

Γ	G kg/m^{2}s	B
≤9.5	<500 500 to 1900 ≥1900	4.8 2400/G 55/G$^{1/2}$
9.5 to 28	≤600 >600	520/(ΓG$^{1/2}$) 21/Γ
≥28	----	15000/(Γ^2G$^{1/2}$)

Friedel (1979) (as quoted by Whalley, 1990) suggested a complicated empirical equation for Φ^2_{LO} which is applicable to any fluid as long as μ_l/μ_v <1000:

$$\Phi^2_{LO} = E + \frac{3.24FH}{Fr^{0.045}We^{0.035}} \tag{2.32}$$

where

$$E = (1-x)^2 + x^2\frac{\rho_l f_{VO}}{\rho_v f_{LO}} \tag{2.33}$$

$$F = x^{0.78}(1-x)^{0.224} \tag{2.34}$$

$$H = \left(\frac{\rho_l}{\rho_v}\right)^{0.91}\left(\frac{\mu_v}{\mu_l}\right)^{0.19}\left(1-\frac{\mu_v}{\mu_l}\right)^{0.7} \tag{2.35}$$

$$Fr = \frac{G^2}{gD\rho_H^2} \tag{2.36}$$

$$We = \frac{G^2 D}{\sigma \rho_H} \tag{2.37}$$

and ρ_H is the homogeneous density defined by Equation (2.16). Here, f_{VO} and f_{LO} are the friction factors, assuming the total mass flux flows as vapour or liquid respectively, σ is the surface tension and g is the acceleration due to gravity.

Souza *et al.* (1993) presented a frictional pressure drop correlation for pure refrigerants flowing within smooth horizontal tubes. The correlation was developed using refrigerants R-134a and R-12 in a 10.9 mm test section. In this correlation, the effect of mass flux is represented by the Froude number Fr to account for strong inertia and body forces, *i.e.* to account for gravitational effects encountered in stratified and wavy flow conditions. Accordingly, Φ^2_{LO} becomes a function of the Lockhart-Martinelli parameter X and the Froude number Fr. The form of the correlation is as follows:

$$\Phi^2_{LO} = (1.376 + c_1 X^{-c_2})(1-x)^{1.75} \tag{2.38}$$

For	$0<Fr\leq 0.7$	*For*	$Fr>0.7$
	$c_1 = 4.172 + 5.480Fr - 1.564Fr^2$		$c_1 = 7.242$
	$c_2 = 1.773 - 0.169Fr$		$c_2 = 1.655$

In general, the separated flow models are expected to perform well when stratified or annular flow patterns exist, as the phase velocities often differ significantly in these regimes of flow. Among predictive methods discussed in this review, Cotton *et al.* (1996) suggested the Souza correlation was the best at predicting frictional pressure drops. In their investigation, the pressure drop was determined to be within ±30% of all measured values, which was attributed to the fact that stratification effects may be accounted for by modifying the correlation depending on the Froude number stratification criterion. This is similar to the stratified flow threshold criterion proposed by Shah (1982), Gungor and Winterton (1986 ,1987) and Kandlikar (1990) for heat transfer coefficient evaluation.

The pressure drop due to acceleration can be obtained by a simplified momentum equation, in which the vapour and liquid velocities are assumed to be uniform in each phase (Souza *et al.*, 1993):

$$\Delta p_{acc} = G^2\left(\left[\frac{x_o^2}{\rho_v \alpha_o} + \frac{(1 - x_o)^2}{\rho_l(1 - \alpha_o)}\right] - \left[\frac{x_i^2}{\rho_v \alpha_i} + \frac{(1 - x_i)^2}{\rho_l(1 - \alpha_i)}\right]\right) \tag{2.39}$$

Therefore, the total pressure drop during two-phase flow inside a horizontal tube can be represented by the relationship:

$$\Delta p_{tp} = \Delta p_f + \Delta p_{acc} \tag{2.40}$$

which will be used to determine the base case pressure drop in pipe flow.

2.4 Tube-Side Forced Convective Boiling

Flow boiling involves a number of phenomena acting simultaneously, which creates an extremely complex problem when attempting to predict specific parameters such as heat transfer coefficients. Initially the nucleation of bubbles occurs at the surface. These bubbles grow and coalesce into Taylor bubbles (plugs). The liquid and vapour phases segregate into various geometries with complex interfacial effects, as depicted in Figure 2.1b, until the only remaining liquid exists as a thin wall film and/or mist or complete evaporation occurs. Also, gravity introduces the stratification of the phases which further complicates the process when the channel is horizontal. Each flow pattern progression should be considered separately as they affect heat transfer and pressure drop. Currently, the prediction of heat transfer coefficients inside horizontal tubes is not satisfactory, as suggested by Kattan (1996) and Darabi *et al.* (1995). One reason is the various correlations and models do not sufficiently distinguish between the appropriate two-phase flow patterns, which influence heat transfer considerably. Regime identification is an important milestone in the development of an

appropriate methodology for determining the convective vaporization heat transfer coefficient.

As indicated by Darabi *et al.* (1995), there are four different models used in the investigation of flow boiling, which are:

- models based on dimensional analysis
- models that assume the heat transfer coefficient to be the sum of nucleate boiling and convective evaporation contributions (*superposition model*)
- models that utilize the greater of the nucleate and convective components, for example using boiling number (Bo) correlations, (*enhancement model*), and
- the asymptotic models based on the power-type addition of two boiling components (*asymptotic model*).

As the heat transfer coefficient in forced convective boiling is a function of both nucleate boiling and the convective boiling contributions, most of the existing correlations are based on this dual effect in one form or another.

Figure 2.2 presents the boiling curves for pool boiling and forced convective boiling (Rohsenow *et al.*, 1985). The graph is a plot of the applied heat flux versus the excess temperature (wall superheat), the temperature difference between the tube wall (T_w) and the saturation temperature (T_{SAT}). T_b represents the liquid temperature in the subcooled boiling regime. Figure 2.2 suggests that the fully developed curve is an extension of the pool boiling line for the same surface. This observation provides weight to the suggestion that flow boiling may be a superposition of nucleate boiling and convection. Generally, the nucleate boiling component is dominant at high temperature differences and low qualities. At low temperature differentials or higher qualities the convective boiling component is dominant (Kattan, 1996). The following section provides a summary of some of the empirical and

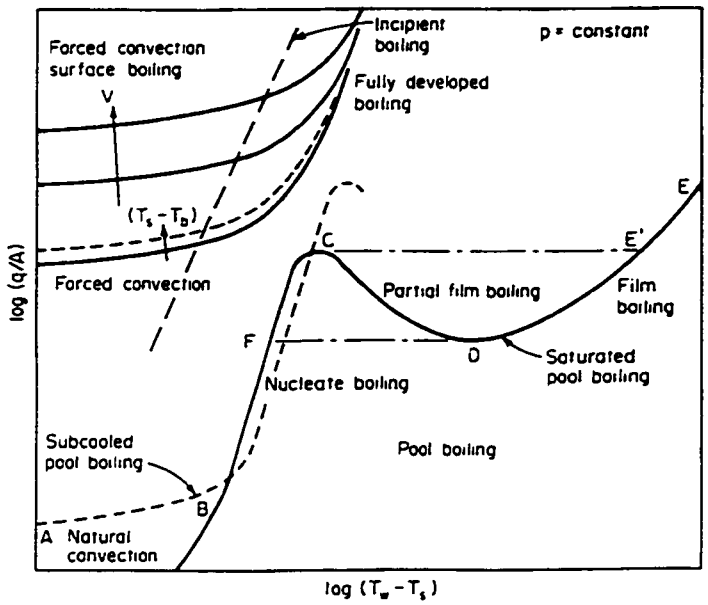

Figure 2.2: Pool Boiling and Forced Convective Boiling Heat Transfer (Rohsenow *et al.*, 1985)

semi-empirical correlations available to predict heat transfer for the flow boiling regime in horizontal and vertical tubes as reviewed by Kandlikar (1990) and Darabi *et al.* (1995).

2.4.1 Forced Convective Tube-Side Boiling Heat Transfer Coefficient Calculations

Numerous studies have clearly indicated the theoretical complexities of flow boiling mechanisms. Hence, all attempts to quantify the heat transfer of flow boiling have been semi-empirical in nature. The reader is referred to Collier and Thome (1994) for a comprehensive survey of available correlations. Kandlikar (1990) and Darabi *et al.* (1995) have provided reviews to include recent advancements in correlation development. Table 2.3 presents several important correlations available in literature.

Usually the evaluation of the predictive models is done by statistical methods. Many authors have used the mean deviation criteria to compare their correlation with the previous correlations (Darabi *et al.*, 1995). The results of the Darabi *et al.* (1995) comparison based on the mean deviation are summarized in Table 2.4.

Table 2.3: Correlations for Flow Boiling Heat Transfer Inside Tubes.

Investigator	Details	Correlation	Comments
Chen (1966)	Vertical flow; water, methanol, cyclohexane, pentane; 600 data points	$h_{tp} = h_{mac} + h_{mic}$ h_{mac} - $h_{Dittus\text{-}Boelter} \times F$ h_{mic} - $h_{Forster\text{-}Zuber} \times S$ F & S functions of Re_L & X_{tt}	Mean deviation of 12% with data of six investigators. Used extensively. Large deviation observed with recent data on refrigerants.
Shah (1982)	Vertical & horizontal flow; water, R-11, R-12, R-22, R-113, cyclohexane; 800 data points	Originally given in a chart form by Shah (1976) Equation fitted as: $h_{tp} = h_{tp}(Co, Bo, Fr_{lo})$	90 % of data falls within 30 %. Large deviation with some recent experimental data.
Bjorge *et al.* (1982)	Vertical flow; water; 8 data sets	High quality region, ($x>0.05$) $q = q_{FC} + q_B - q_{Bi}$ Low quality region ($x<0.05$) $q = [q^2_{FC} + (q_B - q_{Bi})^2]^{0.5}$	Mean deviation of 15% against 17.4% with Chen correlation. Equations using superposition technique. Provides insight into flow boiling mechanisms.
Kandlikar (1983)	Vertical & horizontal flow; water, R-11, R-12, R-114, nitrogen, neon; 1100 data points.	$h_{tp}/h_l = D_1(Co)^{D2}(25Fr_{lo})^{D5} + D_3(Bo)^{D4}(25Fr_{lo})^{D6}$	Mean deviation of 17.1% against 38% with the Shah correlation. A fluid dependent parameter introduced.
Gungor & Winterton (1986)	Vertical & horizontal flow; water, R-11, R-12, R-22, R-113, R-114, ethylene glycol; 3600 data points	$h_{tp} = E\, h_l + S\, h_{pool}$ E & S are functions of Bo, X_{tt}, and Fr_{lo}	Mean deviation of 19.7% with all data tested.
Gungor & Winterton (1987)	Same as Gungor and Winterton (1986)	$h_{tp}/h_l = 1 + 3000Bo^{0.86} + [x/(1-x)]^{0.75}(\rho_l/\rho_v)^{0.41}$ Fr_{lo} correction for horizontal tube	Correlation is simplified as compared to their 1986 correlation. Agreement with data is slightly improved
Jung *et al.* (1989)	Horizontal flow; R-12, R-22, R-114, R-152a & mixtures; 3000 data points	$h_{tp} = Sh_{un} + Fh_l$ F & S: $f(Bo, X_{tt})$, h_{un} pool boiling coef. by Unal (1986). Correction factors added for refrigerant mixtures	Modification of Chen (1966) correlation. Mean deviation of 7.2% for data tested.
Liu & Winterton (1991)	Horizontal flow ;30 data sets; 4200 data points - saturated boiling, 990 data points - subcooled boiling	$h_{tp} = [(E\, h_l)^2 + (S\, h_{pool})^2]^{1/2}$ E & S are functions of Re_l, Pr_l and x	Based on the Kutateladze (1961) power-type addition model *ie.* asymptotic model. Valid for annuli using a heated equivalent diameter. Mean deviation of 20.5%.
Steiner & Taborek (1992)	Vertical flow; large data bank of about 13000 data points	$h_{tp} = (h^n_{nb} + h^n_{cb})^{1/n}$ $h_{nb} = h_{nbo} F_{nb}$: nucleate boiling coef. × correction factor $h_{cb} = h_{lo} F_{tp}$: total flow s-p liquid coef. × t-p multiplier By regression $n=3$	Based on the Kutateladze (1961) power-type addition model *ie.* asymptotic model.

Originally obtained from Kandlikar (1990) modified to include some recent correlations.

Table 2.4: Percentage of Mean Deviation Between Various Correlations and Data.

Correlation	No. of Data Pts.	Chen	Bjorge	Shah	G-W	L-W	Klim.	Kand.	Jung
Chen (1966)	665	12.0	-	-	-	-	-	-	-
Bjorge *et al.* (1982)	800	17.4	15.0	-	-	-	-	-	-
Shah (1982)	780	-	-	14.0	-	-	-	-	-
Gungor-Winterton (1986) G-W	3693	57.7	59.5	21.9	21.4	-	-	-	-
Liu-Winterton (1991) L-W	4183	37.2	-	23.1	24.3	20.5	-	-	-
Klimenko (1990)	3125	-	-	-	-	-	14.4	-	-
Kandlikar (1990) Kand.	4970	43.5	46.5	23.7	24.5	-	-	18.8	-
Jung *et al.* (1989)	3000	-	-	-	-	-	-	-	7.2
Steiner-Taborek (1992)	13000	-	-	-	-	-	-	-	-

(Darabi *et al.*1995)

An important factor in the comparison of the available correlations is to correctly predict the trend of heat transfer coefficients versus quality. Figure 2.3 presents comparisons of the correlations reviewed by Darabi *et al.* (1995) with the experimental data taken from Ha and Bergles (1992). The primary difference between the observed trends of the various correlations, as noted by Darabi *et al.* (1995) is the model used to couple the nucleate boiling and forced convective effects. In general, as quality increases the nucleate boiling is suppressed, while the forced convective effect increases. The method used to determine this transition is extremely important as is apparent from Figure 2.3.

Upon review, Darabi *et al.* (1995) recommended the asymptotic models by Liu and Winterton (1991) and Steiner and Taborek (1992), as their correlations were "the best form with which to correlate the experimental data". Both semi-empirical approaches are derive through rational bases and offered a slight transition between nucleate boiling and convective boiling heat transfer.

As the above review suggests, there is no general model for predicting heat transfer coefficients and pressure drop that is widely accepted in literature. The main reason is that these models do not incorporate the effects of local two-phase flow patterns, flow

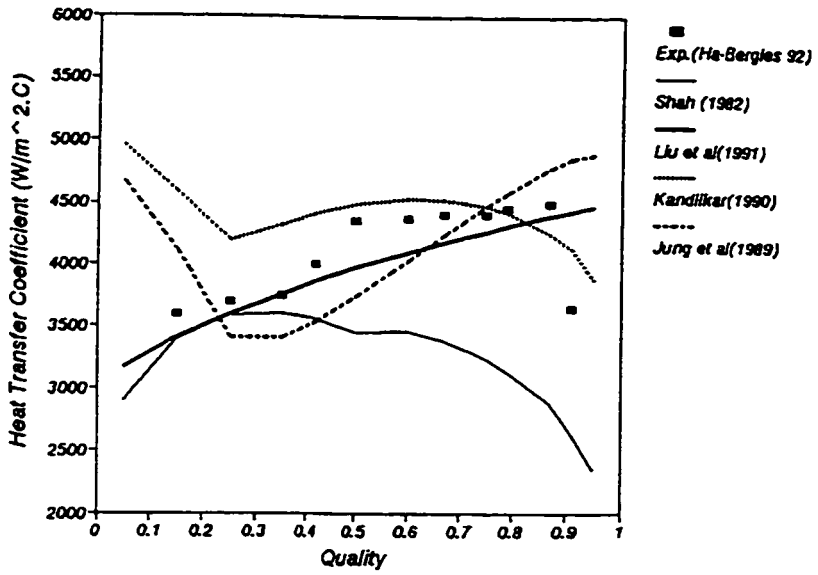

Figure 2.3: Comparison of Different Correlations with Experimental Data for R-12 Boiling Inside a Horizontal Smooth Tube at *327 kPa, q ″= 30 kW/m²*, *G = 295 kg/m²s*, *D = 9.84 mm* (Darabi *et al.*, 1995).

stratification, and partial dryout. Consequently, this omission is the subject of a recent publication series by Kattan *et al.* (1998 a,b,c) which has resulted in the development of a new flow boiling model and correlation in horizontal tubes that includes flow regime effects. The new method is associated with a mean deviation of 13.3% for the 1141 data points tested and predicts most of the trends observed in their experimental investigation. In Kattan *et al.* the prediction of heat transfer is a methodology compared to the semi-empirical/correction factor nature of previous investigations. The Kattan *et al.* (1998c) procedure for calculating the local heat coefficient h_{tp} is summarized in Figure 2.4. This will likely be the direction of research in the future.

The approach initiated by Kattan *et al.* (1998 a,b,c) has been adopted in the present investigation of flow boiling with external electric fields. Although no attempt has been made to directly model heat transfer according to the correlations developed by Kattan *et al.* (1998c) at this stage, significant attention has been designated in Chapters 5 and 6 to predict

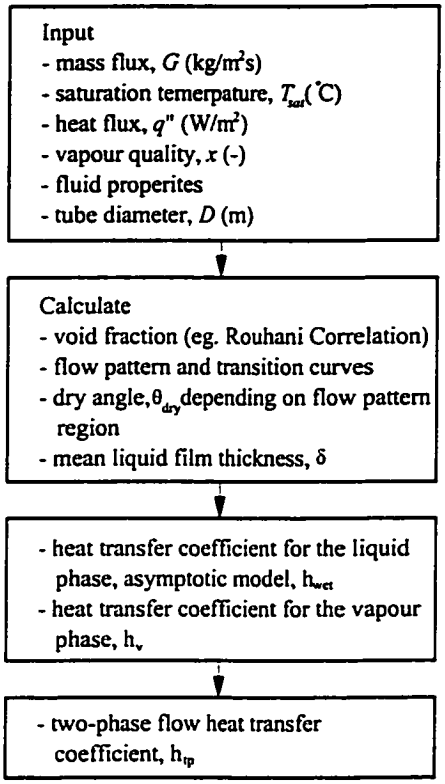

Figure 2.4: Flow Boiling Heat Transfer Coefficient Calculation (Kattan *et al.*, 1998c).

the flow regime in annular geometries with and without the presence of an electric fields. Prior to developing the flow regime transition criterion with an applied electric field, Chapter 3 attempts to introduce the additional complexities involved in the superposition of an electric field to convective boiling channels as observed by previous investigators.

Chapter 3

Electrohydrodynamics

Electrohydrodynamics (EHD) is a technique that couples an electric field with a flow field of a dielectric medium to generate a body force in order to induce a secondary motion in the fluid. The result is the potential to change the flow structure such that the heat transfer characteristics are enhanced. In order to better understand the mechanisms that affect this augmentation, a thorough comprehension of high voltage physics and two-phase thermal phenomena is required. These two fields are rarely encountered together in engineering practice. Therefore, the purpose of this chapter is to review the fundamental theory of electrostatics associated with EHD and study the electrohydrodynamic phenomena for single-phase and phase change processes. Also, this chapter focuses on the recent advances in electrohydrodynamic augmentation of convective boiling.

3.1 Conservation Equations of Electromagnetically Induced Flow

3.1.1 Governing Equations of Electrohydrodynamics

Applications of electromagnetically induced flow are generally restrained to low to moderate Reynolds numbers below Mach numbers of $M = 0.2$. Therefore a subsonic incompressible flow analysis is normally applied. The conservation equations include additional components due to the application of an electric field. These are discussed in detail in the latter part of this section. Free convection flow produced by buoyancy forces

will be included by applying the Boussinesq approximation, for a dimensional analysis comparison. That is, variations of density are ignored, except insofar as they give rise to buoyancy driven gravitational forces. Tritton (1977) provides a thorough systematic examination of the Boussinesq approximation. The fluid is assumed to be Newtonian and continuum fluid mechanics are applied.

With these simplifications and assumptions under consideration, the mass, momentum and energy conservation equations of a laminar fluid influenced by an electromagnetic field can be expressed as follows:

Mass Conservation

$$\frac{\partial \rho}{\partial t} + \rho \nabla \cdot \bar{u} = 0 \tag{3.1}$$

Momentum Conservation

$$\rho \frac{\partial \bar{u}}{\partial t} + \rho(\bar{u} \cdot \nabla)\bar{u} = -\rho F_B - \rho g \beta (T - T_0) - \nabla P + \overline{f_{eB}} + \mu \nabla^2 \bar{u} \tag{3.2}$$

Energy Conservation

$$\rho C_p \frac{\partial T}{\partial t} + \rho C_p \bar{u} \cdot \nabla T = k \nabla^2 T + q_{eB}''' \tag{3.3}$$

where f_{eB} is the body force per unit volume and q_{eB}''' is the energy generation rate per unit volume due to the presence of a magnetic or electric field.

In addition, the equations of electrostatics for a linear ohmic dielectric (Maxwell's Equations) hold and are summarized as follows:

Poisson Equation

$$\nabla \cdot (\varepsilon \bar{E}) = \rho_{ei} \quad , \quad \nabla \times \bar{E} = 0 \tag{3.4 a,b}$$

Charge Conservation for Charge *j*

$$\nabla \cdot \bar{J}_j + \frac{\partial \rho_j}{\partial t} = 0 \tag{3.5}$$

Charge Transport Equation for Positive and Negative Charge Species

$$\bar{J}_j = \rho_j \bar{u} - D_j \bar{\nabla} \rho_j \pm \mu_j \rho_j \bar{E} \tag{3.6}$$

Definition of Electric Potential

$$\overline{E} = -\nabla V \tag{3.7}$$

where ρ_{ei} and σ_e are the net charge density (ρ_e - ρ_i) and conductivity, J, V and D are the current density, electric potential and diffusion coefficient, respectively and the subscript j, e, and i represent charged particles and negative and positive ions. When viscous dissipation cannot be ignored, a mixing coefficient model μ_t or one of the various turbulence models would complete the momentum equation.

3.1.2 Interactions between Electric, Magnetic, Flow and Temperature Fields

The interaction between the electric, magnetic, flow and temperature fields are represented as the additional terms f_{eB} and q_{eB}''' in the conventional momentum and energy equations, respectively. The complete formulation of these additional parameters are presented in the following section and simplified later for particular applications. Without the influence of an electric or magnetic field, the thermophysical state of a fluid can be completely specified with the knowledge of two independent state variables, usually the density and temperature. The thermodynamic behaviour can then be expressed in terms of the Helmholtz free energy per unit mass (A), as a single characteristic function

$$A = A(\rho , T) \tag{3.8}$$

Under the effect of an electromagnetic field, two additional independent 'mechanical' state variables are required. Chu (1959) chose the magnetic flux density B and the dielectric flux density D as the electromagnetic state variables. The Helmholtz free energy becomes

$$A = A(\rho , T , B , D) \tag{3.9}$$

Chu derived the momentum and energy equations of magnetohydrodynamics. The derived equation has been adopted by many in the field including Jones (1978), Ohadi *et al.* (1991), Chang and Watson (1994) and Yabe (1995). The origin of the force lies in the free charge,

electric dipole and magnetic dipole interactions. Chu's equation of electromagnetic hydrodynamics is:

$$\overline{f_{eB}} = \overline{f_1} + \overline{f_2} - \overline{f_3} - \overline{f_4} + \overline{f_5}$$

$$\overline{f_{eB}} = \rho_{et}\overline{E} + J_x\overline{B} - \tfrac{1}{2}E^2\nabla\varepsilon - \tfrac{1}{2}H^2\nabla\mu + \nabla\left[\tfrac{1}{2}\rho E^2\left(\frac{\partial\varepsilon}{\partial\rho}\right)_T + \tfrac{1}{2}\rho H^2\left(\frac{\partial\mu}{\partial\rho}\right)_T\right] \quad (3.10)$$

where

f_1 - force per unit volume due to space charges
f_2 - force per unit volume due to the charge particle motion
f_3 - force per unit volume due to dielectric property changes
f_4 - force per unit volume due to the fluid permeability changes
f_5 - force per unit volume due to the electrostriction and magnetostriction effects

The additional energy term due to the electromagnetic field was also obtained by Chu (1959) and presented in the form:

$$q_{eB}''' = q_1''' + q_2''' + q_3'''$$

$$q_{eB}''' = (\bar{J} - \rho_{et}\bar{u})(\bar{E} + \bar{u} \times \bar{B}) + \nabla\cdot[(\bar{E} + \bar{u} \times \bar{B}) \times (\bar{H} - \bar{u} \times \bar{D})] + \left[\bar{E}\frac{d}{dt}\left(\frac{\bar{D}}{\rho}\right) + \bar{H}\frac{d}{dt}\left(\frac{\bar{B}}{\rho}\right)\right]\rho \quad (3.11)$$

where

q_1''' - heat generation due to flow of charged particles, such as ohmic heating
q_2''' - energy due to the polarization, such as electromagnetic hysteresis loss
q_3''' - energy due to the displacement current and time varying magnetic fields, such as energy storage in an electromagnetic field

The relative importance of each term in Equations (3.10) and (3.11) depends on the working fluid, as summarized by Chang (1998), Table 3.1. Sections 3.2 and 3.3 attempt to elaborate on the effects of the important parameters for non-conducting fluids in single and two-phase flows.

3.1.3 The Electrohydrodynamic Body Force and Electrical Energy

Electrohydrodynamic applications typically refer to the employment of a high voltage-low current electric field, where the magnetic field generated by the current flux can be neglected and only electrohydrodynamically influenced motion and energy generation prevail.

Table 3.1: Relative Importance of EHD Terms (Chang, 1998)

Type of Fluid		Momentum terms due to EMF: f_{eB}	Energy terms due to EMF: q_{eB}'''	Comments
Non-Conducting Fluids (I→small)	Gas Single Phase	$\frac{1}{2}\varepsilon_0(\varepsilon_r - 1)\nabla E^2 + \frac{1}{2}\mu_0(\mu_r - 1)\nabla H^2$	$\nabla\cdot(\bar{E}\times\bar{H}) + [\bar{E}\cdot d(\bar{D}/\rho)/dt + \bar{H}\cdot d(\bar{B}/\rho)/dt]\rho$	$\mu_r \doteq 1$, $\varepsilon_r \doteq 1$, $\nabla\varepsilon$, $\nabla\mu$ *-small*
	Liquid Single Phase	$\frac{1}{2}E^2(\partial\varepsilon/\partial T)_\rho \nabla T$	(same as for gas)	$\rho\partial\varepsilon/\partial\rho$, $\rho\partial\mu/\partial\rho$, $\nabla\mu$ *-small*
	Gas-Liquid Two-Phase	$-\frac{1}{2}E^2\nabla\varepsilon - \frac{1}{2}H^2\nabla\mu$ *(for each phase)* $+\nabla(\frac{1}{2}E^2\rho\partial\varepsilon/\partial\rho + \frac{1}{2}\rho H^2\partial\mu/\partial\rho)$	(same as for gas but for each phase)	$\rho_\varphi = \alpha_v\rho_v + (1-\alpha_v)\rho_l$ $\varepsilon_l, \mu_l \gg \varepsilon_v \mu_v$
Conducting Fluids (I≠0)	Gas Single Phase	$\rho_e\bar{E} + \bar{J}\times\bar{B}$ $+\nabla(\frac{1}{2}\rho E^2\partial\varepsilon/\partial\rho + \frac{1}{2}\rho H^2\partial\mu/\partial\rho)$	$\bar{J}\cdot\bar{E} + \nabla\cdot(\bar{E}\times\bar{H}) + [\bar{E}\cdot d(\bar{D}/\rho)/dt + \bar{H}\cdot d(\bar{B}/\rho)/dt]\rho$	$\rho_e = 0, \nabla\varepsilon, \nabla\mu - 0$ $\bar{J} = \bar{u}n \pm \mu' n\bar{E} - D\bar{\nabla}n$
	Liquid Metal Single Phase	$\bar{J}\times\bar{B}$	$\bar{J}^2/\sigma_e + \nabla\cdot(\bar{E}\times\bar{H}) + \rho\bar{H}\cdot d(\bar{B}/\rho)/dt$	$\rho\partial\varepsilon/\partial\rho$, $\rho\partial\mu/\partial\rho$ -0 $\bar{J} = \mu\bar{E}$, $\rho_e = 0$, $\nabla\varepsilon$, $\nabla\mu$ -0
	Liquid Single Phase	$\rho_e\bar{E} + \bar{J}\times\bar{B} + \frac{1}{2}E^2(\partial\varepsilon/\partial T)_\rho \nabla T$	(same as for gas)	$\nabla\mu$, $\rho\partial\varepsilon/\partial\rho$, $\rho\partial\mu/\partial\rho$ -0 $\rho_e = \rho_+ - \rho_-$
	Gas-Liquid Two-Phase	$-\frac{1}{2}E^2\nabla\varepsilon - \frac{1}{2}H^2\nabla\mu +$ $\nabla(\frac{1}{2}\rho E^2\partial\varepsilon/\partial\rho + \frac{1}{2}\rho H^2\partial\mu/\partial\rho) +$ $\bar{J}\times\bar{B} + \rho_e\bar{E}$ *(for each phase)*	(same as for gas but for each phase)	$\bar{J} = \sigma'\bar{E}^*$ $\bar{E}^* = \bar{E} + \bar{U}\times\bar{B}$ $\bar{H}^* = \bar{H} - \bar{U}\times\bar{D}$

[D : diffusion coefficient, μ : mobility, I : current, σ : electrical conductivity, α_v : void fraction]

For single-phase fluids, the predominant forces depend on the electric field strength, frequency (of alternating fields) and the free charge density existing in the fluid. In phase change processes the contributing factors are the difference in the relative permittivity of the two-phases and their dependence on both density and temperature. The application to single and two-phase mediums with a description of the different models used to explain the effect of the electric field is considered in later sections.

In general, the influence of strong electric fields on heat transfer in fluids may be divided into the effects on the fluid motion and the effects on the thermophysical and transport properties. The latter, including electric field-dependent thermal conductivity and viscosity, have been largely discounted with respect to their influence on heat transfer (Jones, 1978).

With these considerations, the electric body force and the additional electric energy

can be reduced to:

$$\overline{f_{eB}} = \rho_{et}\overline{E} - \frac{1}{2}E^2\nabla\varepsilon + \frac{1}{2}\nabla[\rho E^2(\frac{\partial\varepsilon}{\partial\rho})_T] \tag{3.12}$$

and

$$q_{eB}''' = \sigma_e E^2 \tag{3.13}$$

respectively. However, Equation (3.13) is considered negligible when applied to a dielectric fluid, given that the magnitude for conductivity in typical dielectrics ranges from approximately 10^{-10} to 10^{-16} $\Omega^{-1}m^{-1}$. In the present investigation for properties of HFC-134a at the maximum applied voltage potential $q_{eB}''' \sim 1$ W, see Appendix A for property data.

The three terms on the right-hand side of Equation (3.12) represent the *electrophoretic*, *dielectrophoretic* and *electrostrictive* components of the force, respectively. The electrophoretic force results from the net free charge within the fluid and/or injected from the electrodes. For adiabatic single-phase flows, under the application of direct current, the permittivity is generally constant. Therefore, the second and third terms become negligible and the main driving force behind the EHD-induced secondary motion is $\rho_{et}E$, as depicted in Figure 3.1a.

The dielectrophoretic term is a consequence of an inhomogeneity or spatial change in the permittivity of the dielectric medium due to nonuniform electric fields, temperature gradients or phase differences. The dielectrophoretic force is usually weaker than the free charge force in single-phase flows. However, it may induce a translational motion resulting from the generation of the polarization force in a nonuniform electric field, Figure 3.1b. If two phases exist, then the polarization force due to the dielectrophoretic component may become significant, resulting in a change in the liquid and vapour distribution due to liquid extraction, Figure 3.2c, or the migration of suspended droplets or bubbles, Figure 3.1d. The influence on droplets and bubbles have been extensively studied by previous researchers and

are reviewed in Section 3.3. The effects of liquid extraction on two-phase flow are the primary focus of the present investigation.

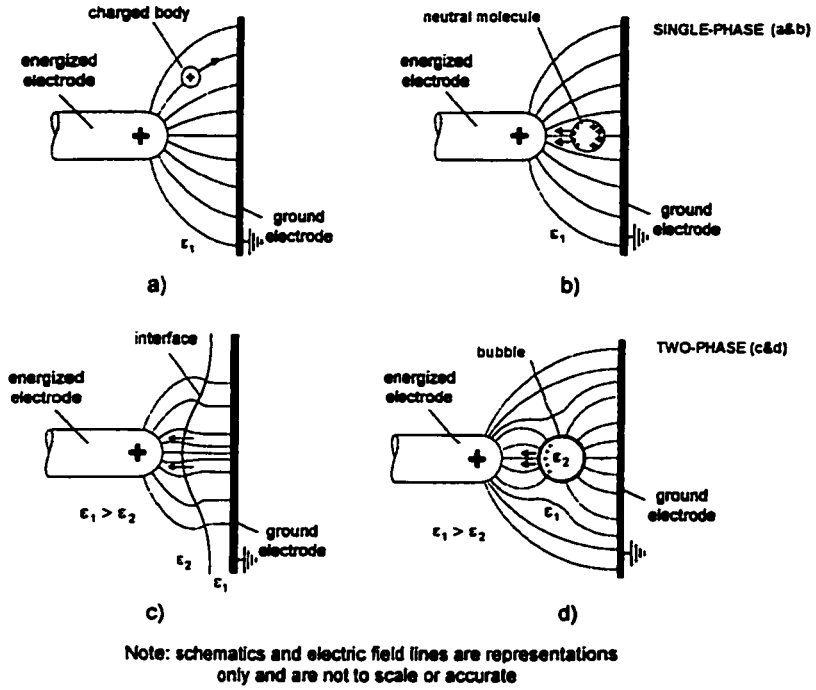

Figure 3.1: Simple Representation of Electric Body Force Density Components on a a) charged body, b) neutral molecule, c) interface and d) bubble (or droplet) (Adopted from Bryan, 1998).

Electrostriction is caused by the inhomogeneity of a fluid either due to additives or to a variation with density/temperature that creates local concentrations or gradients of polarization, as might be encountered in a thermal boundary layer. In general, electrostriction is considered a gradient force and is often neglected, being essentially an "electric pressure" that cannot induce vortex motion within the fluid. Therefore, electrostriction seems not to have an effect on the hydrodynamics (Jones, 1978, Peters *et al.*, 1980a,b, Fujino *et al.*, 1989, Yabe, 1995), although this is a subject of debate as discussed by Bryan (1998). Other reviews describing the influence of an electric field on various fluid systems are by Jones (1978), Chang and Watson (1994), Singh (1995), Yabe (1995), Bryan (1998) and Seyed-Yagoobi and Bryan (1999).

The application of EHD to systems, such as an evaporator, significantly complicates the interactions between the electric field, flow field and temperature field within the system. Figure 3.2 presents an overview of the relationship between the various components of an electrohydrodynamic system.

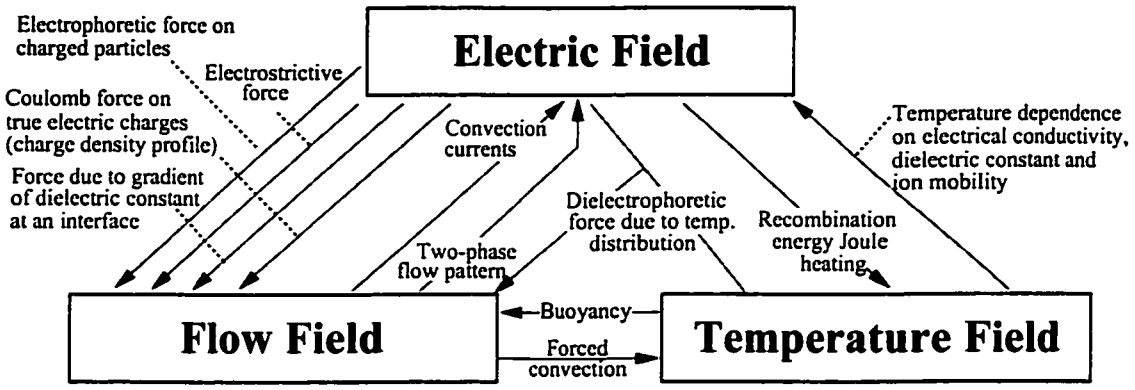

Figure 3.2: Relationship of Electric Fields, Flow Fields and Temperature Fields in Two-Phase Systems.

3.1.4 Dimensional Analysis of the EHD Body Force

The equations of electrohydrodynamics, in spite of their complexity, may be resolved through a dimensional analysis which, as in classical theory, is a powerful procedure to elucidate flow behaviour that cannot be rigorously calculated (Chang, 1989a, Chang and Watson, 1994). In order to develop the dimensionless EHD terms, the analysis is performed for liquid single-phase laminar flow. The complete form of the laminar Navier-Stokes equation, including EHD, free convection terms (approximated by Boussinesq) and incorporating gravity with the pressure term is:

$$\rho\frac{\partial \bar{u}}{\partial t} + \rho(\bar{u}\cdot\nabla)\bar{u} = -\rho\bar{g}\beta\,(T - T_0) - \nabla P + \mu\nabla^2\bar{u} + \rho_e\bar{E} - \frac{1}{2}E^2\nabla\varepsilon + \nabla\left(\frac{1}{2}\rho\,E^2\left(\frac{\partial\varepsilon}{\partial\rho}\right)_T\right) \tag{3.14}$$

By multiplying Equation (3.14) by $L/\rho_0 U_0^2$, where L is the characteristic length of the system and ρ_0 and U_0 are a reference density and velocity characteristic of the system,

and introducing the nondimensional variables:

$$\tilde{u} = \frac{\bar{u}}{U_0} \qquad p = \frac{P}{\rho_0 U_0} \qquad \tau = \frac{tU_0}{L} \qquad \tilde{\nabla} = L\nabla \qquad \gamma = \frac{\rho}{\rho_0} \qquad \theta = \frac{T}{T_0}$$

$$Re = \frac{U_0 L}{\nu} \qquad Pr = \frac{\nu}{\alpha} \qquad Ra = \frac{g\beta T_0 L^3}{\nu\alpha}$$

the nondimensional form of Equation (3.14) may be derived. The subscript *0* is used to describe a reference value. *Pr*, *Re* and *Ra* are the Prandtl, Reynolds and Rayleigh numbers, respectively, ν is the kinematic viscosity, α is the thermal diffusivity and γ is the density ratio, which is approximately unity according to the Boussinesq approximation.

The development of the nondimensional form of the first five terms of Equation (3.14) may be found in any fluid text but the EHD body force will be presented in detail. Considering the sixth term of Equation (3.14), the electrophoretic component of the body force is:

$$\frac{L}{\rho_0 U_0^2}\rho_{ei}\bar{E} = \left(\frac{\sigma_e E_0 L^3}{\rho_0 \nu^2 \mu_c}\right)\left(\frac{1}{Re^2}\right)\tilde{\eta} = \frac{E_{t\sigma}}{Re^2}\,\tilde{\eta} \tag{3.15}$$

where the dimensionless electric field $\tilde{\eta} = \bar{E}/E_0$ and the free charge density definition $\rho_{ei}=\sigma_e/\mu_c$, (*i.e.*, the conductivity over the ion mobility) is used. Here $E_{t\sigma}$ has been termed the *Conductive Rayleigh number* by previous researchers and may be presented in a more measurable quantity by assuming that the free charge density within the fluid is equal to the charge injected by the electrodes, (*i.e.*, $\sigma_e E_0 = J_0 = I_0/A$). That is, if the reference electric field is taken to be at the electrode surface, the current flux may be represented by the total current over the surface area of the electrode assuming uniform charge injection. Therefore, the *Conductive Rayleigh number* becomes:

$$E_{t\sigma} = \frac{\sigma_e E_0 L^3}{\rho_0 \nu^2 \mu_c} = \frac{J_0 L^3}{\rho_0 \nu^2 \mu_c} = \frac{I_0 L^3}{\rho_0 \nu^2 \mu_c A} \tag{3.16}$$

A similar analysis may be presented for the dielectrophoretic force:

$$\frac{1}{2}\frac{L}{\rho_0 U_0^2} E^2 \nabla\varepsilon = \frac{1}{2}\left(\frac{\nu^2}{L^2 U_0^2}\right)\left(\frac{E_0^2 \varepsilon_0 L^2}{\rho_0 \nu^2}\right) \tilde{\eta}^2 \tilde{\nabla}\varepsilon_s \tag{3.17}$$

where ε_0 is the permittivity of free space and $\varepsilon_s = \varepsilon/\varepsilon_0$ is the dielectric constant. Expanding the gradient of the dielectric constant to account for temperature effects:

$$\nabla\varepsilon_s = \left(\frac{\partial\varepsilon_s}{\partial T}\right)_\rho \nabla T + \left(\frac{\partial\varepsilon_s}{\partial\rho}\right)_T \nabla\rho \tag{3.18}$$

and assuming constant density, $\nabla\rho \approx 0$, the dielectrophoretic term becomes:

$$\left(\frac{1}{Re^2}\right)\left(\frac{T_0}{T_0}\right)\left(\frac{E_0^2 \varepsilon_0 L^2 (\partial\varepsilon_s/\partial T)_\rho}{\rho_0 \nu^2}\right) \tilde{\eta}^2 \nabla T = \frac{E_{t\varepsilon}}{Re^2} \tilde{\eta}^2 \tilde{\nabla}\theta \tag{3.19}$$

where

$$E_{t\varepsilon} = \frac{\varepsilon_0 E_0^2 T_0 (\partial\varepsilon_s/\partial T)_\rho L^2}{2\rho_0 \nu^2} \tag{3.20}$$

and $\nabla\theta$ is the dimensionless temperature gradient.

Finally, the electrostrictive term may be expressed in dimensionless form, with the approximation $\rho(\partial\varepsilon/\partial\rho)_T \sim T_0 \varepsilon_0 d\varepsilon_s/dT$ (Landau and Lifshitz, 1963) for liquids and the definition of the gradient of the dielectric constant, as follows:

$$\frac{L}{\rho_0 U_0^2} \nabla\left(\frac{1}{2} E^2 \rho\left(\frac{\partial\varepsilon}{\partial\rho}\right)_T\right) = \frac{\nu^2}{L^2 U_0^2} L\nabla\left(\frac{\varepsilon_0 L^2 E_0^2}{2\rho_0 \nu^2}\frac{d(\varepsilon_s - 1)}{dT} \tilde{\eta}^2\right) = \frac{E_{t\varepsilon}}{Re^2}\tilde{\nabla}(\theta\tilde{\eta}^2) \tag{3.21}$$

where the *EHD number* in Equation (3.21) is identical to that defined by Equation (3.20). Combining the three dimensionless terms of the EHD body force (Equations 3.15, 3.19 and 3.21) with the nondimensional form of the first five terms of Equation (3.14), the governing equation becomes:

$$\frac{\partial\tilde{u}}{\partial\tau} + \tilde{u}\cdot\tilde{\nabla}\tilde{u} = \frac{Gr}{Re^2}(\theta - 1) - \tilde{\nabla}p - \frac{1}{Re}\tilde{\nabla}^2\tilde{u} + \frac{\left(E_{t\sigma}\tilde{\eta} - E_{t\varepsilon}\tilde{\eta}^2\tilde{\nabla}\theta + E_{t\varepsilon}\tilde{\nabla}(\theta\tilde{\eta}^2)\right)}{Re^2} \tag{3.22}$$

When a liquid and gas are combined to form a two-phase mixture, the arguments are complicated by the interfacial jump in electric field strength and the singularity of the

dielectric constant at the liquid-vapour interface. This creates a problem as the EHD effects at the interface are typically the subject of interest in the field of EHD.

Confusion arises when one considers the terminology of *Electric Rayleigh numbers* used to describe $E_{t\sigma}$ and $E_{t\varepsilon}$ by previous investigators (Ashmann and Kronig, 1951). A more appropriate terminology would be to describe the EHD numbers as *Electric Grashof numbers* due to the similarity between the electrical parameters and the dimensionless parameter, the Grashof number, which is used to describe free convective flow as exemplified by Equation (3.22). The Grashof number indicates the ratio of the buoyancy forces to the viscous force acting on the fluid and the EHD numbers, $E_{t\sigma}$ and $E_{t\varepsilon}$, represent the ratio of electrophoretic and dielectrophoretic/electrostrictive forces to viscous forces acting on a fluid element, respectively.

Using an analogy to free convective flows, it is proposed that the combined effects of electric and forced convection must be considered when $(E_{t\sigma}/Re^2)\sim 1$ and/or $(E_{t\varepsilon}/Re^2)\sim 1$. If the inequalities $(E_{t\sigma}/Re^2)<<1$ or $(E_{t\varepsilon}/Re^2)<<1$ are satisfied, electric convection effects may be neglected and conversely, if $(E_{t\sigma}/Re^2)>>1$ or $(E_{t\varepsilon}/Re^2)>>1$, forced convection effects may be neglected. This is analogous to buoyancy driven flows and a similar argument may be made by comparing the EHD numbers to the Grashof number.

Chang and Watson (1994) successfully presented a similar comparison for single-phase air in an attempt to provide regimes of electrically induced motion over free convective motion by combining the dimensional analysis of the electrophoretic and electrostrictive terms with typical experimental data taken from both Chang and Tran (1980) and Haidra and Atten (1985). Chang and Watson show that the influences of EHD flow increase with increased electric field for both components of the dimensionless EHD terms, and increased with charged particle density and smaller electrode gap distances for the

electrophoretic and electrostrictive components, respectively. The regimes are clearly identified when the EHD numbers are compared to the Grashof number in a similar fashion to the comparison between the EHD numbers and the Reynolds number described above. When the ratio $E_t/Gr \leq 10^{-2}$, electrical influences may be ignored and when $E_t/Gr \leq 10^{2}$, free convection may be neglected. However, between these extremes both influences should be considered.

The influence of the thermophysical properties with respect to temperature and the applied voltage on the EHD dimensionless numbers for saturated liquid and vapour refrigerant HFC-134a are presented in Appendix A.

3.2 The EHD Flow Phenomena in Single-Phase Liquids and Gases

Investigations involving the mechanisms of single-phase EHD enhanced flow are well documented by several researchers including Schneider and Watson (1970), Melcher (1976), Felici and Lacroix (1978), Peters *et al.* (1980a,b), Atten *et al.* (1987), Fernández and Poulter (1987), Chang and Maezono (1989), Fujino *et al.* (1989) and Cross and Wang (1991). The flows produced by the application of an electric field on single-phase fluids are referred to as the *corona* or *ionic wind* for gases and *electroconvection* for dielectric liquids. These expressions originate as the permittivity ε remains relatively constant for most fluids, irrespective of electric field strength and temperature gradients. In addition, since corona discharge-generated heat is small, the effect of ε variation with temperature is negligible in adiabatic systems. In such cases, the electric body force simplifies to:

$$\overline{f_{eB}} = \rho_{et}\overline{E} \tag{3.23}$$

which is the Coulomb force resulting from the interaction of the electric field with free space-charges.

As Fujino *et al.* (1989) summarized, there are two generally accepted explanations regarding the origin of the charge distribution of net space-charge, ρ_{ie}. One assumes the distribution results from thermally induced variation in the electrical conductivity of the fluid and the other assumes injection of charge from either or both electrodes as the cause of the distribution. The two interpretations arise directly from the charge transport equation and the net charge in a fluid:

$$\bar{J} = (\rho_{e+} - \rho_{e-})\bar{u} + [-(D_+\nabla\rho_{e+} - D_-\nabla\rho_{e-}) + \bar{E}(\mu_+\rho_{e+} - \mu_-\rho_{e-})] \qquad (3.24)$$

where μ_e is the ion mobility and the conductivity has been replaced by $\sigma_e = \mu_e \rho_{ei}$. The first term is the *conductivity component* and the latter term is the *mobility component*, which depend on the origin of the space charge.

Fujino *et al.* stated that for the conductivity version of distribution to be valid, a temperature gradient in the fluid is an indispensable condition for convection to occur and the intensity of the convection depends on the magnitude of the gradient. Peters *et al.* (1980a,b) described the mobility version by two driving mechanisms which govern bulk convection in the absence of a thermal gradient. The first mechanism dominates the low-intensity field motion, denoted as the electroconvection at the wall. Here the diffuse charge present at the layer of liquid adjacent to the wall is swept away by the tangential component of the electric field. A shear stress results, giving rise to circulatory bulk motion. The second mechanism, at high field strengths, is caused by the injection of free charge from the electrodes that are then acted upon by the electric field.

A limitation to the mechanisms of induced flow occurs when a fluid is under the influence of a high frequency alternating current. Under such applications the free space charge will, in a sense, 'not know which direction to go' as its polarity drives it toward the electrode of opposite charge. This action is commonly referred to as the charge relaxation

time (Jones, 1978, Melcher, 1981, Yabe, 1995). The electrical charge relaxation time is defined as:

$$\tau_\sigma = \varepsilon/\sigma_e \tag{3.25}$$

which measures the rate at which free charge relaxes from the bulk to the outer boundary of a dielectric mass. If the electric field is alternating at a frequency f and $f >> 1/\tau_\sigma$, no free charge can accumulate in the fluid bulk or, alternatively, at the interface in two phase flows $\rho_{ei}E \approx 0$. For electrically induced motion to exist, other body forces must be dominant.

If this circumstance is encountered or if the fluid has no free charge and a nonuniform electric field is applied, dielectrophoresis could explain an induced flow. Here polarization forces create a relative displacement of positive and negative bounded charge in a neutral body due to the electric field. The induced dipole resulting from the displacement of charge will experience a net unidirectional force in a nonuniform electric field. For example, if the electric field strength is stronger near the negative charges, $E_N > E_P$ (N≡Negative, P≡Positive) then the electric force generated near the negative charges will be greater and a net translational motion in the direction of the higher field results, $F_N > F_P$. This result holds true regardless of the polarity. Therefore, the flow induced always tends toward the high field strength regions.

3.3 The EHD Phenomena in Liquid-Vapour Phase-Change Process

The focus of recent research on electrohydrodynamics has shifted to applications related to phase-change enhancement. In the category of evaporation, condensation and nucleate boiling heat transfer enhancement, investigators such as Bonjour *et al.* (1992), Velkoff and Miller (1965), Choi (1968), Lovenguth and Hanesian (1971), Dodkoski and Bologa (1981), Chang (1984), Cooper (1992), Ogata *et al.* (1992), Ohadi *et al.* (1992,

1993a,b), Singh (1995), Yabe (1995) and Seyed-Yagoobi and Bryan (1999) have reported significant enhancement results. The major difference is that the dominant forces are both dielectrophoretic and electrostrictive due to the differences in permittivity between the liquid and vapour. Typical values are approximately $\varepsilon_v \sim 1$ for gases and in the range of $\varepsilon_l \sim 2\text{-}10$ for dielectric liquids. Neglecting electrophoretics, the electrohydrodynamic body force is reduced to:

$$\overline{f_{eB}} = \frac{\varepsilon_0}{2} E^2 \nabla \varepsilon_s + \frac{\varepsilon_0}{2} \nabla [E^2 \rho (\frac{\partial \varepsilon_s}{\partial \rho})_T] \tag{3.26}$$

where dielectric constant, $\varepsilon = \varepsilon_0 \varepsilon_s$ has been introduced. Inspection of Equation (3.26) presents some general characteristics inherent to EHD influenced systems as they are applied to heat transfer:

- The higher the non-uniformity in electric field, the higher the EHD force. Thus there is a great potential for heat transfer enhancement effect.
- Force is proportional to electric field strength. Higher electric field strength should give higher enhancement, although limited by the dielectric breakdown voltage.
- For two-phase flow processes, $\nabla \varepsilon_s$ plays a key role as at the liquid-vapour interface the dielectric constant is discontinuous and therefore singular, resulting in a large dielectrophoretic force.

Even the simplest form of the electrohydrodynamic body force is very complex and, when coupled with the flow, state and electric governing equations, a simple solution is not possible. In order to better describe the observed phenomena and mechanisms of motion influencing liquid-vapour interactions and heat transfer characteristics of evaporator channels, the problem is typically reduced to the influences on the nucleate boiling and flow regime transitions (phase redistributions), the latter being attributed to the interfacial instabilities created, which is commonly referred to as the liquid extraction phenomena. The following sections provide a brief overview of these components of flow boiling. In

Chapters 4 and 5 the influences on flow regimes is studied in detail.

3.3.1 Electrohydrodynamic Effects on Boiling Bubbles

The mechanism of bubble migration in conventional boiling phenomena, in very simplistic terms, is bubble generation and growth at nucleation sites on the surface in a superheated liquid until departure occurs when buoyancy forces exceed interfacial tensions. When these forces are coupled with the developed forces under the application of an electric field, the behaviour of the bubbles becomes far more complex due to the imposed Maxwell stresses, *i.e.* the electrohydrodynamic forces. Several researcher including Norris *et al.* (1999), Chang and Watson (1994) and Eames and Sabir (1997) have summarized the possible mechanisms of the EHD technique applied to boiling. In general the dominant influences are:

- Movement of vapour bubbles at the heated surface (Lovenguth and Hanesian, 1971, Ogata and Yabe, 1993a,b).
- Spreading of the vapour bubble base over the heat transfer surface, thus increasing micro-layer evaporation (Pounder, 1980, Ogata and Yabe, 1991, 1993a).
- Increasing the number of bubbles by breaking up large bubbles and decreasing the bubble detachment diameter, thereby creating more turbulence and more interfacial area (Pounder, 1980, Cheng and Chaddock, 1986, Ogata *et al.*, 1985, Kawahira *et al.*, 1990, Ogata and Yabe, 1993a, Eames and Sabir, 1997). Both effects are due to the EHD force elongating the bubble and overcoming surface tension at the liquid/vapour interface (Garton and Krasucki, 1964, Johnson, 1968, Lovenguth and Hanesian,1971).
- Elimination of boiling hysteresis, thereby decreasing the degree of superheat required to initiate nucleate boiling. It has also been reported that, in some cases, once ebullition begins, initiated by an electric field at low superheat temperature, it could be maintained without having to maintain the electric field (Damianidis *et al.*, 1992, Eames and Sabir, 1997, Seyed-Yagoobi *et al.*, 1997, Cooper, 1990).
- Improvement of transitional and minimum film boiling conditions as the electric field tends to destabilizing the blanket vapour film, resulting in a rewetting of the surface (Johnson, 1968, Lovenguth and Hanesian, 1971, Jones and Schaffer, 1976, Berghmans, 1976).

- Increased rewetting of the heated surface through a decrease in surface tension due to the presence of an electric charge (Pounder, 1980).
- Introduction of instabilities on the vapour/liquid interface producing waves and perturbations at the surface of a boiling liquid, which is known to increase the heat transfer across the bulk (Johnson, 1968, Lovenguth and Hanesian, 1971).
- Enhancement of condensation observed in a latent heat transport process (Bologa *et al.*, 1980).
- Enhancement of droplet and bubble motions due to electrostatic charging (Stuetzer, 1963a,b).

It has been shown that the combination of the above mechanisms can enhance heat transfer throughout the boiling regimes. Figure 3.3 is a schematic of the boiling curve with and without EHD observed in numerous experimental investigations involving nucleate boiling with electric fields. The magnitude and the nature of enhancement are a strong function of the electric field strength and dielectric properties of the fluid. Several studies

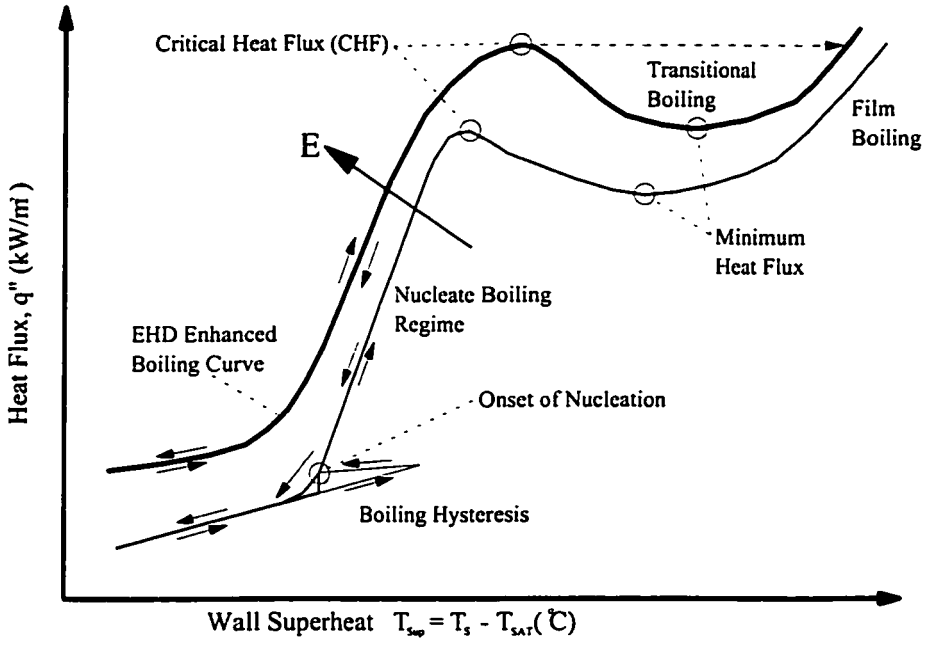

Figure 3.3: Schematic of EHD Enhanced Pool Boiling
(Adopted from Chang and Watson, 1994).

have suggested that the enhancement of nucleate boiling may depend on the relaxation time of the electric charges (Jones and Schaeffer 1976, Jones, 1978, Yabe, 1991, Ogata *et al.*, 1992),

$$\tau_\sigma = \varepsilon/\sigma \tag{3.27}$$

which measures the rate at which a free charge relaxes from the bulk to the outer boundary of a dielectric mass. During boiling, this order of magnitude type analysis implies that the relaxation time of a fluid must be smaller than the generation period of the bubbles for charges to accumulate on the interface such that the electrophoretic term may affect the bubble behaviour. The applicability of this parameter, τ_σ, has been applied in several investigations. For example Ogata *et al.* (1992) applied the McFadden and Grassmann (1962) correlation of bubble detachment period:

$$\tau_{BD} = C\left[\frac{(\rho_l - \rho_g)g}{d_b\rho_l}\right]^{-1/2} \tag{3.28}$$

where C is a constant and d_b is the bubble departure size and found that the departure period of R-11 was approximately 2×10^{-2} sec. Comparing this to the charge relaxation time in Table 3.2 suggests that boiling in refrigerant R-11 may not be affected by the application of a DC electric field. Ogata *et al.* implied that the only influence the electric field could therefore have on nucleation was due to the inhomogeneous electric field. Yokoyama *et al.* (1987) confirmed this criterion ($\tau_{BD} < \tau_\sigma$) in an investigation into the effects of EHD on R-11.

Table 3.2: Relaxation Time of Electric Charges for Various Fluids (Ogata *et al.*, 1992).

Fluid	Relaxation Time τ (sec)	AC Frequency Limit (Hz)
R11	1.3	~1
R11+Ethanol 2^{wt}%	9.2×10^{-3}	~100
HCFC123	0.89×10^{-3}	~1200
Ethanol	1.8×10^{-3}	~600

Similar to single phase flow, the concept of using this order of magnitude analysis to infer the dominant electrical mechanisms, also gives an estimate of the limiting alternating frequency as shown in Table 3.2. For the working fluid used in the present experimental investigation (HFC-134a) the relaxation time is $\sim 5 \times 10^{-2}$ sec under the application of a DC voltage, as presented in Appendix A. As the bubble departure period is expected to be of the same order as R-11, the bubble dynamics of HFC-134a is expected to intensify under the application of an electric field.

The effects described in this section attempt to clarify the characteristics and basic phenomena of bubble behaviour enhanced by EHD. Due to the complexity of conventional boiling combined with electrohydrodynamic effects, most investigations have focussed on qualitatively describing bubble behaviour dynamics. Significant enhancement results have been reported for all processes in heat transfer. The highlights of selected past work involving pool boiling in refrigerants are detailed in the literature review of Singh (1995) and Seyed-Yagoobi and Bryan (1999). Table 3.3 is a summary of Singh's review.

As Table 3.3 suggests, the enhancement varies significantly for different heat transfer surfaces, electrode geometries and processes. By better understanding the mechanisms of bubble behaviour and the nature of phase interactions, successful application of the electrohydrodynamic technique can be achieved by utilizing the EHD effects in ranges or regimes that increase system performance.

3.3.2 The Liquid Extraction Phenomena

The extraction of liquid from a surface by applying EHD is an important characteristic that may, under certain circumstances, increase or decrease evaporative heat transfer through the redistribution of liquid and thinning of the liquid thermal boundary layer or the removal of liquid from a heated surface. As the application of an electric field can

Table 3.3: Selected Previous Work in EHD Enhanced Shell-Side Refrigerant Pool Boiling.

Source	Heat Transfer Surface	Electrode Geometry	Fluid	Applied High Voltage	Max. P/Q (%)	Max. η	Remark
Ohadi *et al.* (1995b)	19 fpi Tube	Wire Electrode	R-123	2 kV	0.1	5	External Boiling
Ohadi *et al.* (1995a)	Flat Plate	Perforated Plate	R-123	0-10kV	0.1	3	External Boiling
Singh *et al.* (1993)	19 fpi Tube	Mesh Wire	R-123	0-20kV	3	8.5	External Boiling
Ohadi *et al.* (1992)	Smooth Tube	Straight Wire	R-123	0-20kV	NA	4.5	External Boiling
Ogata & Yabe (1991)	Smooth Tube	Straight Wire	R-11/ ethanol	0-25kV	NA	8.5	External Boiling
Cheung *et al.* (1995)	40 fpi Tube Bundle	Straight Wire Mesh Wire	R-134a	0-15kV	1.2 3.0	35.5	External Boiling
Ogata *et al.* (1992)	Smooth Tube Bundle	Straight Wire	R-123	0-20kV	NA	8.0[b] 2.5[c]	External Boiling [b]5 tube bundle [c]Blench Scale bundle
Yamashita & Yabe (1995)	Smooth Tube	Rolled Punched Plates	R-123	10-16kV	0.1	6	Falling film

NA: Not Available, P: EHD Power Consumption, Q: Condenser Power, η: EHD Enhancement Factor, fpi: fins per inch.
(Adopted from Singh, 1995)

draw liquid away from the heat transfer surface at high quality values, conversely it may augment condensation heat transfer rates by increased removal of liquid from a condensing surface. These influences are a result of surface instabilities created at the liquid-vapour interface and have been investigated both theoretically and experimentally by many researchers such as Melcher (1961, 1963), Yabe *et al.* (1982, 1987a, 1987b) and Singh (1995). Figure 3.4 presents this effect applied to the simple case of parallel-plate electrode geometries containing an initially stationary stratified liquid and vapour.

In the absence of an electric field, a static planar liquid-vapour interface exists due to surface tension and gravitational restoring forces. In most cases, the vapour phase is highly insulating compared to the liquid phase. Consequently, upon applying the electric field for a period greater than the relaxation time, the electric field in the liquid would decrease to near zero value compared to the vapour electric field and a surface charge would develop at the interface. As discussed in Chapter 6, the development of a surface charge is

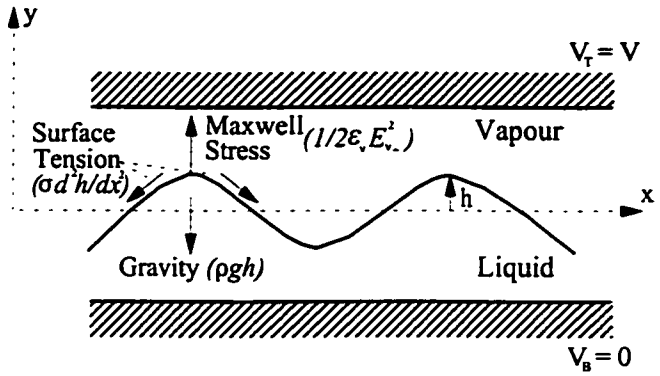

Figure 3.4: Liquid Extraction Phenomena, EHD Instability on the Liquid-Vapour Interface.

not a necessary criterion for liquid extraction although the effect is less significant without it. The result is near zero Maxwell stresses in the horizontal direction and stresses equivalent to $\sim \frac{1}{2}\varepsilon_v E_{v\perp}^2$ in the vertical direction. The vertical stress on the interface attracts the liquid surface toward the upper electrode, extending the surface. This infinitesimal rise in the liquid level will cause a further increase in the Maxwell stresses due to the smaller distance between the electrode and the interface, forcing the liquid height to increase further. The EHD forces become greater than the restoring forces and consequently instability occurs.

The phenomena of liquid extraction can be extended to any nonuniform electric field, such as a needle approaching a horizontal interface as discussed by Singh (1995). Similar to the parallel plate arrangement in Figure 3.4 surface instabilities, which are enhanced by the nonuniformity of the electric field, extend the liquid height toward the needle.

When coupled with fluid flow, either in the form of nucleate bubble motion or forced convection this simple analysis becomes far more complex. However, similar affects have been suggested to contribute to the augmentation of nucleate boiling dynamics as described in Section 3.3.1 and/or lead to flow regime transitions (Brunner and Chang, 1980). The effects created by the latter, flow regime transition in convective evaporation is the subject of investigation in Chapter 6 through 8.

3.4 State-of-the-Art in EHD Convective Evaporation

Although significantly more complicated, these mechanisms may be transferred to the tube-side flow boiling application. Previous work has focussed on the enhancement results of the mechanisms in the form of parametric studies of individual test facilities to describe overall heat transfer and are system dependent. For this reason, it is very difficult to compare the results of the various investigations. Experiments involving EHD augmentation heat transfer in horizontal tube-side flow boiling have been conducted by Yabe *et al.* (1992), Singh *et al.* (1994, 1995), Salehi *et al.* (1995,1996), Seyed-Yagoobi *et al.* (1997), Cotton *et al.* (1998a, 1998b) and Norris *et al.* (1999). Seyed-Yagoobi and Bryan (1999) provided a review of several of these recent investigations. Table 3.4 presents a summary of several recent investigations into the effect of electrohydrodynamics in flow evaporator channels of various electrode configurations and operating parameters. This table includes the type of analysis and typical heat transfer performance compared to the present experimental investigation.

The applicability to heat transfer enhancement of environmentally safe refrigerants has been successfully demonstrated in a number of studies including a 15-ton prototype EHD condenser (Yamashita *et al.*, 1991) and various compact heat exchangers (Ohadi, 1991). A similar arrangement to that conducted in the present investigation was reported by Singh *et al.* (1994, 1995). The investigations were a study of the EHD enhanced heat transfer for R-123 and R-134a in a smooth tube with a straight electrode as a function of mass flux, inlet quality and heat flux at a given applied electric field potential. Singh *et al.* reported enhancement of heat transfer coefficient by as much as 5.5 fold and 3 fold for R-123 and R-134a, respectively, over the range of conditions tested.

Table 3.4: EHD Experiments and Corresponding Operating Parameters From Various Tube-Side EHD Flow Boiling Investigations.

Reference	Fluid	Tube	D_i mm	L m	Electrode	D_e mm	T_{sat} °C	G kg/m²s	x	q'' kW/m²	Voltage	Dim. Anal.	Electric Field Analysis	h_o W/m²K	h_e W/m²K
Yabe *et al.* (1992)	R123 R134a	Smooth	10	3.75	Perforated tube	5	30	33 & 66	0 - 0.9	4[c]	DC	No	No	500 - 1000	1050 - 2000
Singh *et al.* (1994)	R123	Smooth	9.4	1.22	Cylindrical	3	25	50 - 400	0 - 0.5[b]	5 - 20[c]	DC	No	No	800	3800
Single *et al.* (1995)	R134a	Smooth	9.4	1.22	Cylindrical	3	25	50 - 400	0 - 0.5[b]	5 - 20[c]	DC	No	No	2100	4600
Salehi *et al.* (1995)	R134a	Micro-fin	12.7[a]	0.11	Cylindrical	9.5[a]	25	50 & 100	0 - 0.6[b]	25[d]	DC	No	No	5000	50000
Salehi *et al.* (1996)	R404A	Micro-fin	12.7	0.3	Helical	9.8	25	50 - 200	0 - 0.8[b]	10[d]	DC	No	No	3000	7000
Bryan & Seyed-Yagoobi (1997)	R134a	Smooth	14.1	0.3	Cylindrical	1.6	5	100 - 300	0 - 0.6	5 - 150[c]	DC	No	Limited	3484	22733
Norris *et al.* (1999)	R134a	Smooth	10.9	1.5	Cylindrical	3.18	25	100 - 250	0.2 -0.5	10 - 40[c]	DC	No	No	27 (kW/m²)	18 (kW/m²)
Present Work	R134a	Smooth	10.9	1.5	Cylindrical Eccentric	3.18	25	50 - 550	0 - 0.6[b]	10 - 25[c]	DC 60 Hz 6.6 kHz	Yes	Yes	3000	9000

Portions adopted from Seyed-Yagoobi and Bryan (1999)

a: annulus resulting from tube and cylindrical electrode is separated into 12 microchannels, each with a hydraulic diameter of 2 mm.
b: measured at inlet to test section and different from test section quality.
c: heat flux is averaged and is not constant along test section.
d: test section heated by resistive electrical heater.

The heat transfer enhancement decreased with an increase in mass flux and inlet quality. Optimum enhancement was attributed to the flow regime encountered at low qualities (*i.e.* bubbly and slug flow). Various studies have suggested that as the inertial forces increase with increasing mass flux, the EHD forces were suppressed. Similarly, as the quality increased, better boiling dynamics associated with high quality flow reduced the EHD effect. In addition, depending on the mass flux, some studies have shown that at high qualities, above approximately 50%, the rate of heat transfer can be reduced (Singh *et al.*, 1994, 1995, Norris *et al.*, 1999) due to the liquid extraction promoting early partial dryout.

A few researchers have published extensive reports on the subject and the emphasis has been on the final results, the amount of heat transfer enhancement. The present investigation attempts to provide a first step towards a mechanistic approach to resolving the effects of electrohydrodynamics on flow boiling by:

- Studying the behaviour of flow boiling using a more localized method.
- Investigating the interdependence between electric field distributions and flow patterns and its subsequent affect on the heat transfer rate.
- Developing a diabatic EHD flow pattern map for concentric channels.
- Using the dimensionless EHD numbers which in the future may be used for investigation, comparison and design scaling.

In general, all aspects discussed in this chapter contribute to the augmentation of two-phase flow boiling. Potential to accurately determine the various regimes of flow boiling, where flow visualization is not practical or possible, should be increased with the aid of dimensional analysis and a flow regime transition criterion for systems involving electric fields. This will eventually lead to a far more comprehensive understanding of the phenomena for future design and development of systems employing the significant advantages of electrohydrodynamics to improve heat transfer control and enhancement.

Chapter 4

The Test Facility and Data Reduction

This part of the report contains the details of the experimental arrangement. The design and apparatus used in the experiment, the experimental procedure, data reduction methods and experimental uncertainties are examined.

4.1 The Test Facility: Components and Instrumentation

The primary function of the test facility is to measure the two-phase Nusselt number, flow regime, pressure drops and electrical parameters of a counter-current evaporator channel, with and without the application of DC and AC electric fields, in concentric and eccentric electrode configurations.

Figure 4.1 shows a schematic of the experimental test facility. It is a closed loop charged with the refrigerant HFC-134a, which serves as the primary working fluid. The main components of the loop are the pump, electrically heated sections, hot water heated section, condenser, pressurizer, test section and various measuring devices.

Liquid refrigerant, from the condenser, is circulated through the loop by a gear pump driven by a variable speed electric motor. The flow rate of the single-phase liquid refrigerant is measured by one of two turbine flow meters (Omega, FTB-502 or FTB-100) located down stream of the gear pump. These meters cover the flow ranges of 0.1 - 1.0 *l*/min and 1.3 - 13 *l*/min, respectively, both having a calibrated accuracy of within 0.5% of reading.

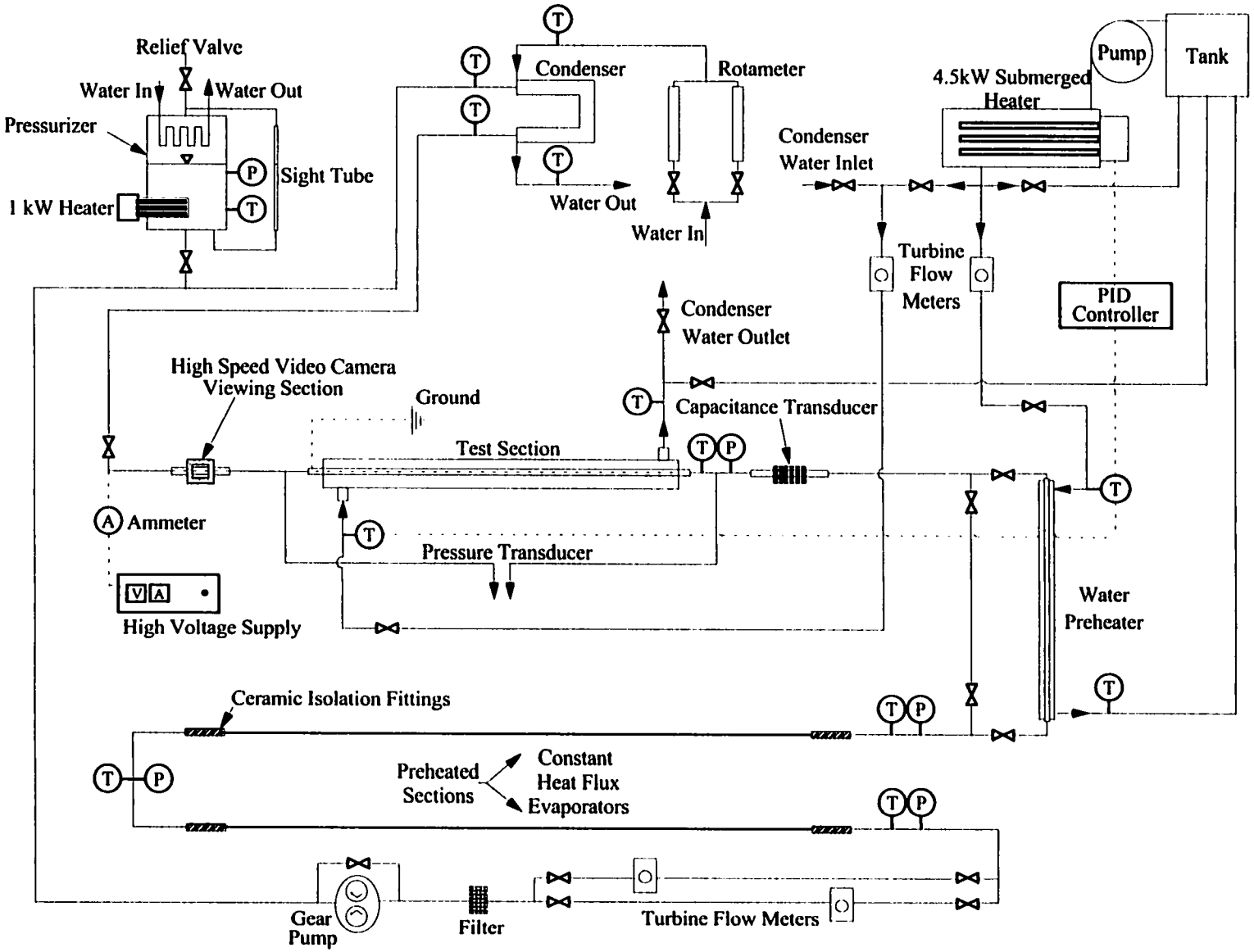

Figure 4.1: Schematic Diagram of Test Facility.

Two methods of heating the refrigerant were used to generate the required two-phase flow conditions at the inlet of the test section: direct electric heating and hot water heating in a heat exchanger. The electrical heating system consisted of two, 1.8 m long, stainless steel tubes having a 12.7 mm outer diameter and 0.25 mm wall thickness. They were connected in parallel to a three-phase rectified 100 kW power supply with a regulated current output and electrically insulated from the rest of the loop by ceramic insulating Swagelok® Unions, as shown in Figure 4.1. The preheaters were also connected in parallel to a water cooled stainless steel tube to reject excess heat and adjust the power supply to the refrigerant loop as required. The power imposed on the flow was determined by measuring the voltage across the 1.8 m long sections and across a shunt resistor in series with the tubes, in order to obtain the current drawn from the power supply.

The hot water preheater was a 1.2 m long single-pass shell-and-tube side heat exchanger, with water flowing through the jacket and refrigerant on the tube side. The heating water flow and temperature were controlled through the secondary water loop, shown in Figure 4.1, and described in Section 4.1.1. The power introduced in this preheater was measured by an overall energy balance on the water side of the heat exchanger through the measurement of the differential temperature and flow rate via inlet and outlet thermocouples and a turbine flow meter (FTB-100). The total amount of heat transferred by both preheating methods was:

$$Q_{PRE} = (V_{e_1} I_{e_1} + V_{e_2} I_{e_2}) + \dot{m}_{W\text{-}PRE}\, C_{p_W} (T_{W\text{-}PRE\text{-}i} - T_{W\text{-}PRE\text{-}o}) \qquad (4.1)$$

applying the description of the measured parameters in Table 4.1. The refrigerant exiting the heat exchanger was then introduced into a straight section of tubing 50 diameters in length (0.55 m) to achieve fully developed conditions prior to entering the test section.

A 30 kW (max) co-axial single-pass condenser returned the two-phase mixture

exiting the test section to its original single-phase conditions. The water which flowed through the shell side in an open loop configuration was supplied by the municipal line and expelled upon exiting the condenser. The flow, controlled by throttle valves, was measured by one of two Fischer & Porter®, Series 10 A, Flowrator meters having maximum capacities of 3.07 l/min and 10.22 l/min, respectively, with an accuracy of ±2 % of full scale. The inlet and outlet temperatures were measured by two type-T thermocouples to determine the total heat extracted from the refrigerant:

$$Q_{COND} = \dot{m}_{W\text{-}COND} C_{p_W} (T_{W\text{-}COND\text{-}o} - T_{W\text{-}COND\text{-}i}) \quad (4.2)$$

As a method of validating the experimental measurement, the power extracted from the refrigerant, measured by the energy balance on the water side of the condenser, was compared to the sum of the power dissipated in the preheaters and the test section. The energy balance for all conditions tested was found to be within ±5 %.

The section between the condenser and the pump was connected to a pressurizer used to manually control the pressure of the entire loop in the range of 0.3 MPa to 0.9 MPa. The pressurizer, made of a stainless steel cylinder (15.24 cm in diameter x 30.48 cm height), was equipped with an immersed electrical heater and a submerged coiled water cooler to increase and decrease the pressure, respectively.

The temperature and pressure of the system were monitored at various locations around the test facility as shown in Figure 4.1. Temperature measurements were conducted by 1.6 mm, T-type thermocouple probes and pressure was monitored using spring type pressure gauges. Measurements related to the test section and high voltage system are discussed in Section 4.1.2 and 4.1.3, respectively.

4.1.1 The Secondary Water Loop

Water was heated in a closed loop to provide hot water for evaporating the refrigerant in the preheater and test section. The loop consisted of a reservoir, centrifugal pump, submerged heater, two turbine flow meters and a control system. Water flowed from the reservoir, through the pump and into the heater, which consisted of a 15.24 cm diameter horizontal cylinder containing a 4.5 kW, 3-coil, single-phase, screwplug-type heater. The heater was powered by a 600 V AC power supply using a Proportional-Integral-Derivative (PID) controller. The controller thermocouple was located at the water side inlet to the test section, and the temperature was set and held constant to within ±0.1 °C. Water flowed from the heater through a filter then branched either to the test section, the preheater or was recirculated back to the reservoir through a back-flow loop. Prior to entering the test section or preheater, the volumetric flow was measured by one of the two (FTB-100) turbine flow meters. The test section could also act as a condenser by introducing chilled water (system not shown) downstream of the heater as shown in Figure 4.1. For condensation experiments, the control thermocouple was located at the water side inlet of the preheater.

4.1.2 The Test Section

The test section consists of inlet and outlet viewing sections, the evaporator channel consisting of the water jacket and test section tube, the high voltage electrode and the accompanying system instrumentation. A schematic diagram is shown in Figure 4.2. The evaporator channel used was a concentric tube single-pass counter-current flow device 1.5 m in length. The tube, containing the two-phase refrigerant mixture, was stainless steel 1.8 m in length, 12.7±0.5 mm outside diameter and 10.9±0.5 mm inside diameter. The heating jacket, using water as the working fluid, was a PVC pipe, 1.5 m in

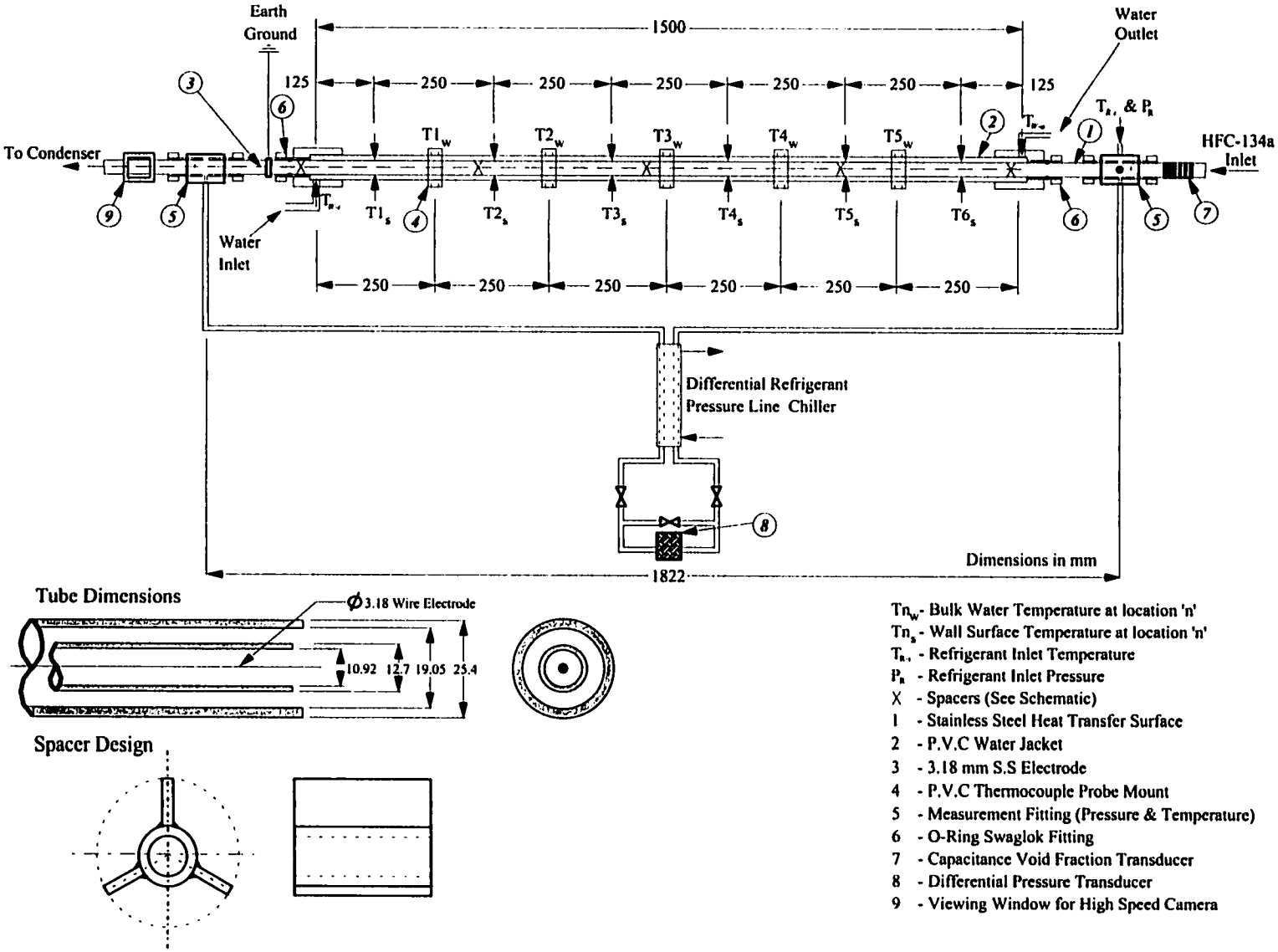

Figure 4.2: Schematic Diagram of Test Section : The Electrohydrodynamic Heat Exchanger.

length with an inner diameter of 20.8 mm and an outer diameter of 26.7 mm. The shell was insulated from the surroundings by 19.0 mm thick foam insulation (Rubatex: R-1 80 FS).

The surface of the test section tube was equipped with thermocouples at six axial locations, 250 mm apart, top and bottom, for tube wall temperature measurement. The 0.5 mm diameter thermocouple probes were embedded in 25.0 mm × 0.5 mm × 0.5 mm grooves along the length of the test section and were affixed using a high thermal conductivity adhesive and insulated by "shrink wrap" in an attempt to measure the average wall temperature. The axial water temperature was measured at five locations, top and bottom (at the centre of the shell annular gap), in addition to both inlet and outlet measurements. The inlet and outlet temperatures of the refrigerant were also measured by 1.6 mm T-type thermocouple probes. The electrode was a 3.18 mm diameter stainless steel rod, described in Section 4.1.3. The dimensions of the test section and thermocouple spacing are shown in Figure 4.2.

The inlet test section pressure was measured by means of a Heise optical (diaphragm type) pressure sensor accurate to within ±0.15 % of the reading.

The pressure drop across the test section was measured with an 8.62 kPa (1.25 psi) Validyne differential pressure transducer, calibrated against a Meri-Cal® piezoresistive sensor calibrator, certified to be accurate within ±0.1 % of the reading. The pressure transducer was connected to the inlet and outlet of the test section by two custom designed measurement fittings to reduce entrance effects (shown in Figure 4.2). The 6.35 mm tubes connecting the ends of the test section to the pressure transducer were passed through a water jacket that served to condense any vapour in the tubes in order to equalize the hydrostatic head on each side of the transducer. As the sections of tube above the water jacket were exposed to atmospheric temperatures, it was difficult to completely eliminate

the hydrostatic component because of the influence of flow regime. Since the flow regime was single-phase, stratified wavy or annular at the inlet, a valid assumption is that the upstream side of the pressure transducer is completely filled with liquid. However at the outlet, when investigating the dryout or mist regimes, there is difficulty determining the exact location where the vapour changes to liquid in the pressure tap tube. As the distance was less than 25 cm, the contribution of a hydrostatic head to the pressure drop was assumed negligible.

High speed video imagining of the flow regime at the exit of the test section, as shown in Figure 4.2, was performed at 500-1000 frames/s by a Kodak EktaPro® EM 1000 Imager. The flow patterns were observed through a transparent viewing box affixed to a polycarbonate tube. The viewing box was filled with mineral oil (in early experiments distilled water), which had a refractive index similar to the tube, in order to minimize light refraction by the curved tube surface.

A multi-ring type capacitance transducer was used to measure the inlet void fraction and aid in the evaluation of the flow pattern entering the test section. A comprehensive comparison of several different void fraction measurement techniques with the capacitance void meter used in this facility and the calibration procedures are presented in detail by Abdul-Razzak *et al.* (1994).

4.1.2.1 Void Fraction Measurement

As recommended by Abdul-Razzak *et al.* (1994), a six-ring capacitance transducer was used to increase the sensitivity of the measurement (Chang *et al.*, 1991) and eliminate flow regime effects (except bubbly flow). A schematic of the transducer is shown in Figure 4.3. Each ring was 6.5 mm wide and spaced 4.5 mm apart. The transducer was covered by a grounded brass sheet to shield it from electromagnetic interference. The

capacitance transducer was connected to a Boonton capacitance meter (Type 72B; 0.1 pF to 3 μF) accurate to ±0.5 %.

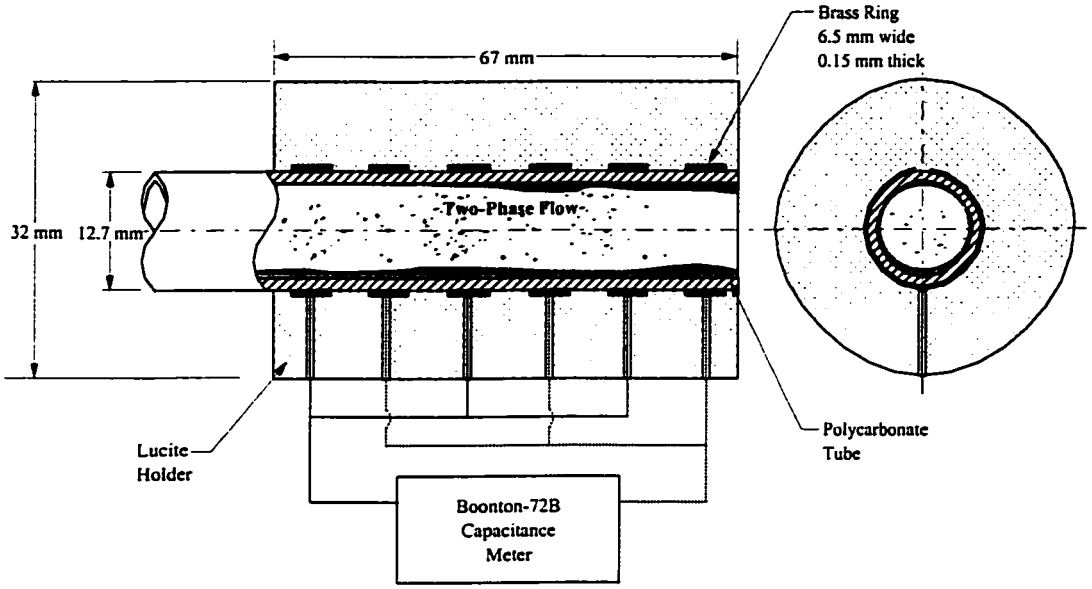

Figure 4.3: Schematic Diagram of Multi-Ring Capacitance Transducer.

The sensitivity of the transducer to various flow patterns encountered during the experiments was tested to be insignificant as it covered a large volume of the test tube as compared to the size of any individual slug or bubble passing through the tube. Accordingly, the measured mixture capacitance is truly a volume-averaged value and as such, is a unique function of the volume-averaged vapour fraction (α). To confirm the insensitivity of the six-ring capacitance transducer output to flow regime, separate experiments were conducted, where the liquid phase was simulated by plastic Lucite pieces machined to represent stratified, annular and slug flow patterns with different known void. The Lucite has a dielectric constant similar to that of the liquid refrigerant. It was observed that for the same value of volume average void fraction, the output signals of the three flow regimes were within ±3 %.

The capacitance transducer was calibrated in-situ for static stratified liquid of various levels using an ultrasonic system as described by Abdul-Razzak *et al.* (1994). The results

were correlated to give the void fraction in terms of the normalized capacitance C_{tp}^{*} as:

$$\alpha = 0.990773 - 0.62797C_{tp}^{*} - 0.57575C_{tp}^{*} + 0.211382C_{tp}^{*} \quad (4.3)$$

where C_{tp}^{*} is normalized capacitance defined by:

$$C_{tp}^{*} = \frac{C_{tp} - C_V}{C_L - C_V} \quad (4.4)$$

and C_V and C_L are the measured capacitance when the pipe is completely filled with vapour and liquid, respectively.

4.1.3 The Electrode, Spacer Design and Voltage Supply

For the purpose of the fundamental investigation of EHD, a coaxial tube with a cylinder rod electrode design was selected (herein referred to as the concentric arrangement), Figure 4.4a. The electrode was a stainless steel 3.18 mm diameter rod, chosen for its rigidity to maximize the electrode spacing and minimize the number of spacers, in an attempt to reduce flow regime interference (see Section 5.3). The annular gap was maintained by five custom made nonconducting spacers at intervals of 0.38 m. The spacers were designed to provide adequate support and minimal intrusion to the fluid flow and were machined out of a plastic material called 'Delrin' (having a dielectric constant of approximately 2.5) to occupy only approximately 20% of the flow area. A drawing of the spacers is shown in Figure 4.5.

The final set of experiments were conducted for an eccentric geometry where the electrode position was varied by offsetting it from the centerline by ±2.73 mm in the vertical direction, Figure 4.4b,c.

Electric potentials were applied to the electrode through a brass connector at the exit of the test section. The electrode was introduced at the exit of the test section by means of nonconducting Teflon Swagelok® fittings as shown in Figure 4.1. The electrode then

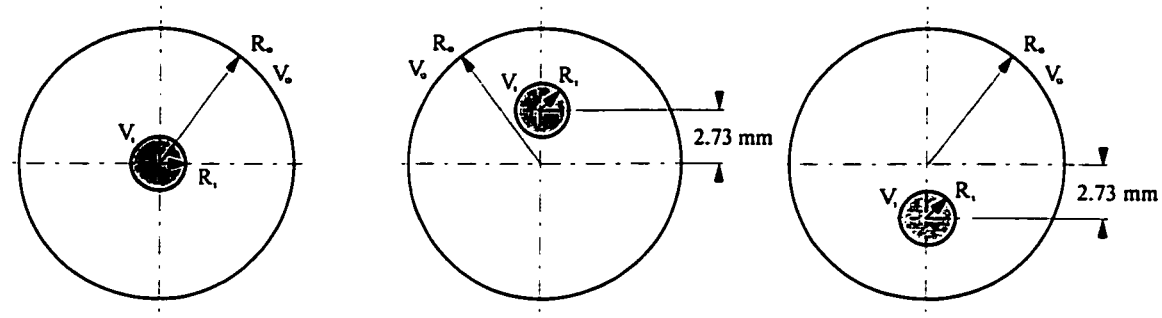

a) Concentric b) Eccentric +2.37 mm c) Eccentric -2.73 mm

Figure 4.4: Electrode Spacing and Voltage Range.

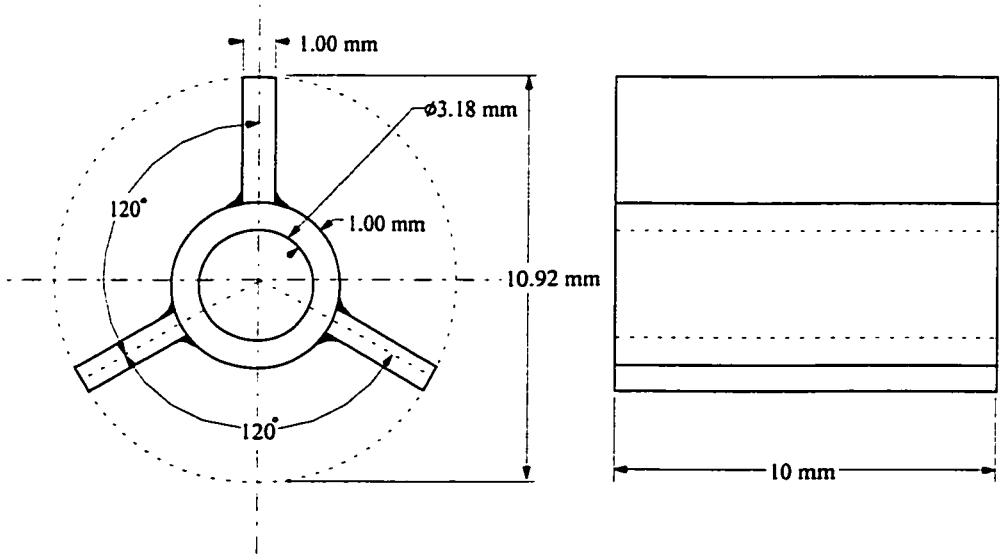

a) Concentric Electrode Spacer

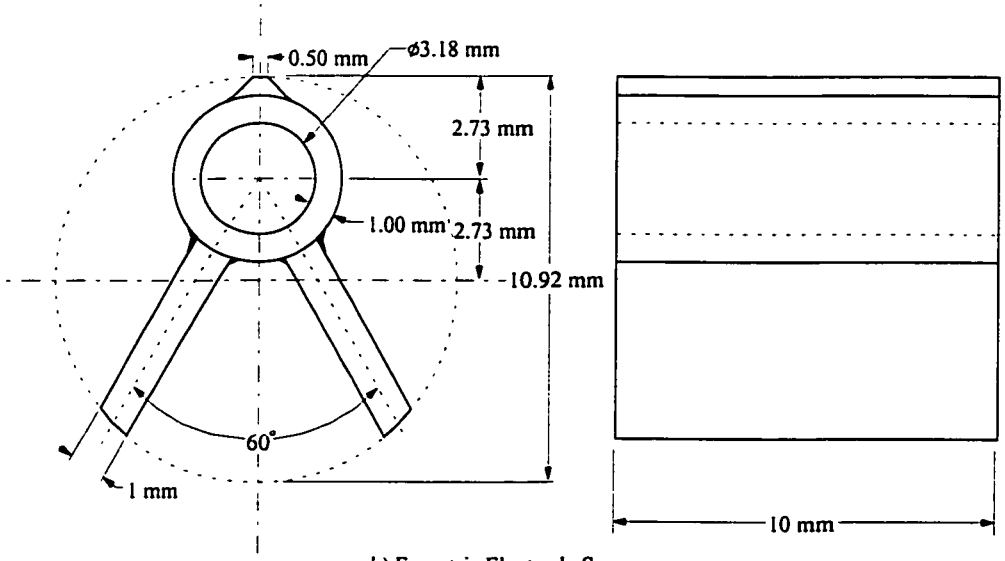

b) Eccentric Electrode Spacer

Figure 4.5: The Electrode Spacer Designs.

proceeded through a polycarbonate transparent tube (the viewing section), to ensure an electric field was not established prior to the test section. The test section was electrically isolated from the rest of the facility and earth grounded, making it the receiving electrode.

The voltage potential for the DC experiments was supplied by a Glassman high voltage power supply, Series EL model EL30R1.5, with reversible polarity up to 30 kV. The voltage was set to the target voltage by means of a potentiometer, to a maximum applied voltage approximately 20% below the breakdown voltage of the refrigerant (Appendix A). The accuracy was 1% of rated load + 1% of setting with a ripple better than 0.03% RMS of rated voltage at full load. For the low and high frequency AC experiments performed, the high voltage was generated by a 60 Hz Jefferson Magnetek power supply (0 - 25 kV peak to peak) and a 6.6 kHz Kyoto Denkiki Neon transformer (9 kV peak to peak) controlled by a 120 V variable transformer.

Current measurements were performed by either an Armaco® 0 - 25 μA analog current meter or an IPC® wide band current transformer 1mA (CM-01-L) for the DC and AC experiments, respectively. The voltage and current traces were recorded through a Tektronix 200 MHz digital oscilloscope (TDS 420A). Figures 4.6 and 4.7 present typical low and high frequency AC waveforms for the concentric electrode arrangement.

4.2 Data Acquisition System

The data acquisition system consisted of two National Instruments® 8-channel data acquisition boards; one for use with the high voltage signals and one for use with an analog multiplexer. The multiplexer was connected to the 32 thermocouples and it sampled between channels. The data acquisition software package used was Labview®.

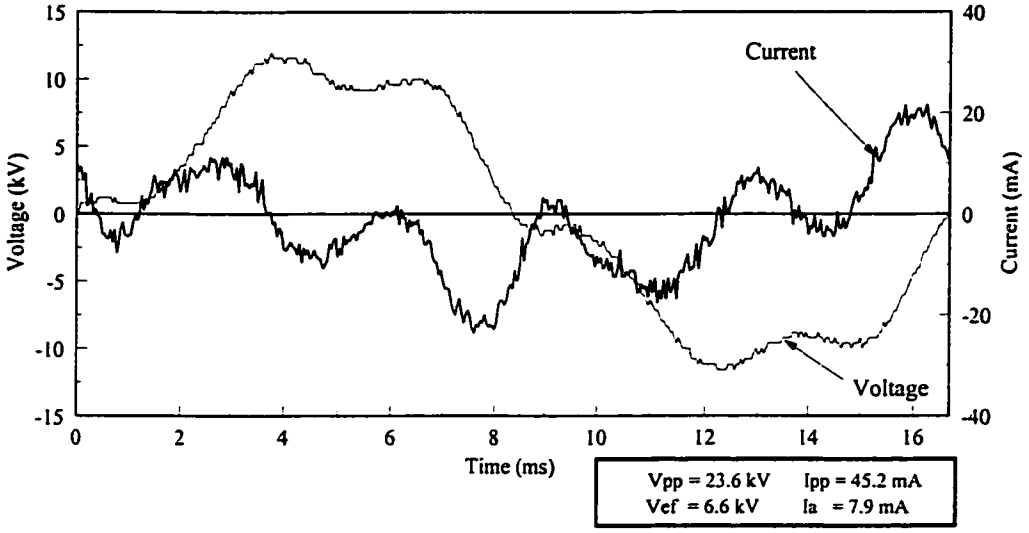

Figure 4.6: Typical Current and Voltage Waveforms obtained by the 60 Hz Power Supply.

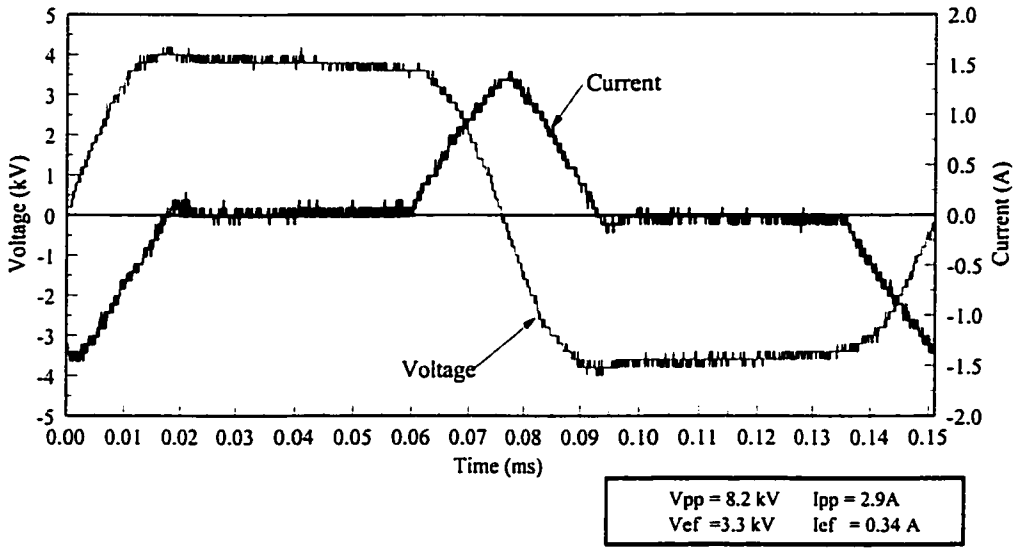

Figure 4.7: Typical Current and Voltage Waveforms obtained by the 6.6 kHz Transformer.

A 16-bit MIO board was used in combination with the multiplexer to provide adequate resolution for the thermocouple readings. The input voltage range on the MIO board was set to ±5V DC, such that each bit covered a range of 0.153 mV. The maximum gain of 100 was used, reducing the range covered by one bit to 1.53μV (ie. the least significant bit (LSB) size). Converting the LSB to temperature, using the NIST polynomial calibration curves, gave an accuracy in the temperature reading of 0.04°C. Thus, the

calibrated error of ±0.1 °C, discussed subsequently, was adequately covered by a range of 5 LSB's.

To avoid hardware and software cold junction compensation errors, an ice bath was constructed to the specifications outlined in ASTM STP 470 (1970). The bath was assumed isothermal at a temperature of 0.01 °C, as the standard specified. The total emf was then converted to a temperature using the individual calibration curve of each thermocouple. The calibrated accuracy was within ±0.1 °C.

To avoid inaccuracies due to settling time, the sampling rate between channels was reduced to 0.01s to allow the amplifier to settle out. The scanning order was such that one channel would be sampled for 10 s at 100 Samples/s, then the multiplexer would switch to the next channel and repeat the procedure. Using this sampling method, the time traces in the results are each taken at different intervals. Consequently, no inference may be made regarding their relative position on the graph.

4.3 Experimental Procedure

The experimental procedure for the base case (V_i = 0.0 kV) is outlined below and includes the additional steps required when an electric field was applied. The variables controlled during the course of an individual set of experiments were the refrigerant mass flow rate, and therefore the Reynolds number, the inlet refrigerant quality, pressure and temperature, the heat flux imposed through the water jacket and the voltage applied to the inner electrode. The initial start-up consists of the following steps:

- The desired refrigerant mass flux was set by varying the gear pump speed.
- The condenser water line was opened and the flow rate adjusted using throttle and bypass valve to achieve the desired subcooling at the electrical preheater inlet. The pump was adjusted to maintain the desired refrigerant mass flow rate.

- The preheater current levels were set and regulated and the hot water preheater flow and temperature adjusted to achieve the desired inlet quality entering the test section.

- The PID controller was set to the desired temperature and the water flow adjusted until the desired heat flux was obtained.

- The inlet pressure and temperature was regulated and all above mentioned variables adjusted accordingly.

- The criterion for steady state was:
  i) A temperature fluctuation of any thermocouple reading of less than ±0.1 °C.
  ii) A fluctuation of less than 2% of any analog signal.
  Typically, the first test took 3 hours, due to start up transients, while subsequent tests took approximately 1 hour to reach steady state.

- The data acquisition was then initiated to record the parameters listed in Table 4.1 of the following section. High speed video was taken of the outlet flow pattern and recorded on SVHS format (later the footage was digitized for analysis). The inlet and outlet flow patterns observed by the naked eye were documented along with any manual analog measurements (*i.e.* rotameter readings and barometric pressure).

- Data conversion and reduction was then performed as described in Section 4.5.

Upon completion of a base case experiment, a voltage was applied to the electrode. This had the effect of augmenting the rate of heat removal from the test section and pressure drop across the evaporator. Subsequently, all parameters were adjusted until the base case conditions (refrigerant mass flux, water side heat flux, inlet pressure, temperature and quality) were restored. Once steady state was reached, data acquisition was initiated and the oscilloscope programmed to record the voltage and current waveforms (AC).

The control parameters and procedure required for the Wilson technique of evaporation heat transfer coefficient analysis (Wilson, 1915, Kattan, 1996, Kattan *et al.*, 1998b) are discussed in the next section and Appendix B .

4.4 Experimentally Measured Parameters and Test Conditions

The following sections deal with the use of the experimental data to evaluate heat

transfer augmentation in an evaporator under the application of an electric field. The measured experimental parameters used EHD experimental analysis are listed in Table 4.1. With the knowledge of the measured quantities listed, the absolute temperatures at each location were used to determine the various refrigerant thermophysical and electrical properties based on the analysis and relationships described in Appendix A.

The range of experimental test conditions for water and refrigerant HFC-134a flow loops are shown in Table 4.2, where the following definitions were used to describe the non-dimensional parameters involved in this study.

The water and refrigerant flow rates are related to the Reynolds number according to:

$$Re_i = \frac{\dot{m}_R D_{h_R}}{A_i \mu_R} \quad , \quad Re_o = \frac{\dot{m}_W D_{h_W}}{A_o \mu_W} \qquad (4.5)\ a,b$$

where $\dot{m}$ is the mass flow rate and the subscripts W and R refer to outside (water) and inside (HFC-134a) fluids, respectively. A_o is the water jacket annular cross section and A_i is the tube-electrode annular cross section area. The tube diameter used in each formulation is the hydraulic diameter of an annulus ($D_h = D_o - D_i$) for the respective inner and outer diameters of the channel. During two-phase conditions, the Reynolds number used throughout this analysis was determined by the saturated liquid properties of the refrigerant. The refrigerant inlet quality, x_{in}, is obtained from an energy balance across the preheaters as follows:

$$x_{in} = \frac{\frac{Q_{PRE}}{\dot{m}_R} - C_{p_L}(T_{SAT} - T_{R\text{-}SUB})}{i_{fg}} \qquad (4.6)$$

where Q_{PRE} is the sum of the heat input introduced by the direct electric heat and hot water preheater, C_{pL} is the liquid specific heat, T_{SAT} and $T_{R\text{-}Sub}$ are the saturation and subcooled inlet temperatures and i_{fg} is the latent heat of evaporation. The void fraction was measured via the capacitance void meter as described in Section 4.1.2.1.

Table 4.1: The Measured Parameters

Experimentally Measured Parameters	
$T_{R\text{-}SUB}$	Refrigerant inlet temperature (subcooled)
$T_{R\text{-}i}$	Refrigerant test section inlet temperature
$T_{R\text{-}o}$	Refrigerant test section outlet/condenser inlet temperature
$T_{R\text{-}COND\text{-}o}$	Refrigerant condenser outlet temperature
$T_{W\text{-}COND\text{-}i}$	Condensing water inlet temperature
$T_{W\text{-}COND\text{-}o}$	Condensing water outlet temperature
$T_{W\text{-}i}$	Test section heating water inlet temperature
$T_{W\text{-}o}$	Test section heating water outlet temperature
$T_{W\text{-}PRE\text{-}i}$	Preheater inlet water temperature
$T_{W\text{-}PRE\text{-}o}$	Preheater outlet water temperature
$T1_{W\text{-}b}$	Test section axial bottom water temperature at location 1
$T1_{W\text{-}t}$	Test section axial top water temperature at location 1
$T2_{W\text{-}b}$	Test section axial bottom water temperature at location 2
$T2_{W\text{-}t}$	Test section axial top water temperature at location 2
$T3_{W\text{-}b}$	Test section axial bottom water temperature at location 3
$T3_{W\text{-}t}$	Test section axial top water temperature at location 3
$T4_{W\text{-}b}$	Test section axial bottom water temperature at location 4
$T4_{W\text{-}t}$	Test section axial top water temperature at location 4
$T5_{W\text{-}b}$	Test section axial bottom water temperature at location 5
$T5_{W\text{-}t}$	Test section axial top water temperature at location 5
$T1_{S\text{-}b}$	Test section axial bottom surface temperature at location 1
$T1_{S\text{-}t}$	Test section axial top surface temperature at location 1
$T2_{S\text{-}b}$	Test section axial bottom surface temperature at location 2
$T2_{S\text{-}t}$	Test section axial top surface temperature at location 2
$T3_{S\text{-}b}$	Test section axial bottom surface temperature at location 3
$T3_{S\text{-}t}$	Test section axial top surface temperature at location 3
$T4_{S\text{-}b}$	Test section axial bottom surface temperature at location 4
$T4_{S\text{-}b}$	Test section axial top surface temperature at location 4
$T5_{S\text{-}b}$	Test section axial bottom surface temperature at location 5
$T5_{S\text{-}t}$	Test section axial top surface temperature at location 5
$T6_{S\text{-}b}$	Test section axial bottom surface temperature at location 6
$T6_{S\text{-}t}$	Test section axial top surface temperature at location 6
P_R	Test section refrigerant inlet pressure (gauge)
ΔP	Differential pressure across the test section
P_{ATM}	Atmospheric pressure
$\dot{Q}_R$	Volumetric flow rate of single-phase subcooled refrigerant
$\dot{Q}_W$	Volumetric flow rate of test section water
$\dot{Q}_{W\text{-}PRE}$	Volumetric flow rate of preheater water
$\dot{Q}_{W\text{-}COND}$	Volumetric flow rate of condenser water
V_i	Direct electric heating preheater voltages
I_i	Direct electric heating preheater current
α	Capacitive void fraction of refrigerant at test section inlet
V	Electrohydrodynamic voltage potential
I	Electrohydrodynamic current

Table 4.2: Experimental Test Conditions

Variable	Refrigerant		Heating Water	
	min.	max.	min.	max.
Evaporation Experiments				
Mass Flux (kg/m^2s)	94	525	236	623
Reynold's Number[1], Re	3314	19148	2076	5563
Heat Flux[2] (kW/m^2)	-	-	7.5	21.2
Pressure (kPa_a)	595	740	~atm	~atm
Inlet Quality, x (%)	0	48%	-	-
Inlet Void Fraction, α (%)	0	83%	-	-
DC Voltage (kV)	0	8	-	-
60 Hz AC Voltage Amplitude (kV)	0	12.4	-	-
6.6 kHz AC Voltage Amplitude (kV)	0	4.7	-	-
1 - Saturated Liquid Refrigerant Re, 2 - Referred to the outside surface.				

Section 4.5 describes the data reduction method of the parameters used to define the heat transfer and pressure difference for a fixed set of operating conditions.

4.5 Data Reduction

Three methods of evaluating the overall heat transfer coefficients were performed throughout this investigation: a Wilson plot technique as suggested by Kattan (1996), an average surface temperature method and a local method. For each method, the calculation of evaporation heat transfer coefficients are '*quasi-local*' in nature as they are mean values for a test zone containing a range of vapour qualities. In the present investigation, the local method has been selected as it was determined that the heat transfer is not circumferentially uniform over the length of the tube due to flow stratification on the refrigerant side. The comparison of each method is presented in Appendix B. Other data reduction related to the flow pattern analysis and the dimensional and dimensionless electrical parameter

calculations are in their related sections.

4.5.1 The Wilson Technique

Wilson (1915) developed what has become known as the *Wilson Plot Method* or *Wilson Technique* to develop heat transfer correlations. The technique is an energy balance of two single-phase fluids across a heat exchanging device that correlates heat transfer to the fluid properties and flow rate of each fluid. The correlation for one of the fluids is then extended (for the same heat exchanging device) to applications where it is being used as a heating or cooling source for evaporating or condensing the other fluid (during flow). In Wilson's original investigation, it was proposed the h_i was an exponential function of the fluids velocity to the exponential value 0.82. More recently, the Wilson plot method has been developed on the basis of the Dittus-Boelter (1930) equation or other similar correlations to define the outside heat transfer coefficient.

In this investigation twenty five separate single-phase experiments were conducted in order to develop a correlation to predict the outside heat transfer coefficient (water side), the range of experimental conditions are presented in Table 4.3.

Table 4.3: Single-Phase Energy Balance Experimental Test Conditions.

Variable	Refrigerant		Heating Water	
	min.	max.	min.	max.
Wilson Method Experiments				
Mass Flux (kg/m^2s)	151	541	300	545
Reynold's Number	5066	17585	2062	4000
Heat Flux[1] (kW/m^2)	-	-	1.92	5.81
Pressure (kPa_a)	620	680	~atm	~atm
Outlet Subcooling (°C)	2.7	7.4	-	-
Applied Voltage (kV)	0	0	-	-
1 - Referred to the outside surface.				

The analysis followed the procedure proposed by Briggs and Young (1969) and extended by Kattan (1996) using the Dittus-Boelter (1930) and/or the Petukhov-Popov (1963) (a modification of the Prandtl (1944) relationship relating pressure drop to heat transfer) equations for either the shell or tube side heat transfer coefficients:

$$Nu_{D_h} = \frac{hD_h}{k} = C_1 \, Re^{\,a} \, Pr^{\,b} \tag{4.7}$$

$$Nu_{D_h} = \frac{hD_h}{k} = C_2 \frac{(f/8)\, Re_{D_h} \, Pr}{1 + 12.7\,(f/8)^{1/2}\,(Pr^{2/3} - 1)} \tag{4.8}$$

respectively. The exponent b in the Dittus-Boelter relation, Equation (4.7), is 0.3 when applied to the cooling medium and 0.4 to the fluid being heated. In Equation (4.8), f is the drag coefficient on the tube through which flow is taking place. In the present work, drag is approximated from the equation given by Filonenko (1954) for isothermal flows in smooth tube using the Reynolds number of the annulus (Equation 4.5b) as suggested by Kattan (1996):

$$f = [1.82 \log(Re_{D_h}) - 1.64]^{-2} \tag{4.9}$$

These equations were solved by substituting the corresponding inner and outer heat transfer coefficient into the overall heat transfer coefficient U_o, based on the following defining equation in terms of inside surface area:

$$\frac{1}{U_o} = \frac{1}{h_o} + \frac{D_o}{2k_s} \ln\left(\frac{D_o}{D_i}\right) + \frac{D_o}{D_i}\frac{1}{h_i} \tag{4.10}$$

where the thermal resistance due to the tube is included, assuming heat is conducted only radially inwards (or outwards), and the thermal conductivity of the stainless steel tube is constant over the range of temperatures investigated (14.9 W/m·K).

The overall heat transfer coefficient is determined using the inlet and outlet fluid temperatures and the total surface area. Applying the log mean temperature difference, the

overall heat transfer coefficient for a counterflow heat exchanger is:

$$U_o = \frac{q_W}{S_o \Delta T_{lm}} \tag{4.11}$$

where

$$\Delta T_{lm} = \frac{\Delta T_2 - \Delta T_1}{\ln (\Delta T_2 / \Delta T_1)} = \frac{\Delta T_1 - \Delta T_2}{\ln (\Delta T_1 / \Delta T_2)} \tag{4.12}$$

and the counterflow exchanger endpoint temperature differences are defined as

$$\begin{aligned} \Delta T_1 &\equiv T_{h,i} - T_{c,o} = T_{W\text{-}i} - T_{R\text{-}o} \\ \Delta T_2 &\equiv T_{h,o} - T_{c,i} = T_{W\text{-}o} - T_{R\text{-}i} \end{aligned} \tag{4.13}$$

The area S_o is the outer heated surface area

$$S_o = \pi D_o L \tag{4.14}$$

and the heat transfer rate q_W is obtained from the measured water inlet ($T_{W\text{-}i}$) and outlet ($T_{W\text{-}o}$) temperature and the water mass flux $\dot{m}_W$ according to:

$$q_W = \dot{m}_W C_{p_W} (T_{W\text{-}i} - T_{W\text{-}o})) \tag{4.15}$$

Thus, in Equation (4.10) h_i and h_o are the only unknowns. Consequently, to ensure a high accuracy in the measured heat transfer coefficient for the inside tube, it is important to accurately define the outside heat transfer coefficient. This is defined through "The Wilson Experiments" presented in Table 4.2. For these experiments, the water mass flow rates and water heat fluxes were chosen to be similar to those used in the convective boiling test. However, the refrigerant pressure was increased such that evaporation was avoided.

Combining the above equations, the resulting equations were put into linear form by suitable manipulation and the required constants are solved in an iterative fashion as presented in Appendix B. The final expression selected for determining the water side heat transfer coefficient was:

$$Nu_{D_h} = \frac{hD_h}{k} = 0.81 \frac{(f/8)\, Re_{D_h}\, Pr}{1 + 12.7\, (f/8)^{1/2} (Pr^{2/3} - 1)} \tag{4.16}$$

Upon calculating the overall heat transfer coefficient and the water side heat transfer

coefficient, the internal refrigerant heat transfer coefficient could be determined by rearranging Equation 4.10. The Nusselt number was calculated based upon the heat transfer coefficient and hydraulic diameter of the annular gap between the electrode and the inside of the stainless steel heat exchanger tube:

$$Nu_{D_h} = \frac{h_i(D_i - D_e)}{k} \tag{4.17}$$

where D_e is the electrode diameter and k is the saturated liquid thermal conductivity.

4.5.2 Overall Heat Transfer Coefficient

As a preliminary analysis the overall heat transfer coefficient of the evaporating refrigerant was determined by calculating the total heat transfer rate on the water side, according to Equation 4.15, and averaging the measurements of the twelve surface thermocouples. This effectively suggests that the rate of heat transfer is uniform both circumferentially and axially, which is inherently incorrect for indirect heating systems as previously stated. The average temperature of the surface was obtained according to:

$$T_{S_{avg}} = \frac{1}{12}\sum_{1-t,b}^{6-t,b} Ti_{S-t,b} \tag{4.18}$$

Subsequently the inner heat transfer coefficient was determined according to:

$$\overline{h_i} = \frac{q_w}{S_i\,(T_{S_{avg}} - T_{SAT})} \tag{4.19}$$

where S_i is the surface area of the inside of the stainless steel tube. The thermal resistance of the tube has been excluded as the surface temperature measurement is effectively the average wall temperature. Further, the maximum temperature difference across the wall was determined to be less than 0.07°C. The Nusselt number was again calculated based upon the heat transfer coefficient and hydraulic diameter as presented in Equation 4.17.

4.5.3 Local Heat Transfer Coefficients

The calculation of the local heat transfer coefficients was based upon an energy

balance on the water side at any two axial positions along the test section. For the present analysis, the top and bottom water temperatures were averaged and local values of heat transfer rates were determined for 0.5 m lengths. The heat flux was assumed to be circumferentially uniform over a 0.5 m long length and divided into twelve sections, each 0.25 m in length, six to represent the top and six the bottom halves of the tube:

$$q_{i \to i+2} = \dot{m}_W C_{p_W} (\overline{T_{W_{i+2}}} - \overline{T_{W_i}}) \tag{4.20}$$

With the quasi local heat transfer rates determined, the average heat transfer coefficient of the top and bottom portions of the tube was determined by assuming the two local measurements of surface temperature were approximately equivalent to the temperature of the 0.25 m section for the bottom and top half of the channel, respectively. The top and bottom heat transfer coefficients were determined by:

$$h_{i_t} = \frac{q_{i-i+1}}{4S\,(T_{i-s_t} - T_{SAT})} \quad , \quad h_{i_b} = \frac{q_{i-i+1}}{4S\,(T_{i-s_b} - T_{SAT})} \tag{4.21}$$

where the area is $S = \frac{1}{2} \pi L D_i$. The overall heat transfer coefficient was then determined by averaging the local bottom and top heat transfer coefficients:

$$\overline{h_i} = \frac{1}{12} \sum_{1-t,b}^{6-t,b} h_{i_{t,b}} \tag{4.22}$$

Again the Nusselt number was calculated.

The associated measurement error and calculation uncertainty of the data processed in this section and throughout the thesis is presented in Appendix B.

Chapter 5

Flow Pattern Identification With and Without Applied Electric Fields

In single phase flow analysis, it is necessary to know whether the flow is laminar or turbulent and whether or not any secondary effects exist. In two phase flow studies, this information is equally necessary but it is even more important to know how the phases are distributed relative to each other in the channel. That is, what is the flow configuration or flow pattern? This knowledge of flow pattern is important since it dictates, to a large extent, which mode of analysis or correlation should be used in predicting the fluid flow, pressure drop and heat transfer. Consequently, the identification and assignment of flow regimes with and without the EHD effect will be the focus of the next two chapters.

The objective of this chapter is to describe the flow patterns observed during horizontal flow phase change processes, with and without applied electric fields (both AC and DC), and to present a methodology for predicting the flow regimes in a diabatic annular channel not under the influence of an electric field. In the following chapter, the interaction between flow regimes and electric field distributions is studied in order to incorporate the interfacial electric forces that are a consequence of adding a high voltage to a system into the flow pattern map developed in this chapter.

5.1 Flow Patterns

Assigning a flow pattern to a given condition is not an exact procedure. It is normally

based on visual interpretation of the flow condition, discussed in Chapter 4, and is a subjective judgement on the part of the observer. As presented in Chapter 2, there are numerous configurations that may be observed as the flow moves along a heated channel. The typical description of flow patterns in smooth pipe flow, as proposed in such texts as Collier and Thome (1994) and Carey (1992), will be adopted in the present work. However, due to the presence of the electrode for the purpose of applying an electric field, this section outlines the proposed definition for applications of two-phase flow in annular geometries without applied electric field, with DC electric fields and with low and high frequency AC fields.

5.1.1 Flow Patterns Observed without EHD

In horizontal flow in an annular channel, with and without EHD, the common types of flow patterns that exist are bubble, plug, stratified, stratified wavy, bridged-stratified wavy, slug, annular-dispersed, annular and mist flow. These are depicted schematically in Figure 5.1. The description of these flow patterns, adopted and modified to include annular geometries, as employed in numerous texts (*eg.* Carey, 1992, Collier and Thome, 1994) are summarized as follows:

- *Bubble Flow*: Bubbles of vapour are distributed in the continuous liquid phase. At low velocities, the bubbles tend to move along the upper section of the tube and at moderate velocities, they are fairly well distributed over the whole duct.

- *Plug Flow*: The bubbles coalesce and alternate plugs of liquid and vapour move along the upper portion of the tube and occasionally envelop the electrode.

- *Stratified Flow*: The two phases separate with the liquid flowing in the lower part of the duct and the vapour in the upper part with a relatively smooth interface. This pattern was not observed in the present investigation.

- *Stratified Wavy*: This is similar to stratified flow except that the vapour moves at a higher velocity and the interface is disturbed by waves travelling in the direction of the flow. In annular geometries these waves may bridge the gap between the bottom

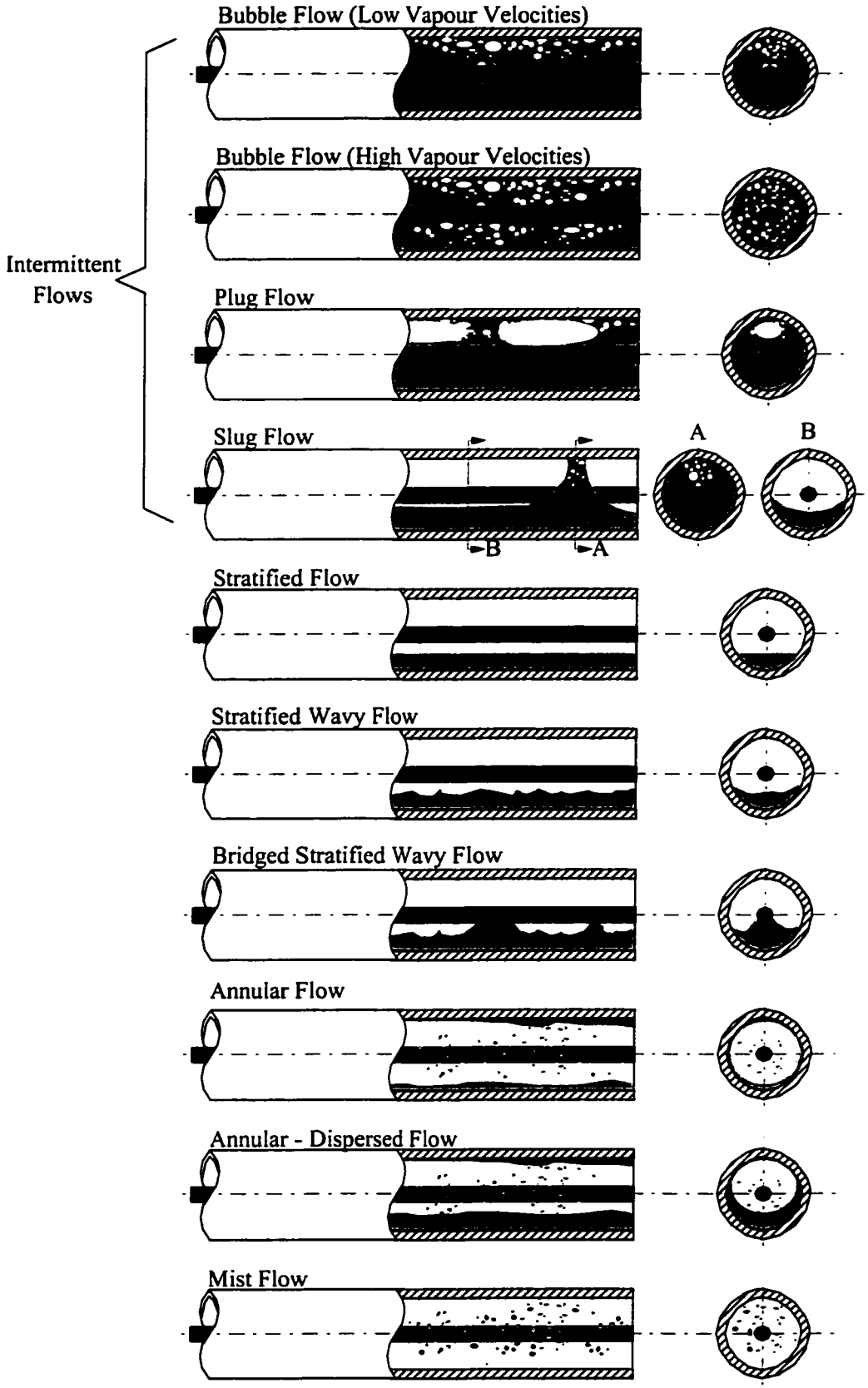

Figure 5.1: Flow Regimes in Horizontal Annular Channels.

of the tube and the electrode, which may significantly increase pressure drop. Osamusali and Chang (1988) also observed flows of this nature and referred to them as *annular-slug* and *annular-plug,* depending on the amount of gas entrainment. However, as these regimes are not expected to drastically influence heat transfer, they have been grouped with the stratified flows in this study.

- *Slug Flow*: The crests of the waves seal or bridge the duct and periodic frothy slugs pass along the duct with a higher velocity than the mean liquid velocity. The upper surface of the tube behind the wave is wetted by a residual film which drains into the bulk of the liquid.

- *Annular Flow*: This consists of a symmetric liquid film around the periphery of the tube with a core of vapour around the circumference of the electrode. Waves are present on the surface of the interface due to the high vapour velocity. These waves provide the source for liquid drop entrainment in the vapour core.

- *Annular-Dispersed Flow*: This is similar to annular flow with the exception that the film thickness is nonuniform, the film being thicker on the bottom portion of the tube due to gravitational effects.

- *Mist Flow*: Droplets of liquid are distributed in the continuous vapour phase. This is the last flow regime prior to vapour flow in an evaporator.

For the experimental test conditions covered in this investigation not all flow patterns were observed at the exit of the transparent test section. The flow conditions commonly encountered were plug and slug, referred to as intermittent, stratified wavy, annular and annular dispersed. These flow patterns for refrigerant HFC-134a have been observed using high speed photography and are presented in Figure 5.2.

In addition to the typical flow patterns, the application of an electric field contributes secondary effects, as described in Chapter 3, that can produce different flow behaviour not typically observed in evaporative flow boiling.

5.1.2 Flow Patterns Observed in DC Electric Fields

Recently, Norris *et al.* (1999) and Seyed-Yagoobi and Bryan (1999) have suggested that imposing an electric field on a flowing two-phase fluid may present flow regime characteristics unique to electrohydrodynamic convective boiling. However, no attempt has

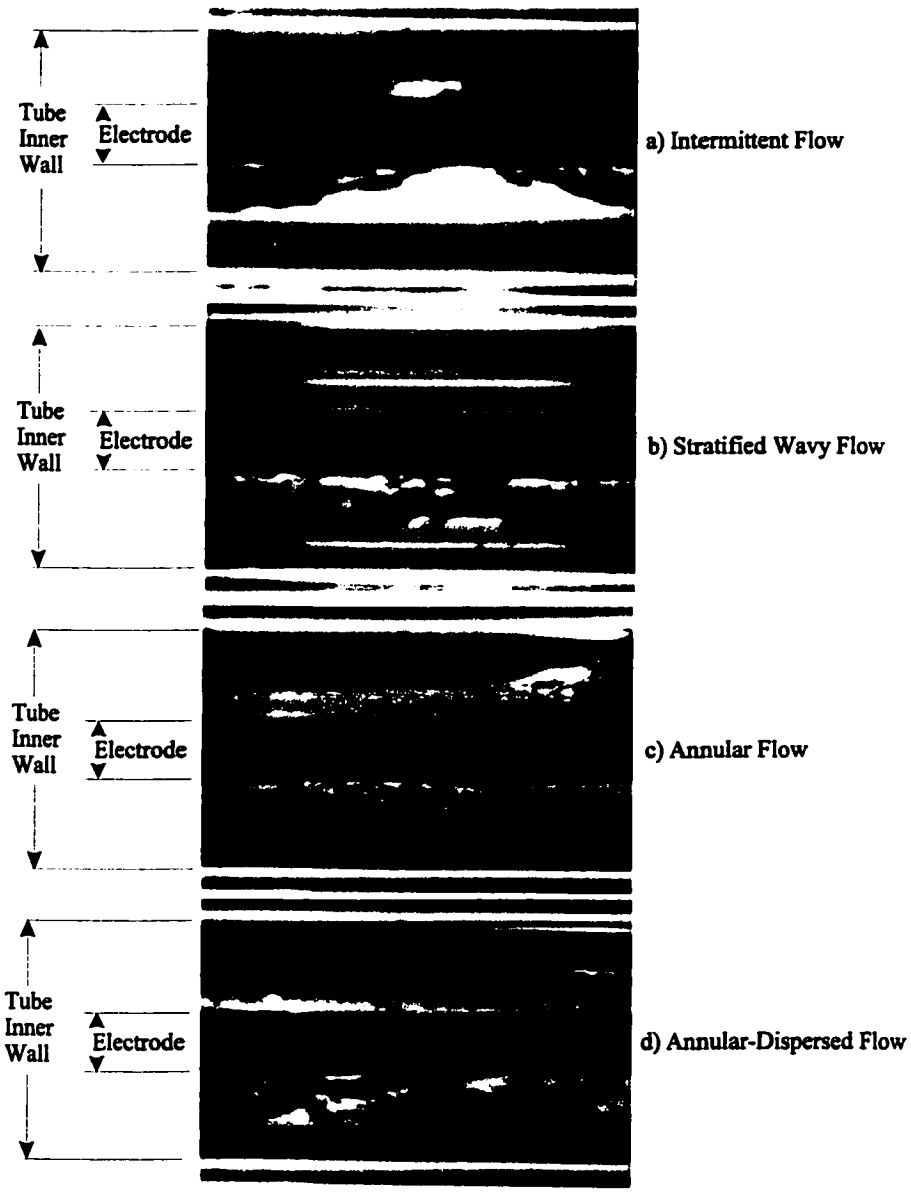

Figure 5.2: Flow Patterns Observed by High Speed Photography.

been made to describe the distributions or predict their occurrence. This section proposes several new designations for the other regimes observed in this study, shown schematically in Figure 5.3.

- *Inverted-annular type flow*: In this configuration, the liquid is drawn inward towards the electrode as a result of the electric field established at relatively high qualities. Liquid, which is originally stratified, is extracted from the tube surface creating intermittent dryout and resulting in a reduction of heat transfer (Norris *et al.*, 1999). The flow is proposed to be similar to inverted annular flow developed due to very high heat flux levels (where a liquid tongue is developed) and is equally unstable.

- *Stratified Wavy/Liquid Encircled Electrode*: At lower quality levels, liquid has been observed migrating from the stratified film to the electrode enveloping it. By surrounding the electrode, the result is a significant increase in pressure drop due to increased wall friction.

- *Multi-Layer Annular Flow*: As in the stratified case, liquid is attracted to the electrode, from the annular film, encircling it to form a multi-layered annulus featuring liquid-vapour-liquid from inside to out.

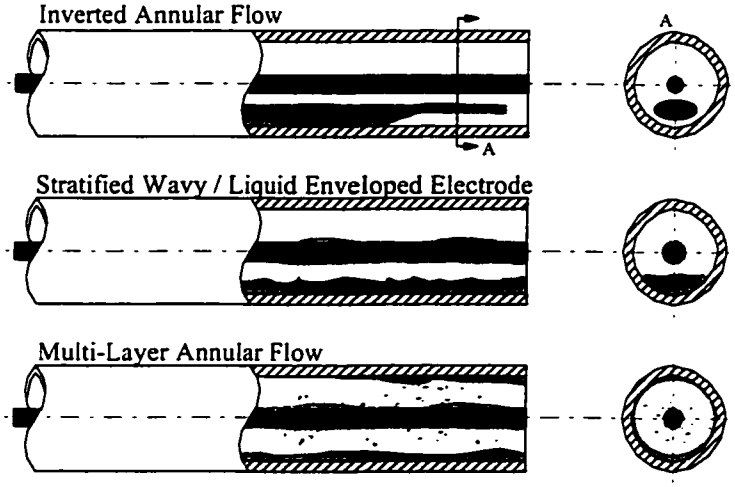

Figure 5.3: Schematic Diagram of EHD Induced Flow Patterns.

The generation of these orientations depend highly upon how significant the EHD force density components are with respect to the fluid momentum. The mechanisms of flow and electric field interaction inducing these regimes are discussed in the following chapter.

5.1.3 Flow Patterns Observed in Low Frequency AC Electric Fields

In the present investigation, experimentation with a 60 Hz AC voltage potential has led to the observation of a regime that may not have been observed previously. It is an oscillatory flow, where droplets as large as 2 mm in diameter are entrained in a vapour core that is surrounded by an annular liquid film around the circumference of the tube and electrode, like a multi-layered annular flow. The droplets oscillate radially in the lower portion of the annulus at a frequency of approximately 120 Hz, twice the frequency of the applied field, occasionally being entrained into the inner or outer annular film. In addition

to the droplet formation, small spouts or jets of liquid were observed on the upper half of the annular film surrounding the electrode. These spouts seemed to form randomly on the crest of a wave created by interfacial instabilities present in the film and would spray a fine mist into the upper portion of the vapour core, as shown in the top image of Figure 5.4.

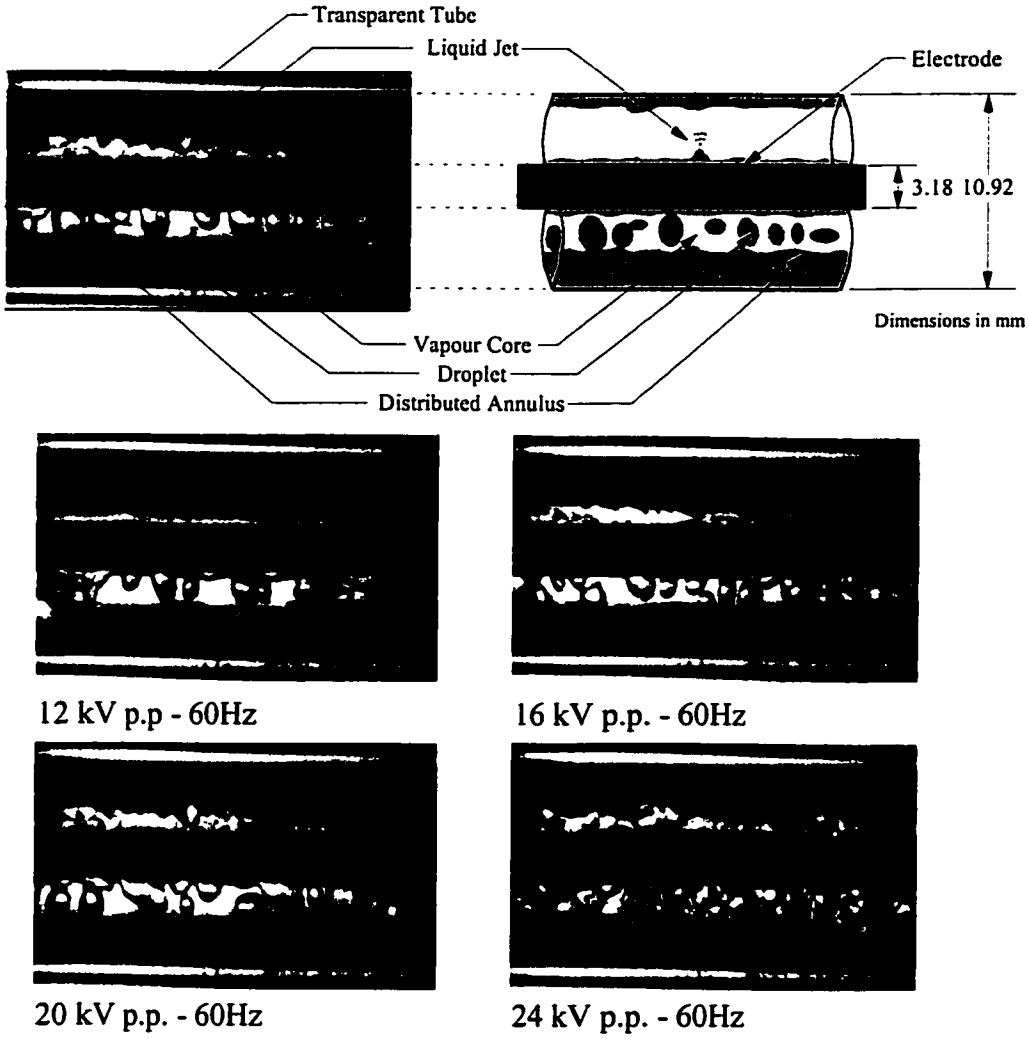

Figure 5.4: Oscillatory-Entrained Droplet Flow Pattern

The size of the droplets, intensity of motion, rate of deposition and the occurrence of spouts were highly dependent on the amplitude of the 60 Hz applied voltage. Figure 5.4 presents several images of the flow during condensation at different applied voltages. The mechanisms behind this unique flow pattern will be discussed in Chapter 6.

5.1.4 Flow Patterns Observed in High Frequency AC Electric Fields

Experimentation with a 6.6 kHz AC voltage potential in this work suggests that there is no difference between high frequency electric fields and those observed under the application of DC fields.

5.2 Flow Pattern Maps

As discussed in Chapter 2, there have been several attempts to theoretically describe how and why the flow regimes change. These theoretical or semi-theoretical approaches provide a method of extrapolating experimental investigations to other conditions with relatively good agreement. Of the investigations previously mentioned, the most comprehensive model of flow pattern transition is that developed by Taitel and Dukler (1976) and the modifications of their initial model by Osamusali and Chang (1987, 1988), Chang (1989b), Taitel (1990), Steiner (1993) and Kattan *et al.* (1998a). The basis of the model for tube flow is the assumption that stratified flow will prevail unless secondary variables imposed by the inertia of the flow create instabilities that may act to transform the simple orientation created by gravitational forces accumulating liquid on the bottom of the channel. Unlike most other flow regime maps, Taitel and Dukler considered the mechanisms that act to change each regime and applied related simplified assumptions to obtain the flow regime transition criterion.

Numerous researchers have applied the Taitel and Dukler map with a varying degree of success for two-component (*e.g.* air-water) two-phase flow. Work in single-component flows include previous investigations in the present test facility by Abdul-Razzak *et al.* (1995) for HFC-134a in a 10.7 mm diameter tube. The study presented the map as a function of superficial velocities for over 150 experiments and suggested that the extrapolation to

refrigerants is relatively good. Conversely, a recent study by Kattan (1996) and Kattan *et al.* (1998a) involving the development of a flow pattern database for five refrigerants and a comparison of several of the most commonly used flow pattern maps, showed that the Taitel and Dukler map only correctly identified 47% of the HCF-134a flow pattern data and 40% of all of the refrigerant data collected in the study. Several possible explanations for the poor performance of this map are presented in Section 5.4.

Table 5.1 provides a summary of the experimental conditions and the performance of several flow pattern maps for the refrigerants investigated in the Kattan (1996) study of tube flow. The evaporator inner tube and sight glass diameters were 12.0 mm for all test

Table 5.1: Two-Phase Flow Conditions and Map Performance

Fluid	T_{SAT} °C	P_{SAT} Bar	G kg/m²s	x %	Total Points	Number of Correct Data Points				
						K	S	T&D	H	K&F
R134a	10.3	4.19	100-500	4-90	106	100	98	49	65	61
R134a	4.44	3.42	100-400	18-100	101	97	76	55	69	66
R134a	2	3.14	300-500	5-57	60	60	60	25	50	36
R134a	-1.3	2.79	100-300	12-82	32	29	27	11	21	17
R402A	10.2	8.88	303	11-88	34	33	31	11	7	4
R402A	2.4	7.05	100-318	9-91	94	88	92	25	15	44
R402A	-1.3	6.3	317	13-63	24	24	24	10	9	6
R404A	10.2	8.36	300	7-98	34	34	32	14	9	9
R404A	2.4	6.61	100-318	7-92	95	90	89	24	20	47
R404A	-1.3	5.89	320	12-63	24	24	24	10	10	9
R502	2.5	6.19	100-300	8-97	60	60	57	21	30	40
R123	30.7	1.12	100-300	7-98	38	36	37	23	27	35
Total Data Points Correct					702	675	647	278	332	374
% Correct						96.2%	92.2%	39.6%	47.3%	53.3%

K : Kattan *et al.* (1998a); S : Steiner (1993); T&D : Taitel & Dukler (1976); H : Hashizume (1983); K&F : Klimenko & Fyodorov (1990)

(Adopted from Kattan, 1996 and Kattan *et al.*, 1998a)

data except for those with HFC-134a at 4.44°C. These tests were conducted with an inner evaporator tube diameter of 10.92 mm and a sight glass inner diameter of 12.0 mm..

As shown in Table 5.1, the performance of the Hashizume map and Klimenko and Fyodorov map is rather poor, only correctly identifying 47.3% and 53.3% of the flow pattern data, respectively. As Kattan (1996) suggested, the Klimenko and Fyodorov model is a threshold criterion between stratified and unstratified flow and the random probability of selecting either condition is 50%. Thus 53.3% is inadequate and the model is not recommended for refrigerants. With the insight provided by Kattan, neither model will be covered in any depth in the present investigation due to their poor performance. On the other hand, the modified Taitel and Dukler models recommended by Steiner (1993) and Kattan *et al.* (1998a) were relatively successful in properly identifying flow patterns, correctly identifying over 90% of the data points (Kattan *et al.*, 1998a).

Osamusali and Chang (1987, 1988) contributed to the mechanistic identification of flow regimes by accounting for the effect of interfacial surface tension in the Helmholz instability model for the stratified to intermittent transition criterion in two-component two phase flow at low Reynolds numbers. Their model was then extended to include horizontal coaxial and eccentric annuli and rod bundle geometries. As the Taitel and Dukler approach is the foundation to these models investigated by Steiner (1993) Kattan *et al.* (1998a) and Osamusali and Chang (1987, 1988), this will be the starting point of the analytical approach for an annulus detailed in the following section.

5.3 An Analytic Approach for Flow Regime Transitions in Horizontal Annular Channels without EHD Forces

In the present model, the assumption used by Taitel and Dukler (1976) for tube flow

will be adopted for an annular geometry without EHD. The effects of an applied voltage will be included in Chapter 6. The basic principle is that all flow regimes are manifested due to secondary effects or a perturbation from the horizontal stratified flow regime. The following section will outline the parameters and relevant transitions pertaining to this investigation in equilibrium stratified flow.

5.3.1 One-Dimensional Equilibrium Stratified Flow in an Annulus

The basis of this analytical approach, the transition of flow regimes from stratified flow in an annulus, is illustrated in Figure 5.5. The most significant parameter of stratified flow is the liquid level denoted by h_L in the figure. As Taitel and Dukler showed for horizontal flows, h_L can be uniquely related to all of the major transition parameters.

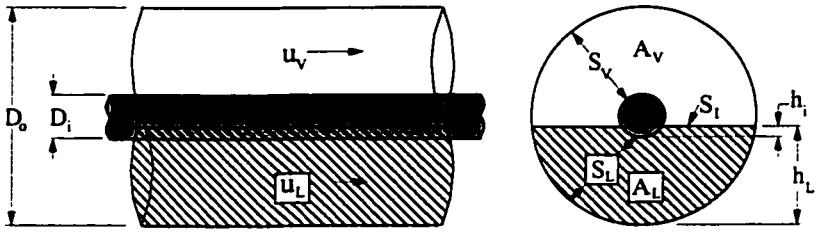

Figure 5.5: Parameters in Equilibrium Stratified Flow in an Annulus.

As the primary assumption is that the system in Figure 5.5 is in equilibrium, thus the momentum transfer between the top and bottom of the tube must be zero. Further, as suggested by Taitel and Dukler (1976), we will neglect the effects of acceleration and the hydrostatic head in the liquid phase. Therefore, the momentum balances for the liquid and vapour phases are, respectively:

$$-A_L \frac{dp}{dz} - \tau_{0_L} S_L + \tau_I S_I = 0 \qquad (5.1)$$

$$-A_V \frac{dp}{dz} - \tau_{0_V} S_V - \tau_I S_I = 0 \qquad (5.2)$$

where, as depicted in Figure 5.5, A_L and A_V are the cross sectional areas of the liquid and vapour phases, respectively, τ_{0L} and τ_{0V} are the wall shear stress for the fluids in contact with

the tube and/or electrode wall, τ_I is the interfacial shear stress, S_L and S_V are the summation of the tube and electrode perimeters in contact with the liquid and vapour phases, respectively, and S_I is the interfacial perimeter. Combining Equations (5.1) and (5.2) gives:

$$\tau_{0_V} \frac{S_V}{A_V} - \tau_{0_L} \frac{S_L}{A_L} + \tau_I S_I \left(\frac{1}{A_L} + \frac{1}{A_V} \right) = 0 \tag{5.3}$$

Applying the Blasius (1913) expression for the wall and interfacial shear stress:

$$\tau_{0_L} = \frac{f_L \rho_L u_L^2}{2} \tag{5.4}$$

$$\tau_{0_V} = \frac{f_V \rho_V u_V^2}{2} \tag{5.5}$$

$$\tau_I = \frac{f_I \rho_V (u_V - u_L)^2}{2} \tag{5.6}$$

where the liquid and vapour friction factors f_L and f_V are evaluated by Taitel & Dukler (1976) as:

$$f_L = \frac{C_L}{Re_L^n} \quad , \quad f_V = \frac{C_V}{Re_V^m} \tag{5.7)a.b}$$

and the Reynolds numbers:

$$Re_L = \frac{D_L u_L \rho_L}{\mu_L} \quad , \quad Re_L = \frac{D_V u_V \rho_V}{\mu_V} \tag{5.8)a,b}$$

are defined in terms of their respective hydraulic diameters:

$$D_L = \frac{4 A_L}{S_L} \quad , \quad D_V = \frac{4 A_V}{S_V + S_I} \tag{5.9)a,b}$$

and the constants C_L, C_V, n and m in Equation (5.7) depend on whether the individual fluids are in laminar or turbulent flow. Here the Moody friction factor (Moody, 1944) will be adopted for laminar flow ($Re_{L,V} < 2000$) $C_L = C_V = 16$, $n = m = 1$ and $C_L = C_V = 0.316$, $n = m = 0.25$ for turbulent flow ($Re_{L,V} > 2000$) although it has been suggested that these parameters may also be a function of flow pattern (see Lightstone *et al.*, 1991). Further, it

has been shown by Melcher (1981) that the interfacial shear stress is approximately equal to the vapour shear stress, which explains why $f_I = f_V$ in Equation (5.6). Introducing Equations (5.4) to (5.9) into Equation (5.3) and nondimensionalizing using the inner tube diameter, D_o , with the nondimensional quantities denoted by an overline "$\bar{}$", the momentum balance may be redefined as a sole function of the dimensionless liquid level, $\bar{h}_L = h_L/D_o$, and the fluid properties as:

$$X^2 \, (\bar{u}_L \, \bar{D}_L)^{-n} \, \bar{u}_L^2 \, \frac{\bar{S}_L}{\bar{A}_L} - (\bar{u}_V \, \bar{D}_V)^{-n} \, \bar{u}_V^2 \left(\frac{\bar{S}_V}{\bar{A}_V} + \frac{\bar{S}_I}{\bar{A}_L} + \frac{\bar{S}_I}{\bar{A}_V} \right) = 0 \tag{5.10}$$

or

$$X = \left[\left(\frac{\bar{S}_V + \bar{S}_I}{\bar{S}_L} \right)^n \left(\frac{\bar{A}_L}{\bar{A}_V} \right)^2 \left(\frac{\bar{S}_V}{\bar{A}_V} + \frac{\bar{S}_I}{\bar{A}_V} + \frac{\bar{S}_I}{\bar{A}_L} \right) \left(\frac{\bar{A}_L}{\bar{S}_L} \right) \right]^{1/2} \tag{5.11}$$

where X is the Martinelli parameter:

$$X = \frac{(dp_F \, / \, dz)_L}{(dp_F \, / \, dz)_V} = \left(\frac{1 - x}{x} \right)^{\frac{2-n}{2}} \left(\frac{\mu_L}{\mu_V} \right)^{\frac{n}{2}} \left(\frac{\rho_V}{\rho_L} \right)^{\frac{1}{2}} \tag{5.12}$$

The dimensionless peripheral and cross-sectional variables required to solve Equations (5.10) or (5.11) can be derived from the geometry depicted in Figure 5.5 for a given liquid level. For an annular geometry, these variables are:

$$\bar{h}_i = 0 \quad if \quad \bar{h}_L < \frac{D_o - D_i}{2D_o}$$

$$\bar{h}_i = \frac{h_i}{D_i} = \left(h_L - \frac{D_o - D_i}{2} \right) \frac{1}{D_i} \quad if \quad \frac{D_o - D_i}{2D_o} \le \bar{h}_L \le \frac{D_o + D_i}{2D_o} \tag{5.13}$$

$$\bar{h}_i = 1 \quad if \quad \bar{h}_L > \frac{D_o + D_i}{2D_o}$$

$$\bar{A}_L = \frac{A_L}{D_o^2} = \frac{1}{4} \left[\pi - \cos^{-1} (2\bar{h}_L - 1) + (2\bar{h}_L - 1) \sqrt{1 - (2\bar{h}_L - 1)^2} \right]$$
$$- \left(\frac{1}{4} \left[\pi - \cos^{-1} (2\bar{h}_i - 1) + (2\bar{h}_i - 1) \sqrt{1 - (2\bar{h}_i - 1)^2} \right] \frac{D_i^2}{D_o^2} \right) \tag{5.14}$$

$$\bar{A}_V = \frac{A_V}{D_o^2} = \frac{\pi}{4} - \frac{\pi}{4}\frac{D_i^2}{D_0^2} - \bar{A}_L \tag{5.15}$$

$$\bar{S}_L = \frac{S_L}{D_o} = \pi - \cos^{-1}(2\bar{h}_L - 1) + (\pi - \cos^{-1}(2\bar{h}_i - 1))\frac{D_i}{D_o} \tag{5.16}$$

$$\bar{S}_V = \frac{S_V}{D_o} = \pi + \frac{\pi D_i}{D_o} - \bar{S}_L \tag{5.17}$$

$$\bar{S}_I = \frac{S_I}{D_o} = \sqrt{1 - (2\bar{h}_L - 1)^2} - \sqrt{1 - (2\bar{h}_i - 1)^2}\left(\frac{D_i}{D_o}\right) \tag{5.18}$$

$$\bar{D}_L = \frac{D_L}{D_o} = \frac{4A_L}{S_L D_o} = \frac{4\bar{A}_L}{\bar{S}_L} \tag{5.19}$$

$$\bar{D}_V = \frac{D_V}{D_o} = \frac{4A_V}{(S_V + S_I)D_o} = \frac{4\bar{A}_V}{\bar{S}_V + \bar{S}_I} \tag{5.20}$$

$$\bar{u}_V = \frac{u_V}{U_V} = \frac{\bar{A}}{\bar{A}_V} \tag{5.21}$$

$$\bar{u}_L = \frac{u_L}{U_L} = \frac{\bar{A}}{\bar{A}_L} \tag{5.22}$$

In Equation (5.13), h_i is the height of the liquid level above the bottom of the electrode as shown in Figure 5.5, U_L and U_V are the superficial velocities for the liquid and vapour velocities and $\bar{A}$ is the dimensionless cross sectional area of the annulus (Hewitt, 1982).

Once the reference liquid level h_L is known, the dimensionless variables defined by Equations (5.13) through (5.22) may be calculated to determine the Martinelli parameter, X, and to calculate the transitional curves to aid in the identification of the different flow regimes as shown in the following section.

5.3.2 Flow Regime Transition Criteria

As mentioned in Section 5.1, not all flow patterns were observed for the experimental test conditions covered in this investigation. The conditions encountered were intermittent flow (plug and slug), stratified wavy flow, annular flow and annular-dispersed flow.

Therefore, only the boundaries separating these regimes will be explored.

a) Transition from Stratified to Intermittent or Annular/Annular Dispersed

Taitel and Dukler described this transition in terms of the classical Kelvin-Helmholtz instability. Suppose that a small perturbation occurs on the interface in stratified flow. The vapour flowing over the protrusion will accelerate, giving a drop in the vapour pressure and producing a suction on the protrusion that will cause it to grow unless the suction is more than offset by the gravitational force acting downward on the protrusion. Taitel and Dukler derived the following expression as a condition for the growth of the protrusion (Hewitt, 1982):

$$F^2 \frac{1}{C_2^2} \frac{\bar{u}_V^{\,2} \, d\bar{A}_L / d\bar{h}_L}{\bar{A}_V} \geq 1 \tag{5.23}$$

where F is a modified Froude number given by:

$$F = \frac{xG}{(\rho_V (\rho_L - \rho_V) D_o g)^{1/2}} \tag{5.24}$$

and as explained by Osamusali (1988):

$$C_2 = 1 - \bar{h}_L \tag{5.25}$$

In dimensionless form the derivative of the liquid cross-sectional area with respect to the liquid level is:

$$\frac{d\bar{A}_L}{d\bar{h}_L} = \sqrt{1 - (2\bar{h}_L - 1)^2} - \sqrt{1 - (2\bar{h}_i - 1)^2} \left(\frac{D_i}{D_o} \right) \tag{5.26}$$

Rearranging Equation (5.23) and introducing Equations (5.21) and (5.25), the boundary between these regimes is a unique function of the liquid level h_L. Subsequently, F is given by:

$$F = \left((1 - \bar{h}_L)^2 \frac{\bar{A}_V^{\,3}}{\bar{A}^2} \frac{1}{d\bar{A}_L / d\bar{h}_L} \right)^{1/2} \qquad \textit{Taitel and Dukler} \tag{5.27}$$

If the wave criterion is satisfied, large waves are formed. Taitel and Dukler speculated that the formation of these waves led to either intermittent or annular flow depending on the liquid level. Hewitt (1982) summarized the Taitel and Dukler hypothesis as follows:

i) At lower values of $\bar{h}_L$, the wave may be swept up and around the tube to form an annulus, thus giving annular or dispersed-annular flow with some of the liquid being entrained in the vapour core due to interfacial waves on the liquid-vapour interface of the annulus. This mechanism for the formation of annular flow in horizontal tubes was suggested by Butterworth (1972).

ii) For large values of $\bar{h}_L$, the waves formed on the interface may grow and be swept along by the vapour phase (pseudo-slug flow) or touch the upper surface of the tube (plug and slug flow), giving a transition to the intermittent regime.

It is postulated that for an annular geometry, these mechanisms presented for tube flow by Taitel and Dukler should hold. The only notable difference is that for large values of $\bar{h}_L$, as the wave grows and approaches the upper portion of the tube, there would be greater vapour entrainment by the liquid slug due to the presence of the electrode.

Three adaptations of the Taitel and Dukler model have recently been presented and involve modifications to the transition criterion between separated and intermittent or annular flow according to Osamusali and Chang (1987, 1988), Steiner (1993) and Kattan *et al.* (1998a). The primary difference is the introduction of surface tension directly (Osamusali and Chang, 1987, 1988) or through the ratio between the Froude number and the Weber number (Steiner, 1993), where the Weber number is the ratio of inertia to the surface tension force and the Froude number is the ratio of inertia to gravity forces. For brevity sake, only the adaptation proposed by Steiner (1993) will be presented in this study due to the extensive database of refrigerant experiments establishing its effectiveness. The boundary curve for an annulus including the surface tension terms is given as follows:

$$F = \left(\frac{\bar{A}_V^3}{\bar{A}^2 \cdot d\bar{A}_L / d\bar{h}_L} \left[\frac{\pi^2}{25\ \bar{h}_L^2} \left(\frac{Fr}{We} \right)_L + 1 \right] \right)^{1/2} \quad \textit{Steiner} \qquad (5.28)$$

where the Froude - Weber number ratio is:

$$\left(\frac{Fr}{We} \right)_L = \frac{\sigma_L}{g\ D_o^2\ \rho_L} \qquad (5.29)$$

Including Equation (5.29), and hence surface tension effects, acts to increase Steiner's modified Froude number (Equation 5.28) over the Taitel and Dukler Froude number (Equation 5.27) for the same Martinelli parameter. That is, surface tension augments the gravitational force acting downward on the protrusion. Therefore, according to Equation (5.24), the mass flux or inertia of the vapour phase must be higher for the transition from stratified flow to occur.

The contributions of Kattan *et al.* (1998a) to the modified Taitel and Dukler map for this transition curve was to transform the axis coordinates from dimensionless quantities to mass flux and quality, to add 50 kg/m^{2}s to the transition boundary curve to suit their refrigerant data and to account for the influence of heat flux on the onset of dryout at high vapour qualities. The latter is not a factor in the present study and the addition of a fixed mass flux is an empirical 'fix' and therefore neither modification is considered in this analysis.

b) Transition between Intermittent and Annular/Annular Dispersed

For this transition, Taitel and Dukler (1976) hypothesized that if a sinusoidal wave existed on the interface, the wave would grow according to the previous criterion and if the liquid level exceeded a critical value, the wave crest would touch the top of the tube before its trough reached the bottom of the tube such that intermittent flow might be sustained. This critical value $\bar{h}_L = 0.5$ for horizontal flow which corresponds to a Martinelli parameter

of $X = 1.6$ in a tube flow and $X = 1.35$ for an annulus flow of radius ratio: $R_i / R_o = 0.291$. As reviewed by Hewitt (1982), several researchers, including Husain and Weisman (1978) Choe *et al.* (1978) and Weisman (1979), have indicated that their experimental evidence is inconsistent with this assumption. Steiner (1993) also defined an arbitrary fixed Martinelli parameter for turbulent flow, $X = 0.34$ to coincide with refrigerant data.

5.3.3 Flow Pattern Map For Flow in an Annulus

The results of the transition criterion from turbulent stratified wavy to annular and intermittent flows and from intermittent to annular flow for HFC-134a in an annulus are presented in Figure 5.6. In this figure, the dimensions correspond to those of the present investigation where the inner and outer diameters of the annuli are 3.18 mm and 10.92 mm, respectively. A comparison with the smooth tube transition boundaries predicted for the same diameter is included. The transitional values of these groups are calculated in

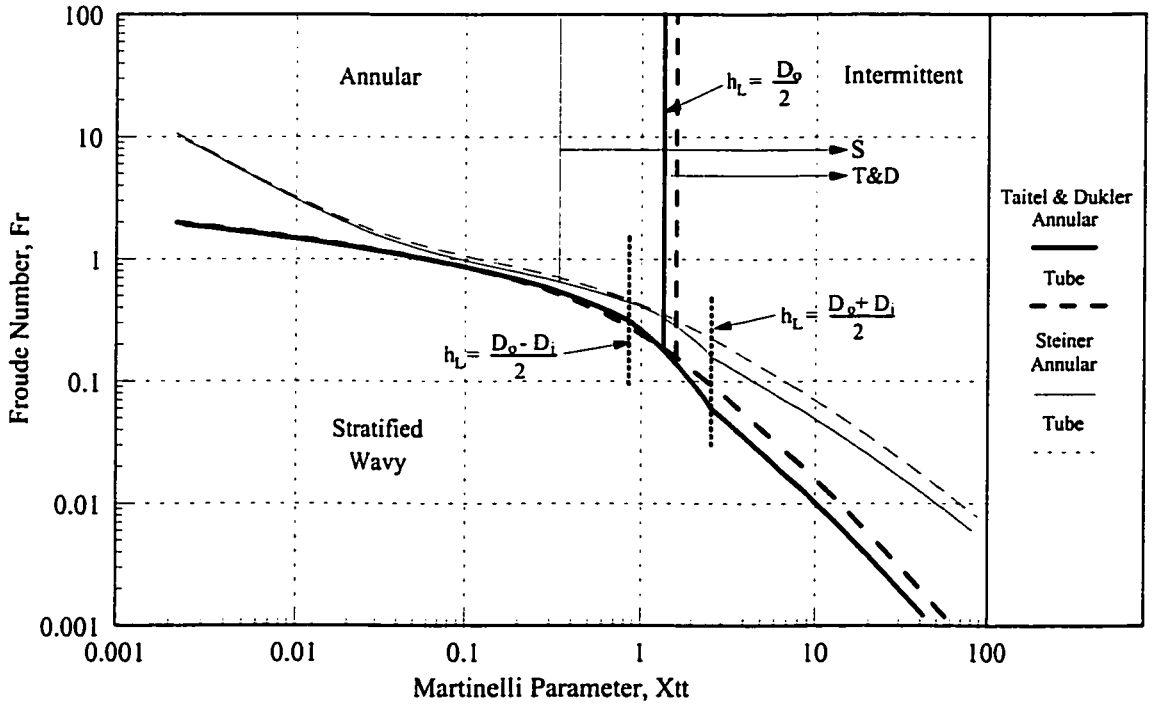

Figure 5.6: A Comparison of the Taitel & Dukler Map and Steiner Map for Tube and Annular Geometries.

terms of the dimensionless variables defined in Equations (5.13) - (5.22), where for a tube D_i and h_i are set equal to zero, and are thus related to h_L and hence to X (Equation, 5.11). The boundary curves in the Steiner map are functions of the fluid properties and have been evaluated at 25°C, the mean value of the experimental observations of this work.

By introducing the effects of surface tension through the inclusion of the Froude - Weber number ratio in Steiner's map, Equation (5.28), the transition Froude number increases as compared with that of the Taitel and Dukler, which suggests that higher inertia forces are required for transition to occur. In effect, surface tension acts to suppress the transition. When an electrode is included in the tube to form an annulus, there are further deviations from the two models. To describe how the geometry affects the acceleration of a small perturbation on the interface, it is convenient to consider the annular geometry broken into three regions:

For $0 < h_L < (D_o - D_i)/2$:

Initially, there is only a modest deviation between the tube and annular geometries in both maps as the liquid stratification level h_L is not influenced by the presence of the electrode. As the liquid level increases and approaches the electrode, the presence of the electrode decreases the vapour area and hence increases the vapour superficial velocity while not influencing the rate of change of the liquid area. This acts to increase the Froude number of the annulus over the tube Froude number in the Taitel and Dukler model. In this range, the Steiner model continues to predict a modest decrease in the annular Froude number over the tube Froude number as the inertia effects on the suction pressure are countered by surface tension.

In this range, there is a modest increase in the Martinelli parameter for the annulus over that of the Martinelli parameter for the tube geometry calculated at the same h_L. This

is due to the increased shear stress between the vapour and the electrode which acts to reduce the impact of the smaller flow area, decreasing the Froude number of the annulus over the tube Froude number.

For $(D_o - D_i)/2 \leq h_L \leq (D_o + D_i)/2$:

As the liquid comes into contact with the electrode, the Froude number begins to decrease rapidly as the Martinelli parameter increases. For the case of a smooth tube, the rate of change of the interfacial liquid area with height continues to increase until the level reaches the center of the tube where it decreases until the level reaches the top of the tube. Whereas in the presence of the electrode, the rate of change in interfacial liquid area decreases until the level reaches the tube center and then begins to increase. At the same time, the liquid contact with the electrode drastically increases the overall shear stress, decreasing the Martinelli parameter of the annulus over that of the tube. This is particularly apparent when the centerline Martinelli parameters are compared, $X = 1.60$ verus $X = 1.35$, for the tube and annulus, respectively. According to the Taitel and Dukler hypothesis, this corresponds to an earlier transition from intermittent flow to annular flow, although as the experimental data shows, this hypothesis does not hold for an annular geometry.

For $(D_o + D_i)/2 \leq h_L \leq D_o$:

In this range of liquid levels, the main difference is the electrodes' influence on Martinelli parameters due to the increased liquid shear stress. This is noted by observing the Martinelli parameter when the liquid level encompasses the electrode compared to the same liquid level for an empty tube. At this location, the Martinelli parameter is approximately 54% larger for tube flow, while the Froude number is essentially unaffected. Hence, an offset in transition boundaries is observed.

These results are consistent with the trends observed in the experimental and

numerical study by Osamusali and Chang (1988) for a two-component air-water system. Included in the Osamusali and Chang (1988) investigation was the effect of inner-to-outer radius ratios from 0.375 to 0.625. In their study it was noted that the stratified to intermittent transitions were significantly affected but not as much as predicted theoretically. This transition was seen to occur at lower liquid flow rates for larger diameter ratios. The study also suggested that the introduction of the inner rod had a negligible effect on the transition from stratified smooth to stratified wavy flows. One discrepancy between the two investigations is the transition from intermittent to annular flows. In the Osamusali and Chang study, the results suggested that the intermittent region was wider for the annular geometry than the pipe flow, as waves that would otherwise grow to form slugs were "damped" on encountering the annulus-rod in the system. Conversely, in the present investigation it was shown that these waves would continue to grow and were swept around the channel forming annular flow. This discrepancy is likely due to one of three differences in the studies: the minimum diameter ratio investigated by Osamusali's investigation was 30% larger than that used in the present work, the system investigated an air-water, two-component system and the differences in surface tension between the two liquids is an order of magnitude.

5.4 Two-Phase Flow Pattern Test Results

To assess the effectiveness of the proposed model for an annular geometry and develop a method to ascertain the flow regime through the EHD heat exchanger, the transition criterion have been compared to the inlet and outlet flow patterns observed by the naked eye, high speed photography and transient void fraction measurements. Observations made at the inlet are those of a smooth tube as they are made just upstream of the heat

exchanger, Figure 4.1, and are considered adiabatic fully developed flow patterns. At the outlet of the heat exchanger, the observations are essentially diabatic as the influence of acceleration or deceleration is present due to changes in flow density by evaporating or condensing the mixture.

Figures 5.7 and 5.8 show, respectively, the inlet (tube) and outlet (annulus) HFC-134a data for a wide range of qualities (4 - 95 %) and mass fluxes (90 - 550 kg/m^{2}s) plotted against both models described in the previous section.

For the inlet conditions, the transition boundaries proposed by Taitel and Dukler (1976) predict the flow regimes very well although there are some deviations in the vicinity of the stratified wavy to annular transition curve. For the 118 experiments where the flow was two-phase at the inlet, the original model of Taitel and Dukler correctly identified 106 (90%) of the data points within the experimental error of the measured Froude numbers and

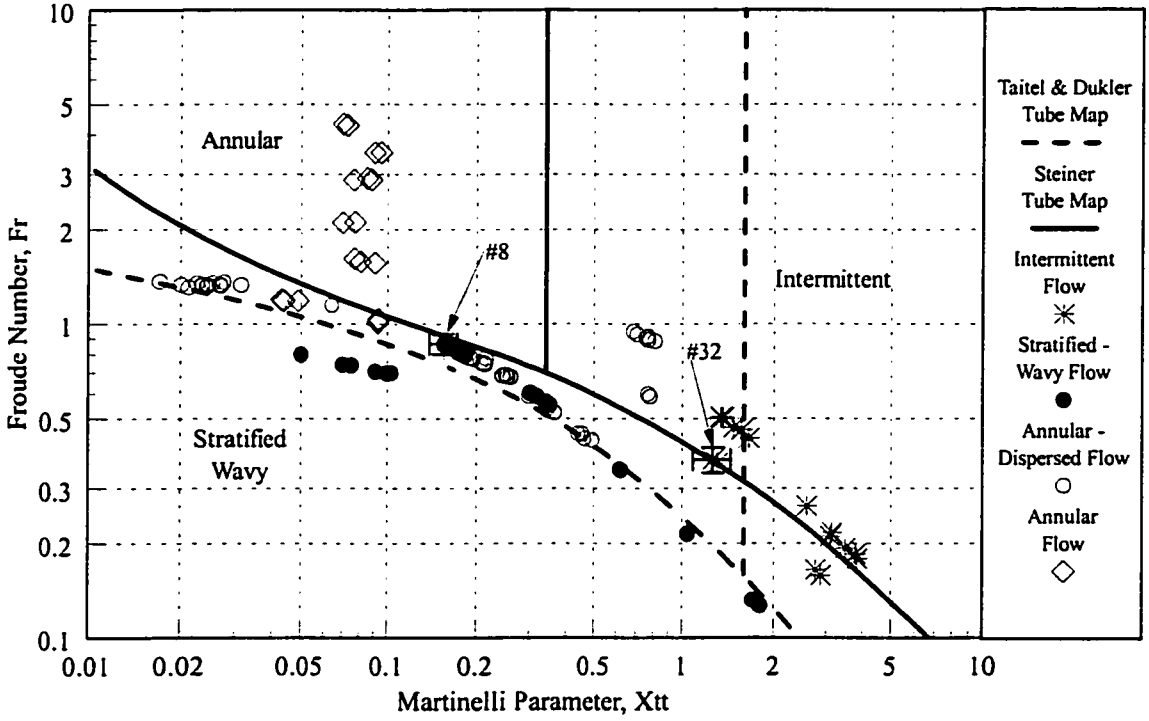

Figure 5.7: Inlet Flow Pattern Data Compared Against the Taitel & Dukler and Steiner Flow Pattern Maps at 25°C.

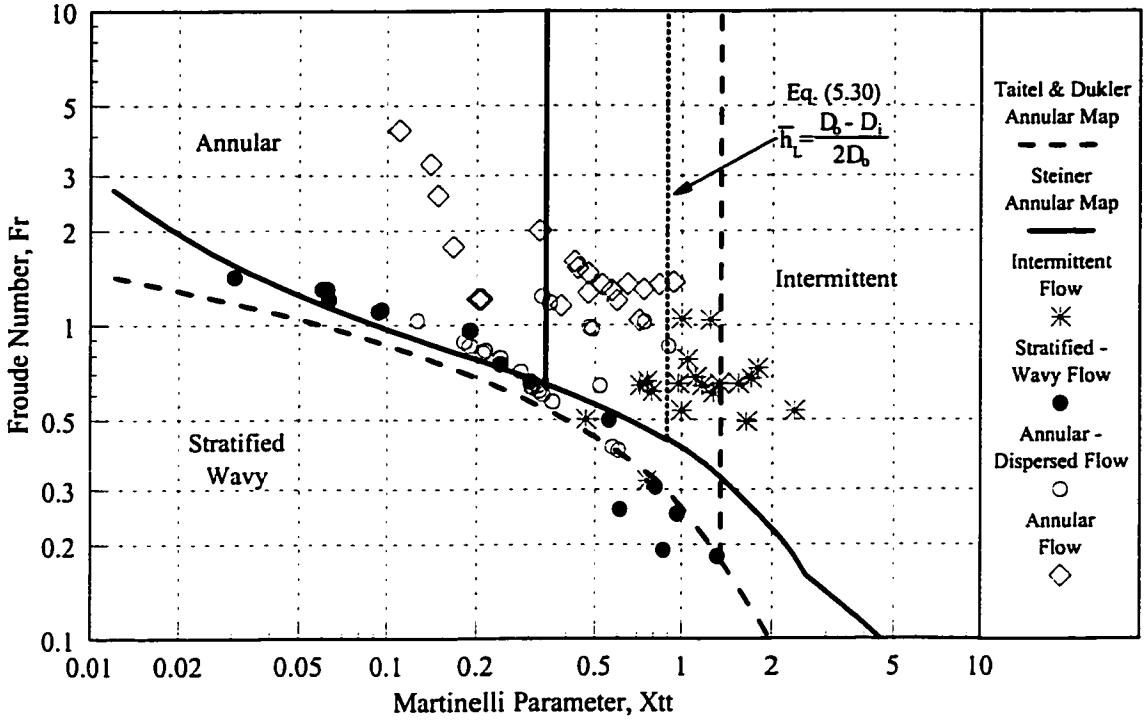

Figure 5.8: Outlet Flow Pattern Data Compared Against the Taitel & Dukler and Steiner Flow Pattern Maps Developed for Annular Geometries at 25°C.

Martinelli parameters. The procedure for evaluating the measurement error associated with the flow regime mapping is presented in Appendix B. The results of test # 8 and # 32 are fitted with error bars in Figure 5.7. When the data is compared against the Steiner map for a tube flow, it is apparent that the introduction of the surface tension effects are overemphasized and the arbitrary selection of $X = 0.34$ as the boundary between intermittent and annular flow is incorrect as the model only correctly identified 65% of the measurements within the experimental error. This is completely opposite to the results of Kattan (1996) and Kattan *et al.* (1998a), while consistent with the conclusions presented by Abdul-Razzak *et al.* (1995). As Abdul-Razzak *et al.* stated, as the surface tension of HFC-134a is one order of magnitude less than that of water, the effect of surface tension on the transition boundary of the system should be negligible. There are four probable reasons for the differences between the results of the present investigations and the results of Kattan.

i) The identification and assignment of flow regimes is a subjective judgement on the part of the observer so that the difference might be partially due to the method of visualizing the liquid and vapour configuration.

ii) Kattan (1996) observations for HFC-134a at 4.4°C were made through a 12.00 mm diameter sight glass while the heat exchanger diameter was 10.92 mm. The sudden expansion results is a deceleration of the flow, possibly leading to a change in flow regime. In the present investigation, the polycarbonate sight tube was bored out to match the heat exchanger diameter.

iii) The investigation by Kattan *et al.* (1998a) presented data at a much lower temperature than the present investigation (-1.3°C to 10.3°C verus 25°C), which corresponds to approximately a 30% larger value of surface tension. The Kattan *et al.* results did suggest that the ability to identify flow patterns decreased with increasing temperature, although it was not explicitly stated.

iv) Kattan *et al.* (1998a) made the visual observations at the exit of an evaporator and suggested that their data be considered diabatic. Therefore, an acceleration component exists in the flow because of changes in flow density due either to changes in quality or expansion of the vapour as the pressure varies along the tube. This would correspond to a larger Froude number for the same Martinelli parameter, creating a similar effect to the addition of the surface tension to the Taitel and Dukler model. In the present investigation, the flow is fully developed and adiabatic at the inlet.

When considering the outlet flow pattern map for the annular geometry presented in Figure 5.8, it is convenient to consider the transition boundaries separately. For the transition from stratified wavy to the intermittent or annular/annular-dispersed flow, contrary to the inlet data, the modified Taitel and Dukler map presented by Steiner (1993) performs reasonably well. The Steiner criterion correctly identified 66 of the 77 flow regimes while the Taitel and Dukler model for this annulus identified 65 correctly within experimental error. While not a significant difference, the deviation between the experimental data and the boundary of the annular Steiner map for the points incorrectly predicted was closer than the boundary criterion of the annulus geometry Taitel and Dukler map.

As evident from Figure 5.8, neither model predicts the transition between intermittent and annular flow correctly. This inability to identify experimentally observed flow patterns

in this region has been reported by numerous investigators for a tube flow, as mentioned earlier, and is due to the arbitrary nature of the hypothesis' made by Taitel and Dukler and Steiner. For the case of an annulus, it is believed that as the liquid level reaches the bottom of the electrode (the inner rod), surface tension between the liquid and the electrode creates a capillary effect that acts to 'pull' or accelerate the wave towards the upper portion of the tube before the trough can reach the bottom of the tube. Based on this reasoning and the comparison with experimental data, the boundary between the intermittent and annular flow has been selected to correspond to the hydraulic diameter of the annulus, defined as follows:

$$\bar{h}_L = \frac{D_h}{D_o} = \frac{D_o - D_i}{2D_o} \tag{5.30}$$

5.5 Proposed Graphical Representation for Mapping Flow Patterns

To better identify flow patterns during the flow boiling process at different mass fluxes, the graphical representation for diabatic flow regime transition suggested by Kattan *et al.* (1998) will be used. By converting the axis of the Taitel and Dukler and Steiner maps to mass flux and vapour quality, the evaluation of local flow regimes axially along the evaporator will aid in the interpretation of the local heat transfer data and elude to how flow regime augmentation influences heat exchanger effectiveness.

For that purpose, the abscissa of the Taitel and Dukler (and Steiner) map, the Martinelli parameter, is converted to vapour quality according to:

$$x = \left(\left[X \left(\frac{\rho_L}{\rho_V} \right)^{1/2} \left(\frac{\mu_V}{\mu_L} \right)^{n/2} \right]^{2/(2-n)} + 1 \right)^{-1} \tag{5.31}$$

where the thermodynamic properties are evaluated at the saturation temperature of the experimental flow regime to be identified. By extracting the mass flux from the ordinate parameters of the transition equations, the transition curves obtained are:

$$G = \left[\frac{(1 - \bar{h}_L)^2 \, \bar{A}_V^3 \, \rho_V \, (\rho_L - \rho_V) \, D_o \, g}{\bar{A}^2 \cdot d\bar{A}_L / d\bar{h}_L} \right]^{1/2} \cdot \frac{1}{x} \tag{5.32}$$

and

$$G = \left(\frac{\bar{A}_V^3 \, \rho_V \, (\rho_L - \rho_V) \, D_o \, g}{\bar{A}^2 \cdot d\bar{A}_L / d\bar{h}_L} \left[\frac{\pi^2}{25 \, \bar{h}_L^2} \left(\frac{Fr}{We} \right)_L + 1 \right] \right)^{1/2} \cdot \frac{1}{x} \tag{5.33}$$

for the Taitel and Dukler and Steiner transition boundaries, respectively.

Figure 5.9 presents the comparison of the Taitel and Dukler map and the Steiner map for tube and annulus geometries (Figure 5.6) transformed to this graphical representation, where the thermodynamic properties have been evaluated at a saturation temperature of 25°C. With this representation it is important that temperature effects be considered. Therefore, Figure 5.10 presents the influence of saturation temperature for the range of temperatures (20°C to 30°C) explored in the experimental investigation. As the maximum difference in transition mass fluxes at this range of temperatures did not exceed 10 kg/m²s, the average operating temperature (25°C) was used to calculate the boundaries of the flow patterns being considered. As Kattan *et al.* (1998a) suggested, with this representation it is feasible to follow the changes in flow pattern during the evaporation of a refrigerant at a fixed mass flux. The inflection point at approximately 8% quality corresponds to the liquid level exceeding the top of the electrode and is numerical in nature, therefore in reality the transition boundary is expected to be smooth.

To summarize, based on the experimental observation in Section 5.4, the Taitel and Dukler map will be used to predict the tube flow inlet conditions, while the transition criterion from stratified wavy to annular or intermittent flow proposed by Steiner, and modified for an annulus, will be adopted for the evaporator. To ascertain whether the flow is annular or intermittent, once the transition from stratified wavy has occurred, the

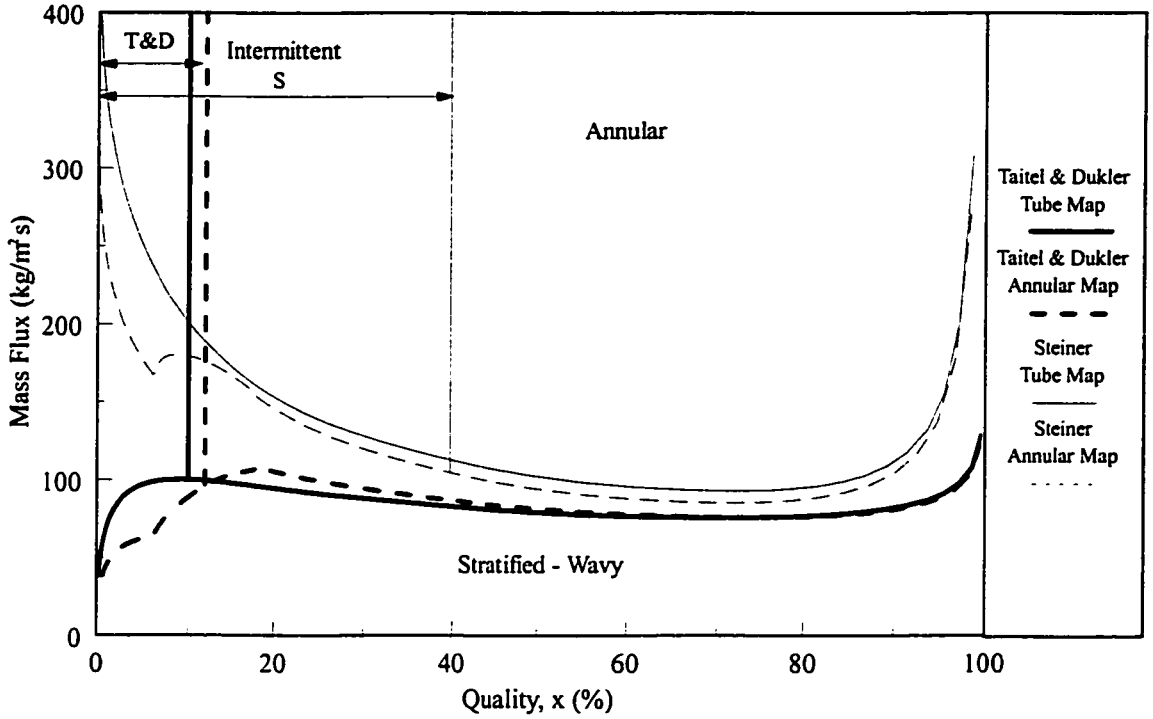

Figure 5.9: Proposed Graphical Representation of the Taitel and Dukler Map and the Steiner Map.

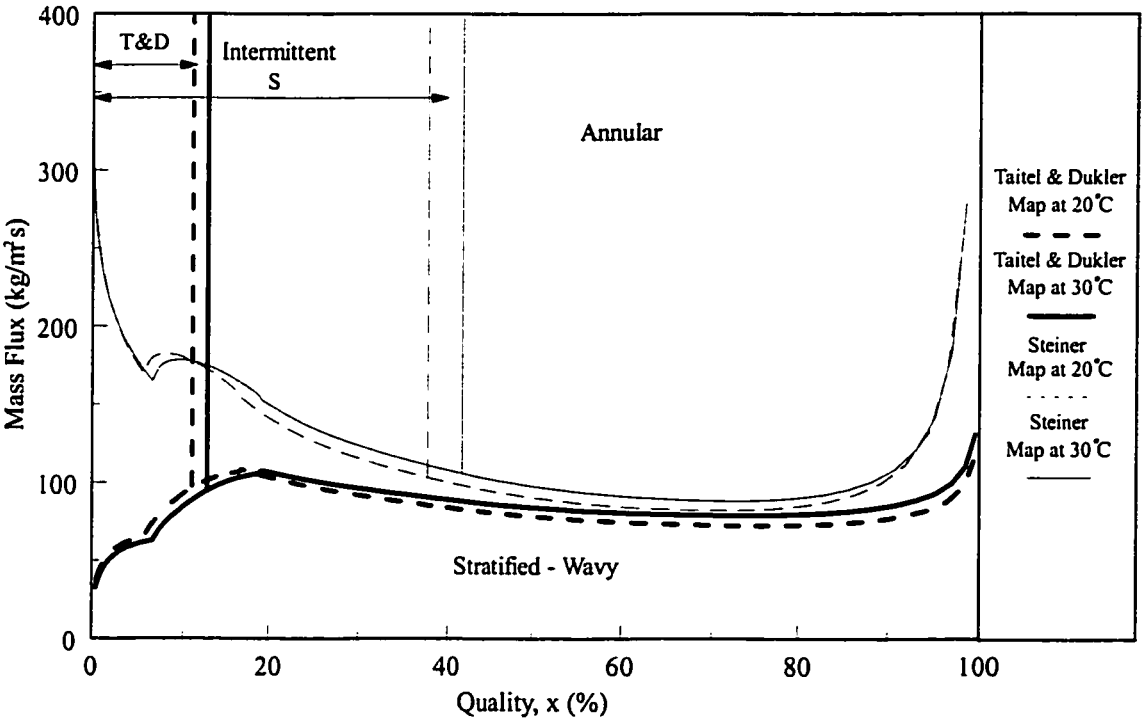

Figure 5.10: The Effect of Temperature on Flow Pattern Transition for Flow in an Annulus.

hypothesis that capillary effects due to the presence of the electrode act to pull a wave growing on the interface to the top of the tube before its trough reaches the bottom will be assumed. Thus, employing Equation (5.30) to determine the corresponding Martinelli parameter leads to $X = 0.89$ or in the recommended graphical representation a vapour quality of $x = 17.8\%$ for the geometry being considered in this investigation.

Determining the flow regime within the evaporator channel without EHD forces will be completed through the graphical representation proposed by Kattan *et al.* (1998a), with support of the measured surface temperatures as outlined in the following chapter. Figures 5.11 and 5.12 present the proposed flow regime maps with the inlet and outlet experimental data. In their final form, the inlet map correctly predicts 90% of the data points and the outlet annulus geometry map identifies 82% of the flow regimes properly, when experimental measurement error and temperature effects are considered.

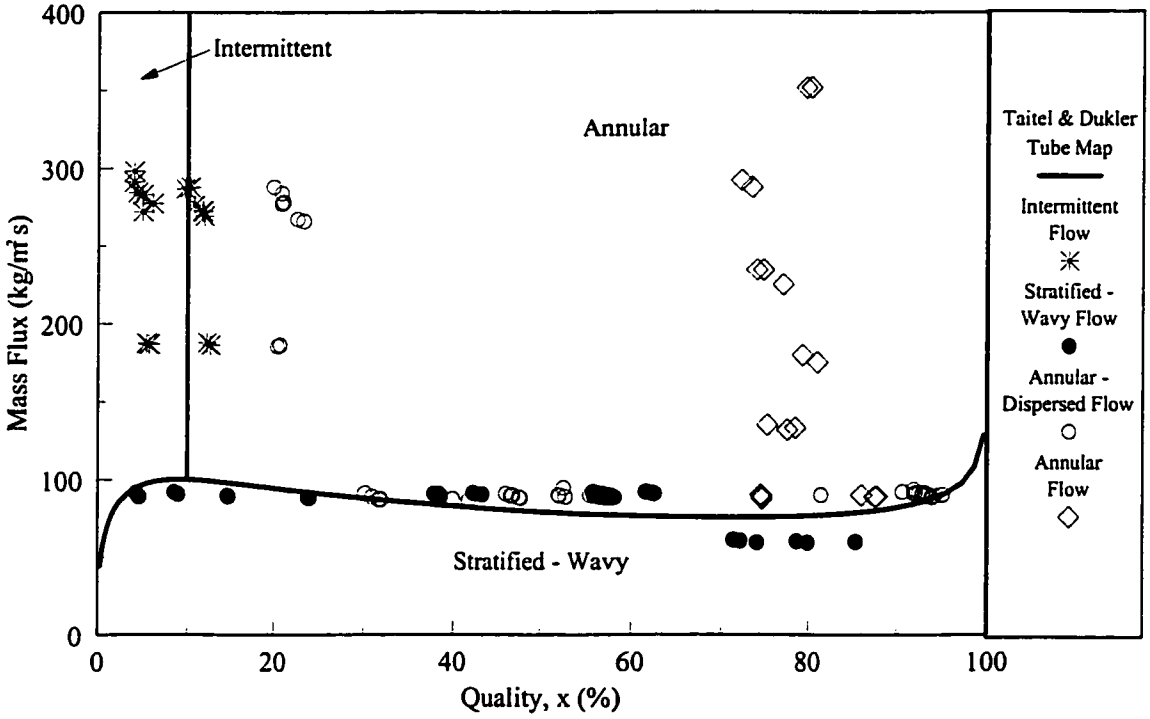

Figure 5.11: Inlet Flow Pattern Data Compared Against the Proposed Graphical Representation of the Taitel & Dukler Flow Pattern Map at 25°C.

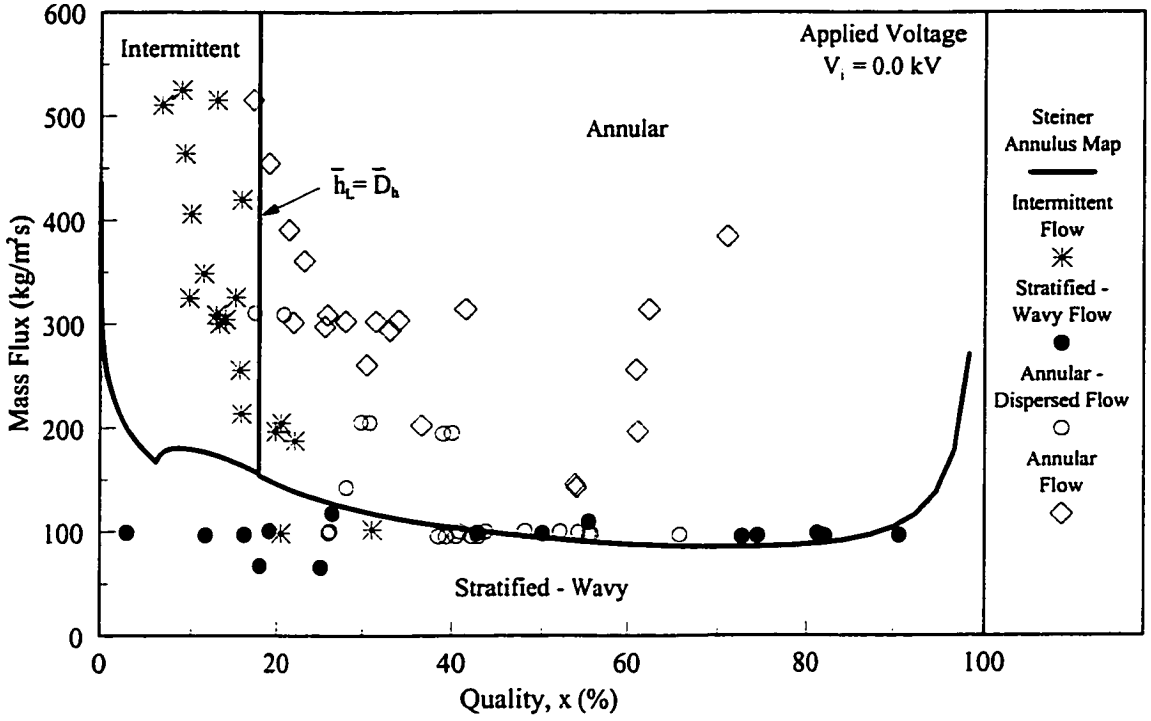

Figure 5.12: Outlet Flow Pattern Data Compared Against the Proposed Graphical Representation of the Modified Steiner Flow Pattern Map at 25°C.

5.6 Two-Phase EHD Flow Patterns and the Modified Steiner Map

When a high voltage is applied to the electrode and the tube is grounded, an electric field is established. Depending on the field established and the electrical body forces acting on the interface, an augmentation in flow regime may be observed. Numerous components simultaneously act upon the flow; a flow transition may occur due to the influence on the individual phases by an increase in radial convection due to electrophoretic forces, migration of bubbles, bubble deformation, instability effects of liquid-vapour interfaces, or possible instabilities and bulk motion due to liquid extraction. This is more than evident when a voltage 8 kV or greater is applied to the electrode for the same flow conditions presented in Figure 5.12. Figure 5.13 shows the observed flow patterns at the exit of the test section plotted against the modified annulus geometry Steiner map.

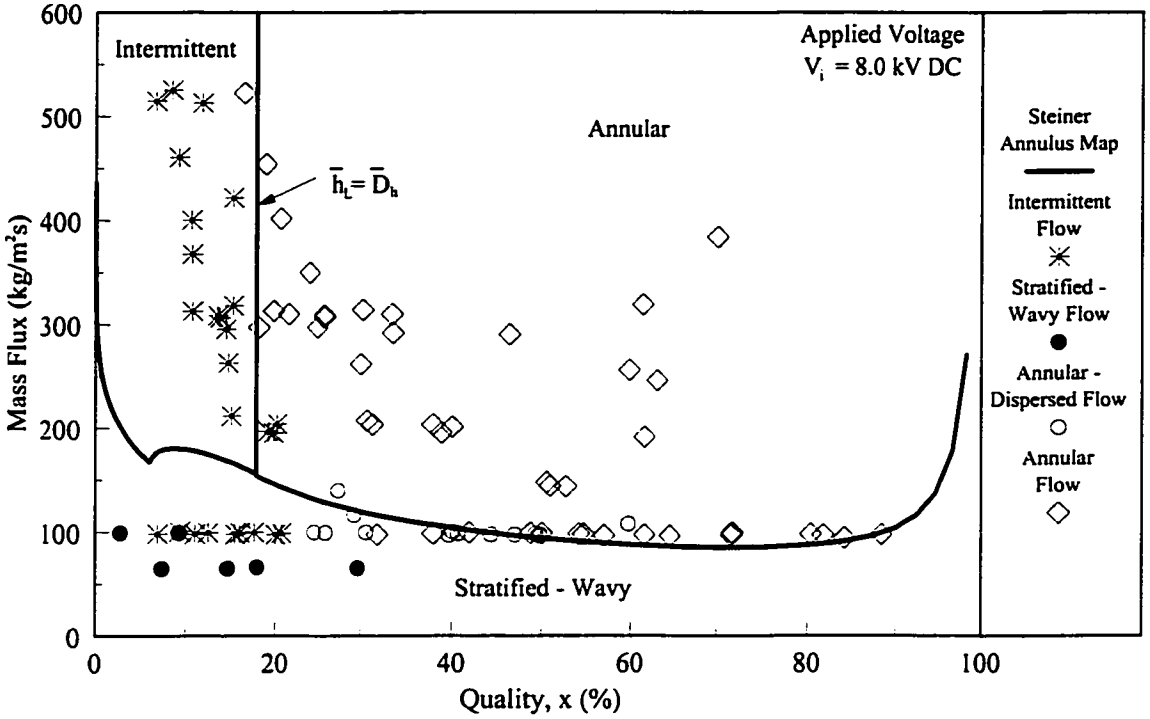

Figure 5.13: Outlet EHD Flow Pattern Data Compared Against the Proposed Graphical Representation of the Modified Steiner Flow Pattern Map at 25°C.

Several differences between the two figures exist. Notable is the transition from stratified to annular or intermittent flow. The origin of this orientation change depends upon how significant the EHD force density components are with respect to the fluid momentum and the quality. The following chapter attempts to clarify the mechanisms that induce a flow pattern augmentation due to the addition of the electrohydrodynamic force and proposes a one-dimensional model to predict flow transition upon the application of an electric field.

Chapter 6

The Interaction of Flow Pattern and Electric Field Distributions

As presented in the last section of the previous chapter, an interdependence exists between the observed flow regime and the applied voltage, and subsequently the electric field distribution established. Unlike single-phase flow, in "phase change" processes the field established is continuously changing as the flow regime changes due to interfacial vaporization or condensation, as outlined in Chapter 2. To further complicate the variation in this dynamic field effect, the interaction between the electric field and the fluid introduce a body force that can also cause a redistribution of the phases. In an effort to understand and analyse this interaction, the electric field distribution must be determined. To contribute to this effort, the evaluation of the static electric field distribution is performed for various flow regimes to provide a qualitative assessment regarding the direction of phase migration and possible flow pattern transition and to determine the net EHD force acting on the flow for an instant in time, *i.e.* for a given phase distribution. Combining this force with the proposed flow pattern map for an annulus geometry presented in Chapter 5, will assist the evaluation of the local flow regimes axially along a heated channel where EHD effects are present. Coupling the proposed EHD flow pattern map with the interpretation of the measured time-averaged and transient surface temperatures, the sequence of convective boiling flow patterns in an annulus is proposed for various flow and electric field conditions as outlined in Chapter 7. By establishing the sequence of flow regimes encountered, insight can be

gained in the interpretation of local heat transfer data and may clarify how EHD forces affect flow regime augmentation to influence heat exchanger effectiveness.

6.1 Analysis of Static Electric Field Distributions in Two-Phase Flow

The analysis of an electric field imposed on a two-phase flow significantly depends on the electrode geometry and liquid-vapour distribution within the electrode assembly. For the purpose of this work, three electrode configurations are considered: a concentric annulus electrode arrangement and two eccentric arrangements according to the specifications of the experimental test section outlined in Chapter 4. The flow patterns considered are the annular, liquid encircled electrode and stratified regimes, and the calculation of the electric field distributions are performed analytically and through a finite element numerical analysis.

6.1.1 Theoretical Electric Field Analysis

The analytical calculation of electric field distribution is obtained from the Maxwell's relation:

$$\nabla \cdot \overline{E} = \frac{1}{\varepsilon}\rho_{ie} \tag{6.1}$$

where the electric field vector is defined as:

$$\overline{E} = -\nabla V \tag{6.2}$$

Combining Equations (6.1) and (6.2) gives:

$$\nabla \cdot \nabla V = -\frac{1}{\varepsilon}\rho_{ie} \tag{6.3}$$

commonly referred to as the Poisson equation, which, when written in cylindrical coordinates, takes the form:

$$\nabla^2 V = \frac{1}{r}\frac{\partial}{\partial r}\left(r\frac{\partial V}{\partial r}\right) + \frac{1}{r^2}\left(\frac{\partial^2 V}{\partial \varphi^2}\right) + \frac{\partial^2 V}{\partial z^2} = -\frac{\rho_{ie}}{\varepsilon} \tag{6.4}$$

The solution of Equation (6.4) is valid for any flow or electrode configuration. However, due to the mathematical complexity involved in a complete solution, the only flow configurations considered analytically are single-phase, annular and liquid encircled electrode flow in a concentric annulus, as presented in Figure 6.1, with their respective boundary conditions corresponding to the experimental part of this investigation.

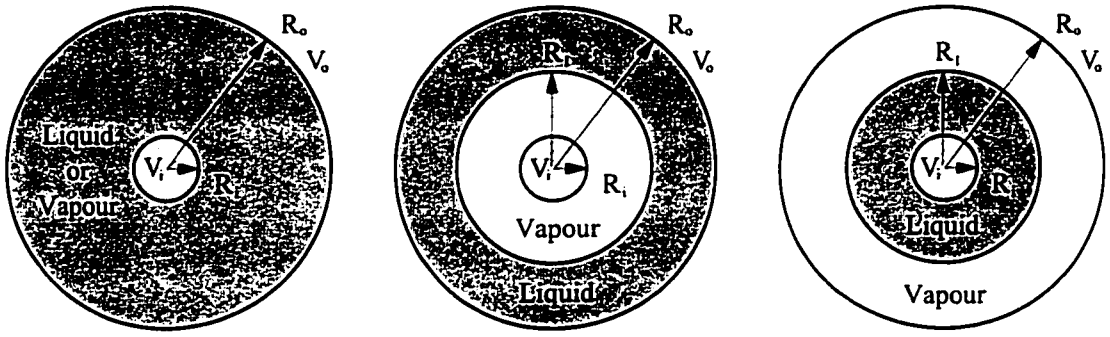

$V = V_i = 8.0$ kV @ $r = R_i = 1.59$ mm
$V = V_o = 0.0$ kV @ $r = R_o = 5.46$ mm

a) Single-Phase Flow b) Annular Flow c) Liquid Encircled Electrode Flow

Figure 6.1: Boundary Conditions of Flow Regimes Analyzed Theoretically to Determine their Electric Field Distribution.

It is assumed that both fluids are isotropic and completely separate from one another and that the tube and electrode are infinitely long. Finally, for the fluid under consideration (HFC-134a) and the fact that the phases are in motion, it is reasonable to suggest there is no net space charge and there is insufficient time for a surface charge to establish on the liquid-vapour interface. Appendix A presents the fluid properties and addresses the issue of charge relaxation time in detail. Consequently, the right hand side of Equation (6.4) is negligible. The result is the Laplace equation. For a homogeneous single-phase fluid, the solution is simply:

$$E_{Sp_r} = \frac{V_i}{r \ln(R_o / R_i)} \tag{6.5}$$

For the annular and the encircled electrode cases, the boundary conditions at an

interface between dielectric materials are required and may be determined by considering a plane boundary between regions of different dielectric constants ε_1 and ε_2. As found in any introductory text on electricity such as Kip (1969), these interfacial boundary conditions are:

- *The normal component of the electric displacement vector, **D**, is the same on each side of the boundary.*

$$D_{n1} = D_{n2}$$
$$\varepsilon_1 E_{n1} = \varepsilon_2 E_{n2} \tag{6.6}$$

- *The component of the electric field, **E**, tangent to the boundary is the same on each side of the boundary.*

$$E_{t1} = E_{t2} \tag{6.7}$$

Due to the symmetry of liquid and vapour, with respect to the electrodes, for the two-phase concentric cases analyzed theoretically, the electric field intersects the interface normally at all radial positions. Applying Equation (6.6) where *1* represents the vapour, *v*, and *2* the liquid, *l*, the interfacial voltage may be determined.

First, solving the vapour radial field distribution for the annular case:

$$\boldsymbol{E}_{r\text{-}v} = \frac{V_i - V_I}{r \ln (R_I / R_i)} \quad ; \quad \boldsymbol{E}_{0\text{-}v} = 0 \tag{6.8}$$

and the liquid gap between the interface and the tube:

$$\boldsymbol{E}_{r\text{-}l} = \frac{V_I - V_o}{r \ln (R_o / R_I)} \quad ; \quad \boldsymbol{E}_{0\text{-}l} = 0 \tag{6.9}$$

Combining $\boldsymbol{E}_{r\text{-}v}$ and $\boldsymbol{E}_{r\text{-}l}$ through the interfacial boundary condition, Equation (6.6), and solving for the voltage at the interface, V_I, gives:

$$V_I = \frac{V_i}{\frac{\varepsilon_l}{\varepsilon_v}\left(\frac{\ln (R_I / R_i)}{\ln (R_o / R_I)}\right) + 1} \tag{6.10}$$

The interfacial voltage is substituted into $\boldsymbol{E}_{r\text{-}v}$ and $\boldsymbol{E}_{r\text{-}l}$ to determine the radial electric field distribution for various annular thicknesses, t_I, or void fractions, α.

The analysis for liquid encircled electrode flow is identical. However, when determining the interfacial voltage, the dielectric constant ratio in the denominator of

Equation (6.10) is inverted. The results of this analysis and a discussion of the interaction of electric field distribution and flow regime is discussed in Section 6.2.

The analysis of stratified flow is more complicated as the symmetry condition no longer applies and therefore a numerical analysis is performed. However, insight into the forces acting on the interface and their relative vector directions may be gained by making the assumption that the vector direction of the electric field through the vapour phase is radially outward from the inner electrode to the outer electrode. Applying the boundary conditions described in Equations (6.6) and (6.7) at a dielectric surface with the isotropic assumption, it is apparent that the direction of the incident electric field will change as it passes through the interface as depicted in Figure 6.2.

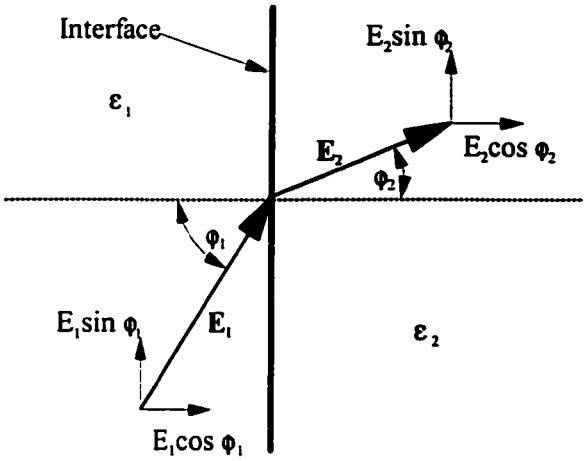

Figure 6.2: Change in Direction and Magnitude of $\boldsymbol{E}$ at a Dielectric Surface.

To determine the relationship between the angles φ_1 and φ_2, the conditions $\boldsymbol{E}_{t1} = \boldsymbol{E}_{t2}$, $(E_1 \sin\varphi_1 = E_2 \sin\varphi_2)$ and $\boldsymbol{D}_{n1} = \boldsymbol{D}_{n2}$, $(\varepsilon_1 E_1 \cos\varphi_1 = \varepsilon_2 E_2 \cos\varphi_2)$ are applied. Combining results for **D** and **E** and rearranging to solve for φ_2 gives the corresponding vector direction of the electric field leaving the surface:

$$\varphi_2 = \tan^{-1}\left(\frac{\varepsilon_2}{\varepsilon_1} \tan\varphi_1\right) \tag{6.11}$$

Application of Equation (6.11) to the case of concentric electrodes used in the present investigation with a 2.7 mm liquid stratified thickness under the stipulated simplification is presented in Figure 6.3. As shown, an incident electric field vector having an angle of 10°

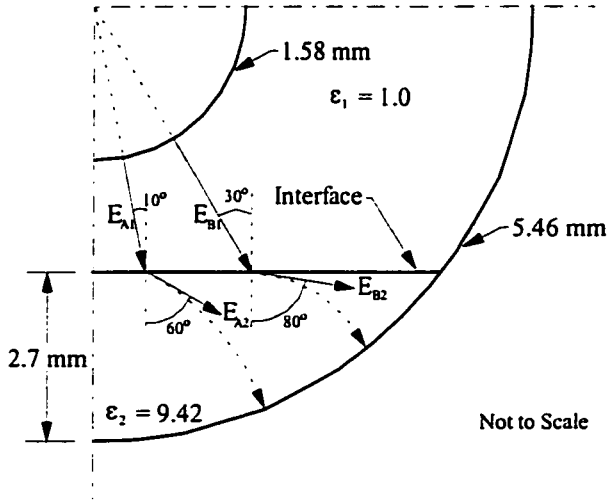

Figure 6.3: Direction of Electric Field Vectors Applied to Stratified Flow in a Concentric Electrode Channel.

will change direction by 50° as it exits the interface (Case A), while an incident field vector of 30° would exit at an angle of 80° from vertical (Case B). Further, it may be shown that the magnitude of each vector would decrease as a function of the incident vector, for the examples shown in the above figure $E_{A2} = 0.11E_{A1}$ and $E_{B2} = 0.51E_{B1}$, respectively. The relevance as applied to the electric body force is two-fold:

- A change in direction of the electric field as it crosses the interface will result in a change in the direction of the electrophoretic forces acting in the bulk of the vapour and liquid, respectively.

- The significant non-uniformity in the field distribution would result in a bulk migration of the liquid from the relatively lower field strength region to regions where the field strength is more intense via what is commonly referred to as the liquid extraction phenomena, as described in Chapter 3.

Figure 6.4 presents the effect of incident angles on the direction of the exiting electric field vector and the ratio of electric field strength of an electric field that crosses an interface when the liquid level is below and above the electrode, respectively.

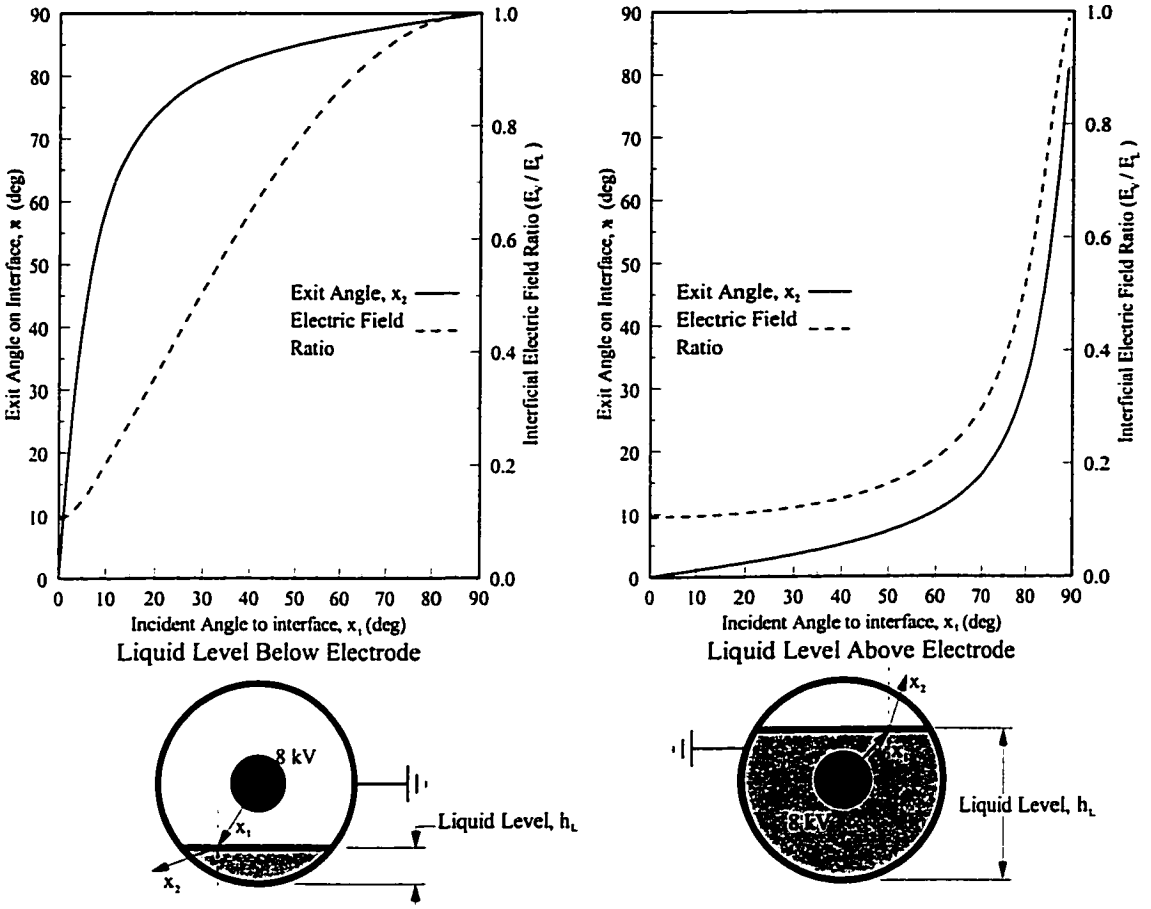

Figure 6.4: Change in Direction and Magnitude of the Electric Field as a Function of the Incident Angle for Stratified Flow in Concentric Electrodes.

For the condition when the liquid is below the electrode, as presented in Figure 6.3, the significant increase in the exit angle creates an electrophoretic force in the liquid that could cause a migration towards the outer edges of the interface near the tube wall, while the stronger field strength in the vapour would suggest a possible extraction of liquid vertically upwards. Combined, both effects act against gravity and may lead to liquid being forced towards the electrode or around the tube wall, resulting in a change in flow regime from stratified to intermittent or annular flow. When the liquid is above the electrode, it is conjectured that there will be less of an influence on the phases based on the same reasoning; the change in direction of the electric field creates an upward force in the vapour which is already above the liquid, and while the ratio of the field amplitude is larger in the vapour

phase, the difference is insignificant until the incident angle approaches 75°. Although this analysis is revealing, the simplifying assumption prevents any quantitative measure of the absolute electric field strength. To determine the field distribution in non-symmetric flow regimes, such as the stratified flow regime, a numerical approach is described in the following section.

6.1.2 Finite Element Analysis of Electric Fields

The finite element analysis represents an approximate numerical solution of a problem described by the Laplace equation, as was performed analytically for the symmetric flow regimes. The code used is a modification of Brocilo (1997) for the determination of the electric field distribution in buried transmission lines and is described in Appendix C. The analysis is performed in Cartesian coordinates for the three electrode configurations explored experimentally under the following assumptions:

- The problem is Laplacian since both space charge and surface charge are negligible, as discussed in the analytical analysis.
- The system is symmetric from left to right.
- The electrodes are parallel and infinitely long. Thus, end effects are negligible and the problem is two-dimensional.
- Surface effects are negligible.
- The analysis is performed with saturated refrigerant HFC-134a as the working fluid, at a temperature of 25°C. Therefore, the dielectric constant of the vapour phase is 1.09 and the liquid phase is 9.42.
- The conductivity of the conductors (the tube and the electrode) is assumed to be $\sigma_e = 5.8 \times 10^6\ \Omega^{-1}\cdot m^{-1}$.

In general, the finite element code is described by the flow diagram shown in Figure 6.5. An overview of the necessary preprocessing is provided in Appendix C under the aforementioned assumption and modelling the system as Laplacian. The discretization of

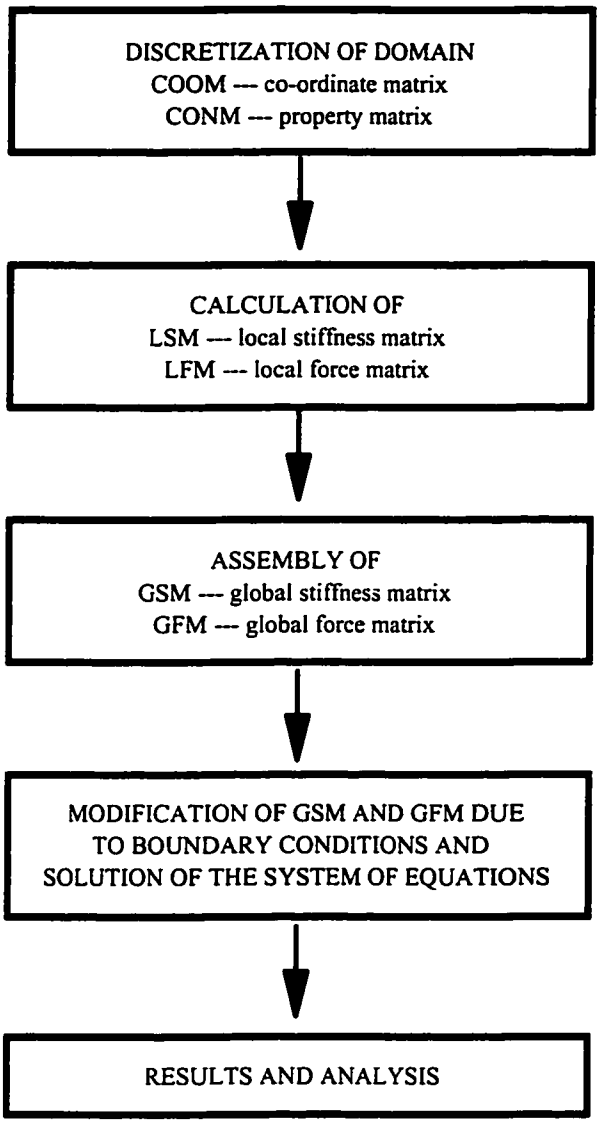

Figure 6.5: Finite Element Code Flow Chart (Cotton *et al.*, 1998a).

the electrode arrangement used triangular elements and was performed manually based on the design of the experimental electrode assemblies, Figure 6.6. The mesh could calculate the field distribution of a single-phase fluid, 32 liquid levels of stratification (h_L) and an annular flow case having a liquid thickness of t_L = 0.85 mm for analytical bench-marking and grid sizing. For code verification, the finite element predictions are compared against the theoretical analysis in the following section and the discussion of the results of the numerical analysis is presented in Section 6.2.

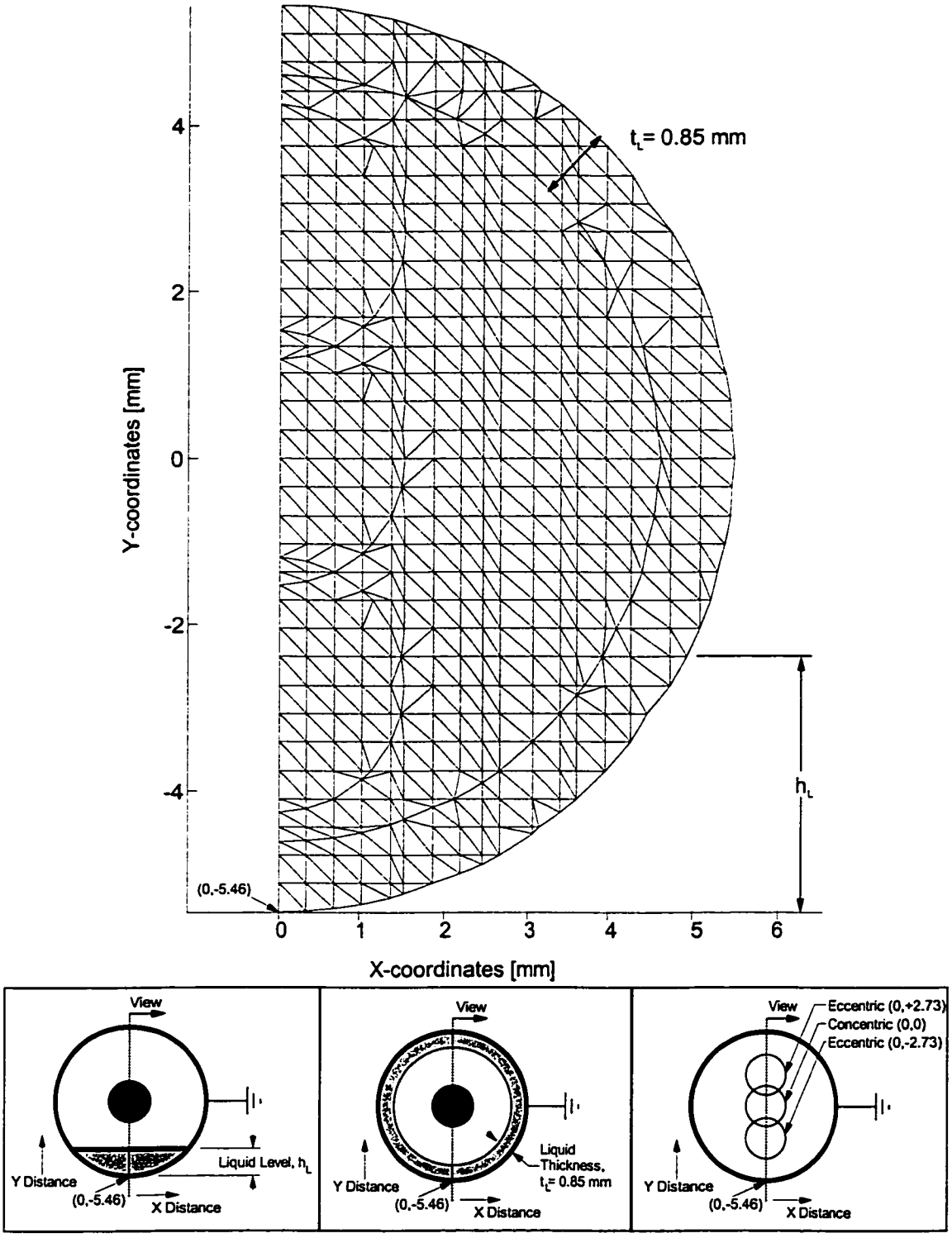

Figure 6.6: Finite Element Mesh and Conditions Investigated Numerically.

6.1.3 Comparison of Analytical and Finite Element Results: Code Verification

To confirm the validity of the finite element analysis, Figures 6.7 and 6.8 present a comparison of the analytical results and the results computed numerically for a single-phase fluid and an annular flow of film thickness equal to 0.85 mm, respectively. The analysis is performed at 25°C at the maximum applied voltage investigated experimentally (8.0 kV). The grid size was increased from 43 x 22 (0.273 mm) to 113 x 57 (0.100 mm), in order to investigate grid dependence. As shown, the results within the bulk of the individual phases are essentially identical, deviating by less than 3.0%, and the mesh size has no significant effect, suggesting the solution is independent of the grid spacing used. At the liquid-vapour interface for the annular case, Figure 6.8, a rather significant gradient is observed for the large grid spacing. In order to minimize this effect, the remainder of the finite element analysis was performed using the finer mesh size 113 x 57 (0.100 mm).

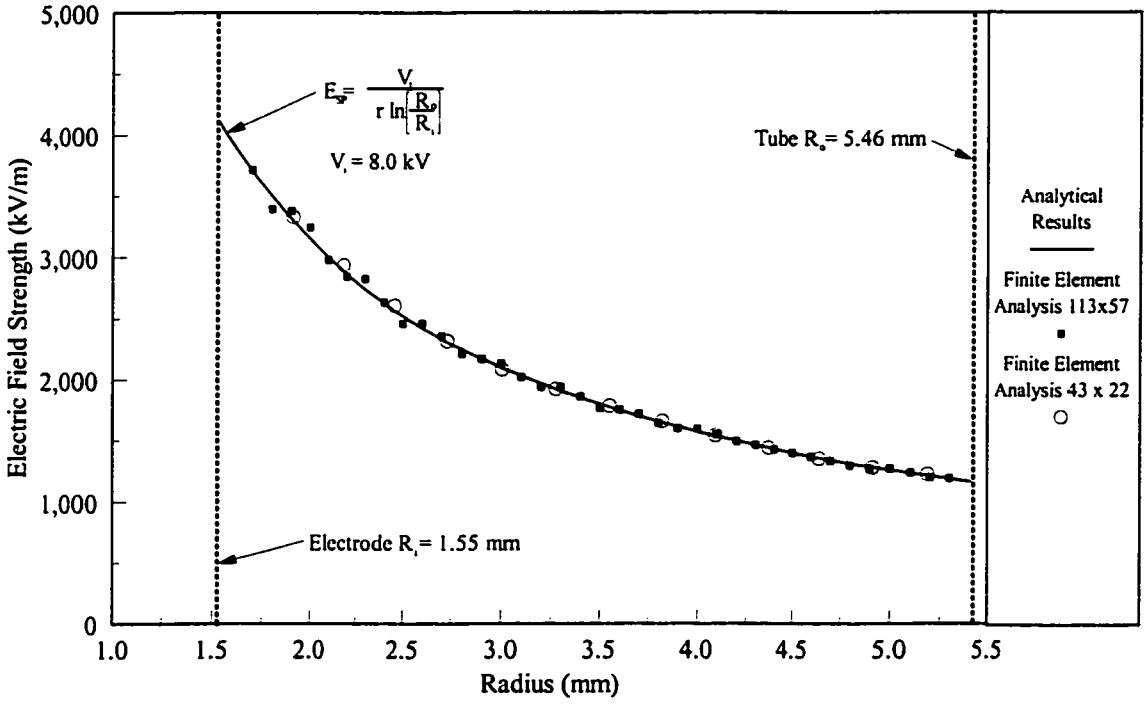

Figure 6.7: Comparison of Analytical and Finite Element Prediction of the Electric Field Distribution for Single-Phase Liquid in Concentric Electrodes.

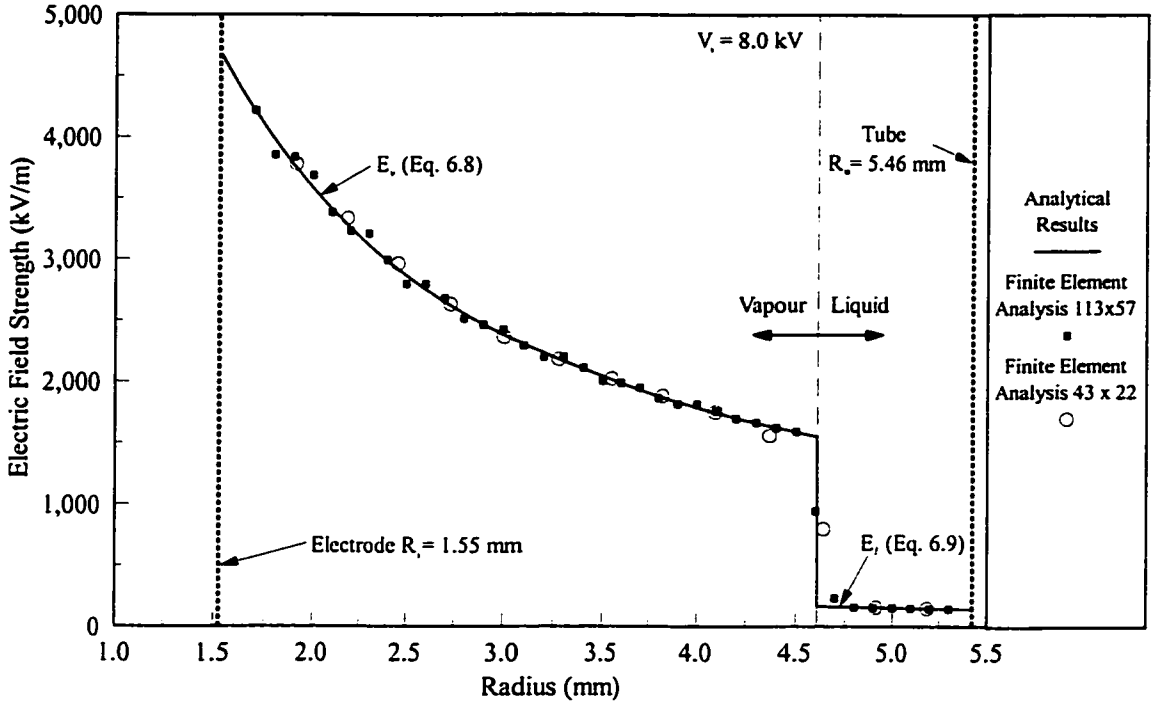

Figure 6.8: Comparison of Analytical and Finite Element Prediction of the Electric Field Distribution for Annular Flow, t_L = *0.85 mm*, in Concentric Electrodes.

6.2 The Impact of Electric Field on Flow Regimes

The analytical work provides significant insight into the field distribution for the simple symmetrical cases. As presented in Chapter 3, previous research has shown that the fluid having higher specific dielectric constant (ε_s) will tend to move from regions of weak electric field to those of higher field. Hence, vapour ($\varepsilon_s \approx 1.0$) in the absence of gravity will be ejected from an intense field to a weak field, while the liquid ($\varepsilon_s \approx 9.5$) will be forced towards highly intense regions of the electric field (liquid extraction). Therefore, the evaluation of the electric field distribution is essential in the prediction of phase redistribution. In Figures 6.9 and 6.10 the radial electric field distribution for various annular film thicknesses and the effect of void fraction on field strength are presented, respectively. Annular flow is a particularly important flow pattern as it occurs for a wide range of flow conditions, as presented in Figure 5.12. The results indicate an interfacial jump in field

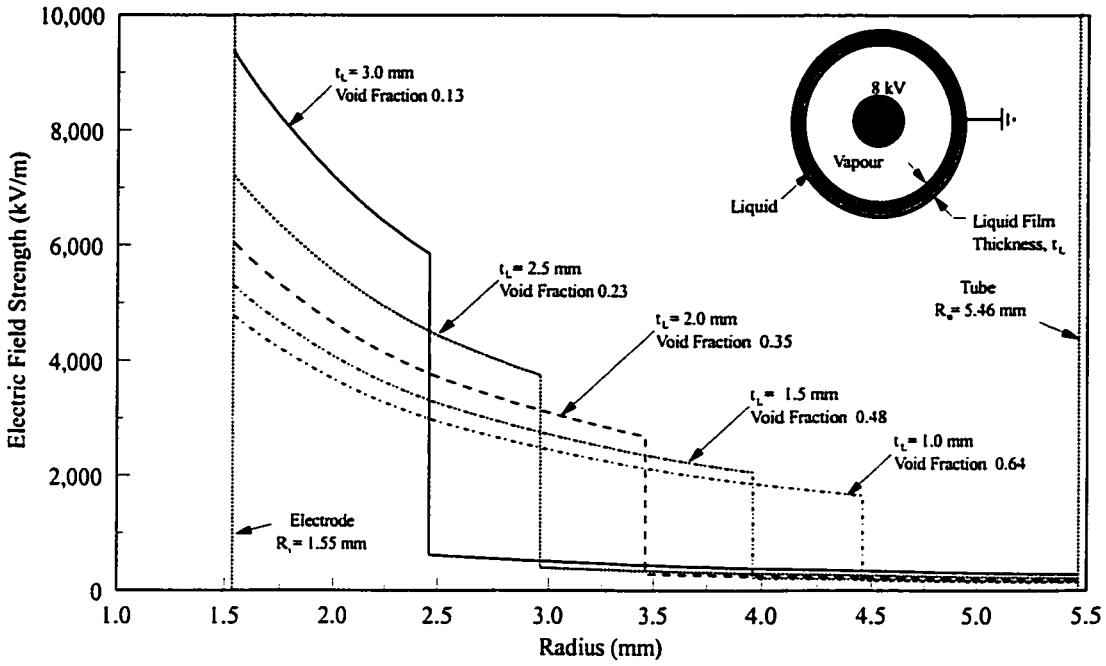

Figure 6.9: The Effect of Liquid Film Thickness, t_L, on the Electric Field Distribution for Annular Flow in a Concentric Electrode Arrangement.

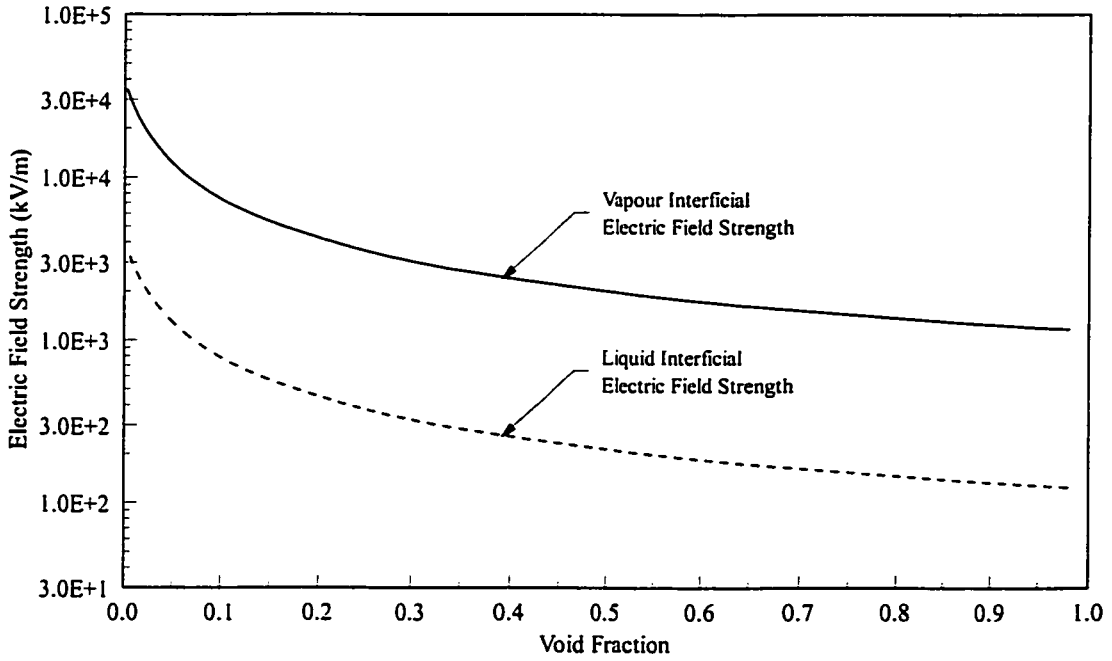

Figure 6.10: The Effect of Void Fraction on the Electric Field Strength at the Liquid-Vapour Interface for an 8.0 kV Applied Voltage in Annular Flow.

strength that increases with increased film thickness. Further, it is apparent that the maximum electric field strength is in the near vicinity of the inner electrode, suggesting that liquid will be extracted from the outer tube wall. By extracting liquid from the liquid annulus towards the central electrode or into the annular core in the form of droplet entrainment, an increase in interfacial vaporization and consequently an increase in heat transfer is expected. In practice, the range of flow conditions over which the entire liquid mass flow rate is contained in a smooth symmetrical film is essentially negligible, particularly in single component flows. In general, a significant fraction of liquid will be entrained in the vapour core and the interface between the film and the vapour core will become wavy and unstable. This will influence the electric field distribution and consequently increase the bulk phase migration and entrainment, and hence deposition of droplets. Although simplistic, the present analysis is a first attempt to describe the change of flow patterns through the interdependence of the electric field and flow distribution.

If the body force density is sufficient enough to yield an accumulation of liquid on the central electrode surface due to droplet deposition, the electric field distribution will be significantly changed near the liquid-vapour interface. Figure 6.11 presents the extreme case where the liquid and vapour are inverted and a smooth symmetrical film encompasses the electrode while the vapour replaces the liquid. In this exaggerated condition, it is apparent that the maximum field strength is not at the inner electrode, as theory for single-phase electric fields would suggest, but at the liquid-vapour interface and that it is higher in the vapour phase than the liquid surrounding the electrode. For this condition, the electric body force will be in the opposite direction acting towards the tube and consequently the liquid will tend to migrate back towards the heat transfer surface. As a result, an equilibrium situation, where there is no net transfer of phases, is impossible even in an isothermal

system. Thus, it is expected that continuous process of net liquid exchange will occur between liquid films encompassing the electrode and tube, and the rate of entrainment will be significantly enhanced. This fundamental feature of EHD influenced flow must be considered in any attempt to reconstruct the process of flow pattern behaviour through a heated channel.

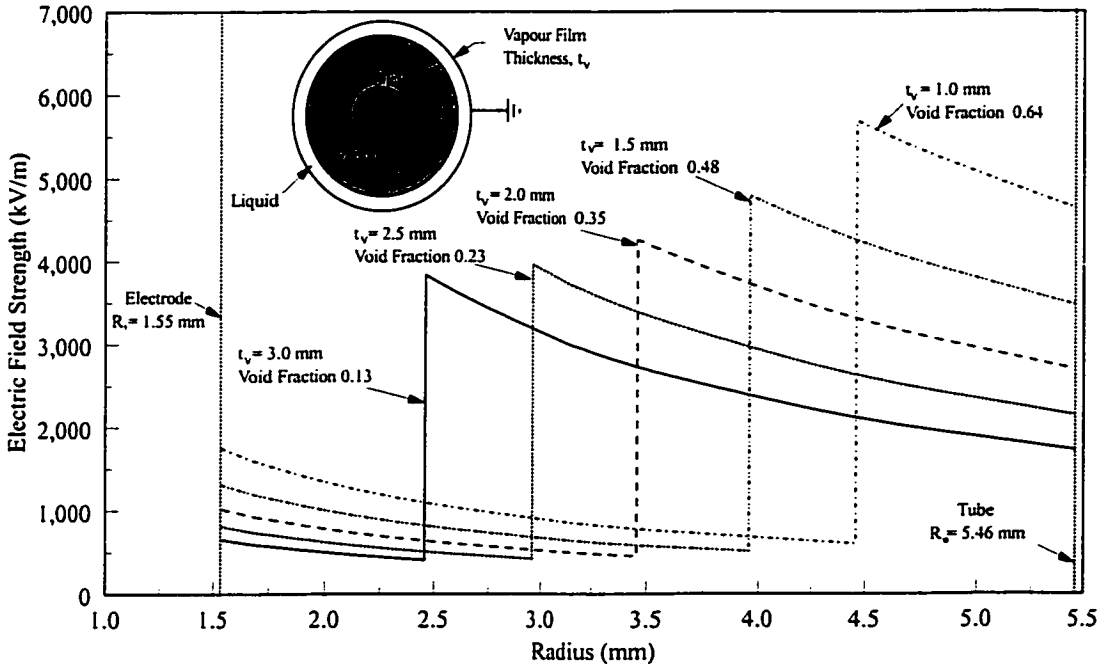

Figure 6.11: The Effect of Vapour Film Thickness, t_v, on the Electric Field Distribution for Liquid Encircled Electrode Flow in a Concentric Electrode Arrangement.

The physical process of entrainment and deposition of a liquid in a non-equilibrium annular flow (without EHD) has been the focus of several investigations including Hewitt and Hall-Taylor (1970), Hewitt (1978) and Govan *et al.* (1988), primarily due to its relation to the transition to dryout in heated systems. The physical process of enhanced entrainment rates due to EHD is postulated to be the mechanism that led to the deteriorations of heat transfer rates in the studies by Singh *et al.* (1994, 1995) and Norris *et al.* (1999). Although not comprehensive, the following chapter presents how this reduction in film thickness and

increased entrainment rate influences the behaviour of the system, in particular with respect to pressure drop and heat transfer.

As discussed in Section 6.1, in order to calculate the electric field distribution of non-symmetric flow regimes, such as stratified flow, a numerical procedure is required. As one would expect, a non-symmetric liquid and vapour distribution will result in a non-uniform electric field distribution. For this reason, it is convenient to present the distribution of stratified flow in a three-dimensional format. For comparison purposes, the results of the validation conditions considered in Figures 6.7 and 6.8, single-phase and annular flow at 25°C with an 8.0 kV voltage applied to the electrode, are represented in this three-dimensional (*3D*) format in Figures 6.12 and 6.13, respectively. As shown, the electric field distribution is symmetric and independent of the angular position, as the second term in the right hand side of Equation (6.4) is zero.

When the electric field is calculated for non-symmetric flow conditions, such as stratified, the radial distribution is no longer independent of angular position. Further, as presented in Section 6.1.1, the electric field vector will change direction as it crosses the liquid vapour interface. Consequently, two plots are required to describe the established field strength distribution and the electric field vector direction: a field strength distribution plot, similar to Figures 6.12 and 6.13, and a plot of the voltage gradient vectors. The finite element mesh presented in Figure 6.6 allowed for the possibility of 32 liquid levels, h_L, in 0.341 mm increments. However, upon calculating numerous values of h_L, it was apparent that the electric field for stratified flow could be grouped into three distinct categories and qualitatively assessed based upon the interaction between the fields and possible flow augmentation. These groups are distinguished by the liquid level with respect to the

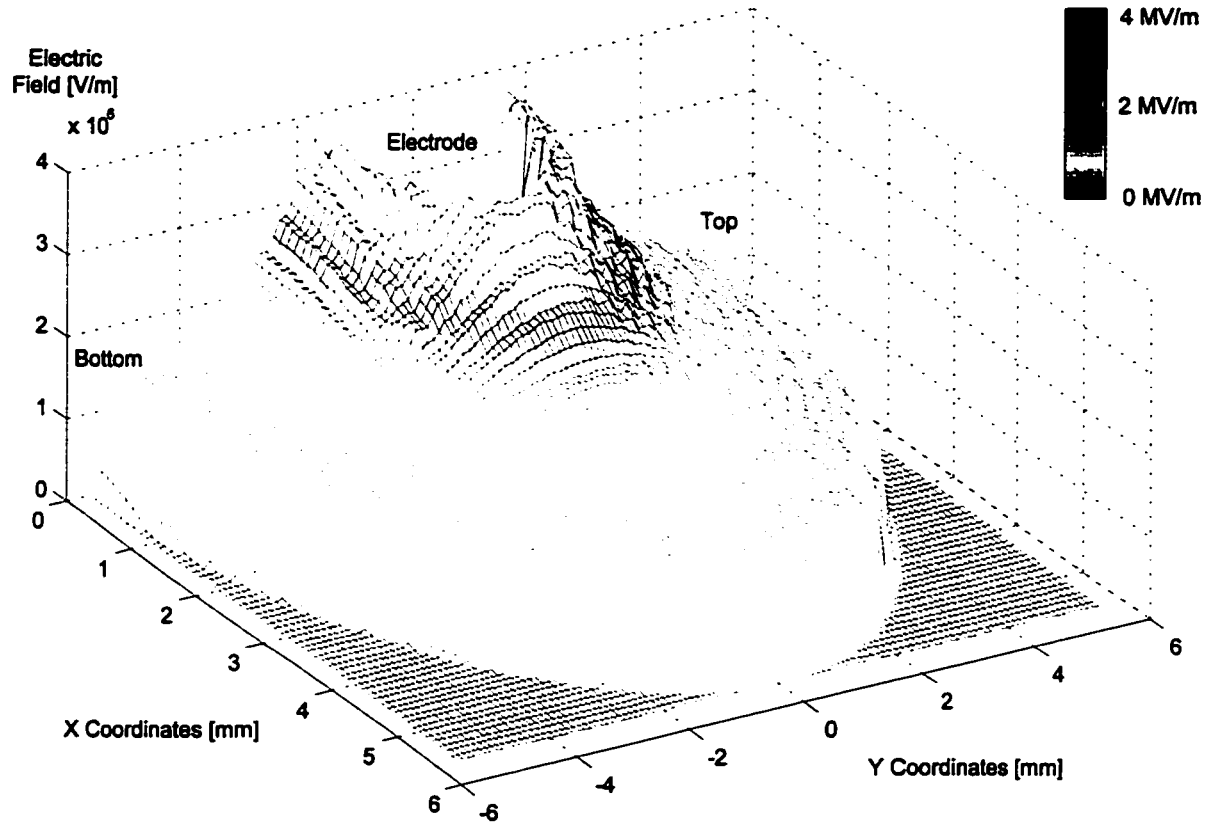

Figure 6.12: Electric Field Distribution of Concentric Electrodes for a Single-Phase Liquid.

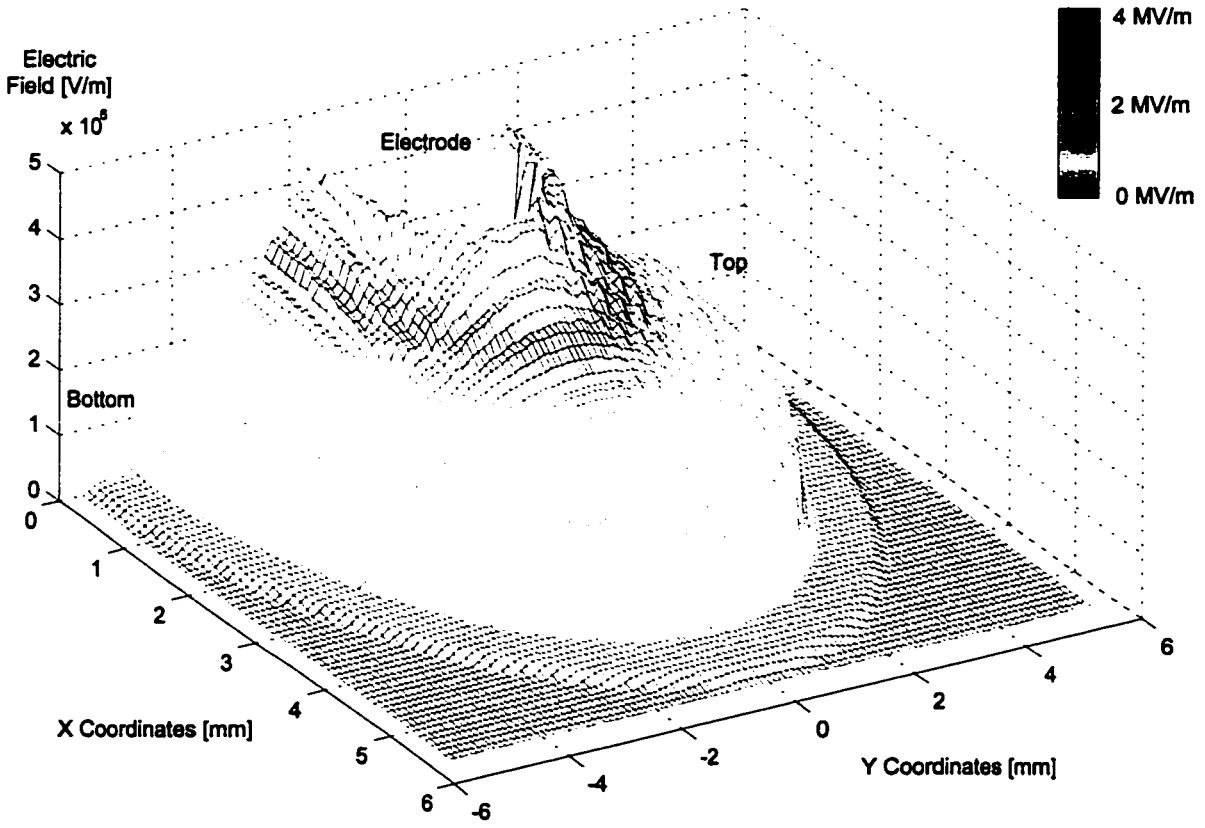

Figure 6.13: Electric Field Distribution of Concentric Electrodes for Annular Flow, Liquid Thickness $t_L = 0.85\ mm$.

electrode, that is:

- Liquid levels below the electrode; $0.00\ mm < h_L < 3.87\ mm$
- Liquid levels in contact with the electrode; $3.87\ mm \leq h_L \leq 7.05\ mm$
- Liquid levels above the electrode; $7.05\ mm < h_L < 10.92\ mm$

To represent these classifications, three levels have been selected: $h_L = 2.73\ mm$, Figures 6.14 and 6.15, $h_L = 6.48\ mm$, Figures 6.16 and 6.17, and $h_L = 8.19\ mm$, presented in Figures 6.18 and 6.19. See Appendix C for the presentation of several other liquid levels. The various forms of electric field distribution and their influence on the fluids are interpreted as follows:

Stratified Flow with a Liquid Level Below the Concentric Electrode

A liquid height of $h_L = 2.73\ mm$ was used to represent the electric field distribution for this group, which corresponds to the presentation of the incident and departure electric field vectors in Figure 6.3. As the numerical results show in Figure 6.14, the assumption in the analytical analysis that the electric field direction in the vapour phase is radially outward is relatively accurate. The direction change is not apparent upon inspection of Figure 6.14 due to the relatively low field strength in the liquid phase but it is supported by the data. Therefore, the influences described in Section 6.1.1 are valid and may be used to interpret the effects of the electric body forces.

Although the difference in the liquid and vapour electric field gradient are obvious from the plot of the voltage gradient, Figure 6.15 gives a global picture of the variation in strength. In the liquid phase, the electric field is essentially constant at approximately 500 kV/m, while in the vapour phase a significant deviation exists from 7,000 kV/m directly below the electrode to 1,500 kV/m near the tube wall. For such a complex distribution, a true description of the change in the liquid and vapour orientation is extremely difficult.

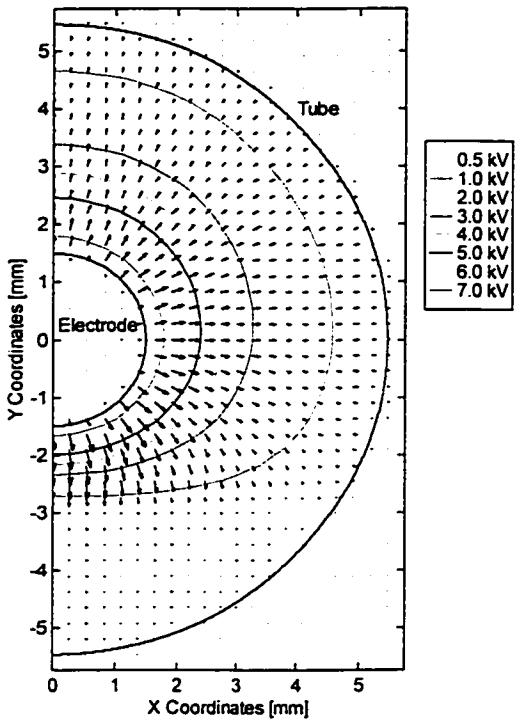

Figure 6.14: Voltage Contour and Gradient for Stratified Flow, Liquid Level h_L = *2.73 mm.*

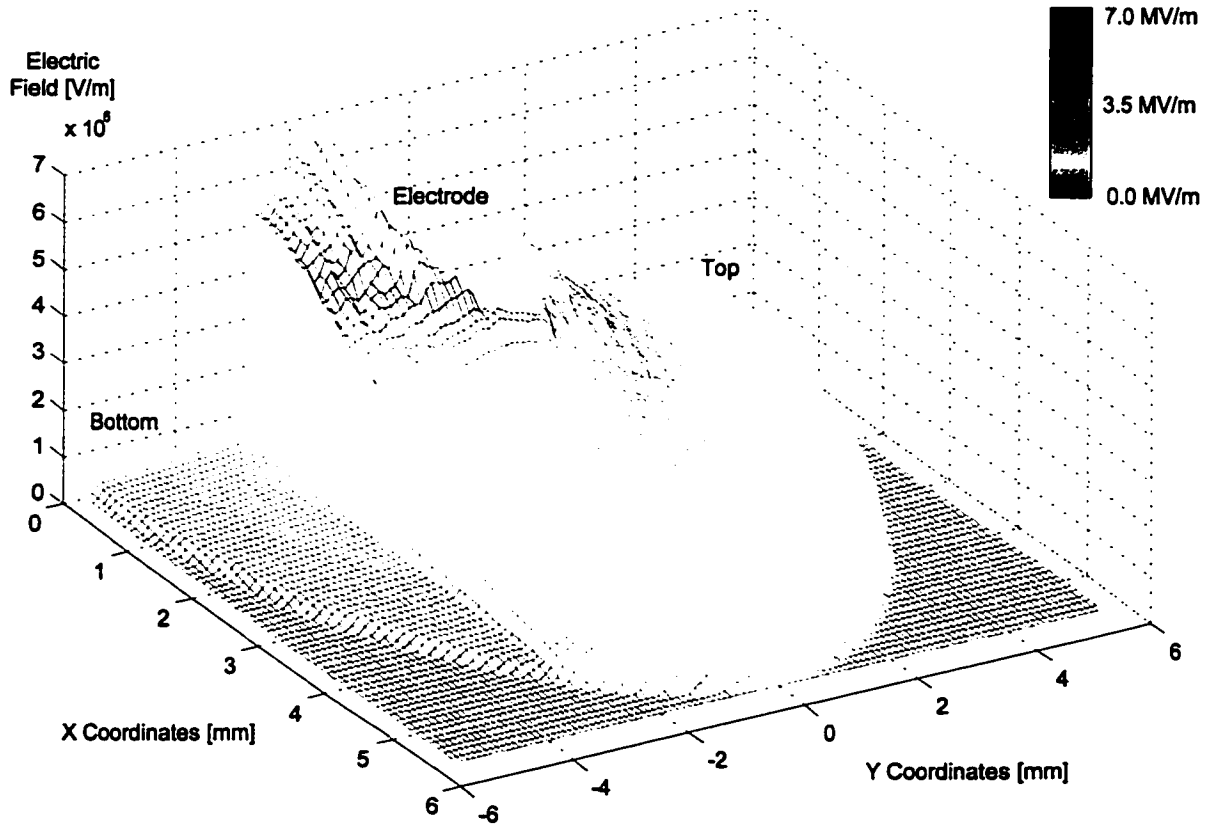

Figure 6.15: Electric Field Distribution of Concentric Electrodes for Stratified Flow, Liquid Level h_L = *2.73 mm.*

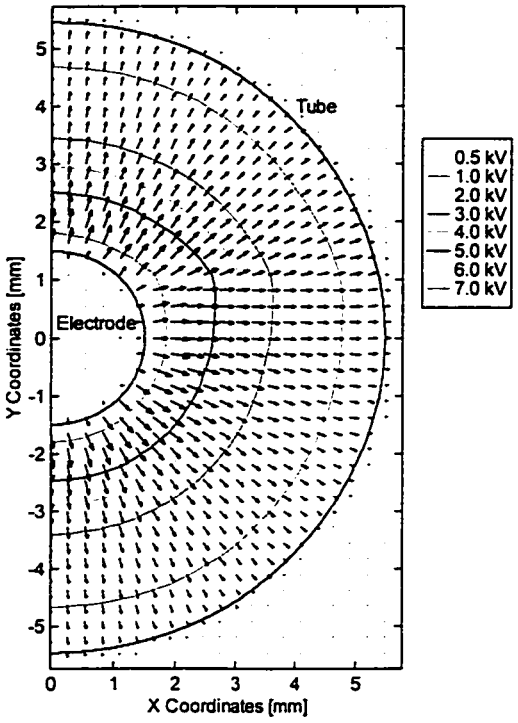

Figure 6.16: Voltage Contour and Gradient for Stratified Flow, Liquid Level $h_L = 6.48$ *mm.*

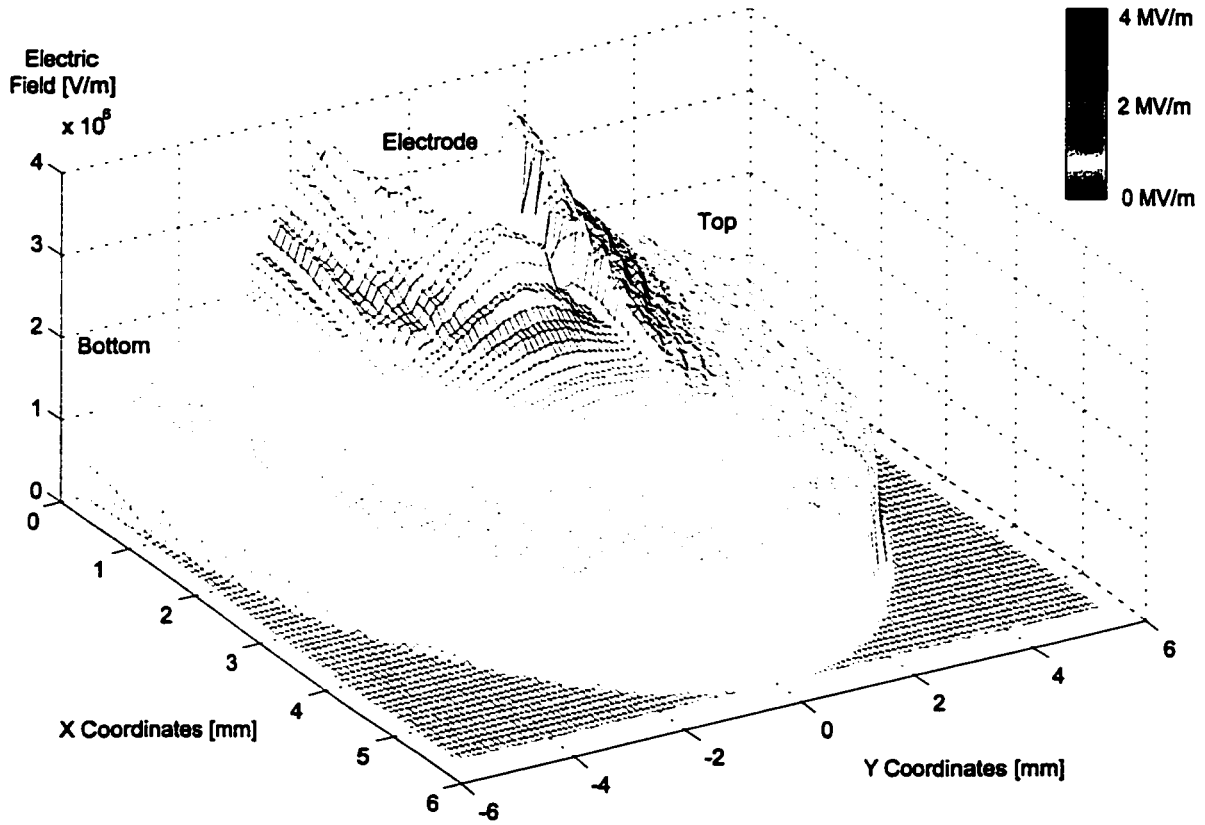

Figure 6.17: Electric Field Distribution of Concentric Electrodes for Stratified Flow, Liquid Level $h_L = 6.48$ *mm.*

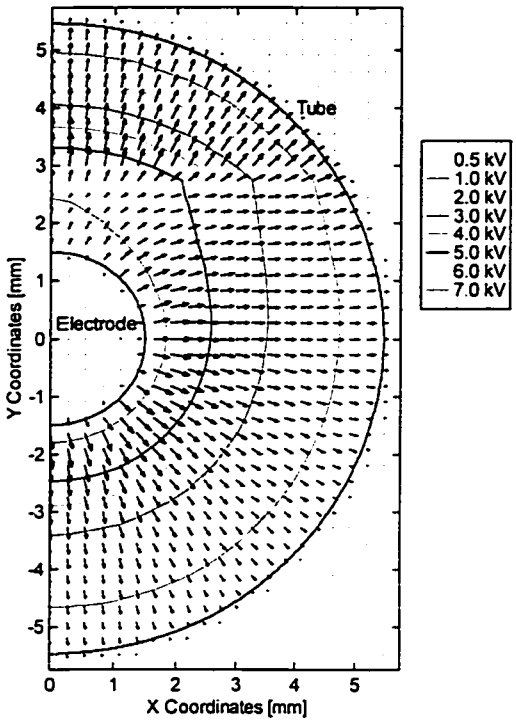

Figure 6.18: Voltage Contour and Gradient for Stratified Flow, Liquid Level $h_L = 8.19$ *mm.*

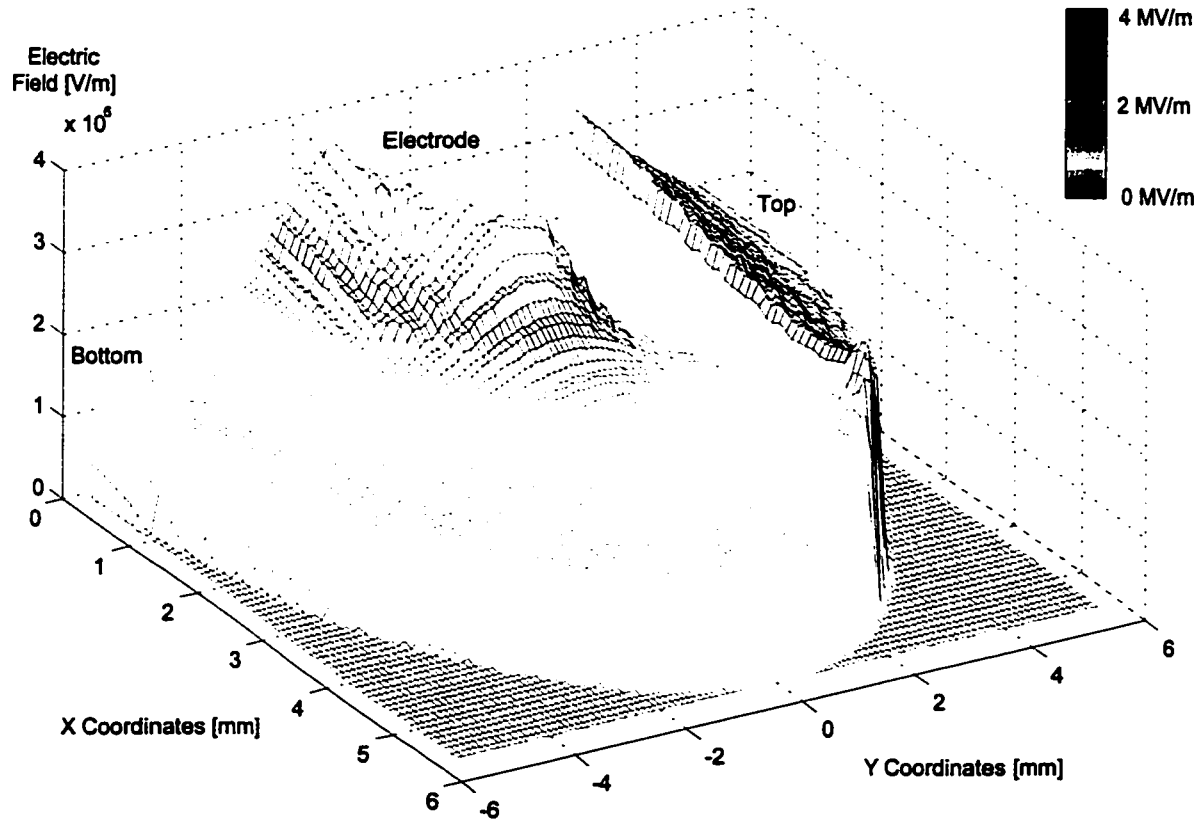

Figure 6.19: Electric Field Distribution of Concentric Electrodes for Stratified Flow, Liquid Level $h_L = 8.19$ *mm.*

However, several qualitative observations are discernible. At the interface below the electrode, there is an order of magnitude difference in the field strength. This nonuniformity would create an attraction force that draws the liquid, having higher permittivity, towards the region of higher electric field strength in the vapour. A similar effect is expected near the tube wall due to the lower strength, 1,500 kV/m compared to 7,000 kV/m. Hence, the forces acting on the interface are expected to be relatively smaller.

To provide better insight into the electric field effects on the liquid-vapour interface, Figure 6.20 presents the electric field in the X-direction in the liquid and vapour phases slightly above and below the interface at two different liquid levels below the electrode, h_L = 0.68 mm and h_L = 2.73 mm, respectively. In both phases, the electric field strength decreases along the interface at a distance further away from the electrode center. The net effect is an attraction force acting against gravity across the entire interface, that when

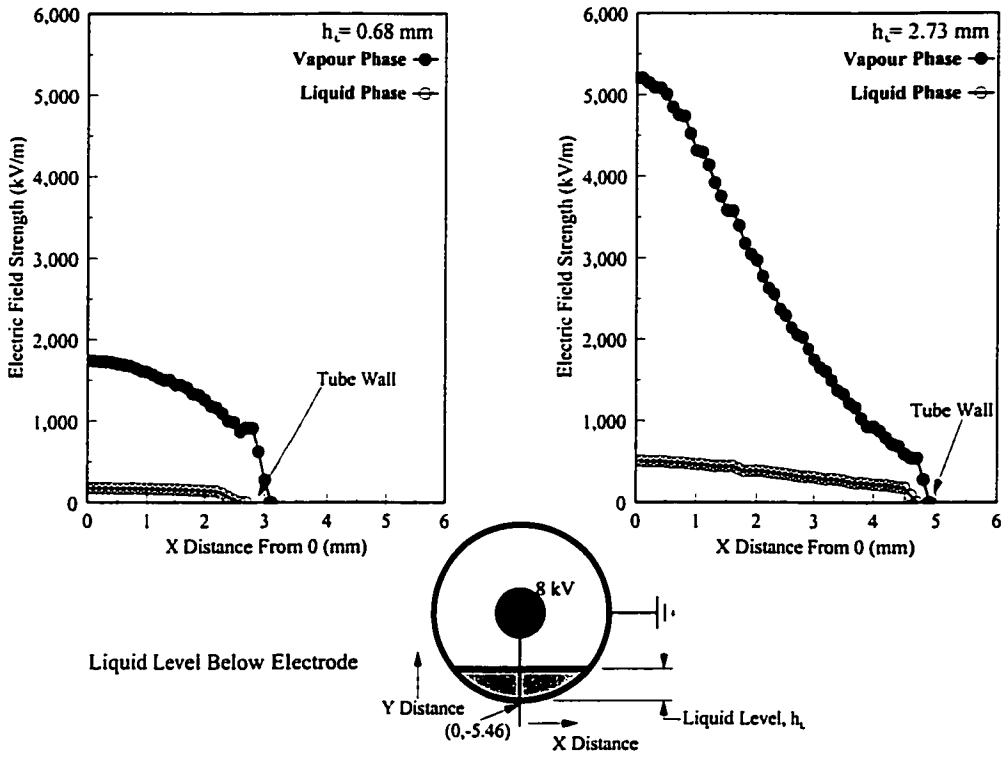

Figure 6.20: Interfacial Electric Field Strength for Stratified Flow with Liquid Levels Below the Electrode.

combined with the suction pressure as described in Section 5.3.2a, will potentially lead to an earlier transition to intermittent or annular/annular dispersed flow. The following section will use the results presented in Figure 6.20 to obtain the force acting on the interface to include it in the transition criterion described by Equation (5.23).

Stratified Flow with the Interface in Contact with the Concentric Electrode

As the liquid height reaches the electrode ($h_L = 6.48\ mm$), as shown in Figures 6.16 and 6.17, there is a considerable change in the electric field distribution. For this range of liquid levels it is apparent that the field distribution is not very different from the single-phase case presented in Figure 6.12. Plotting the electric field strength in the liquid and vapour phases slightly below and above the interface, Figure 6.21, shows that the difference is virtually negligible. Consequently, there is unlikely to be a significant vertical force acting

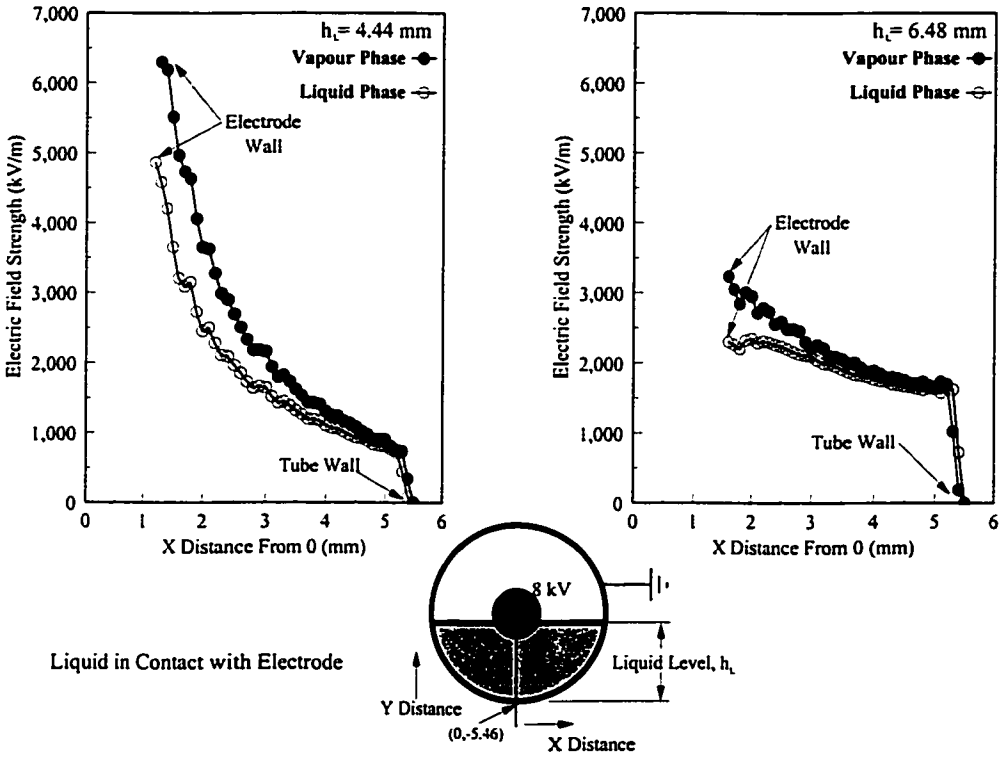

Figure 6.21: Interfacial Electric Field Strength for Stratified Flow when the Liquid Interface is in Contact with the Electrode.

across the entire interface. Such a distribution would likely yield attraction forces that would draw the liquid near the tube towards the region of higher electric field strength in the vapour phase in the vicinity of the electrode.

Stratified Flow with a Liquid Level Above the Concentric Electrode

A value of $h_L = 8.19\ mm$ has been chosen to represent liquid levels where the interface exceeds the top of the electrode. Unlike the voltage contour and electric field plot for heights below the electrode for the present case, Figure 6.18 clearly shows the change in vector direction of the electric field passing through the interface. At this level, because the field passes through the liquid first, the corresponding vector direction of the electric field leaving the surface will be in the opposite direction compared to the example presented in Figure 6.3, creating a force in the vapour upwards toward the top of the tube. Further, it is clear that the electric field vector in the liquid is not radially outwards as assumed in the simple analysis in Section 6.1.1 and is commonly above 75°, suggesting that there will be a significant interfacial jump in electric field strength. This is obvious from the three dimensional plot of the electric field distribution in Figure 6.19. Therefore, the simple analysis used to describe liquid heights below the electrode, Figure 6.3, is not valid for this condition.

As already mentioned, a considerable interfacial jump in the electric field strength as the incident electric field passes from the liquid to the vapour is expected, and is apparent in Figure 6.19 for $h_L = 8.19\ mm$. The magnitude of this difference is a strong function of how far the liquid level is above the electrode, which is depicted in Figure 6.22 and Appendix C, a plot of the interfacial field strength for $h_L = 8.19\ mm$ and $h_L = 10.24\ mm$, respectively. Similar to the discussion of liquid heights below the electrode, this difference will create an attraction force in the vertical direction against gravity. Based on the criterion

of flow regime transition, this additional vertical force could yield an earlier redistribution from stratified to intermittent flow and could possibly affect the frequency of slugs in the intermittent regime.

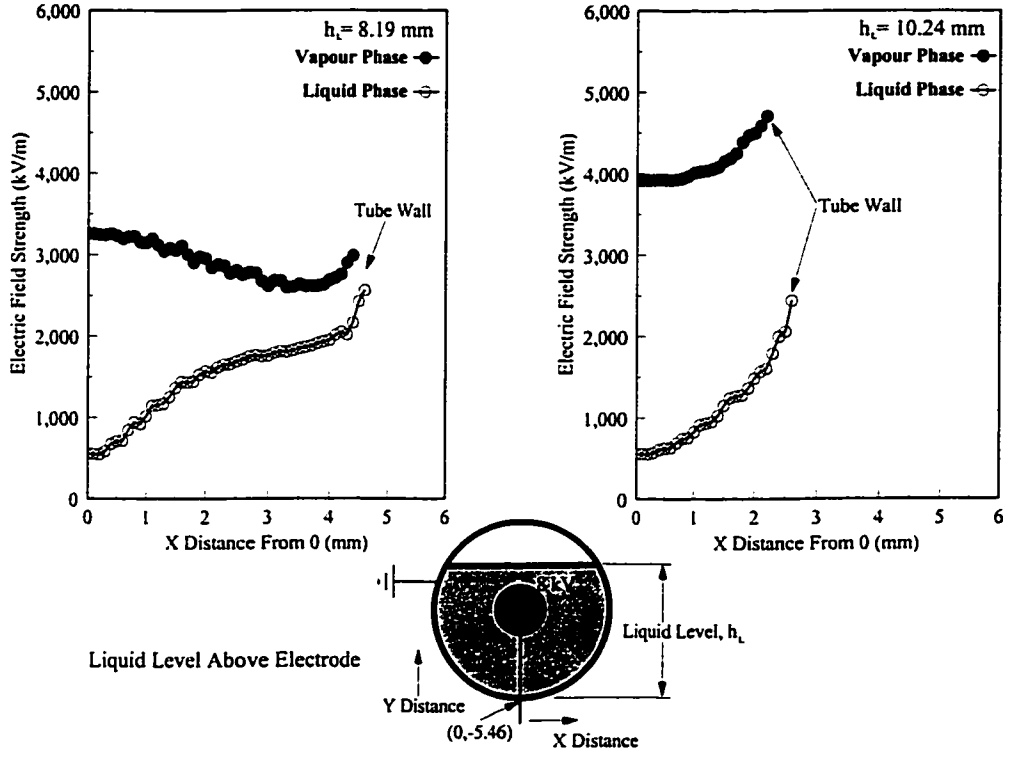

Figure 6.22: Interfacial Electric Field Strength for Stratified Flow with Liquid Levels Above the Electrode.

6.3 The Interfacial Electrical Force

As mentioned at the onset of this chapter, the determination of the electric field distribution is required in order to calculate the forces acting on the interface that are postulated to cause phase redistribution *i.e.*, flow regime transition. The examination of these forces may be categorized based on the surface interactions, as presented by Melcher (1963). For the present investigation, the goal is to introduce the perpendicular component of the interfacial electrical force acting against gravity into the classical Kelvin-Helmholtz instability analysis performed by Taitel and Dukler (1976).

As a first step, in order to understand the basic character of the possible additional instabilities, the forces are considered in a situation of greatest possible simplicity, that is uniform fields and plane geometry. As suggested by Melcher (1963), certain phenomena, often associated with nonuniform fields, are accounted for by the dynamics of a surface acted on by a uniform field. Based on this reasoning, the analysis of the two interfacial force categories, a charge-free and a conducting interface, explored by previous investigators for two immiscible fluids separated by a plane interface between two parallel rigid boundaries was employed (Koa, 1961, Melcher, 1963, Johnson, 1968, Duffin, 1973, Chang and Watson, 1994, Chang, 1998) . The fluids are presumed inviscid, incompressible, perfect dielectrics and it has been assumed that the motion of the fluids does not disturb the source of the electric field.

For the polarization-charge interaction where the interface does not support free-charge, the charge density, ρ_{ei}, in the electrophoretic component not only vanishes everywhere in the bulk, but at the interface as well. Melcher (1963) derived the interfacial force by means of a direct dynamic analysis, as follows:

$$f_{e_d}{}'' = \frac{\varepsilon_L(\varepsilon_L - \varepsilon_V)^2}{\varepsilon_V(\varepsilon_L + \varepsilon_V)} \varepsilon_0 E_L^2 = \frac{\varepsilon_V(\varepsilon_L - \varepsilon_V)^2}{\varepsilon_L(\varepsilon_L + \varepsilon_V)} \varepsilon_0 E_V^2 \tag{6.12}$$

where E_L and E_V are the electric field in the liquid and vapour phases at the interface.

The normal forces acting on the boundary in which the interface is perfectly conducting and supports free-charge has been derived by Kao (1961), on the basis of the minimum potential energy, to be:

$$f_{e_c}{}'' = \frac{1}{2} \frac{\varepsilon_0 \varepsilon_V (\varepsilon_L - \varepsilon_V)}{\varepsilon_L} E_V^2 \tag{6.13}$$

These mechanical stresses tend to cause the dielectric having the higher permittivity to move

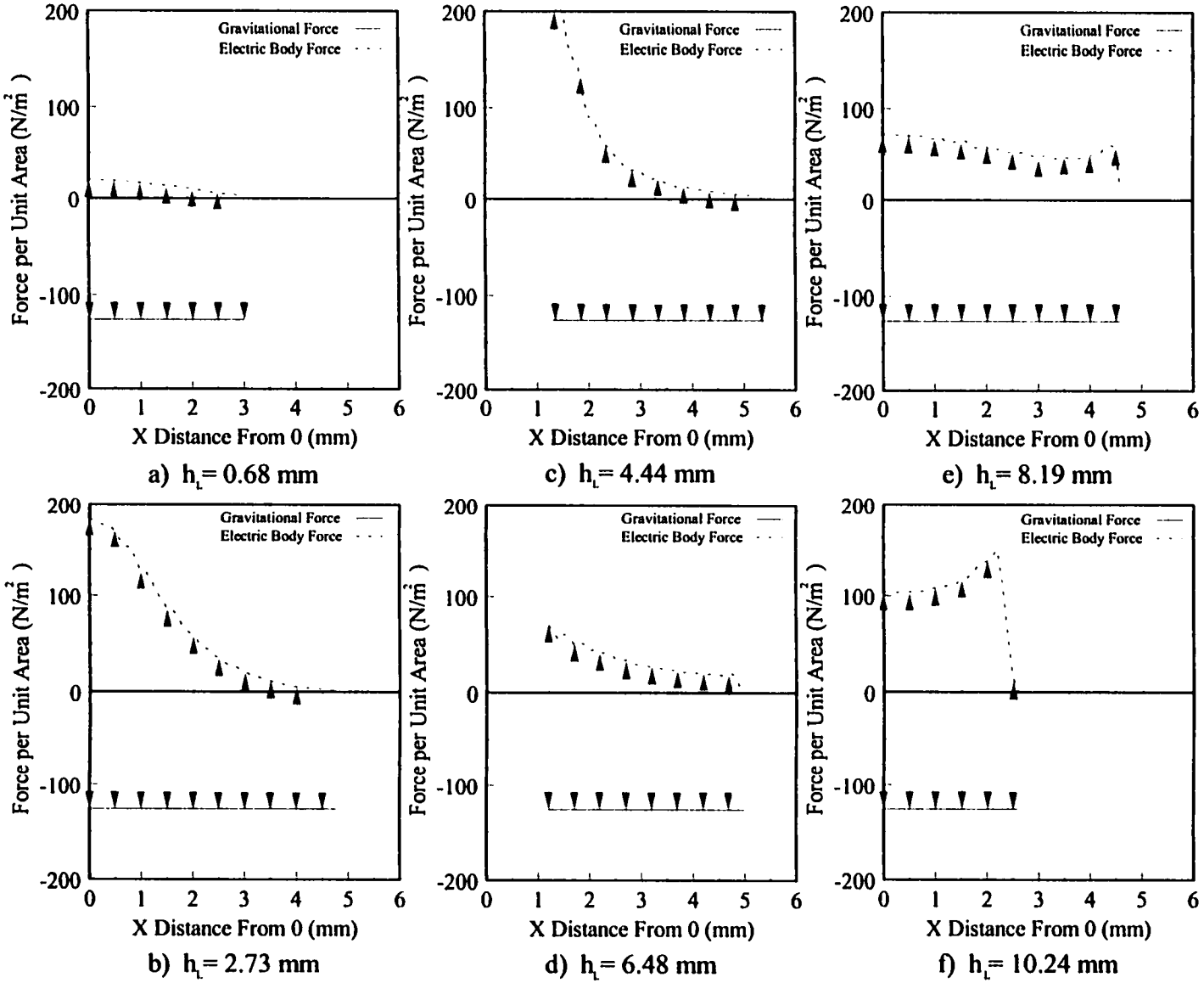

Figure 6.23: Charge-Free Interfacial Electric and Gravitational Forces at Increasing Liquid Levels.

into the space occupied by the other (Kao, 1961). Based on the electric field distribution observed through the finite element analysis in the previous section, this migration is vertically upwards against gravity.

Figure 6.23 presents the charge-free interfacial electric force (Equation 6.12) for an applied voltage of $V_i = 8.0\ kV$ offset by the interfacial gravitational force for the three ranges of stratification considered in Section 6.2 and Appendix C. For the cases considered, the change in the hydrostatic head is regarded as negligible and the vapour interfacial electric field is employed over the liquids field strength, the right hand side of Equation (6.12). The vapour is deemed more appropriate as the vector direction of the electric field entering or leaving the surface of the vapour is closer to being normal to the interface for all liquid levels, as presented in Figures 6.14, 6.16 and 6.18.

The qualitative discussion, in Section 6.2, regarding the interaction of the fluid and electric field distribution for the three ranges of liquid levels is exemplified in the above interfacial force plot. Considering the static condition, as shown in Figure 6.23, the force density (force per unit area) acting on the interface below the electrode is initially negligible compared to gravity (Figure 6.23a), thus no effect is expected, but it rapidly grows as the liquid level is increased. In fact, as the level approaches approximately $h_L \approx 2.4\ mm$, the electrical force exceeds gravity below the electrode and continues to increase as the level approaches the electrode. Once in contact with the electrode the force continues to exceed gravity in the near vicinity of the electrode but drops to zero at an "*x-distance*" near the tube wall, until the planer level reaches approximately the center of the channel. For these conditions, it is hypothesized that for a static system, as the liquid level is increased beyond $h_L \approx 2.4\ mm$, the force of attraction created by the electric field will form a wave that will propagate vertically against gravity. The force rises due to the increased liquid height as the

wave grows until the electric force no longer exceeds gravity at the center of the channel. Figure 6.24 presents a schematic representation of this interaction and the postulated fluid redistribution as the critical liquid level is reached.

For the upper half of the channel, gravity is not exceeded until the planer liquid level is almost at the top of the channel ($h_L \approx 10\ mm$). However, in this case the electrical force is greater near the tube wall than at the smaller "*x-distances*" as depicted in Figure 6.23f.

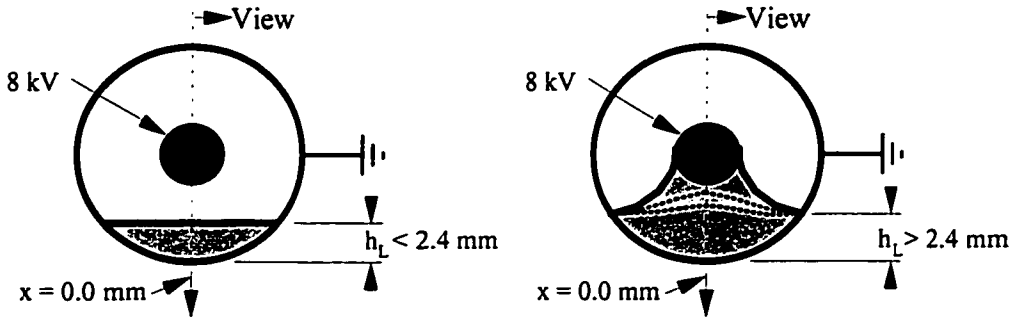

Figure 6.24: Schematic Diagram of Wave Growth when the Electrical Forces Exceed Gravitational Forces.

Modeling the force for a system that can maintain an interfacial charge provides a similar force distribution to that presented in Figure 6.23. However, the calculated strength is approximately 35% lower than the charge-free condition predicted (at 25°C) through Melcher's relation (Equation 6.12). This is due to the fact that for an interface that is perfectly conducting, the electric field is confined to the vapour phase, (*i.e.* $E_L = 0$).

6.4 Proposed Flow Pattern Map with Electrohydrodynamic Forces

As shown in Figure 5.13, the most pronounced effect of the EHD force density can be seen in the region where the flow regime changes from stratified to intermittent or annular. Accordingly, the mechanisms that induce this flow pattern transition are the focus of this section. The origin of this orientation change depends upon how significant the EHD

force density components are with respect to the fluid momentum and the quality. To determine this relation the electrical force acting on the interface was incorporated into the classical Kelvin-Helmholtz instability analysis performed by Taitel and Dukler (1976), later extended by Steiner (1993) and modified in this work to accommodate annular geometries. A similar approach was proposed for tube flow under the influence of a uniform electric field for semi-conductive fluids, such as tap water, by Brunner and Chang (1980) and for dielectrics by Chang (1998).

In the present model, the assumption used by Taitel and Dukler (1976) and Steiner (1993) for plain tubes will be adopted for an annular geometry with EHD. As reviewed in Chapter 5, the basic principle is that all flow regimes are manifested due to a perturbation from the horizontal stratified flow regime. Suppose that a small perturbation occurs on the interface of a stratified flow in an annular channel where a high voltage is applied to the inner tube. The vapour flowing over the protrusion will accelerate, giving a drop in the vapour pressure and producing a suction on the protrusion that will cause it to grow, unless the suction is more than offset by the surface tension and gravitational forces acting downward on the protrusion. Contributing to the acceleration of the protrusion are the interfacial forces acting against gravity as described above. Therefore, the instability analysis must include the effects of inertia, energy storage in the gravitational field and the molecular formation of the interface (surface tension), as well as the electrical interactions with the interface. Based on the extended Taitel and Dukler (1976) analysis proposed by Steiner (1993), the condition for the growth of the protrusion is:

$$F_e^2 \left(\frac{\bar{A}_V^3}{\bar{A}^2 \cdot d\bar{A}_L / d\bar{h}_L} \left[\frac{\pi^2}{25\ \bar{h}_L^2} \left(\frac{Fr}{We} \right)_L + 1 \right] \right) \geq 1 \qquad (6.14)$$

where F_e is the modified electric Froude number given by (Chang 1989b, 1998),

$$F_e = \frac{xG}{(\rho_V [(\rho_L - \rho_V) D_o g - f_e''])^{1/2}} \tag{6.15}$$

The dimensionless terms are given in Chapter 5 and the interfacial force, f_e'' depends on the type of surface interactions as discussed in Section 6.3. Converting Equation (6.14) to the graphical representation presented in Chapter 5 as suggested by Kattan *et al.* (1998) the transition curve in EHD annulus systems is:

$$G = \left(\frac{\bar{A}_V^3 \rho_V [(\rho_L - \rho_V) D_o g - f_e'']}{\bar{A}^2 \cdot d\bar{A}_L / d\bar{h}_L} \left[\frac{\pi^2}{25 \bar{h}_L^2} \left(\frac{Fr}{We} \right)_L + 1 \right] \right)^{1/2} \cdot \frac{1}{x} \tag{6.16}$$

For comparison purposes, the flow regime transition criterion with and without an applied voltage is presented in Figure 6.25, using Equation (6.16) with the interfacial electrical forces developed by Melcher (1963) and Koa (1961), Equations (6.12) and (6.13), respectively. The electric field is assumed to be uniformly distributed at a strength equivalent to the maximum electric field strength that could develop if liquid refrigerant were to fill the entire annular gap to demonstrate an order of magnitude effect (ie. Equation 6.5 $\rightarrow r = R_i$). This analytical analysis is performed for an electrode voltage of $V_i = 8.0\,kV$ at a system temperature of 25°C.

As expected, the interfacial electrical force reduced the required inertia generated suction pressure for transition to occur at a given liquid level as shown in Figure 6.25. The degree to which the transition is augmented depends strongly on the interface conditions. Comparing the two extremes, it is apparent in Figure 6.25 that the charge-free interface assumption under investigation in this work results a in further reduction in the mas flux required for transition from stratified flow as compared with the assumption of a perfectly conducting surface for the same electric field strength. As stated above, this is due to the

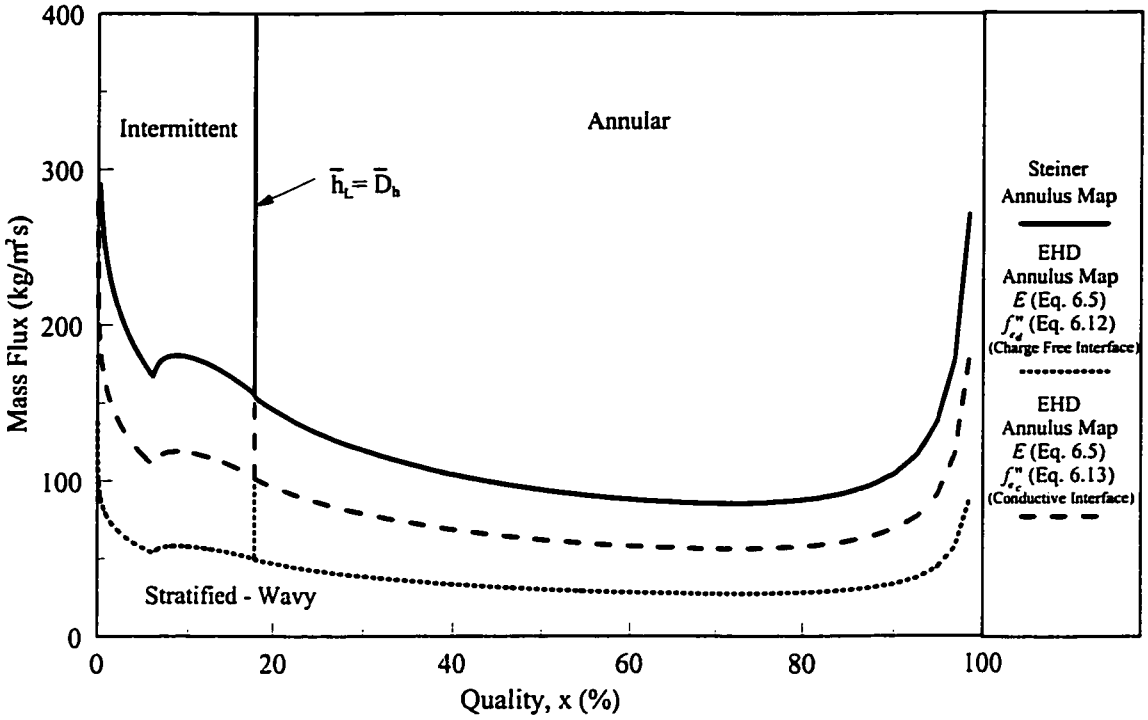

Figure 6.25: Proposed Flow Pattern Map for an Annular Channel under the Influence of an 8.0 kV DC Voltage Potential.

fact that the liquid does not support an electric field which decreases the interfacial electrical force. Not apparent from the plot is the fact that the boundary prediction of the charged surface configuration does not account for the position of the electrode. As the liquid level increases to the point where it contacts the electrode, the surface charge would discharge through the electrode. As this is not a concern for the fluid under investigation, the analysis is presented in its simplest form such that the basic character of the effect of an electric field may be developed.

As presented in Figure 6.23, the electric field for a stratified flow in an annular geometry is far from uniform. Consequently, the one-dimensional procedure developed by Taitel and Dukler (1976) and extended by Chang (1989b) to incorporate electric fields is not comprehensive enough to completely describe the coupling of flow regimes and an electric field for the present problem. However, as suggested by Melcher (1963), phenomena

associated with nonuniform fields are often accounted for by the dynamics of a surface stressed by a uniform field. Assuming this statement to be true for the dynamic action of electrical effect on flow patterns, the problem is to determine how a certain nonuniform field may be transformed into a uniform field.

Considering the discussion for static systems in Section 6.3, in general, as the liquid height is increased, the forces acting on the interface increase. This is better depicted when the average and maximum interfacial electric forces (based on the average and maximum interfacial electric field strength as predicted by the finite element analysis) are plotted against the liquid height, Figure 6.26. As the plot depicts, the interfacial force increases with the increasing liquid level for more than 85% of the channel area. Further, in the range where the interfacial force is decreasing, the magnitude of the maximum force is above the energy stored in the gravitational field. Therefore, if a protrusion were to exist on the

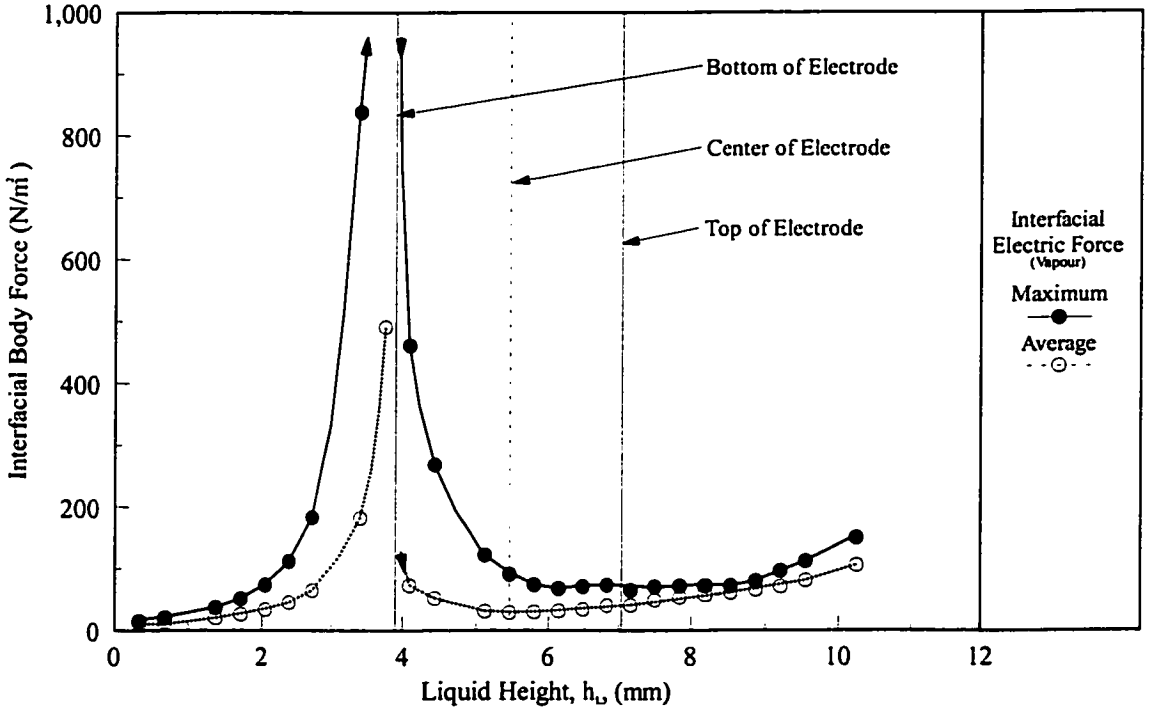

Figure 6.26: Average and Maximum Stratified Interfacial Electric Force as a function of the Liquid Height.

interface, a localized electric force would develop, at least in the maximum strength region, that would be self-propagating. Although this is a local phenomena, due to interfacial tension effects the surrounding liquid would be "dragged" upwards with the fluid into the region of the maximum field strength.

Consequently, considering the self-propagating nature of a perturbation in the vicinity of the maximum electric field, the corresponding maximum interfacial electrical force is conjectured to be the appropriate force to represent the uniform field in the one-dimensional instability analysis above.

Figure 6.27 is a reproduction of Figure 5.13, which presents the outlet flow pattern data, for the experiments where an 8.0 kV voltage was applied to the electrode, against the modified Steiner flow pattern map at 25°C, with and without the incorporation of the charge-free interfacial electric force, f_{e_d}'', in Equation (6.16). The proposed transition boundary correctly identifies the transition from stratified flow for all but four conditions investigated. As previously mentioned, the EHD effect seems to have a minimal influence on the proposed transition criterion from intermittent to annular flow as presented in Chapter 5.

As shown in Figure 6.27, the effect of the body force is not as dominant at high qualities as suggested in Figure 6.25 but it increases as the liquid level increases , or alternatively, as the quality decreases. This continues until the quality exceeds approximately 40%, at which point ($h_L \approx 2.4\ mm$) where the interfacial electric force exceeds the combined effect of gravity and surface tension. At this level, it is assumed that the liquid will be drawn increasingly upwards until these restraining forces are no longer exceeded. This zone is represented by the crosshatched line. As the quality decreases further, the mass flux must be increased for transition to occur due to the increased surface tension effects which

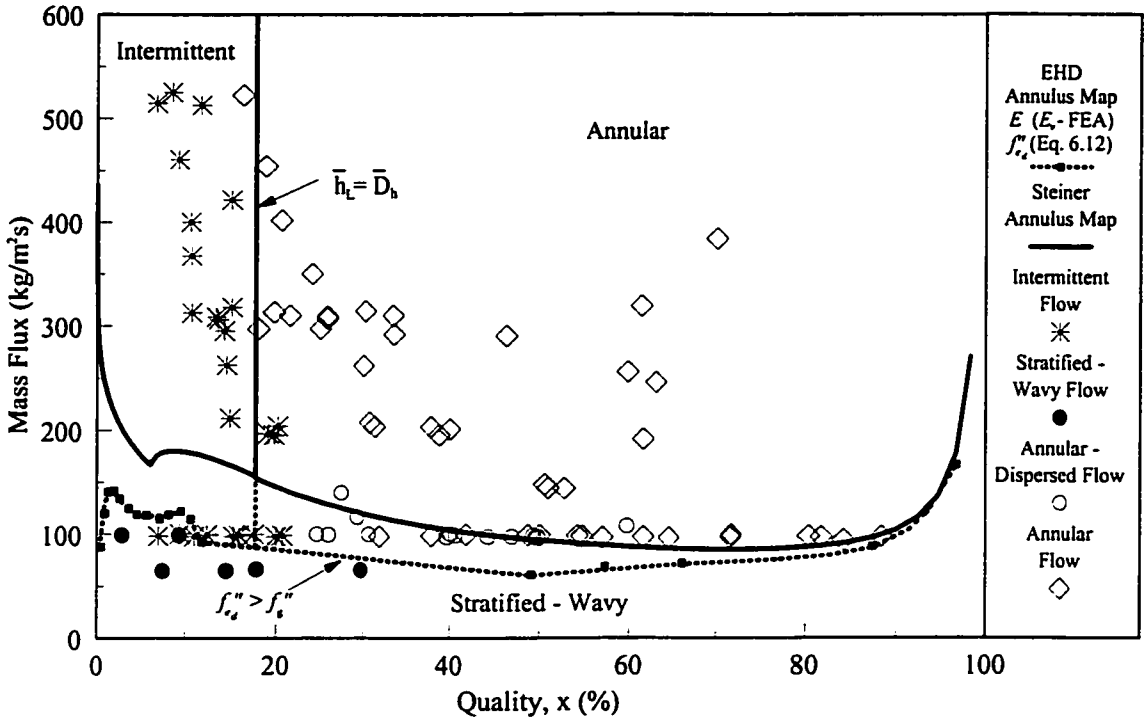

Figure 6.27: Outlet EHD Flow Pattern Data (8 kV DC) Compared Against the Proposed EHD Flow Pattern Map Applying the Maximum Interfacial Body Force Determined through a Finite Element Analysis.

reduce the impact of the electric field. This trend continues until the electrical force again exceeds the restraining forces, creating a state were transition is presumed to occur at negligible mass flow levels.

The following chapter will couple the proposed EHD flow pattern map with the interpretation of the measured time-averaged and transient surface temperatures and heat transfer data, in order to establish the sequence of convective boiling flow patterns in an annulus for various flow and electric field conditions. It is believed that through the analysis of the local structure of the flow, insight can be gained into the interpretation of how EHD forces influence heat exchanger effectiveness. In Chapter 8 the finite element analysis for the eccentric conditions investigated will be presented with the corresponding experimental data.

Chapter 7

Concentric Electrode Electrohydrodynamic Evaporator Experimental Results and Discussion

Although a complete understanding of EHD phenomena applied to convective boiling does not exist, an extensive research survey has proven the feasibility of EHD-enhanced convective boiling heat transfer. Consequently, little effort is made in design optimization with EHD enhancement in this section. Rather, the purpose is to illustrate the expected interaction between the EHD forces and convective boiling that are derived through a dimensional analysis of the momentum equation. These interactions are examined by considering the effect of flow regime on both the local and overall heat transfer and the overall pressure drop. The analysis of local experimental data, heat transfer, pressure drop and power consumption results are presented. With these parameters, a sequence of convective boiling flow regimes for various flow and electric field conditions are developed along the annular channel. Through analysis of the local flow structure, more information will become available regarding the effect of a superimposed electric field on the overall effectiveness of the heat exchanger.

7.1 The Dimensionless Analysis of HFC-134a Fluid Flow

Resolving the equations of electrohydrodynamics through dimensional analysis is a powerful procedure to explain flow behaviour that cannot be derived directly. Several

investigations have suggested the primary mechanisms of electrohydrodynamic flow in two phase systems are due to the last two terms in Equation (3.12). Quantifying the importance of each component has not been possible because of the complicated nature of convective boiling.

The influence of thermophysical properties, with respect to temperature and applied DC voltage, on the dimensionless EHD conductive ($E_{t\sigma}$) and dielectric ($E_{t\varepsilon}$) Rayleigh numbers for both a saturated liquid and vapour in a concentric channel, are presented for HFC-134a in Appendix A. These are calculated according to:

$$E_{t\sigma} = \frac{I_0 L^3}{\rho_0 \nu^2 \mu_c A} \tag{7.1}$$

$$E_{t\varepsilon} = \frac{\varepsilon_0 E_0^2 T_0 (\partial \varepsilon_s / \partial T)_\rho \, L^2}{2\rho_0 \, \nu^2} \tag{7.2}$$

as derived from the momentum equation in Chapter 3 and based on the assumptions described in Appendix A, in particular with respect to the fluid properties. Considering Figures A.4 to A.7, an electric field superimposed on fluid flow is expected to have the following influences:

- Both the conductive and dielectric contributions increase with increasing temperatures and applied voltages (consequently current levels) for both liquid and vapour phases.

- When comparing the effect of the electric body forces on the individual phases, both components of the body force are stronger in the liquid phase than the vapour phase, consequently the liquid will be the phase most affected by an electric field in a two-phase medium. Noting that the influences on the vapour is based on the assumption that the free charge density within the fluid is equal to the total charge injected by the electrodes (*i.e.*, $I_0 = dQ_0/dt$) and the current flux is constant irrespective of the void fraction. As discussed in Section 7.4, current tends to decrease with increasing vapour content.

- The dielectric components, being the dielectrophoretic force and the electrostrictive force, are considerably stronger than the conductive component, the electrophoretic term, since $E_{t\varepsilon} > E_{t\sigma}$ by over an order of magnitude.

Based on these estimates, the dimensionless analysis implies an increase in the quality, for example due to flow evaporation, decreases the influences of the electric body forces.

The range and extent to which EHD may influence the flow must be identified to determine the voltage levels required to induce the migration of the liquid in order to affect heat transfer. Accordingly, the ratio between the *liquid* conductive and dielectric Rayleigh numbers and the square of the *liquid* Reynolds number as a function of applied voltage are presented in Figures 7.1 and 7.2, respectively. Here, $E_{t\varepsilon}$ and $E_{t\sigma}$ are calculated based on the assumptions in Appendix A at a temperature of 24°C.

From the dimensionless analysis on other classical flow behaviour (for example natural convection) and previous investigations with EHD (Chang and Watson, 1994), $E_t / Re_t^2 \geq 0.1$ is the expected condition above which significant influences on the flow of liquid in the channel may be observed due to an electric field. Based on an order of magnitude comparison, the combined effects of electric induced flow and forced convection are represented by the shaded regions in Figures 7.1 and 7.2. A comparison of Figures 7.1 and 7.2 suggests the dielectric (polarization) forces are within the same order of magnitude as the inertial forces $E_{t\varepsilon} \sim Re_t^2$ for the conditions considered in this investigation, see Table 4.2. Conversely, based on the estimations implicit in determining the conductive Rayleigh number, the electrophoretic component of the body force is unlikely to play a significant role on a redistribution of the phases in the system.

Figure 7.2 shows that the influence of the dielectrophoretic and electrostrictive components increase with increased voltage (*i.e.*, electric field strength) and decrease with Reynolds number. The dimensionless ratio suggests the EHD component will dominate when the flow is extremely slow, well into the laminar regime, with an applied voltage

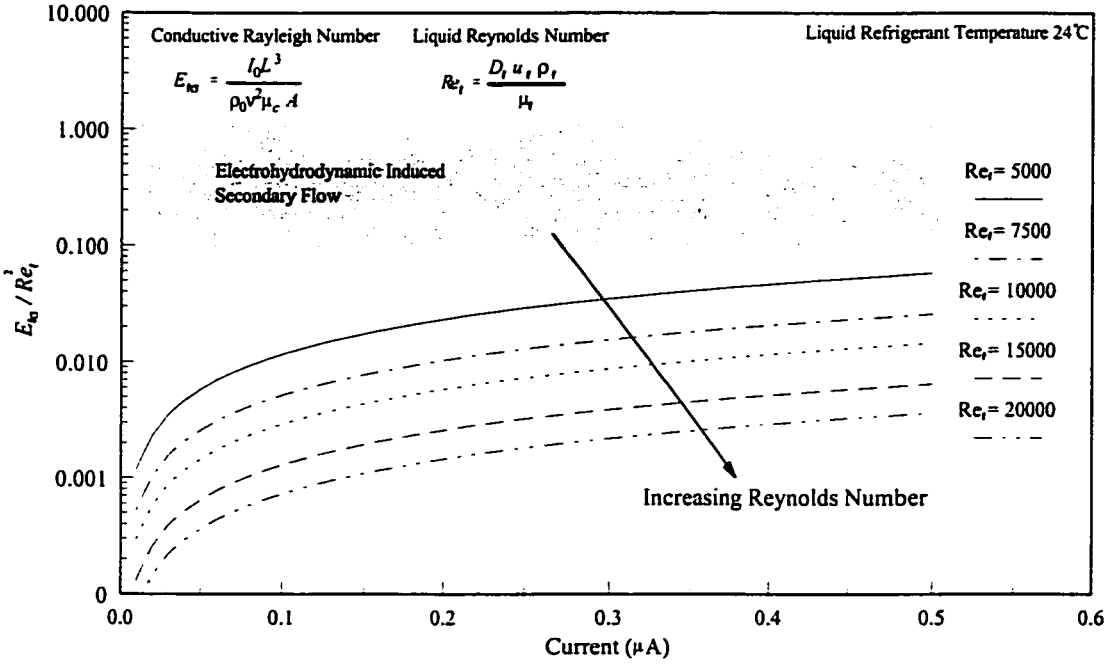

Figure 7.1: The Relationship Between the Conductive Rayleigh Number and Reynolds Number Ratio as a Function of Current for the Experimental Arrangement.

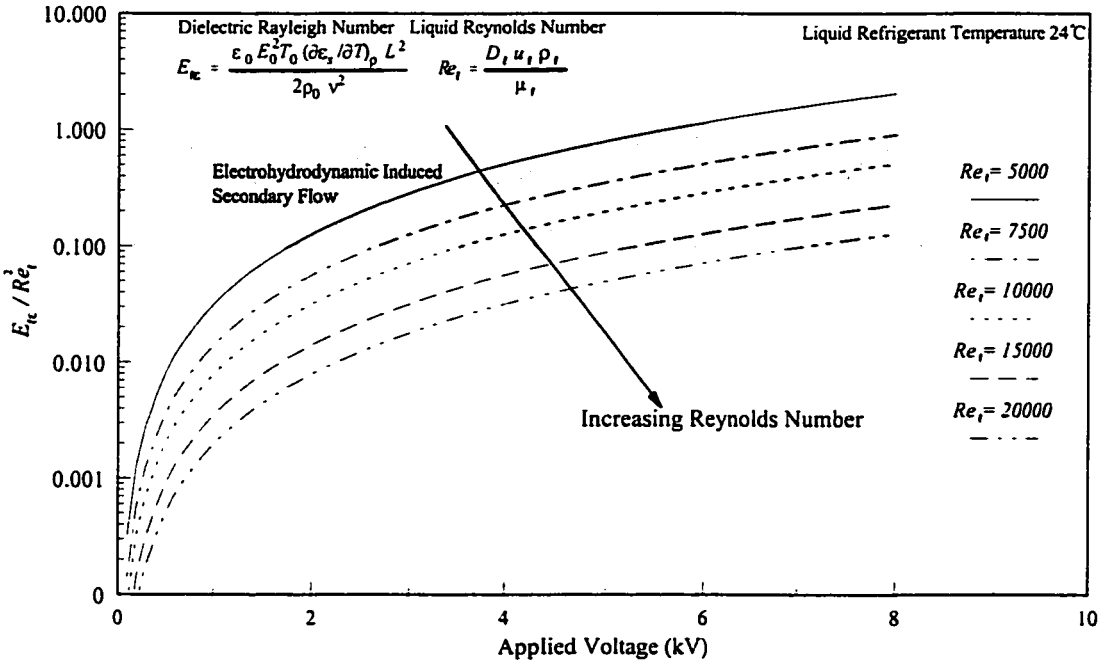

Figure 7.2: The Relationship Between the Dielectric Rayleigh Number and Reynolds Number Ratio as a Function of Applied Voltage for the Experimental Arrangement.

greater than about 6.0 kV. In addition, the dimensional analysis suggests that flow conditions above $Re_f \sim 20{,}000$ or below $V_i \leq 2$ kV will be primarily forced convection. Hence, EHD will not significantly affect the liquid flow and a flow redistribution due to electrohydrodynamic forces becomes unlikely.

In summary, the influences of EHD induced flow on a system are expected to be significant when the Dielectric Rayleigh number is of the same order of magnitude as the square of the liquid Reynolds number, $E_{tc} \sim Re_f^2$. Flow visualization experiments at the exit of the test section have shown that when the proposed dimensionless criterion is satisfied, EHD body forces can have a strong influence on the flow pattern within the channel, resulting in an earlier transition from stratified wavy flow to intermittent (plug or slug) or annular flow and in a transition from dispersed-annular flow to a symmetric annular flow. The range of Reynolds numbers investigated for this experiment were selected in order to confirm this criterion.

7.2 Heat Transfer and Pressure Drop Results

This section presents the parametric investigation of the concentric electrode evaporator channel with and without EHD. The focus of the experimental results presented in this work is to identify the overall (average) heat exchanger performance derived through a local analysis. For a comprehensive analysis of the EHD effect on system performance, several aspects must be considered simultaneously. These include the local heat transfer and temperature measurements, a flow development transient parameter analysis, methods to recognize the flow pattern and the analysis of the local electric field as a function of the flow regime. Hence, the interdependence of these aspects is addressed systematically.

The layout of this section explains the relevant flow and EHD parameters, initially

as they affect the overall performance, by considering the influences that the electrohydrodynamic forces have on the flow using the findings of the dimensionless analysis in Section 7.1. The local measurements of one experimental set of conditions are then considered in detail with reference to the local temperature profiles, the quasi-local heat transfer coefficients and the electric field and flow pattern influences. Finally, this section is completed with a discussion of the effects of both a low and high frequency AC electric field and the unique characteristics revealed through experimentation.

From Appendix B, the quasi-local method of determining the overall heat transfer coefficient and Nusselt number is used in this investigation. The quasi-local method provides a weighted average of the heat transfer coefficient. Accordingly, by calculating the local values and averaging over the length of the channel, the resultant heat transfer coefficient is presumed to be a more accurate representation of the heat transfer condition as the effects associated with a nonlinear axial heat flux and/or refrigerant flow stratification are considered. The results presented here and in the subsequent chapter are based on the calculation of the local refrigerant heat transfer coefficients as discussed in Section 4.5.3.

7.2.1 The Overall Influence of a DC Electric Field

The results of the concentric electrode experiment are presented in Figures 7.3 to 7.8 using both the dimensional and dimensionless forms defined in Chapters 3 and 4. The experimental results are shown in terms of the average boiling heat transfer coefficients and the pressure drop as a function of the parametric values of applied voltage, mass flux, inlet quality and heat flux. The dimensionless parameters used are average the Reynolds number, the Nusselt number and the Dielectric Rayleigh number for the analysis of the experimental data.

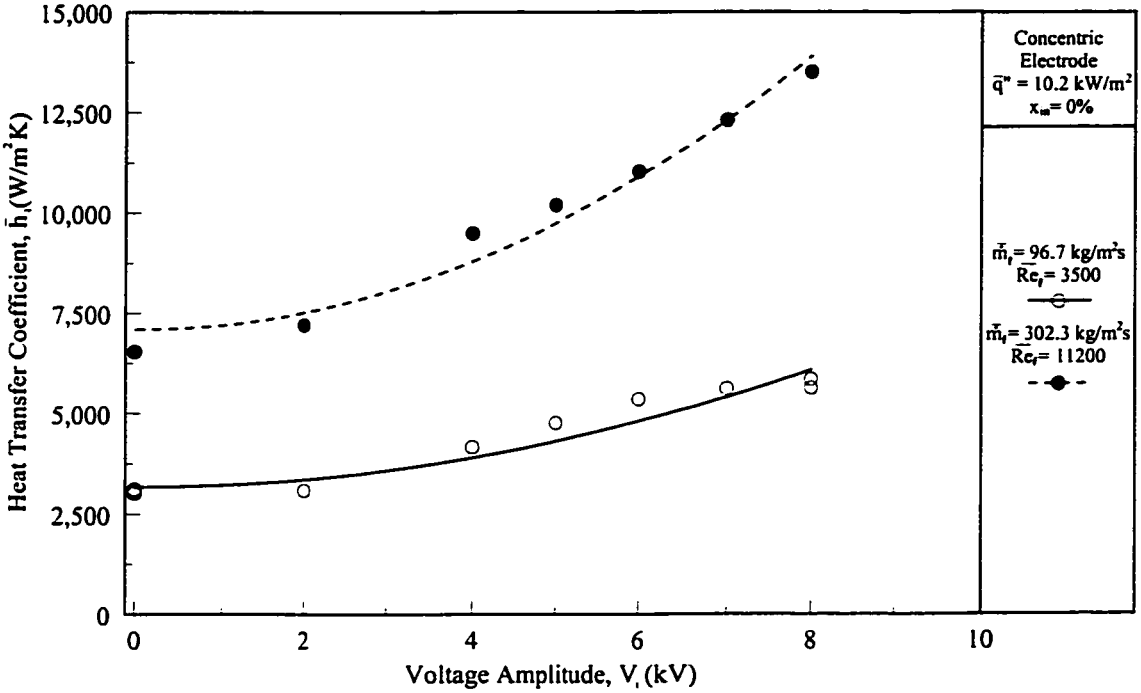

a) Heat Transfer Coefficient vs. Voltage Amplitude

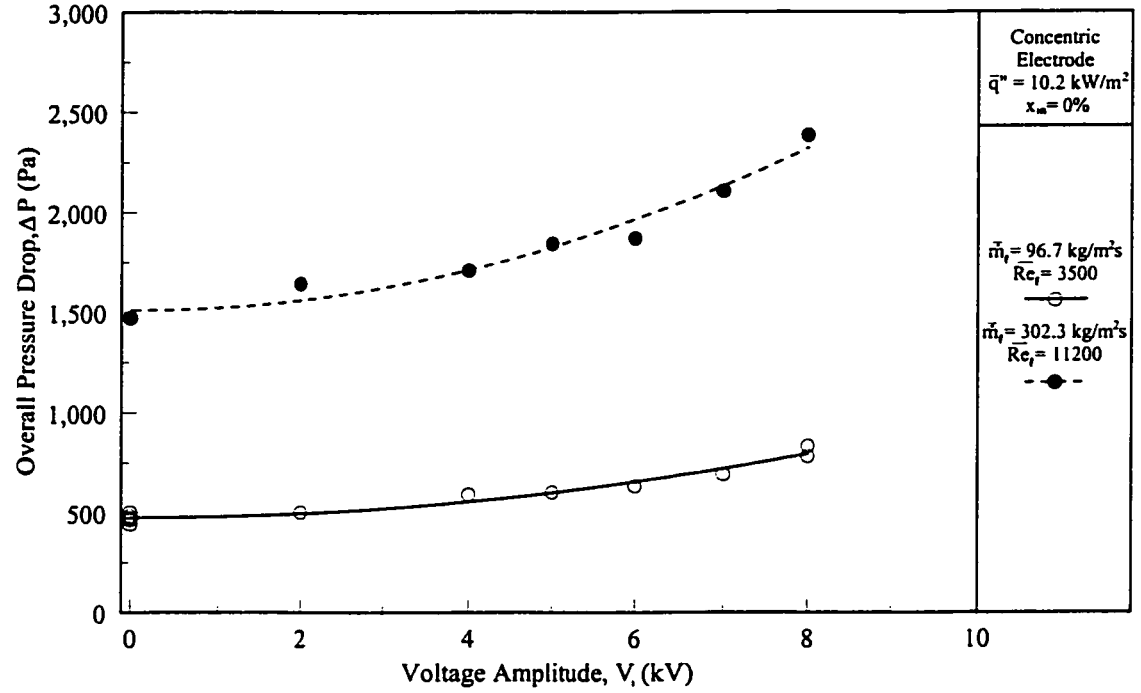

b) Overall Pressure Drop vs. Voltage Amplitude

Figure 7.3: The Effect of Electrode Voltage on the a) Heat Transfer Coefficient and b) Overall Pressure Drop at a Fixed Heat Flux and Inlet Quality for Different Mass Fluxes.

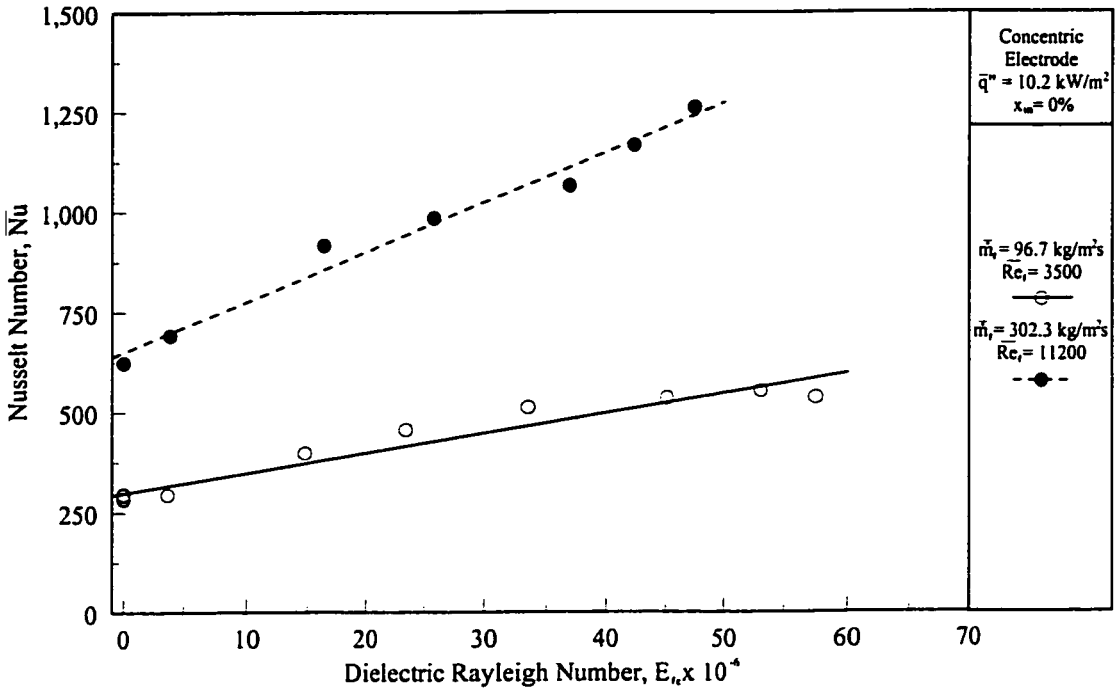

a) Nusselt Number vs. Dielectric Rayleigh Number

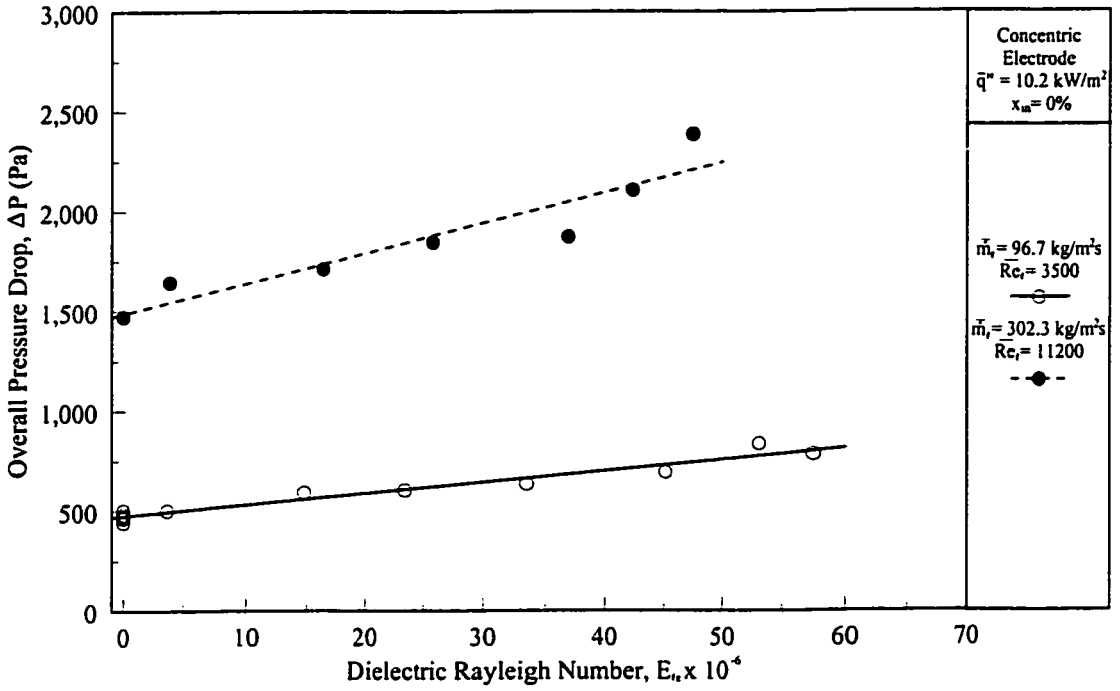

b) Overall Pressure Drop vs. Dielectric Rayleigh Number

Figure 7.4: The Effect of the Dielectric Rayleigh Number on the a) Average Nusselt Number and b) Overall Pressure Drop at a Fixed Heat Flux and Inlet Quality at Different Reynolds Numbers.

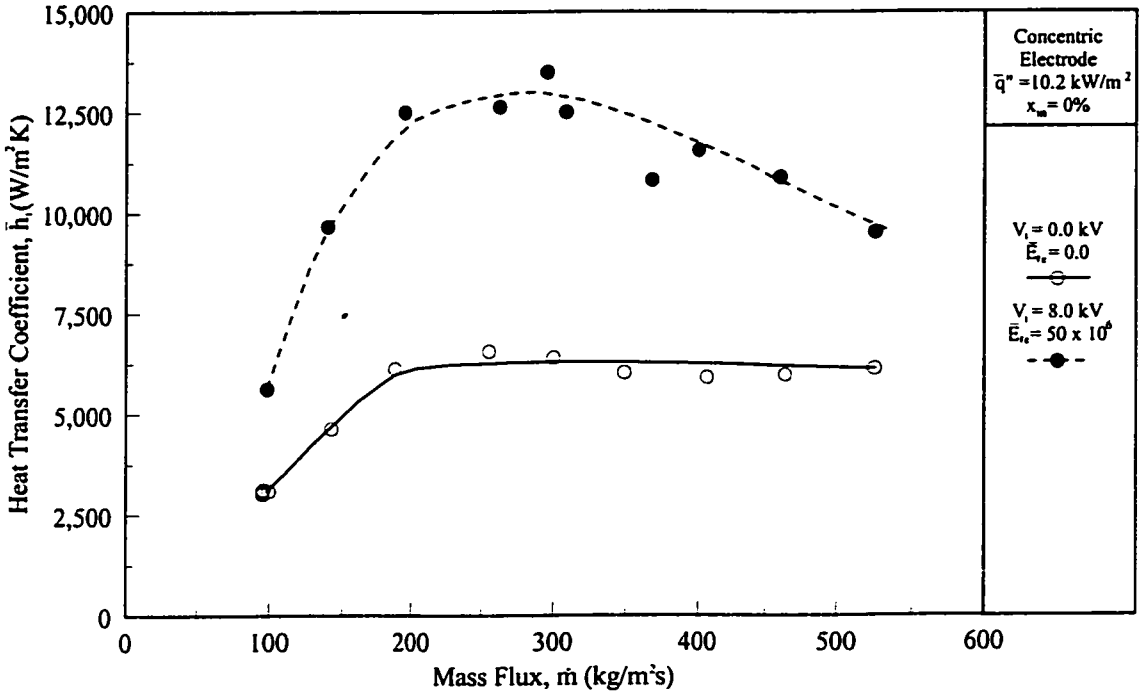

a) Heat Transfer Coefficient vs. Mass Flux

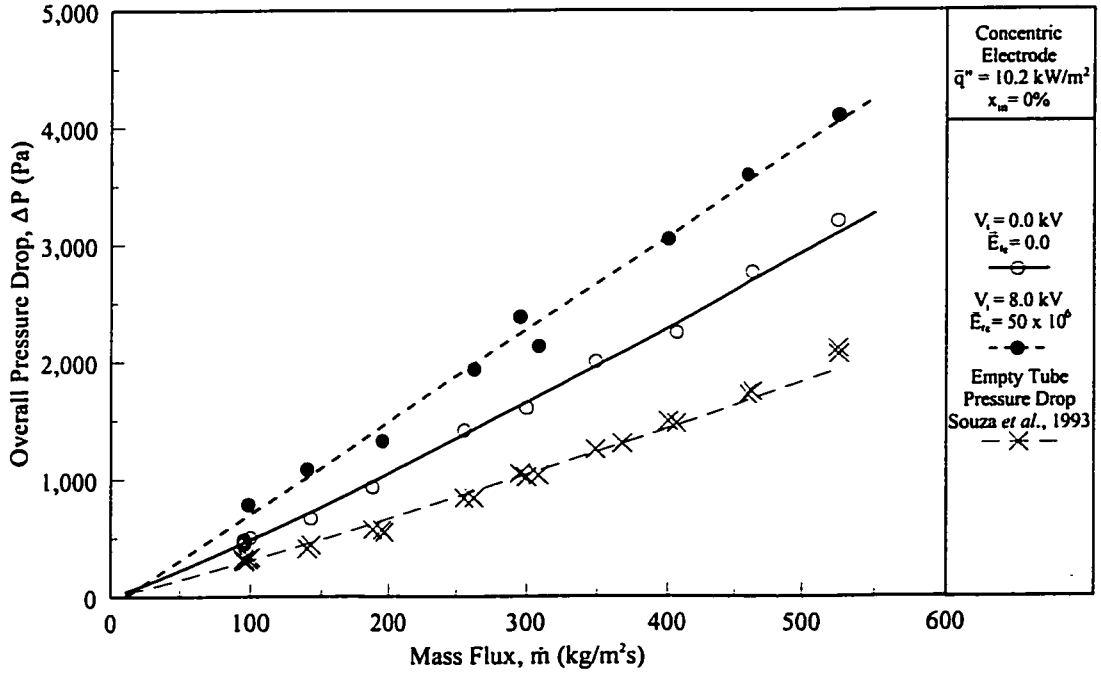

b) Overall Pressure Drop vs. Mass Flux

Figure 7.5: The Effect of Mass Flux on the a) Average Heat Transfer Coefficient and b) Overall Pressure Drop with and without the EHD Effect at a Fixed Heat Flux and Inlet Quality.

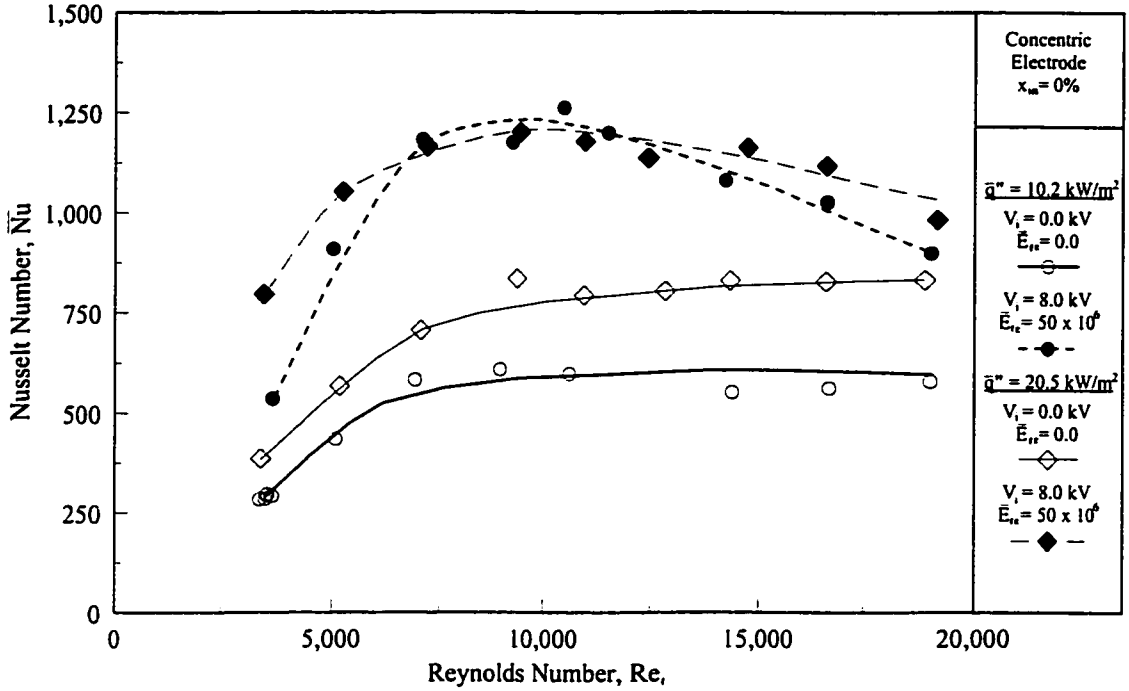

a) Nusselt Number vs. Reynolds Number

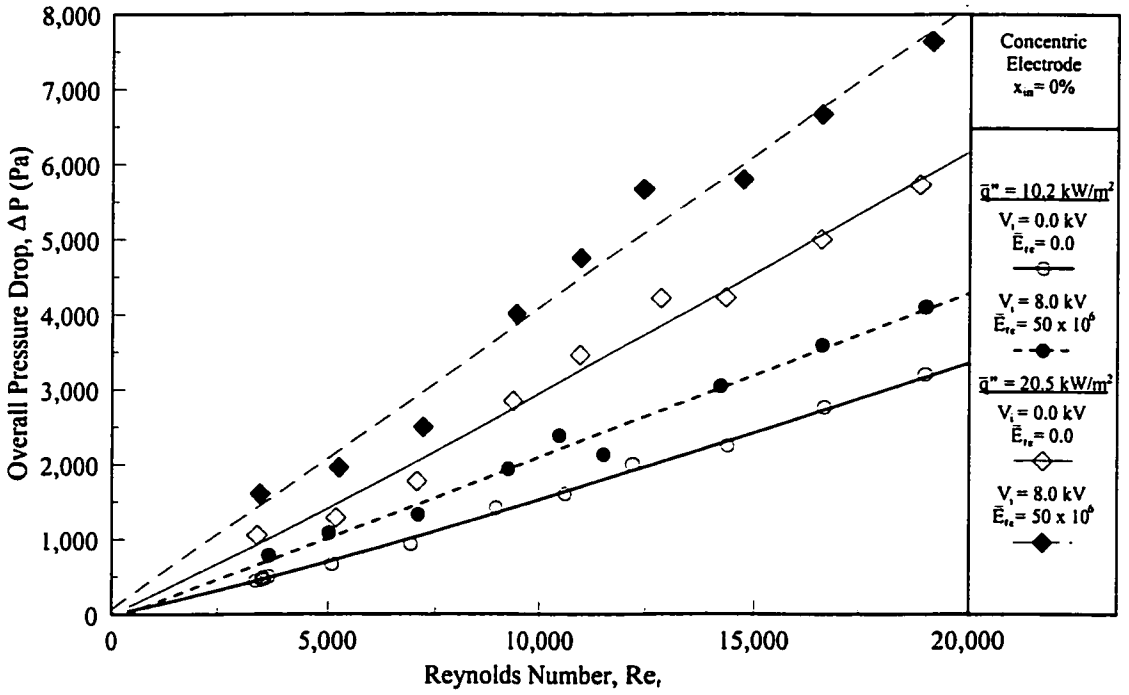

b) Overall Pressure Drop vs. Reynolds Number

Figure 7.6: The Effect of Reynolds Number on the a) Average Nusselt Number and b) Overall Pressure Drop with and without the EHD Effect for an Inlet Quality of 0% at Different Heat Flux Levels.

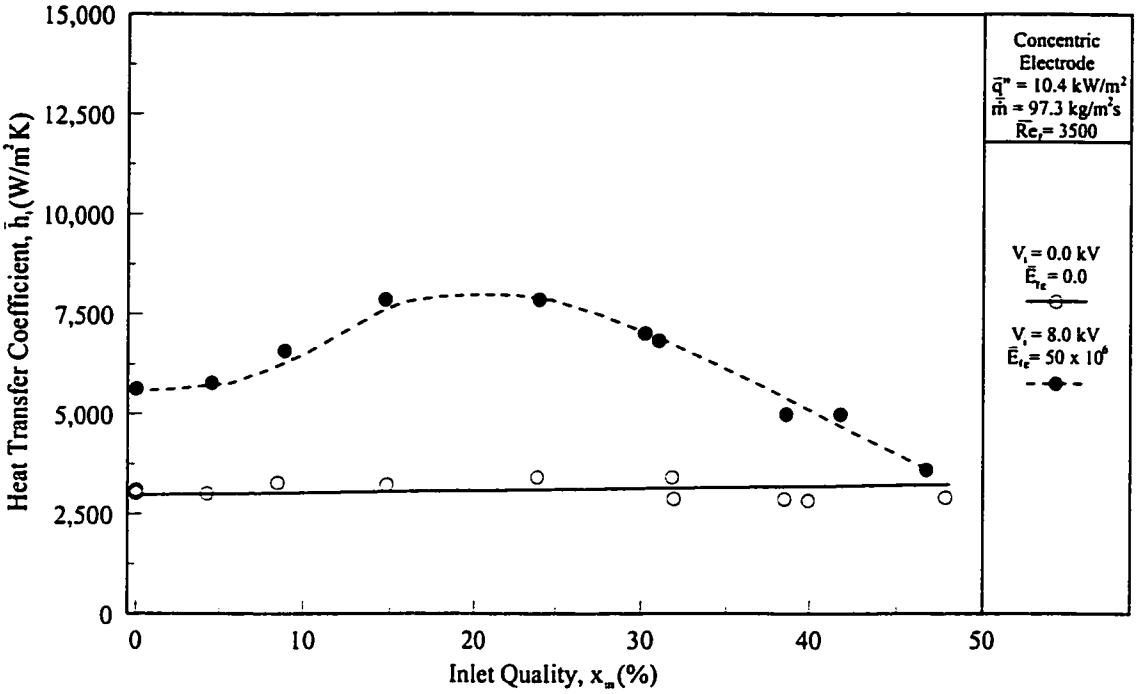

a) Heat Transfer Coefficient vs. Inlet Quality

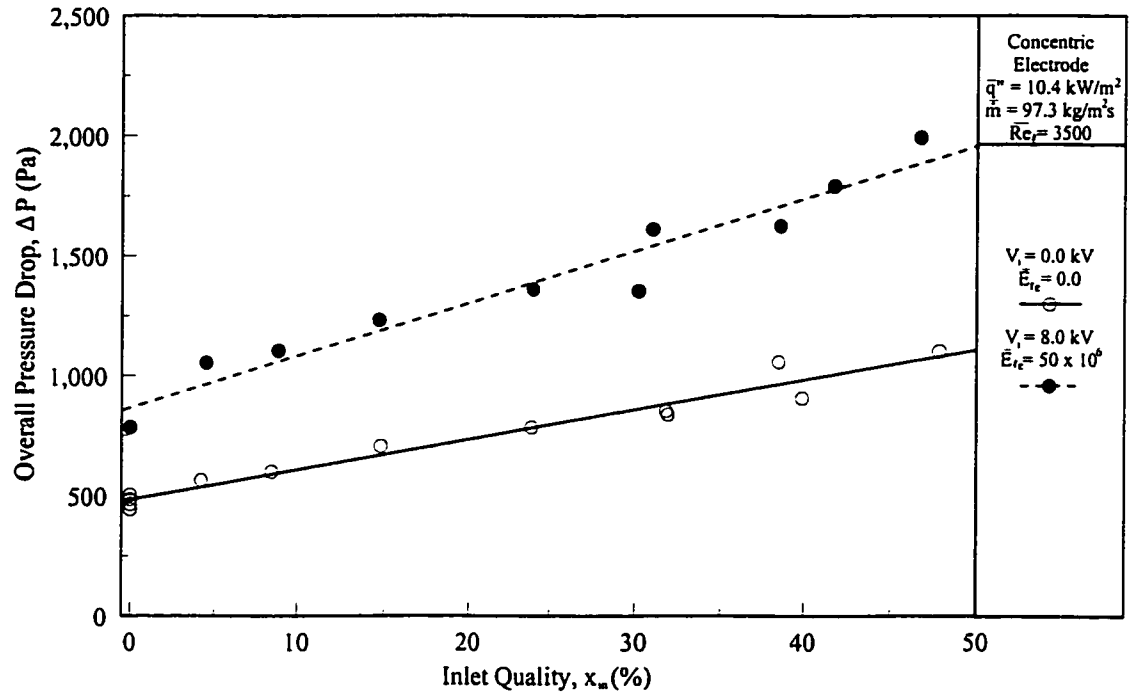

b) Overall Pressure Drop vs. Inlet Quality

Figure 7.7: The Effect of Inlet Quality on the a) Average Heat Transfer Coefficient and b) Overall Pressure Drop with and without the EHD Effect at a Fixed Heat and Mass Flux.

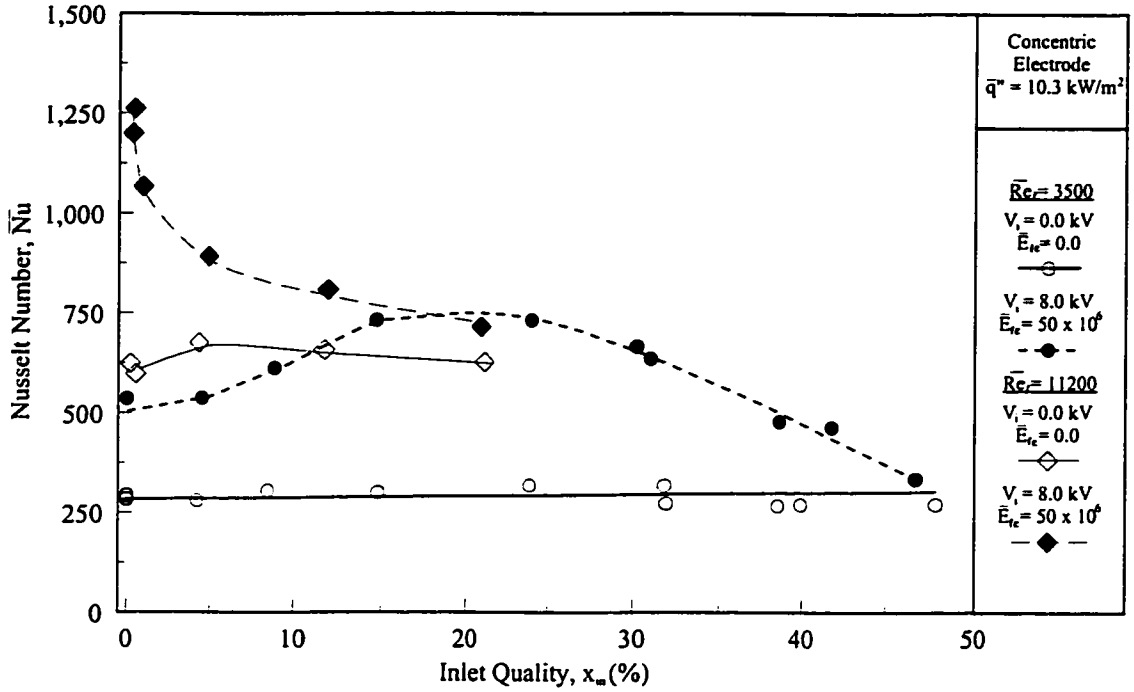

a) Nusselt Number vs. Inlet Quality

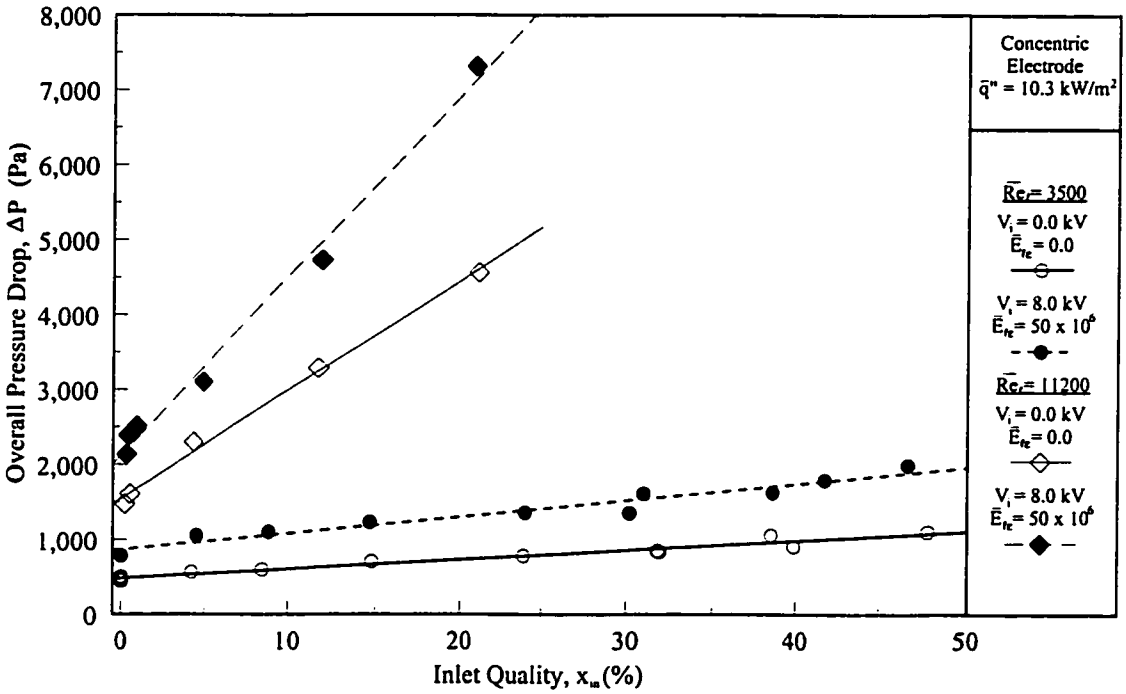

b) Overall Pressure Drop vs. Inlet Quality

Figure 7.8: The Effect of Inlet Quality on the a) Average Nusselt Number and b) Overall Pressure Drop with and without the EHD Effect for a Fixed Heat Flux at Different Reynolds Numbers.

Heat Transfer Augmentation

The Effect of Applied Voltage

The distribution of the average refrigerant heat transfer coefficients and Nusselt numbers for increasing applied voltage levels are presented in Figures 7.3 and 7.4, respectively. For the conditions tested, the effect of voltage increased heat transfer by 85% and 97% at the maximum voltage potential for the two Reynolds numbers shown in Figure 7.4a, $Re_f = 3500$ and $Re_f = 11200$, respectively. In both of these cases, the general trend is an increase in heat transfer coefficient and pressure drop with increasing voltage. The best fit curves with the first order approximation suggest the following, for a given liquid Reynolds number, inlet quality and heat flux:

$$\overline{h} \propto V_i^2$$
$$\nabla P \propto V_i^2$$
$$\overline{Nu} \propto E_{tp}$$
$$\nabla P \propto E_{tp}$$

Although the data sets are limited, the results suggest the change of the heat transfer rate and pressure drop are functions of the radial forces induced by the square of the electric field strength. This implies that the dielectrophoretic force (*i.e.*, $f_{eB} \propto E^2 \propto V_i^2$) induces a secondary motion in the fluid that increases with increasing voltage over the regime of flow conditions tested. In order to better describe the effects of the electric field on heat transfer and pressure drop, the local and transient conditions for $Re_f = 3500$ at different voltage levels is examined in closer detail throughout Section 7.2.2.

The Effect of Mass Flux

Figure 7.5a shows the average heat transfer coefficients as a function of mass flux for a fixed heat flux and a zero inlet refrigerant quality. The results with and without EHD effects (V_i = 8.0 kV) are presented. These results indicate that the EHD effects lead to

substantially higher heat transfer coefficients for the range of qualities and heat fluxes tested. As suggested in the previous section and similar to the results of Singh *et al.* (1994, 1995), when the mass flux (Reynolds number) increases, the EHD forces must overcome the increasing momentum effects, existing surface tension and gravitational influences in order to induce phase migration or draw the liquid away from the wall to reduce the thermal boundary layer or promote dryout. Consequently, although the heat transfer is increased initially with increasing the mass flux, it is reduced with a further increase in mass flux as the ratio of E_{tc} / Re_l^2 decreases.

Figure 7.6a presents a comparison of the effect of mass flux at an increased heat flux level with the data from Figure 7.5 in dimensionless form. With an increase in the heat flux, heat transfer enhancement decreases due to better boiling and evaporation activities associated with higher heat fluxes and hence increased local and average qualities, as has been observed by Singh *et al.* (1994, 1995). Further, as the dominant flow pattern within the channel at these conditions and applied voltage level (V_i = 8.0 kV) is annular, suggested by Figure 6.27, an increase in quality due to an increase in heat flux decreases the liquid film thickness, which results in a lower interfacial jump in the electric field strength and consequently lower interfacial electric forces.

The Effect of Inlet Quality

Figure 7.7a shows the variation of average heat transfer coefficients with inlet quality at a fixed heat and mass flux, q'' = 10.2 kW/m^2 and $\dot{m} \approx$ 100kg/m^{2}s. In general, the effect of the electric field is more dominant in lower quality regions ($x_{in} < 30\%$), which may be due to the electrohydrodynamic effects on the nucleation component as discussed in Section 3.3.1 and suggested by Singh *et al.* (1994, 1995) and the redistribution of the flow pattern from stratified wavy flow to a more uniformly distributed flow, such as annular flow.

The effect of EHD on flow redistribution is based on the transient surface temperature measurements, high speed photography at the test section exit and the proposed flow pattern map in Chapter 6, as discussed in subsequent sections of this chapter. The proposed flow pattern map suggests that at $\dot{m} \approx 100$ kg/m²s the flow is prone to be in the stratified regime for qualities greater than $x = 0\%$ and less than approximately $x \approx 50\%$ in the absence of an electric field. However, for stratified flow to exist upon application of an 8.0 kV voltage, the flow regime map suggests that the quality must be in the range: $0 < x \lesssim 12\%$. Consequently, as the average quality for these experiments is below $x_{in} \approx 30\%$, a flow regime transition due to EHD for at least a portion of the tube may be expected, hence the augmentation in heat transfer coefficient. The effect diminishes at qualities above $x \sim 50\%$, as a flow transition to annular is predicted due to the suction pressure created by the momentum in the absence of an electric field according to the flow mapping prediction in Chapter 6. As the amount of enhancement depends on the local flow regime, and as a consequence the rate of heat transfer is sensitive to the inlet quality, as the entrance effects can have a strong influence of the flow pattern downstream.

The effects of increasing the mass flux to $\dot{m} \approx 330$ kg/m²s ($Re_l = 11200$), as shown in Figure 7.8a, may also be explained through examination of the proposed flow pattern map in Figure 6.27. For these conditions, the flow is predicted to be either intermittent or annular, therefore an EHD induced flow pattern transition is not expected. At this Reynolds number, the heat transfer enhancement drastically decreases as the inlet quality increases. The primary influences resulting in the positive impact observed in Figure 7.8 are believed to be due to upstream effects where the quality is relatively low, inducing significant nonuniformities in the electric field created by the presence of bubbles, plugs and slugs in the intermittent regime.

As suggested through examination of the electric field distribution for annular flow in Section 6.2, the dielectrophoretic force tends to draw liquid toward the center probe leaving less liquid in direct contact with the wall. At relatively low qualities, this has the effect of decreasing the annular film and thermal boundary layer, thus increasing the heat transfer coefficient. However, the liquid extraction phenomena can create early partial or total dryout of the heat transfer surface, thereby creating a reduction in heat transfer rates as the annular film thickness thins while the quality increases. Locally, this result was observed at various positions downstream of the inlet and is a significant factor in the lower overall enhancements observed in Figure 7.8a. This result is similar to that obtained by Singh *et al.* (1994, 1995) and Norris *et al.* (1999) while monitoring the local heat transfer coefficients and the overall heat flux levels at high inlet qualities ($x_{in} \geq 30$ ~50%). These investigations attributed the suppression in heat transfer to the liquid extraction phenomena as described by Yabe *et al.* (1982, 1987a, 1987b). Increasing the mass flux increased the distance downstream where dryout occurred for the same heat flux as the resident time of the liquid in the channel was reduced and the EHD effect was typically lower, as described in the *Mass Flux Section*. Accordingly, at $\dot{m} \approx 330$ kg/m^{2}s for inlet qualities above $x_{in} \geq 20\%$, the EHD effect was suppressed.

Pressure Drop

The primary drawback of EHD enhanced heat transfer is the pressure drop penalty in this type of electrode arrangement. Figures 7.3b to 7.8b show the total pressure drop of the test section as a function of applied voltage, mass flux and heat flux for the heat transfer characteristics described above. Included in Figure 7.5b is the empirical prediction of the pressure drop for an empty tube, suggested by Souza *et al.* (1993) as previous investigations (Singh *et al.*, 1993, 1994, Salehi *et al.*, 1995, Bryan, 1998) indicate the introduction of the

electrode increases the pressure drop considerably, which is another drawback of this type of electrode arrangement. This additional drawback is apparent from the comparison of the Souza *et al.* (1993) estimation of pressure drop with the measurements obtained through experimentation.

Figures 7.3 and 7.4 show that pressure drop increases with increasing applied voltage and mass flux. As mentioned in the *Applied Voltage Section*, the general trend suggests that the amount of pressure drop increase is a function of the radial forces induced by the square of the electric field strength. This would imply the dielectrophoretic force (*i.e.*, $f_{eB} \propto E^2 \propto V_i^2$) induces a secondary motion in the fluid that increases with increasing voltage over the regime of flow conditions tested. The increase in pressure drop for higher values of mass flux is due to high frictional losses and increased momentum interaction. Under high mass flux conditions, the electric field effect on flow patterns may serve to increase the momentum interaction, particularly due to the enhancement of entrained droplets and bubbles in the respective phases (Stuetzer, 1963a). Further, ion drag near the wall surface tends to increase the pressure drop (Stuetzer, 1959, 1963a). Essentially, pressure drop is increased due to the effect of the electrohydrodynamic body force and the subsequent redistribution of the flow pattern into regimes with increased instability as liquid is drawn toward the upper portion of the tube against gravity.

Consider, for example, that a flow pattern transition occurs from the initially stratified smooth regime of liquid level 2.7 mm, similar to the case in Chapter 6 as depicted in Figure 6.3, to a smooth annular flow. In the stratified state, the wetted perimeter of the annular channel and the interfacial area are 11.37 mm and 9.42 mm^2, respectively. Assuming that the void fraction is the same and that the interfacial conditions are perfectly smooth following the flow transition, the wetted surface area and interfacial area increase to

34.30 mm and 30.83 mm^2, respectively. This represents over a threefold increase in surface area, resulting in a considerable increase in pressure drop from the higher frictional effects of the liquid phase and interaction between the phases.

7.2.2 The Local Influence of a DC Electric Field

In general, if a two-phase flow were redistributed to "wet" parts of the channel that were previously "dry", for example, a change from stratified flow to annular or to "thin" the thermal boundary layer by extracting a quantity of liquid in contact with the tube, then vaporization enhancement is to be expected. Conversely, if the electric field established acts to create an attraction force, drawing the liquid from the surface of the tube such that dryout occurs, then a reduction in heat transfer may be observed. To describe this effect, an example of a local and transient analysis is presented in this section for the following conditions: $Re_l = 3500$, $x_{in} = 0\%$, and $q'' = 10.2$ kW/m^2 at different voltage levels for the top and bottom halves of the tube. This is experimental quasi-local data, Figure 7.9, used to determine the averaged and the overall performance at Re_l = 3500 presented in Figures 7.3 and 7.4. Although the overall performance results show an enhancement of approximately 100%, locally the effects range from enhancement by as much 2000% to a suppression in heat transfer of 40% over the no EHD condition.

For the conditions presented in Figure 7.9, the instantaneous measurement of the local surface temperatures suggests that the dominant flow pattern is likely stratified wavy, which explains the significant difference in heat transfer coefficients from the top to the bottom. When the applied voltage is increased, there is an increase in local heat transfer over the circumference of the tube. This may be explained by considering the resultant forces acting on the liquid - vapour interface. As EHD is applied, the dielectrophoretic force can create instabilities (protrusions) on the interface producing a significantly more disturbed

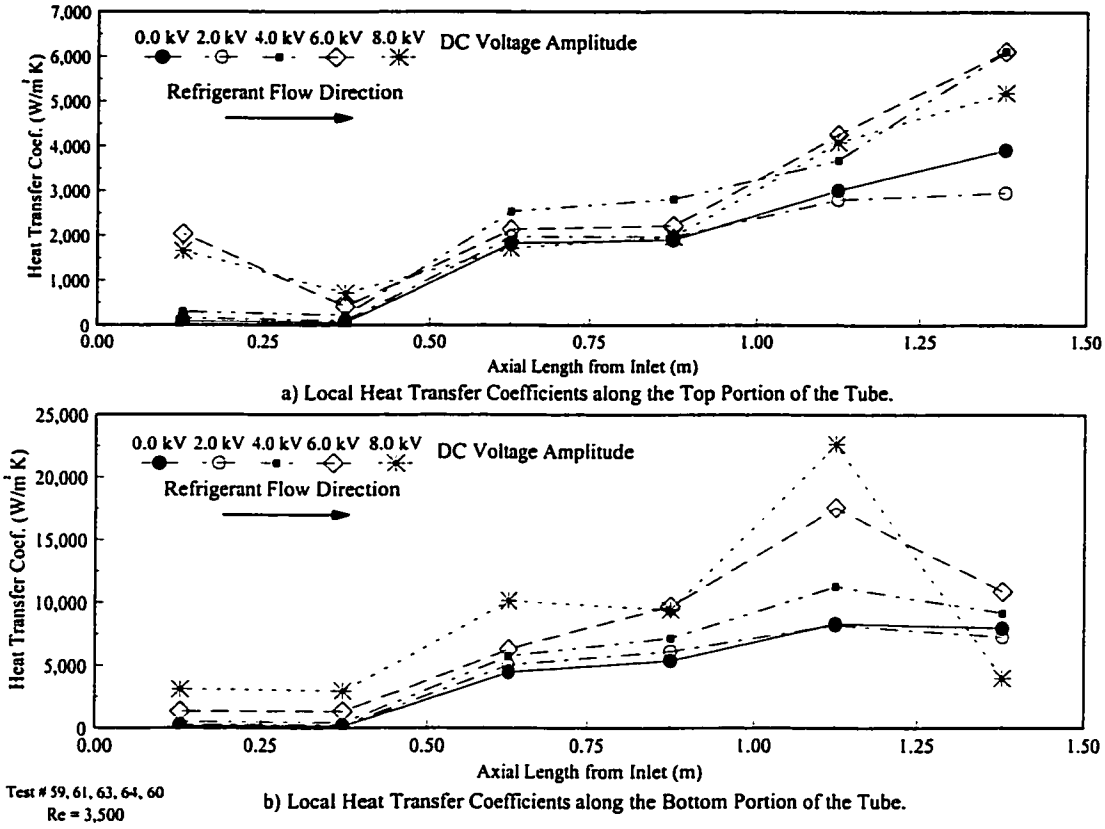

Figure 7.9: Quasi-Local Heat Transfer Coefficients with Increasing Applied DC Voltages.

flow with potentially more frequent and larger amplitude waves. The vapour flowing over the protrusions will accelerate, reducing the vapour pressure which produces an upward force causing a wave to grow unless the force is more than offset by the downward gravitational and surface tension forces. As the protrusion, grows the electric field distribution in the vapour phase increases, as shown in Chapter 6, which in turn increases the attractive force on the liquid, further accelerating the wave upwards. If the combined flow effect is significant enough, a flow regime transition will occur changing the stratified liquid to either intermittent or annular. In either case, the result is a reduction in the liquid thickness on the bottom of the tube and a wetting of the top, which will increase the rate of heat transfer around the tube as a consequence. As heat is added to the system at a voltage level above approximately V_i = 4.0 kV, the quality increases and the rate of heat transfer

becomes more symmetric. Here the flow is believed to be slug or annular flow. In the case of annular flow, the highest electric field is near the electrode in the vapour core. Consequently, liquid will be extracted from the surface by the attraction forces created by the established electric field distribution suggested in Section 6.2. As reported by Norris *et al.* (1999), this results in a regime of intermittent dryout on the bottom surface thereby reducing the overall heat transfer.

Reconstruction of Flow Patterns in a Test Section

Consideration of the forces acting on the interface by examination of the proposed flow pattern map outlined in Chapter 6 provides some insight as to the flow pattern to be expected. The flow pattern map suggests that at $\dot{m} \approx 100$ kg/m^{2}s, the flow is prone to be in the stratified regime for qualities greater than $x = 0\%$ and less than approximately $x \approx 50\%$ in the absence of an electric field. However, for stratified flow to exist upon application of an 8.0 kV electric field the quality must be in the range: $0 < x \lesssim 12\%$. The transition quality is expected to increase with voltage levels below this extreme. As the heat flux is constant for all voltage levels considered, the outlet quality is also constant at $x_{out} \approx 40\%$. Therefore, in the absence of an electric field, the prediction of the flow regime according to Figure 6.27 is stratified flow along the majority of the channel. Whereas for an 8.0 kV electric field the flow is believed to experience two transitions, one from stratified wavy flow to intermittent flow at the approximate location where $x \approx 12\%$ and a second above approximately 20% where the flow is expected to be annular. As the proposed fully developed flow regime map does not account for momentum transfer between the phases, the effects of acceleration and the nonuniform electric force acting on the interface, these boundaries only present a good qualitative estimation. The following section considers the transient traces (instantaneous measurements) of various parameters to provide an understanding of the flow progression

along the channel at various electric field strengths to supplement this discussion.

Wall Surface Temperature Profiles in the Absence of an Applied Electric Field

Figure 7.10a shows the axial profile of the time-averaged superheat temperatures at the top and bottom of the test section tube along the heated test section, which was used for estimating the quasi-local heat transfer coefficients in the absence of an applied voltage (Test #59) formerly presented in Figure 7.9. The refrigerant flows from left to right through the channel. The superheat temperature is the temperature differential by which the wall temperature exceeds the average saturation temperature of the refrigerant in the test section. In this case, the saturation temperature is $T_{sat} = 25.2 \pm 0.1\,°C$. Figure 7.10b shows the corresponding standard deviation temperature fluctuations of the same data set. They are determined according to:

$$\sigma = \left[\frac{1}{n}\sum_{i=1}^{n}(T_i - \overline{T_s})^2\right]^{½} \tag{7.3}$$

which gives an indication of the degree to which each temperature measurement fluctuates around the time-averaged value at that location. Thus, with a higher standard deviation, the temperature at that point varies more over the course of the sampling time. For standard deviations in the range of $\pm$ 0.05 ~ 0.08°C the variation in temperature is on the order of 2-3 LSB's significant bit which is a typical white noise fluctuation due to the method of data acquisition, hence, measurements in this range of standard deviation may be assumed to represent a constant temperature reading. The standard deviation profiles are useful for quickly determining the location of the largest fluctuations in wall temperature occurring along the test section. The surface temperature and standard deviation profiles give an indication of the behaviour of the fluid or the entrainment of droplets or bubbles in contact with the wall and thus the flow pattern at that location. However, an examination of the

instantaneous values of surface temperatures would be required in order to see the nature of the fluctuations and their time dependent responses in more detail.

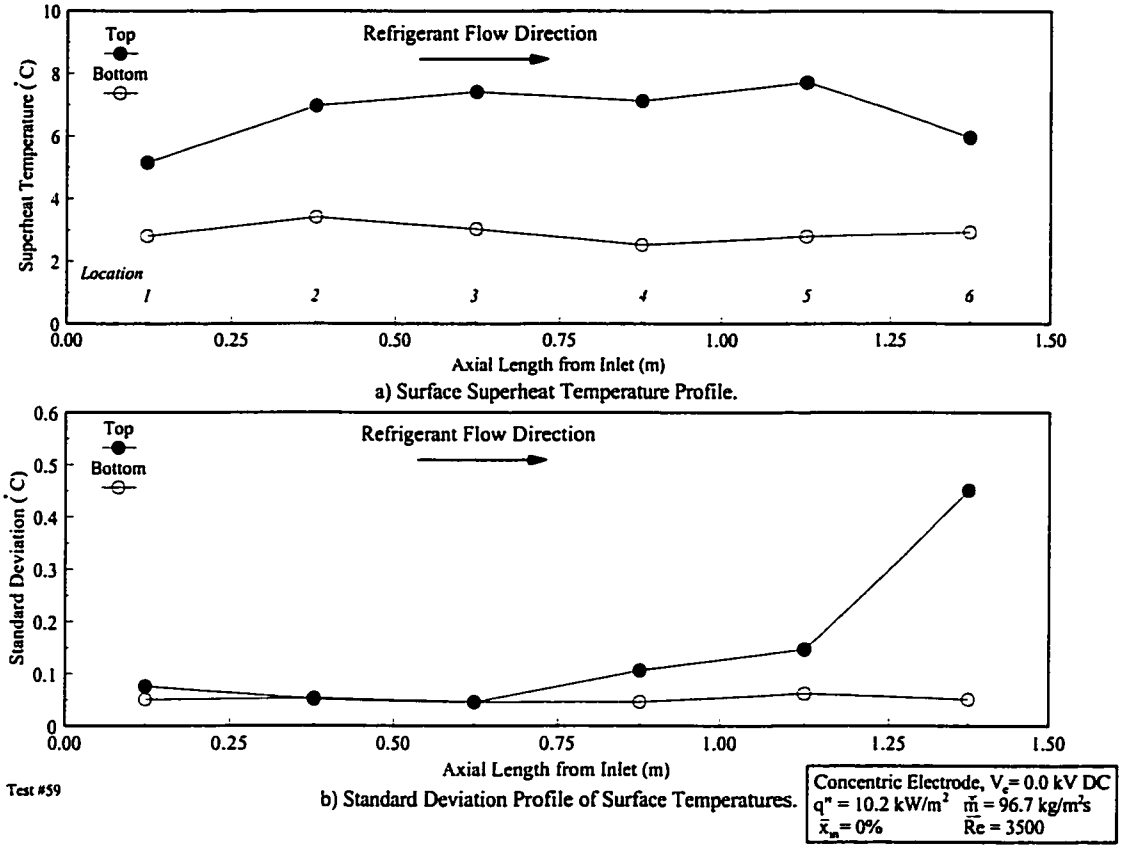

Figure 7.10: Time-Averaged Surface Superheat Temperature and Standard Deviation Profiles of the Concentric Electrode without an Applied Voltage.

For Test #59, the flow entering the test section was a single-phase liquid at a temperature slightly below the saturation temperature of the refrigerant. When the flow reached the first thermocouple station, (location 1), Figure 7.10a indicates that the average temperature of the top surface is more than 2 °C higher than that of the bottom surface. This is an indication of flow and/or thermal stratification inside the tube. For the same location, an examination of the standard deviation profile in Figure 7.10b shows that the standard deviation of the top wall temperature is slightly higher than that of the bottom, indicating that the temperature of the top surface of the tube varies to a greater extent than the bottom. This temperature variance could indicate the flow regime at location 1 intermittently wets

the top surface while the bottom surface is wetted continually.

Figures 7.11 a, b and c are typical time responses of the top and bottom thermocouples and the differential pressure transducer for Test #59. The shape of the temperature trace gives an indication of the flow pattern at any axial location along the tube. Note that the time traces were taken sequentially rather than concurrently, so no inferences can be made with respect to the relative positions of characteristic areas of the transient data. Further, the values of the temperature readings on the surface are affected by the heat capacity of the tube. The heat capacity tends to filter high frequency components in the temperature fluctuations and only show low frequency fluctuations.

Temperature traces at location 1 in Figures 7.11a and b gives more insight into the behaviour of the flow. The top temperature (at location 1) is considerably lower than the top surface temperatures downstream suggesting axial variations of flow regime may exist. The small amplitude fluctuation on the bottom half suggests that the variation is white noise because the fluctuations are within $\pm 0.06°C$. However, a small component of this variation may also be from ebullition as the wall superheat temperature shown in Figure 7.10a is sufficient to produce some nucleation. The temperature indicated by the standard deviation analysis fluctuates by as much as $\pm$ 0.2°C along the top of the tube. Consequently, the dominant flow regime is postulated to be bubbly flow due to nucleate boiling when considering a combination of these results with the small quality, $x \leq 4\%$, at this location. Therefore, the greater standard deviation in the top surface temperature is attributed to ebullition, migration of bubbles upwards due to buoyancy and the flow of vapour plugs as bubbles coalesce.

Referring back to Figure 7.10a, the next thermocouple locations, 2 to 4, are almost identical. The top average surface temperatures at these locations are slightly higher than

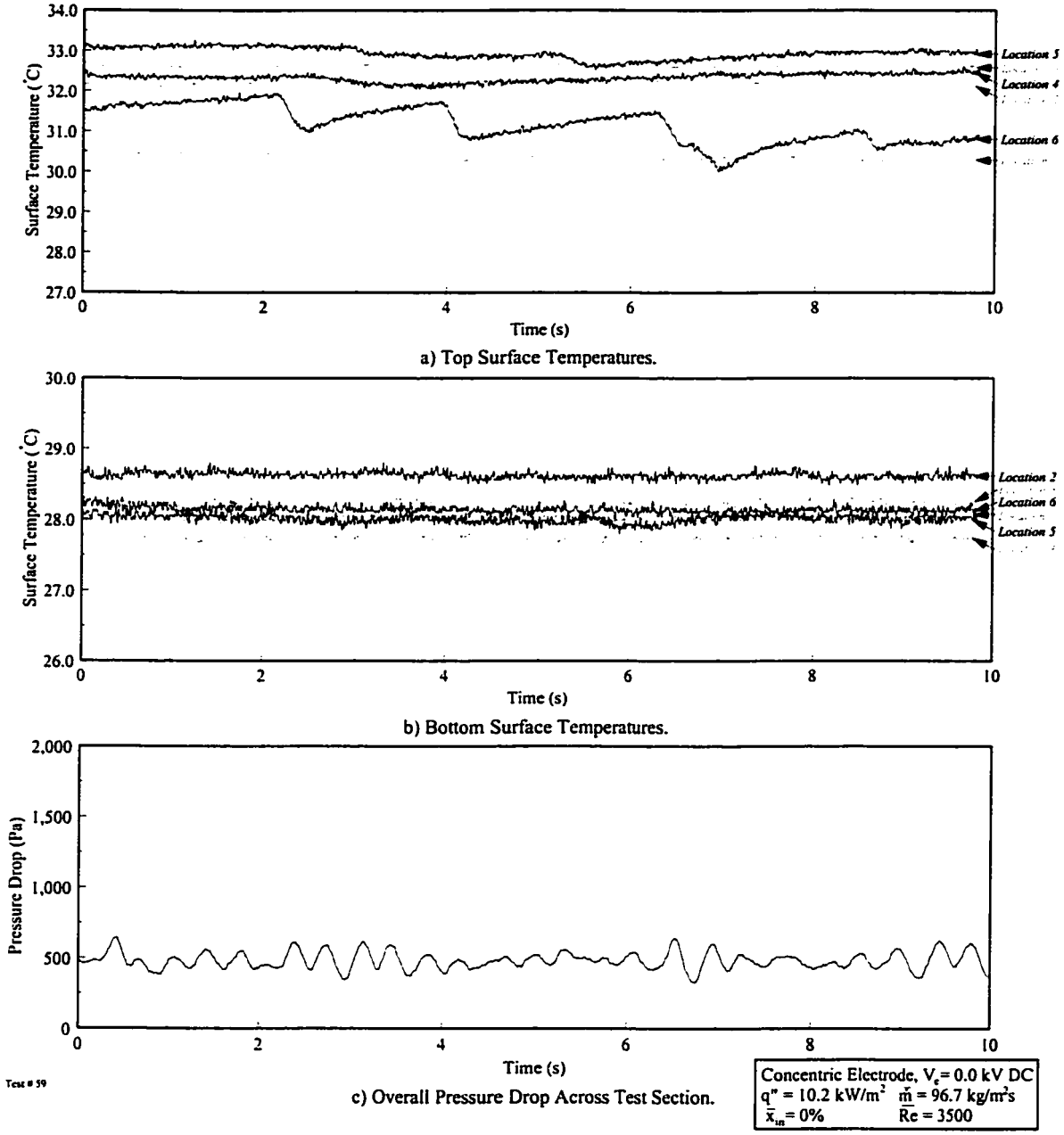

Figure 7.11: Time Trace of Surface Temperature and Pressure Drop of the Concentric Electrode without an Applied Voltage.

their previous location and are only 1°C to 2°C below the outside water temperature measurements. Conversely, the bottom surface temperatures are all approximately constant at $\overline{T_b}$ = 28.1 ± 0.3°C, only three degrees above the refrigerant saturation temperature. Figure 7.10b shows that the standard deviation of all the bottom measurements is negligible when external noise is considered. The flow pattern map analysis suggests that these

conditions are attributed to stratified flow. The trend of increasing temperature on the upper surface may be accredited to the counterflow nature of the test section; the temperature of the heating water on the outside of the tube is higher as the refrigerant flows further down the test section. Therefore, the wall temperature is expected to be higher downstream. Some disturbances in this trend may be a function of the pressure drop along the channel, reducing the refrigerant's saturation temperature. However, this difference did not exceed 0.4°C throughout the entire investigation.

Figure 7.11a reveals that at locations 4 and 5, a modest disturbance exists compared to the previous locations. This could be due to droplets entrained in the vapour, from increased instability on the liquid vapour interface, impinging on the top of the channel since the vapour velocity increases with increasing quality. The time-varying nature of the top surface temperature at locations 4 and 5 increases the standard deviation at these locations to 0.11°C and 0.15°C, respectively.

The final surface temperature measurement at location 6 is 12.5 cm upstream from the exit of the heated section. As shown in Figure 7.11a, the top temperature trace at location 6 varies by as much as 2°C between the extremes of location 1 and locations 2 to 5. The number of fluctuations in the trace indicates that the top surface is alternately dried and rewetted, presumably by slugs bridging the channel gap, significant droplet entrainment in the vapour or the intermittent wetting of the surface due to "climbing" of liquid around the circumference of the tube. The bottom surface temperature trace at location 6 is similar to the upstream bottom surface temperature measurements, with little temperature fluctuation. High speed video imaging at the viewing windows just upstream of the heated section confirmed that the flow regime was stratified wavy with a liquid thickness $h_L \approx 2.7$ mm accompanied by complete dryout on the top portion of the channel, occasionally disturbed

by random large amplitude waves (near slug flow). Figures 7.12a and b show an image of the near stratified wavy flow and large amplitude wave flow, respectively, with the observed flow pattern under the influence of an 8.0 kV electric field, Figure 7.12c.

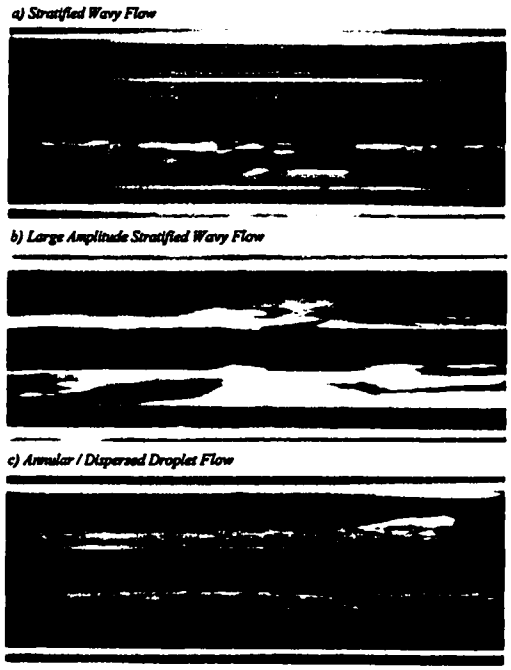

Figure 7.12: High Speed Video Flow Pattern Images at the Exit of the Test Section for the Concentric Electrode under the Influence of a DC Applied Voltage.

Figure 7.11c presents the overall pressure drop variation across the heat exchanger. For this condition, the mean overall pressure drop is 480 Pa with a 60 Pa standard deviation. Compared to the adiabatic experiments conducted by Cotton *et al.* (1996), fluctuations of this magnitude are rather small for a two-phase system and are typical of non-periodic flow regimes such as bubble, annular, stratified wavy or mist flow (Shoukri and Abdul-Razzak, 1996). This is consistent with the inferences made from the temperature traces that the dominant flow regime may be stratified wavy, deviating only at the inlet and exit of the channel.

Based on the above observations, schematics of the flow pattern along the length of the channel without an applied voltage can be reconstructed, as shown in the following

section, to illustrate the process of flow regime transition inferred through the analysis of the flow pattern map, surface temperatures and pressure drop.

Wall Surface Temperature Profiles in the Presence of an Applied Electric Field

Figure 7.13a shows the time averaged axial wall superheat temperature profile for the same flow conditions considered in the previous section, which are G = 100 kg/m²s, q'' = 10 kW/m² and x_{in} = 0%, for three values of applied voltage: 0 kV (as shown in Figure 7.10), 4 kV and 8 kV. Figure 7.13b shows the corresponding standard deviations of the surface temperature fluctuations.

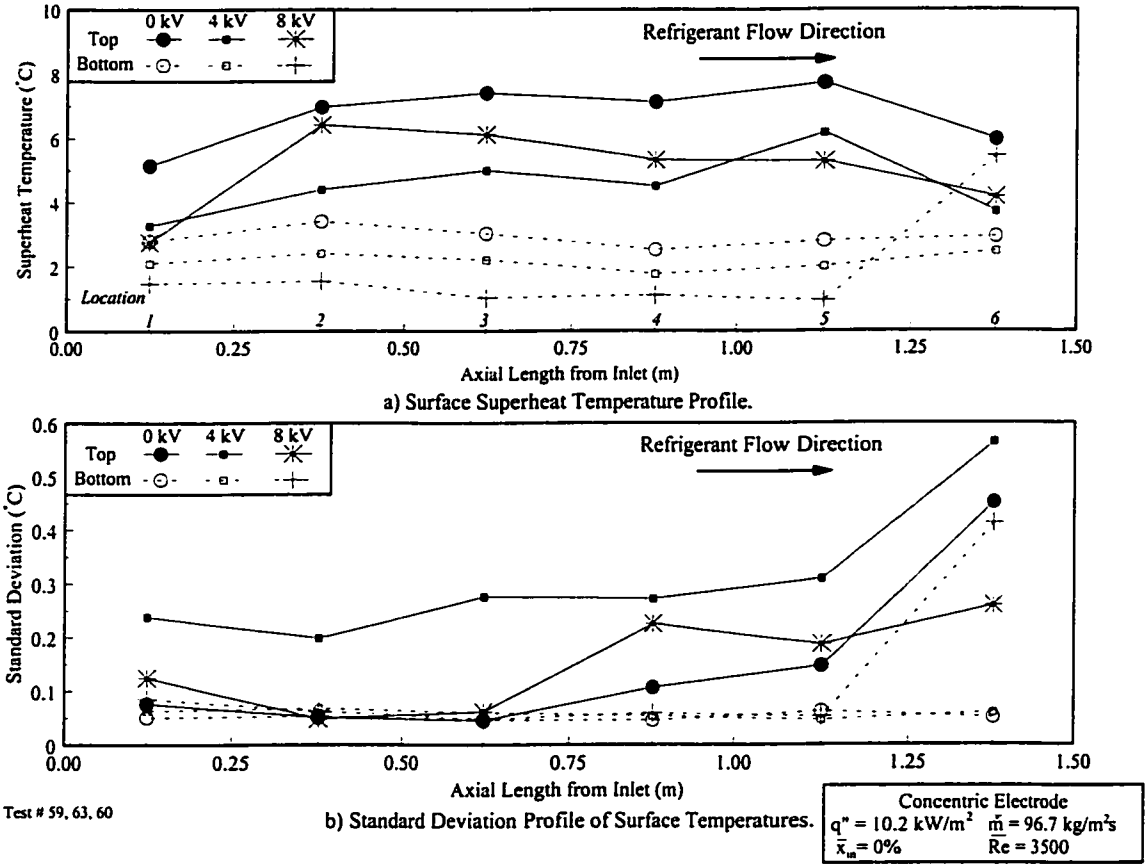

Figure 7.13: Time-Averaged Surface Superheat Temperature and Standard Deviation Profiles of the Concentric Electrode Increasing DC Applied Voltage Levels.

The surface temperatures at locations 1 through 6 in Figures 7.13a and b show that the application of an electric field tends to have a larger effect on the top surface

temperatures than the bottom in terms of dynamic behaviour instantaneous measurements as indicated from the standard deviation. At each location, the average bottom wall superheat temperatures decrease slightly with applied voltage, the only exception being the bottom surface temperature at location 6 under the influence of an 8.0 kV DC voltage. This overall decrease in wall temperature with the EHD application is an indication of the increase of the average heat transfer coefficient. The exception at location 6 is due to intermittent dryout of the bottom surface as discussed later in this section. The top wall surface temperatures do not indicate a clear trend aside from the increase in temperature variation of the transient temperature profile. Two effects occur simultaneously. As the refrigerant moves downstream and the local quality increases, the liquid layer at the bottom becomes thinner which increases the degree to which the bottom surface is cooled thus allowing the temperature of the wall to be lower. The second effect is that as the applied voltage level is increased the interfacial electric force increases, enhancing the momentum suction pressure effect which attracts the liquid towards the upper part of the channel. With decreasing liquid layer thickness, interfacial waves are expected to increase due to the increase in vapour velocity and increased nonuniformity of the electric field as more liquid is drawn upwards and entrained into the vapour core.

Figure 7.13b shows that the standard deviations for the temperature the bottom surface of the tube at locations 2 through 5 are roughly the same, regardless of applied electric field potential. However, the standard deviations for top locations show that there is a large variance in the temperatures with standard deviations as large as $\pm$ 0.55°C at the furthest downstream location.

The time traces of surface temperature are more instructive in determining the EHD effect on flow pattern. Figure 7.14 show the time traces of temperature and pressure drop

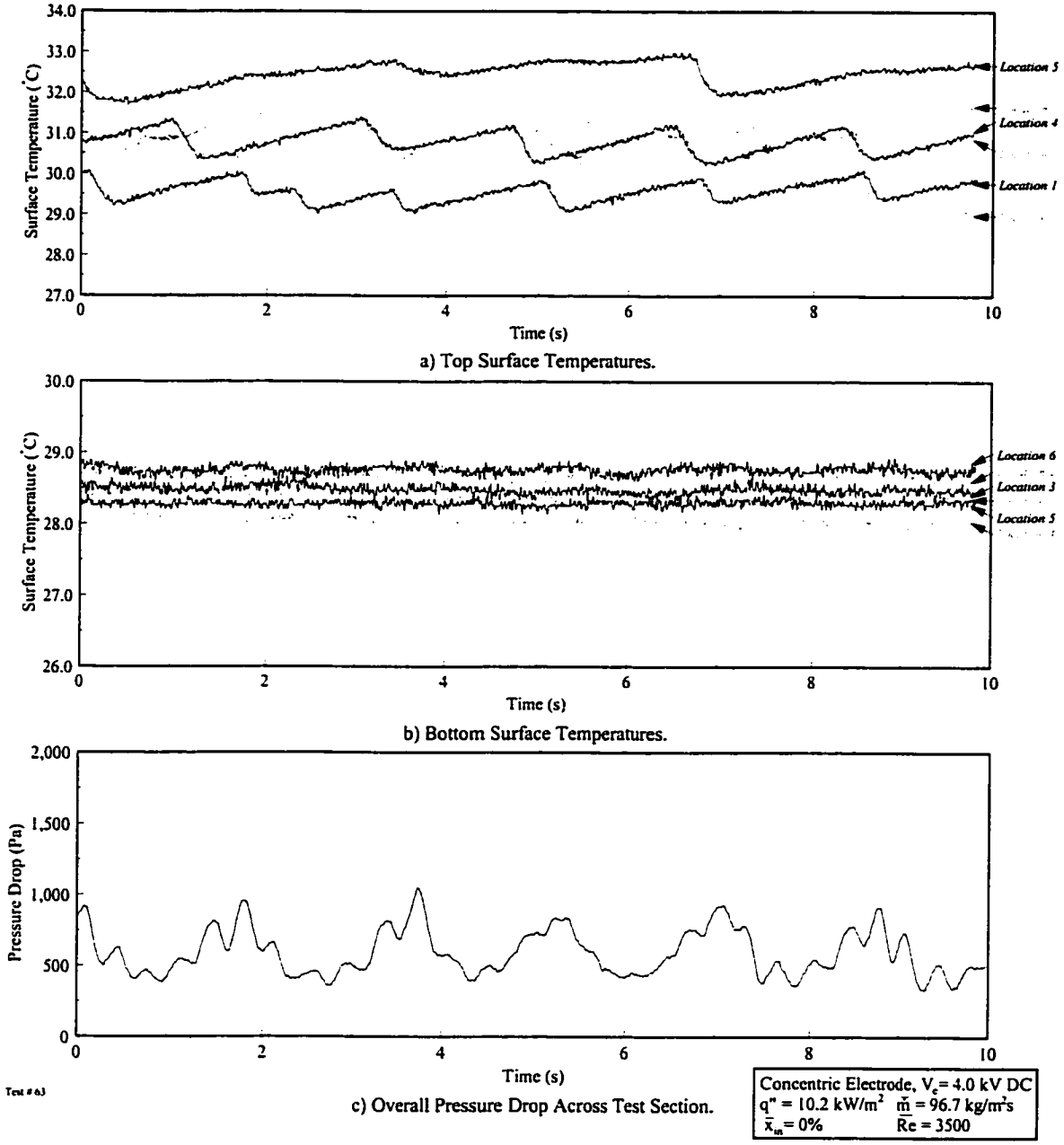

Figure 7.14: Time Trace of Surface Temperature and Pressure Drop of the Concentric Electrode at an Applied Voltage of V_i = 4.0 kV DC.

for an applied voltage of 4.0 kV (Test #63). Likewise, Figure 7.15 shows the traces for an applied potential of 8.0 kV (Test #60).

As presented in Figure 7.9, the V_i = 4.0 kV level appears to be the threshold of the EHD effect, where the inertial effects are of the similar magnitude to the EHD effects as interpreted through the proposed dimensional analysis, *ie.* $E_{t\varepsilon} \sim Re_t^2$. This is further

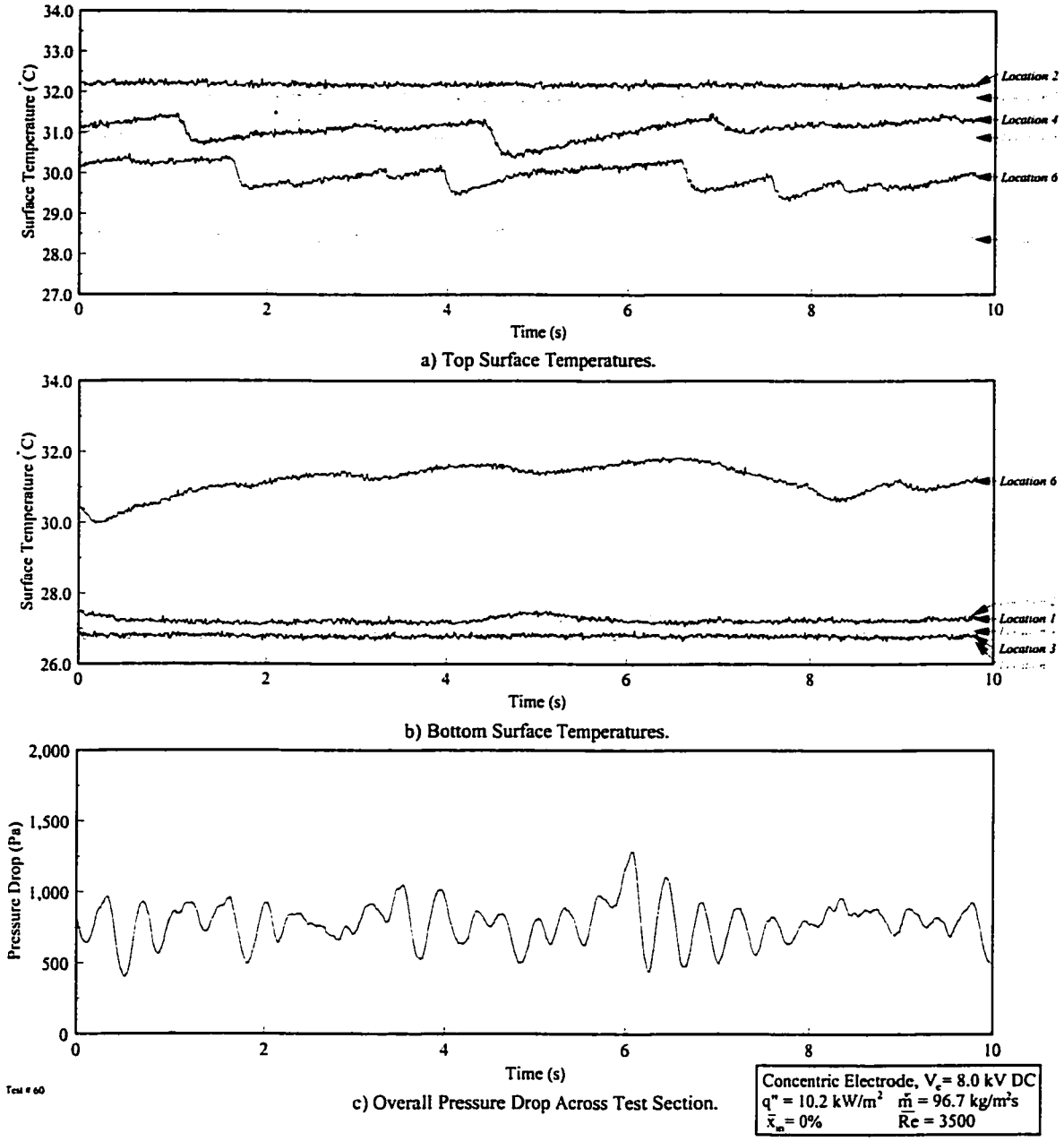

Figure 7.15: Time Trace of Surface Temperature and Pressure Drop of the Concentric Electrode at an Applied Voltage of V_i = 8.0 kV DC.

emphasized in the plot of the transient measurements shown in Figure 7.14, the results are clearly differed from those obtained in the absence of an electric field. Here the fluctuating temperature effects at location 6 for Test #59 at V_i = 0 kV has manifested at the top axial locations 2 through 6 in Test #63, while the variation of the bottom temperatures are almost identical to Test #59. Location 1 is similar to V_i = 0 kV with the exception that the upper

temperature variation has increased, suggesting that the bubble dynamics of this low quality region may have intensified due to the influences affecting bubble behaviour described in Chapter 3, Section 3.3.1. The profile of the last five top instantaneous wall temperature traces are very similar, with 5 ~ 10 fluctuations again in the range of 1°C to 2°C, indicating that the surface is alternately dried and rewetted. This drying and rewetting within the tube occurs presumably by the action of slug flow, significant droplet entrainment or the intermittent wetting due to climbing of liquid around the circumference of the tube. With the condition of a constant overall heat flux regardless of the applied voltage, the liquid must be taken from the previously stratified liquid layer. As previously mentioned, this effect is evident in the comparison of the wall superheats for the different tests. By entraining from the stratified layer upwards against gravity through the influence of the interfacial electric forces, as described in Chapter 6, the thinner liquid layer increases the heat transfer coefficient which in turn decreases the wall superheat. In general, by redistributing the liquid and vapour to wet the upper portions of the channel that were previously dry and reducing the thickness of the liquid layer by extracting a quantity of liquid in contact with the tube, heat transfer enhancement is observed as shown in Figure 7.9.

The transient pressure drop trace, Figure 7.14c, exhibits a similar fluctuation pattern to the top temperature profile. Like the temperature measurements, the pressure trace consists of 5 ~ 10 considerable surges in pressure over the 10 sec data acquisition period, similar to pressure drop fluctuations observed in a slug type flow (Shoukri and Abdul-Razzak, 1996). With the application of V_i = 4.0 kV the mean overall pressure drop and standard deviation has increased to 590 ± 160 Pa due to this more unstable flow regime.

Figures 7.15a and b clearly show the result of the application of a more intense electric field, V_i = 8.0 kV. At location 1, both the top and bottom superheat temperatures

have decreased by ~ 2°C while the fluctuations have increased only slightly over the V_i = 0 kV condition and have converged to approximately the same value. Increasing the number of bubbles by breaking up large bubbles and decreasing the bubble detachment diameter, thereby resulting in the creation of more turbulence and interfacial area, induced by the electric field as described in Chapter 3, are likely causes of these effects. The resulting flow pattern is postulated to be a more concentrated, uniformly dispersed bubble flow at location 1.

The temperature traces at 2 and 3 are similar to the stratified flow traces shown for Test #59, (locations 2 to 5). However, the upper surface temperature at location 3 has dropped below the upstream surface temperature at location 2 by ~ 0.4°C. This is counter intuitive since the temperature is expected to increase downstream whenever the flow configuration is unchanged, owing to the countercurrent nature of the heat exchanger. The decrease in surface temperature is presumably the result of either a rapid uniform droplet impingement or the development of an annular film on the upper surface of the tube. By considering the close resemblance between the top transient temperatures at locations 4 and 5 in Test #60 and #63, a flow regime transition is not believed to have occurred by increasing the voltage level. However, based on the additional reduction in the bottom wall superheat temperature at these locations, 2 to 5, more liquid is believed to have been entrained in the vapour as a function of the EHD forces acting on the interface as discussed in Chapter 6.

Finally, at location 6 a considerable deviation from the previous two tests (#59, #63) is apparent as shown in Figure 7.15b. At this location, the wall temperature of the bottom surface has increased to a point where it exceeds the top surface. Here, the temperature traces of the top and bottom surfaces are very similar and the temperature difference is

believed a result of the different measurement periods. Further, the standard deviation of the temperature trace at the bottom of the channel is considerably higher than the bottom temperature measurements upstream of that location. Due to the similarity between the top and bottom temperature profiles at this location, the flow influences are assumed to be similar here. That is, the tube surface, both top and bottom, is intermittently dried due to the extraction of liquid into the vapour core, which reduces the rate of heat transfer. With the support of high speed video imaging at the viewing windows just upstream of the heated section, this regime was identified as a transitional regime between annular and highly dispersed droplet flow as shown in Figure 7.12c.

The observations made through interpreting the temperature traces and flow visualization are in agreement with the dynamic pressure drop fluctuations presented in Figure 7.15c. The pressure differential is approximately 800 Pa with a standard deviation of 150 Pa and does not maintain a repetitive structure like the former test, V_i = 4.0 kV. At V_i = 8.0 kV, Test #60, the increase in pressure drop is a function of the establishment of unstable flow patterns prone to increase momentum interaction, *ie.* entrained droplet flow, and the less structured nature of the instantaneous values are believed to be due to the numerous flow pattern transitions that seem to occur axially along the length of the channel.

The schematics of the proposed flow pattern reconstruction in the absence of an electric field and at increasing DC applied voltage levels are presented in Figure 7.16. In summary, the interfacial dielectrophoretic forces created by the application of a voltage to the electrode may cause several different flow regime transitions to be observed. The flow patterns developed in the above analysis agree with the postulated flow pattern transitions developed in Chapter 6 through the qualitative and quantitative arguments made through interpretation of the electric field distribution analysis. Further, the proposed range where

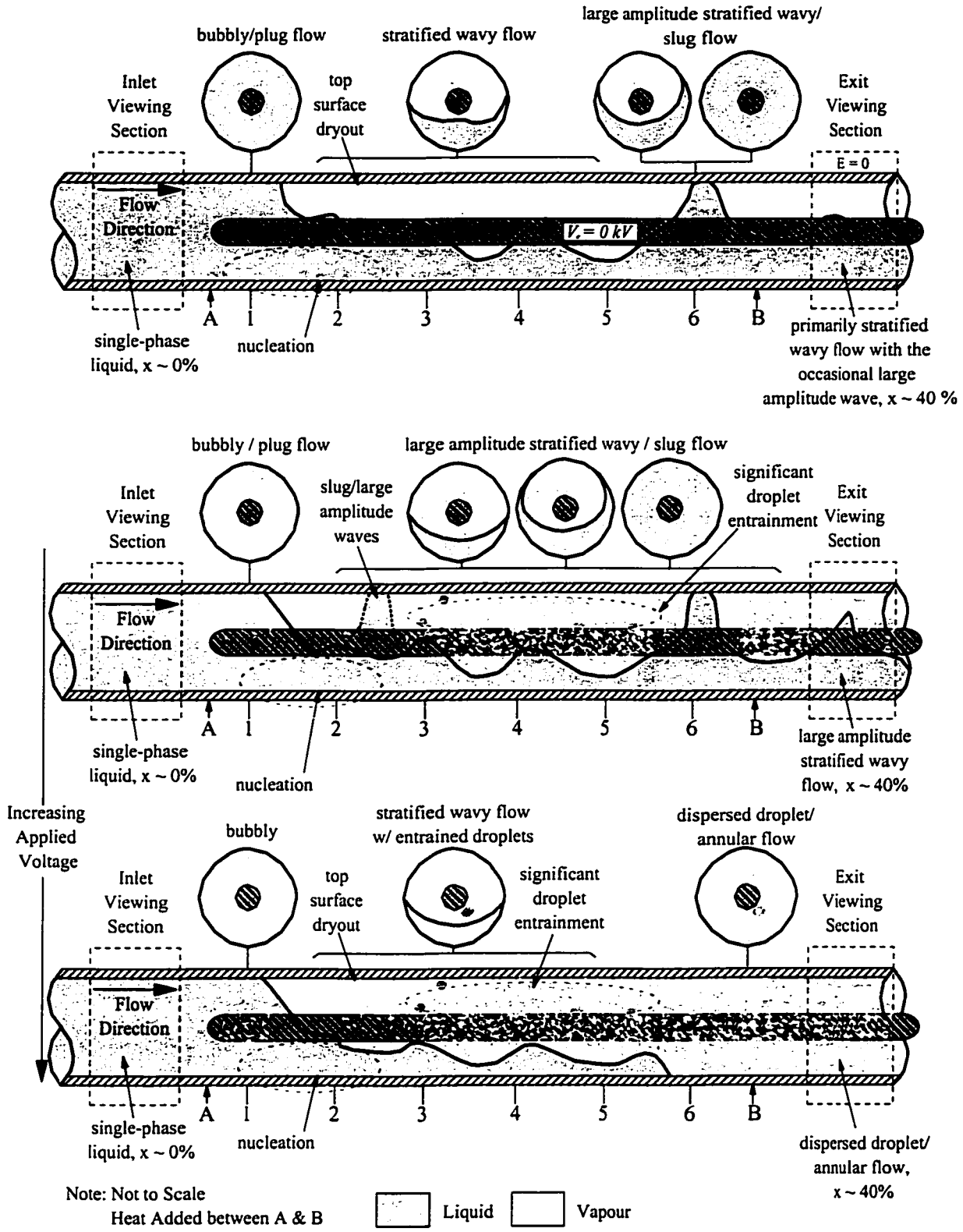

Figure 7.16: Proposed Reconstructed Flow Pattern from Surface Temperature and Pressure Drop Traces and Inlet and Outlet Flow Regime Observations for Increasing DC Voltage Levels ($\dot{m}$ = 100 kg/m²s, q'' = 10.2 kW/m² & x_{in} = 0%).

the combined effects of electric induced flow and forced convection forces concurrently affect the flow when the electric forces are within the same order of magnitude as the inertial forces, $E_{t\varepsilon} \sim Re_t^2$, has been supported by examination of the local and transient experimental data.

In the next section, the average and transient analysis presented for DC voltages is extended to the AC voltage frequencies investigated.

7.2.3 The Overall Influence of an AC Electric Field

Both low (60 Hz) and high frequency (6.6 kHz) AC voltages were investigated in a further attempt to verify the dimensional analysis prediction that the dominant force was dielectrophoretic in nature and to explore an underdeveloped field of investigation in two-phase EHD heat transfer augmentation.

Considering the former objective of applying the concept of charge relaxation time, as presented in Chapter 3 and Appendix A, with the AC electrical conductivity measurements by Fellows *et al.* (1991) gives an order of magnitude assessment regarding the influence of the electrophoretic force. As the analysis in Appendix A suggests, it is unlikely that free charge influences on the bulk and interface will occur for the high frequency condition investigated at $f = 6.6$ kHz $> 1/\tau_\sigma$. Through deductions made by the observation of the flow pattern transition and heat transfer coefficient results, this argument was further corroborated as the 6.6 kHz results coincided with the values observed for the DC electric fields. Figure 7.17 shows a comparison of the experimental data for the DC and AC dielectric Rayleigh number (based on the AC voltage amplitude) explored in this investigation. Agreement between the DC and 6.6 kHz AC results suggests that the electrophoretic component of the electric body force is not a significant factor as free space charges are not expected to accumulate within the annular gap.

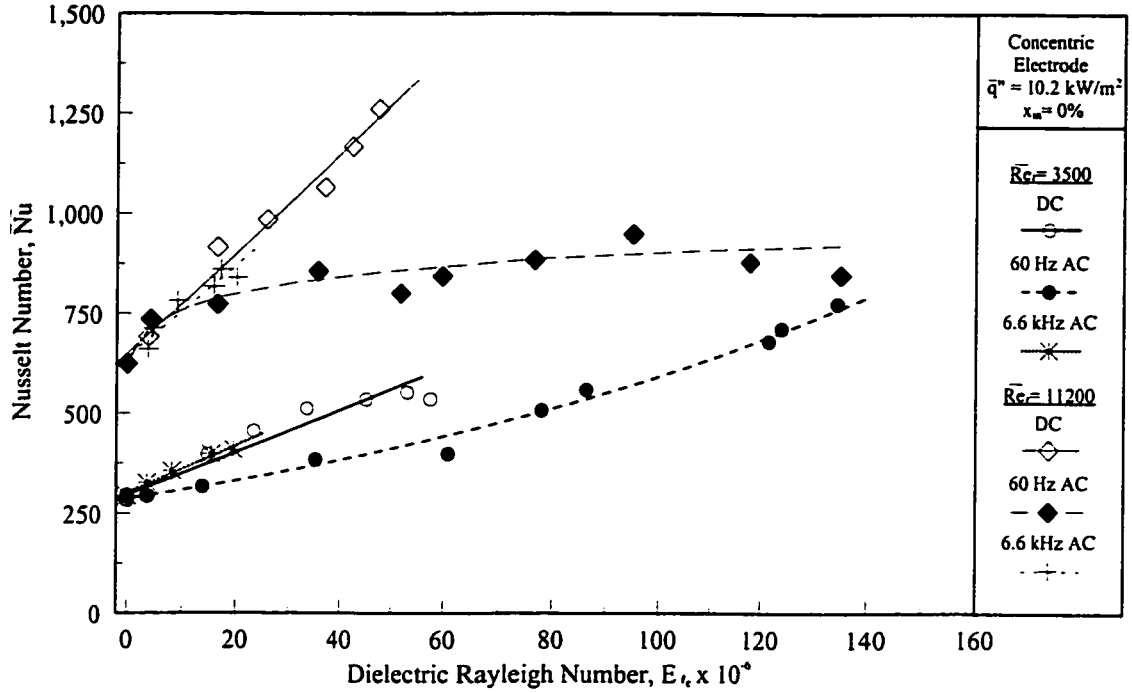

a) Nusselt Number vs. Dielectric Rayleigh Number

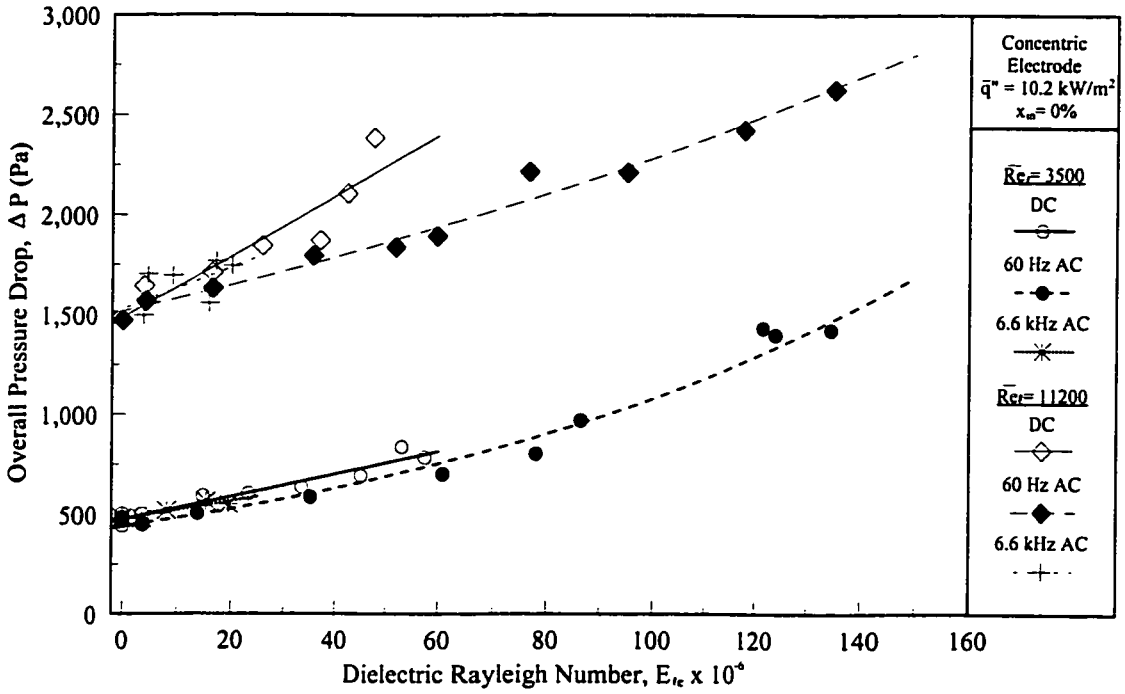

b) Overall Pressure Drop vs. Dielectric Rayleigh Number

Figure 7.17: The Effect of the DC & AC Dielectric Rayleigh Numbers (based on the AC voltage amplitude) on the a) Average Nusselt Number and b) Overall Pressure Drop at a Fixed Heat Flux and Inlet Quality for different Reynolds Numbers.

Conversely, experimentation with the 60 Hz AC power supply has led to the observation of a regime that may have never been encountered previously and a heat transfer and pressure drop change considerably different from the DC conditions investigated. As mentioned in Chapter 5, the exit observations reveal an oscillatory flow, where droplets as large as 2 mm in diameter were entrained in a vapour core surrounded by an annular liquid film around the circumference of the tube and electrode similar to a multi-layered annular flow. The droplets oscillated vertically in the lower portion of the annulus at a frequency of approximately 120 Hz, occasionally being absorbed by the inner or outer annular film. In addition to the droplet formation, small spouts or jets of liquid were observed on the upper half of the annular film surrounding the electrode. These spouts seemed to form randomly on the crest of a wave created by interfacial instabilities present in the liquid film around the electrode and would spray a fine mist into the upper portion of the vapour core, as depicted schematically in the top image in Figure 5.4. The size of the droplets, intensity of motion, rate of deposition and the occurrence of spouts were highly dependent on the amplitude of the 60 Hz applied voltage and the flow conditions under investigation. The interaction between the phases and the extremely high interfacial area created when coupled with the increased turbulent mixing created by the oscillatory motion of the flow, led to significant increases in the Nusselt number (~ 300%) and overall pressure drop when applied under the appropriate conditions as shown in Figure 7.17.

From comparing Figures 7.17a and 7.4a, a significant advantage of applying low frequency AC electric fields becomes apparent, considerably higher voltage amplitudes may be applied without electrical breakdown. As discussed in Appendix A, arcing occurred for the DC applied voltages at approximately 10 kV in both liquid and vapour states. Occasionally, the arcing occurred as low as 9 kV during phase change experiments, which

is believed to be the result of the flow regime within the annular gap. Therefore, the maximum applied DC voltage was established at 8 kV ($E_{te} \sim 50 \times 10^6$) in order to prevent arcing for all flows observed. Investigation of the effects of AC voltages reveals that the maximum voltage amplitude potential of the 60 Hz (0 - 25 kV peak to peak) power supply, V_i = 12.5 kV ($E_{te} \sim 130 \times 10^6$), could be applied to the electrode without breakdown. Consequently, the potential to apply large voltages creates higher interfacial forces and should result in a large influence on the flow.

As with the case of the DC voltage potential experiments discussed in Section 7.2.1, the general trend in the heat transfer coefficient and pressure drop is an augmentation with increasing voltage levels. However, the best fit curves do not suggest a linear relationship between pressure drop and Nusselt number as observed with the DC and 6.6 kHz AC experiments. Further, the 60 Hz heat transfer results are lower than the DC results when comparing their dielectric Rayleigh numbers calculated using the voltage amplitude of the AC waveforms. The difference between the 60 Hz experiments and the DC results, discussed in the previous section, is speculated to be a function of the voltage frequency. The frequency of the vertical droplet fluctuations, determined through high speed video imagining ~ 120 Hz, corresponds to twice the frequency of the applied voltage $f \sim$ 120 Hz. As presented in Figure 7.18, this is approximately the frequency of the "on" and "off" dielectrophoretic body force that is developed at this voltage frequency as $f_{EB} \propto E^2$. The waveform of the electric field strength square, E^2, in Figure 7.18 is determined at the electrode surface of a single-phase fluid.

This pattern suggests that the fluctuations in the flow pattern are actually the continuous transition between flow regimes due to the approximate "on/off" electric field applied to the electrode. It is postulated that the resultant flow regime is the continuous

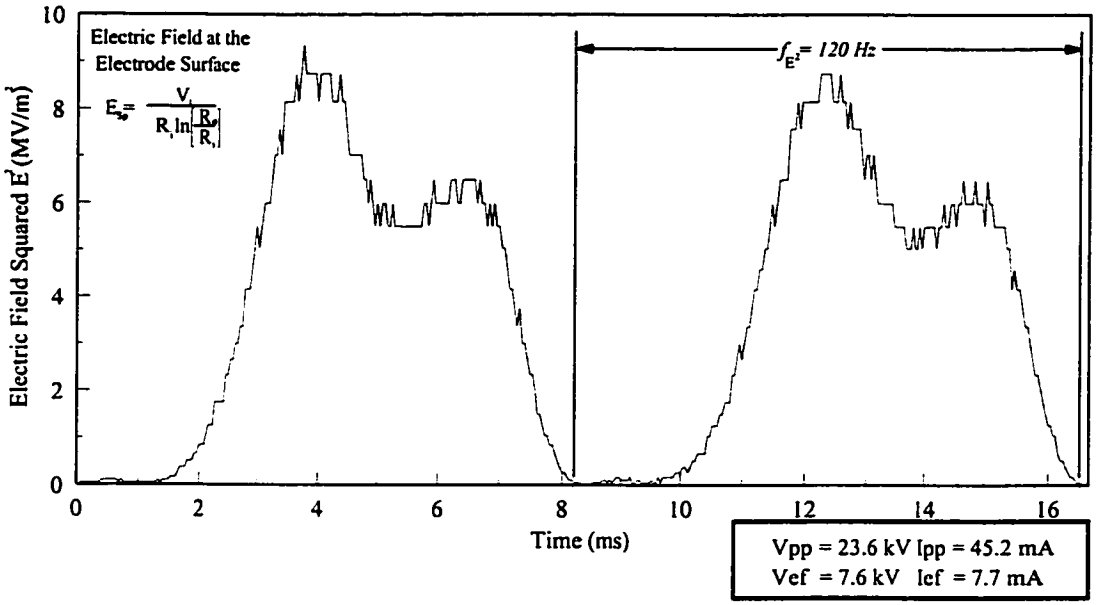

Figure 7.18: Time Trace of the Electric Field Squared for the 60 Hz Power Supply.

construction and destruction of two separate flow regimes. For example, at $Re_l = 3500$ the flow pattern in the absence of the electric field is dominantly stratified flow and intermittent annular or entrained droplet flow at high applied voltage levels. Hence, the oscillatory-entrained droplet flow pattern is believed to be a result of the continuous flow pattern transition between these two regimes.

Also presented in Figure 7.17 is a comparison of the voltage effect at different Reynolds numbers. Similar to the DC experiments, under the influence of a 60 Hz AC electric field, the EHD forces must overcome the increasing momentum effects, the existing surface tension and gravity to produce a migration of the liquid as the mass flux (Reynolds number) increases. Even with the potential to apply higher voltage levels, the 60 Hz AC EHD forces did not dominate the flow at the high mass flux level, $Re_l = 11200$. As a consequence, for the high Reynolds number, the oscillatory motion observed at $Re_l = 3500$ was not observed at the exit of the channel. The result is a lower enhancement in heat transfer and a relative decrease in the pressure drop across the channel.

The following section discusses the quasi-local heat transfer performance of each AC frequency investigated and the local transient wall temperature and pressure drop traces at various 60 Hz AC voltage amplitudes. This will provide an understanding of the flow progression along the channel.

7.2.4 The Local Influence of an AC Electric Field

The local and transient analysis is presented in this section for the following conditions: $Re_f = 3500, x_{in} = 0\%$, and $q'' = 10.2\ kW/m^2$ at different AC voltage amplitudes. This is the experimental quasi-local 6.6 kHz and 60 Hz data, Figures 7.19 and 7.20 respectively, corresponding to the DC data presented in Figure 7.9. First, considering the 6.6 kHz AC experiments as shown in Figure 7.19, the similarity between the DC and high frequency voltages discussed in the previous section is evident. However, compared to the DC experiments, the overall performance results of the 60 Hz AC quasi-local data in Figure 7.20 show a considerably greater enhancement. As shown the 60 Hz data show a maximum enhancement of approximately 300%, with a local heat transfer enhancement over 500% above the case in the absence of an electric field, Test #59.

Through the inferences made in the previous sections, in the absence of the electric field as suggested by both dynamic measurements and flow mapping the dominant flow pattern is stratified wavy. Hence there is a significant difference in heat transfer coefficients from the top to the bottom of the tube. Like the DC voltage experiments, the local heat transfer coefficients increase with increasing 60 Hz voltage amplitude levels over the circumference of the tube. However, the effects on the bottom half of the channel are far greater than the upper half until the amplitude reaches approximately $V_i \sim 9$ kV. Again, by considering the interfacial forces as EHD is applied to the flow, the dielectrophoretic force can create instabilities on the interface resulting in a significantly more disturbed flow with

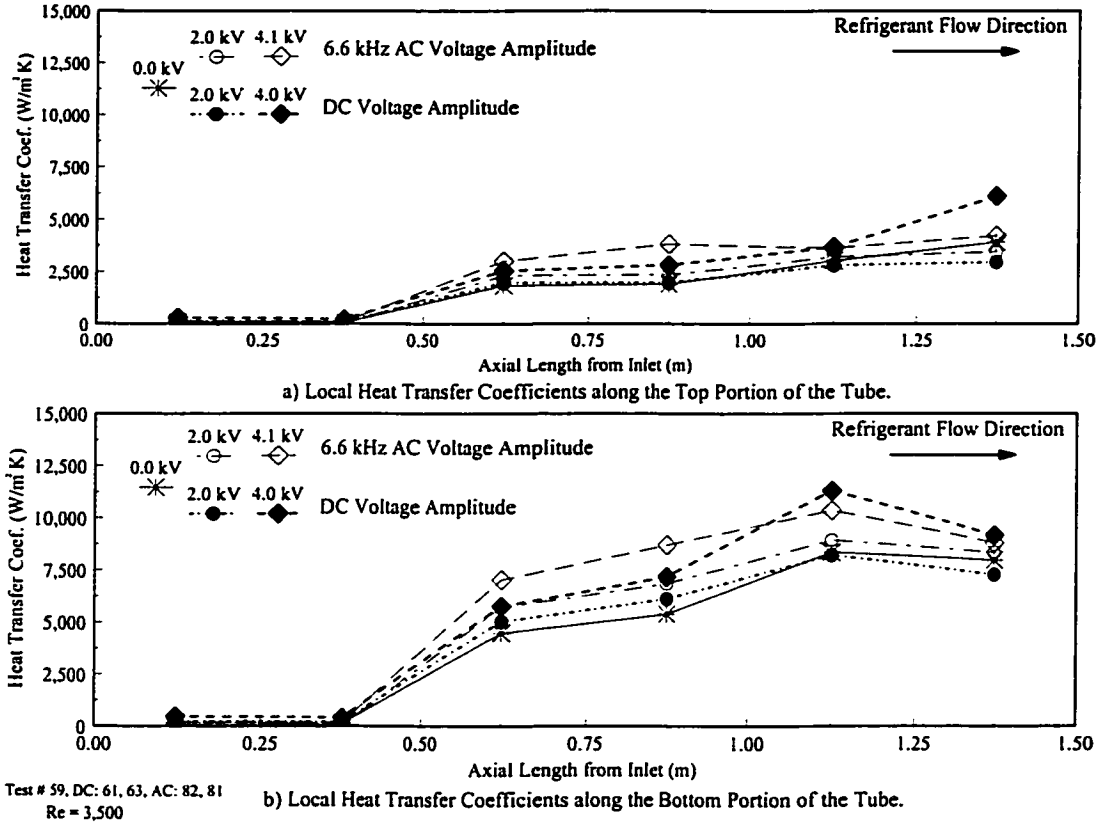

Figure 7.19: A Comparison of the Quasi-Local Heat Transfer Coefficients for the different DC and 6.6 kHz AC Voltage Amplitudes.

larger more frequent waves, which are expected to be amplified by the fluctuations of the alternating electric field. If the EHD effect becomes significant, then migration of the liquid may occur. So, when the liquid is attracted away from the stratified liquid layer towards the electrode against gravity, the result is a reduction in the liquid thickness on the bottom of the tube which is considered to be the mechanism of enhancement for the bottom heat transfer coefficients. At a voltage level of approximately V_i = 12 kV, the rate of heat transfer becomes more symmetric. Here, the predominant flow in the heat exchanger is believed to be the oscillatory-entrained droplet flow discussed above. This flow pattern is more complex and transitional than normal two-phase flow regimes, involving considerable phase interaction and interfacial area due to the vertical flow oscillations, large droplet entrainment and a liquid film encompassing the electrode. Hence, the considerable uniform heat transfer

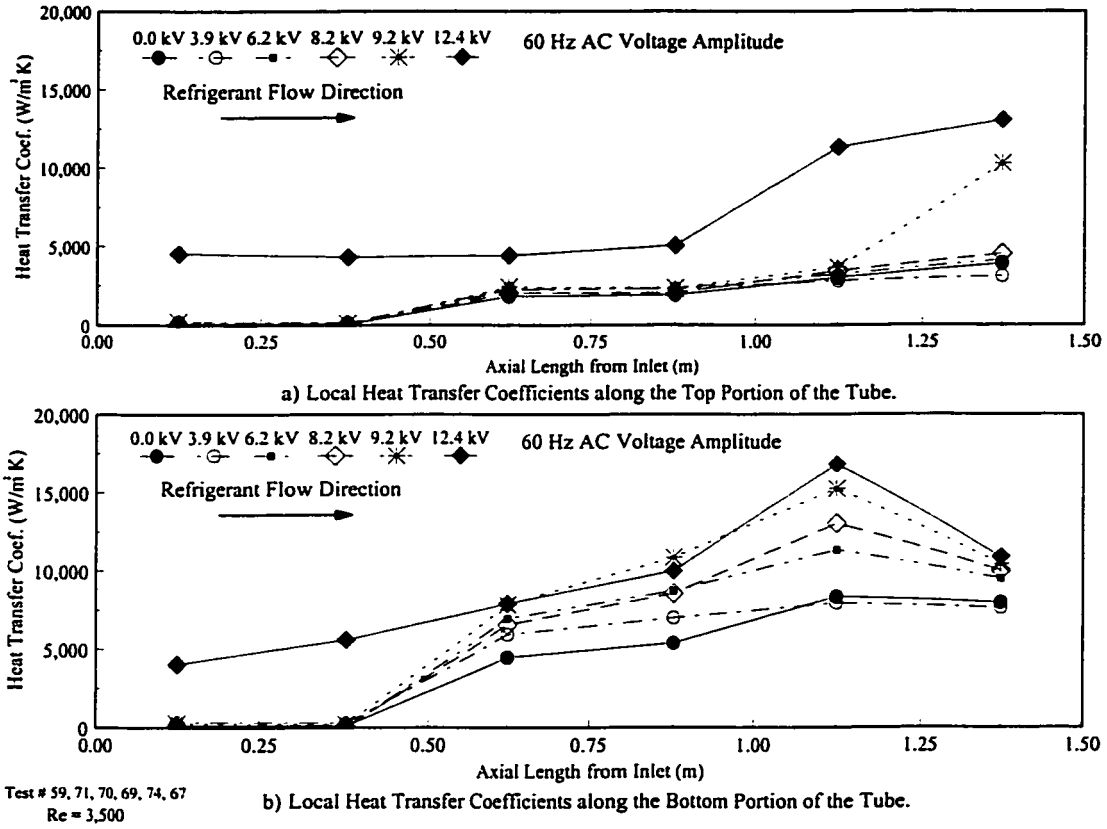

Figure 7.20: Quasi-Local Heat Transfer Coefficients with Increasing 60 Hz AC Voltage Amplitudes.

observed on the top and bottom of the channel. By examining the transient local temperature measurements, the apparent flow regime transitions are revealed in greater detail.

Wall Surface Temperature Profiles in the Presence of a 60 Hz Applied Electric Field

Figure 7.21a shows the time averaged axial superheat temperature profile for the same flow conditions as the DC section of this chapter for three 60 Hz AC voltage amplitudes (6.2 kV, 9.2 kV and 12.4 kV) and the 0 kV case, Test # 59 (as shown in Figure 7.10). Figure 7.21b shows the corresponding standard deviation of the surface temperature fluctuations.

The surface temperature plots at locations 1 through 6 in Figure 7.21a shows the application of a 60 Hz AC voltage decreases the wall superheat on both the bottom and top of the channel, while Figure 7.21b shows that wall temperature variation decreases

considerably with increasing voltage amplitude, diminishing towards a standard deviation within the range of white noise at each location for the maximum voltage potential V_i = 12.4 kV. The only exception to the decreasing fluctuation trend is the intermediate voltage potentials (V_i = 6.2 kV and V_i = 9.2 kV) at location 1. Here, temperature fluctuations on the upper surface increase with voltage until the upper limit of the power supply V_i = 12.4 kV is reach were the variation deceases and steady temperature measurement is again observed.

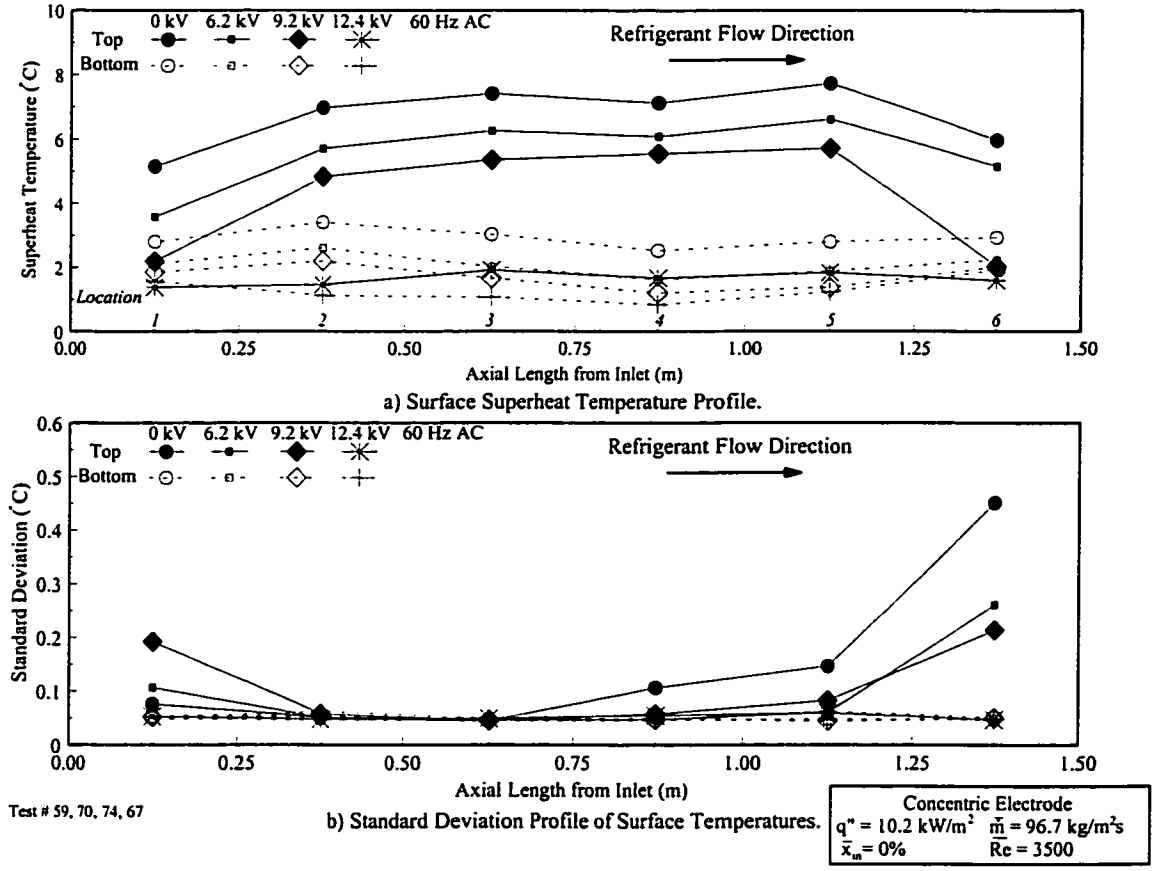

Figure 7.21: Time-Averaged Surface Superheat Temperature and Standard Deviation Profiles of the Concentric Electrode at Increasing Applied 60 Hz AC Voltage Amplitudes.

Similar to the suggested DC influences that increase the upper temperature variation at location 1, the migration, deformation and breaking of vapour bubbles in the flow are the main contributing factors augmenting bubble dynamics and consequently the wall

temperature variation. By combining the dynamic effects of the 60 Hz electric field strength variation with the various EHD effects on nucleate boiling discussed in Section 3.3.1, these influences are expected to be magnified, thereby increasing the temperature variations accordingly.

Downstream, (locations 2 to 6) the applied voltage level increases the interfacial electric force enhancing the momentum suction pressure effect, thereby attracting the liquid upwards. The liquid layer at the bottom becomes thinner which increases the degree of cooling on the bottom surface, causing the temperature of the wall to be lower. This effect is apparent from the measured increase of the heat transfer coefficients and the wall superheat temperature on the lower half of the tube, Figures 7.20a and 7.21a respectively. However, with the exception of location 6 at 9.2 kV, increasing the 60 Hz voltage amplitude only slightly decreased the upper superheat temperatures while the wall temperature fluctuations simultaneously decreased to a minimum. This is contrary to the effect of the DC voltage potentials, where the flow changes to a large amplitude wave flow or slug flow. Here the flow is more likely a considerably agitated stratified wavy flow, where the liquid is attracted as high as the electrode when the electric field is "on" and drops back when the field is "off" during a period of the electric field strength squared (E^2 frequency ~120 Hz as shown in Figure 7.18). The decrease in the top temperature is postulated to be either from an increased vapour circulation slightly increasing the heat transfer coefficient, Figure 7.20 or more from likely the entrainment of small liquid droplets from the agitated waves creating a fine mist that continuously impinges the upper surface.

The top and bottom wall temperature measurements are almost identical both at location 6 for the 9.2 kV voltage potential and at each axial location when the maximum voltage potential, 12.4 kV. Consequently, the quasi-local heat transfer values are relatively

uniform around the circumference of the tube at these locations. This implies a circumferentially uniform flow regime has developed because of the fluctuating electric field. The time traces of surface temperature are more instructive in determining the EHD effect on flow pattern. Figures 7.22 to 7.24 show the time traces of temperature and pressure drop for the voltage amplitudes 6.2 kV, 9.2 kV and 12.4 kV.

For the two intermediate AC voltage amplitudes in Figures 7.22 and 7.23, the deviation of the temperature trace from the traces in the absence of an electric field, Figure 7.11 is minimal. Accordingly, a flow pattern transition has apparently not occurred at these potentials and the differences in the superheat temperatures and standard deviation of the wall temperature traces are due to the EHD effects discussed above. The only significant difference is at location 6, 12.5 mm upstream of the exit of the heated section. Here, the top wall temperature has decreased drastically to approximately the temperature measured at location 1. As shown in Figure 7.21a, the temperature is approximately the same as the bottom measurement. As mentioned above, the flow pattern is believed to be circumferentially uniform around the tube and with the support of high speed video imaging at the exit viewing window, this regime was identified as the oscillatory-entrained droplet flow pattern, described in Chapter 5.

Increasing the voltage amplitude above approximately 10 kV results in a significant change in the transient wall temperatures as shown in Figure 7.24. Applying V_i = 12.4 kV decreases the wall superheat to a point where the channel temperature is almost uniform, both axially and circumferentially. The upper half of the channel decreased by approximately 5°C and the lower half of the channel by about 2°C below the base case Test #59. Further, the temperature fluctuations are all within the band of white noise. Similar to the previous voltage level, the exit flow regime observed visually was the oscillatory-

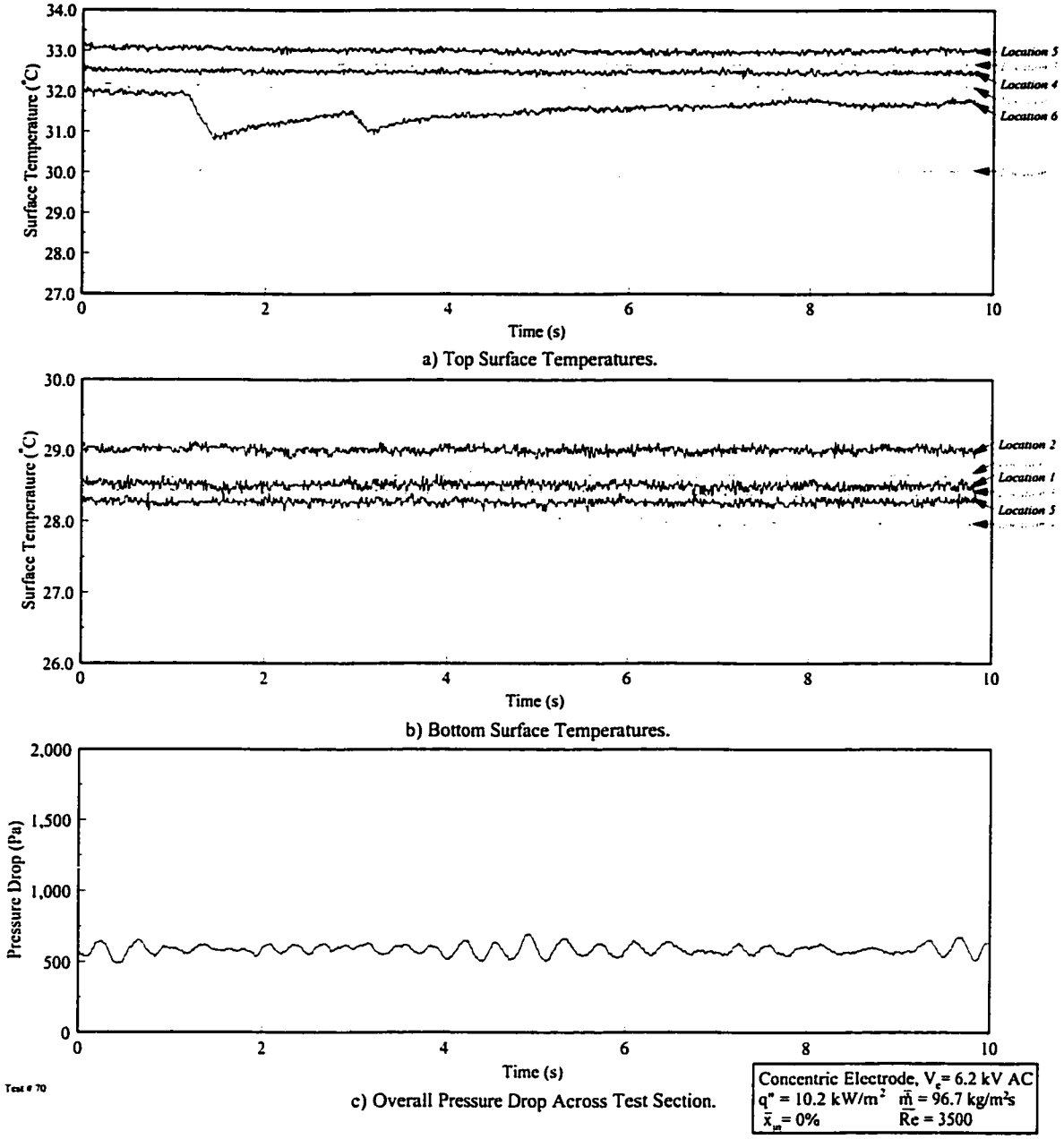

Figure 7.22: Time Trace of Surface Temperature and Pressure Drop of a Concentric Electrode at an Applied Voltage Amplitude of V_i = 6.2 kV 60 Hz AC.

entrained droplet flow pattern. Based on the homogeneity of the surface temperatures, the oscillatory-entrained droplet flow has developed throughout the entire heat exchanger, with the exception of possibly location 1, where the quality is quite low $x \leq 4\%$. At location 1, the flow is similar to the flow observed at the highest DC cases, dispersed bubble flow as depicted in Figure 7.16.

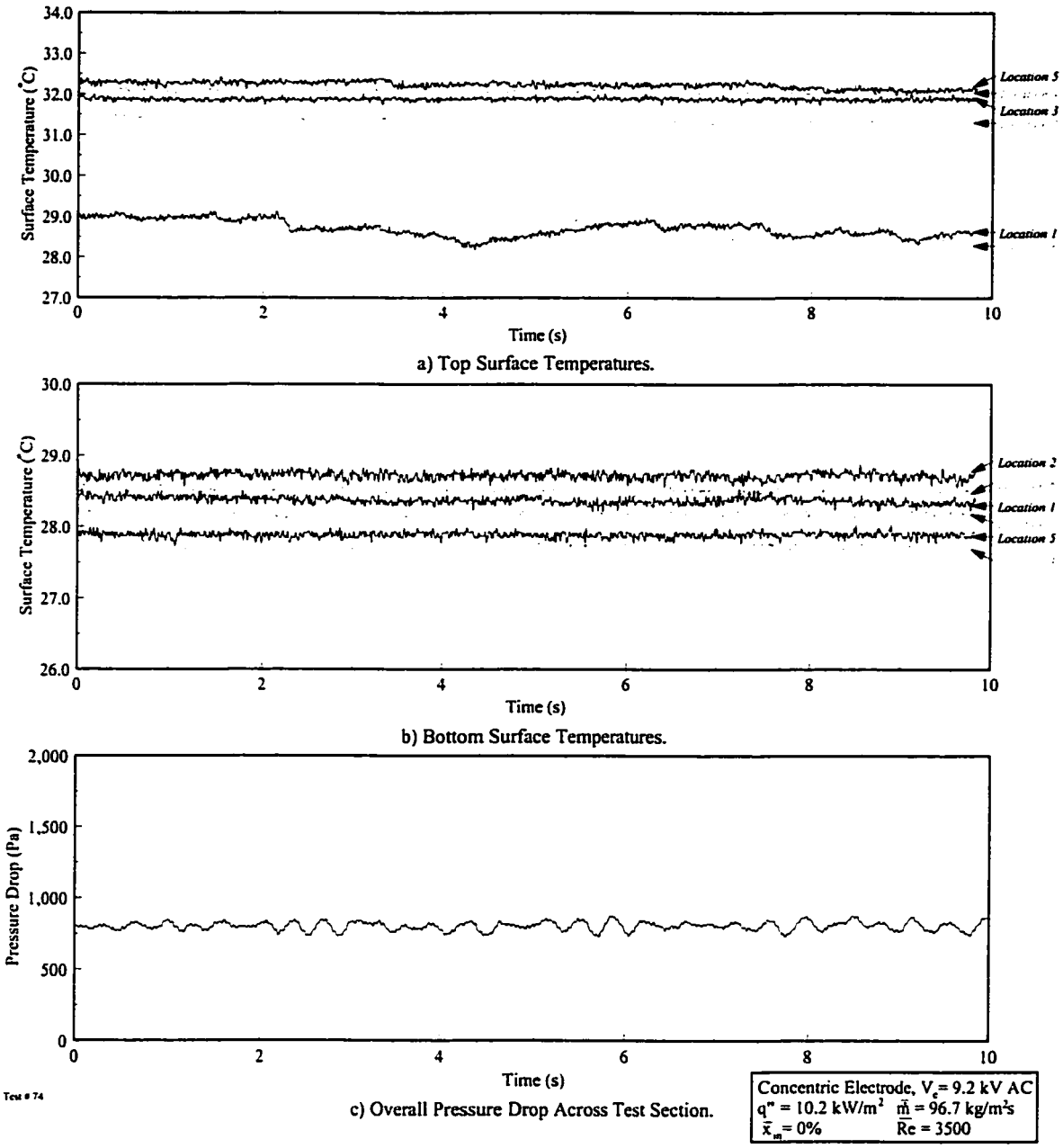

Figure 7.23: Time Trace of Surface Temperature and Pressure Drop of a Concentric Electrode at an Applied Voltage Amplitude of V_i = 9.2 kV 60 Hz AC.

The complex nature of the oscillatory flow pattern results in an augmentation in both phase interaction and interfacial area from the vertical flow oscillations, the large droplet entrainment and the liquid film encompassing the electrode. A uniform rate of heat transfer emerges in Figure 7.20 because of the apparent symmetry in the prevailing flow pattern, as observed through high speed photography. The increase in radial and vertical flow, phase

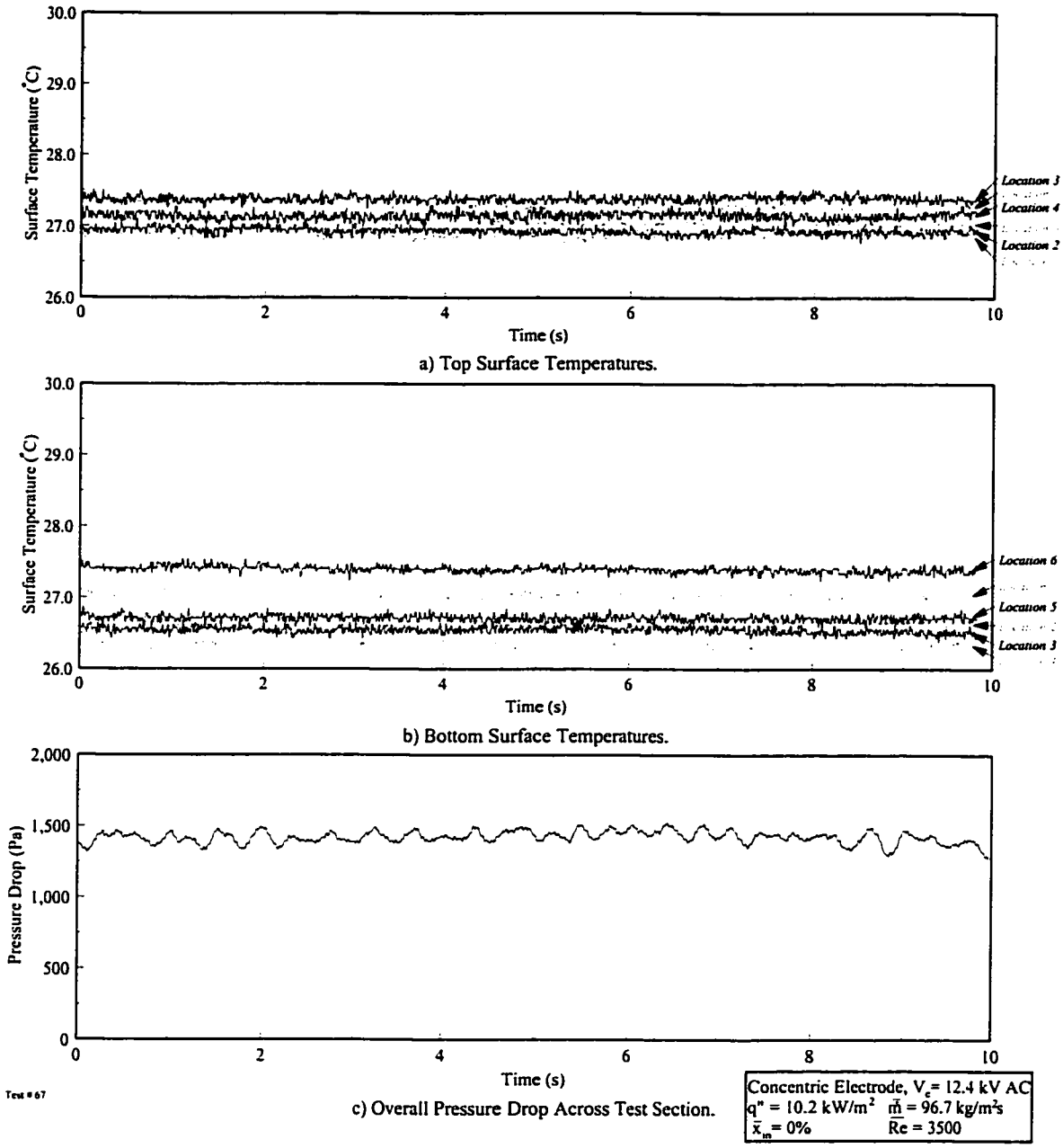

Figure 7.24: Time Trace of Surface Temperature and Pressure Drop of a Concentric Electrode at an Applied Voltage Amplitude of V_i = 12.4 kV 60 Hz AC.

interaction, interfacial area and wetted surface area contact is also evident in the pressure drop traces, Figures 7.23c and 7.24c, being almost three fold. However, unlike the large fluctuations observed for DC voltage, the pressure differential traces at high amplitude AC voltages is rather smooth with a maximum standard deviation of only ± 40 Pa. The smooth, non-structured instantaneous measurements corresponds to the inferences made through the

temperature measurements that the flow pattern does not exhibit a coherent structure like the large amplitude wavy flow / slug flow postulated in the DC voltage experiments. The schematics of the proposed flow pattern reconstruction both in the absence of an electric field and at increasing 60 Hz AC applied voltages is presented in Figure 7.25.

In summary, the interfacial dielectrophoretic forces created by the application of a AC voltage to the electrode develop an oscillatory flow regime, different from any encountered in previous investigations. Based on visual observation, these oscillations in the flow pattern are suspected to be the continuous transition between flow regimes due to the approximate "on/off" electric field applied to the electrode. The resultant flow regime is postulated to be the continuous construction and destruction of two flow regimes, the two flow regimes being stratified wavy and possibly a large amplitude wavy flow or dispersed droplet flow. The interaction and interfacial area of this phase was extremely high, which, when coupled with the increased turbulent mixing created by the oscillatory motion of the flow, led to significant enhancements in heat transfer under the appropriate conditions.

7.3 Current and Voltage Characteristics

The current and voltage characteristics for the concentric electrode refrigerant evaporator channel are presented for the DC and AC experiments in this section. The DC current is measured directly using the 0 - 25 μA analog current meter. However, due to the highly dielectric nature of refrigerant HFC-134a, the current levels are very low, so that the reliability of the reading is poor. In general, the DC current measurements are slightly lower than those measured by Singh (1995), although both investigations present similar trends. The AC current was measured with a wide band current transformer and was recorded with a 200 MHz digital oscilloscope. Figures 4.6 and 4.7 show typical current and voltage

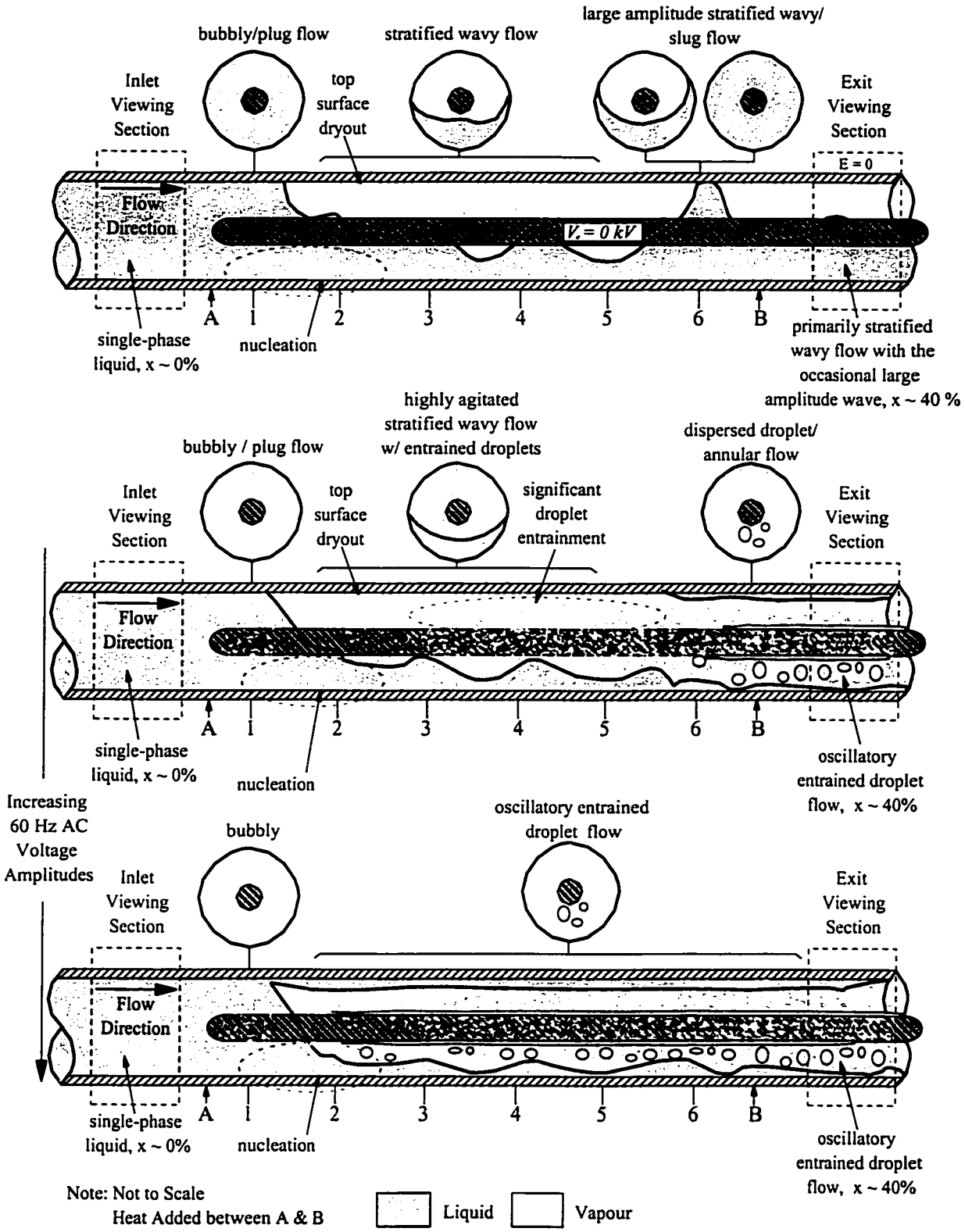

Figure 7.25: Proposed Reconstructed Flow Pattern from Surface Temperature and Pressure Drop Traces and Inlet and Outlet Flow Regime Observations for Increasing 60 Hz AC Voltage Amplitudes ($\dot{m}$ = 100 kg/m^{2}s, q'' = 10.2 kW/m^2 & x_{in} = 0%).

waveforms for the low and high frequency AC power supplied in the concentric electrode arrangement. The power associated with the AC current and voltage requires an evaluation of their *effective* values, as which is presented in Appendix D.

The experimental flow DC current-voltage characteristics are presented in Figures 7.26 and 7.27. The AC data is presented in Figures 7.28 through 7.33 for the following flow conditions:

Heat Flux:	q'' = 10 kW/m^2	Heat Flux:	q'' = 10 kW/m^2
Mass Flux:	$\dot{m}$ = 100 kg/m^{2}s	Mass Flux:	$\dot{m}$ = 300 kg/m^{2}s
Inlet Quality:	x_{in} = 0%	Inlet Quality:	x_{in} = 0%

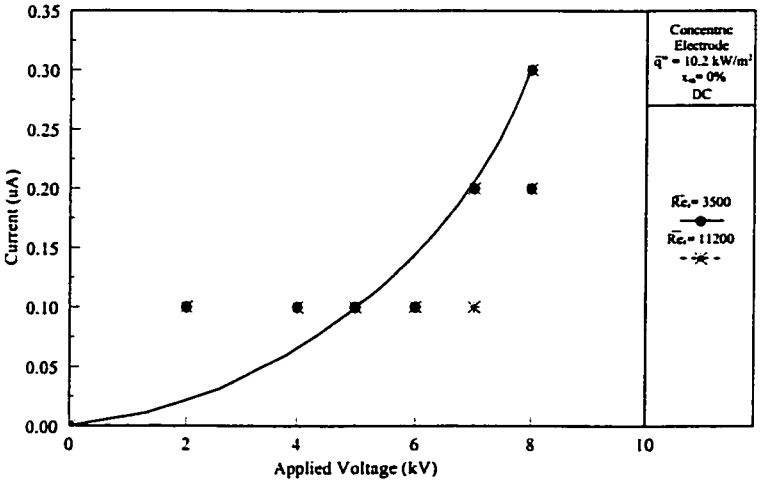

Figure 7.26: Current - Voltage Characteristics for DC Power Supply.

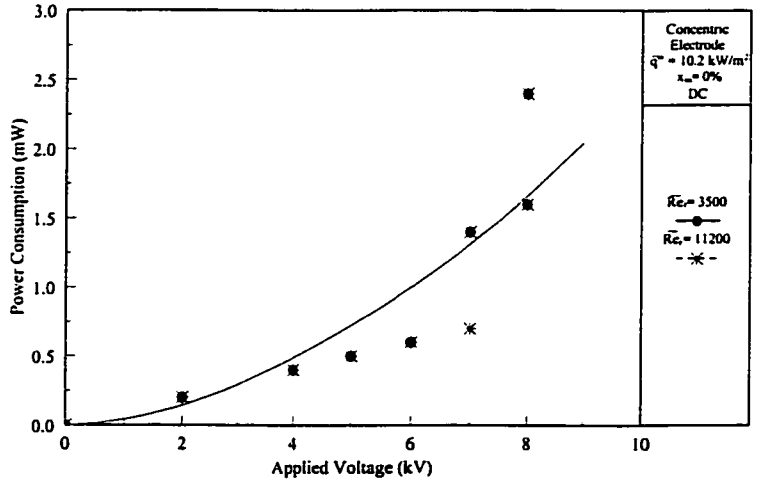

Figure 7.27: Effective Power Consumption vs Effective Voltage DC Power Supply.

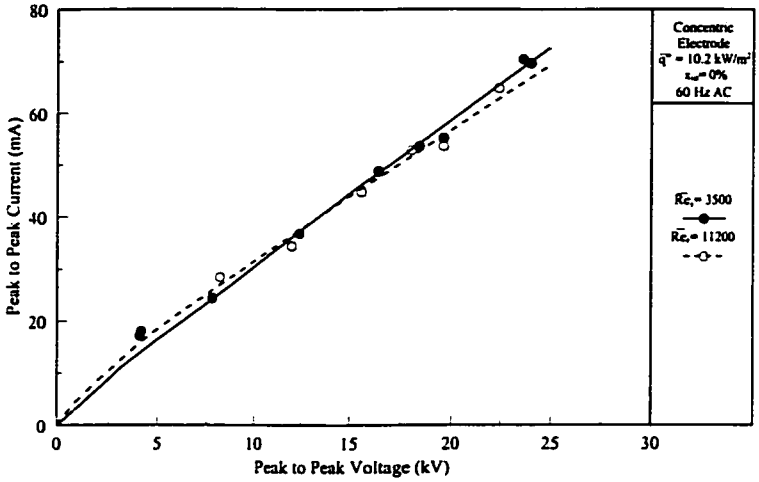

Figure 7.28: Peak to Peak Voltage - Current Characteristics for 60 Hz AC Power Supply.

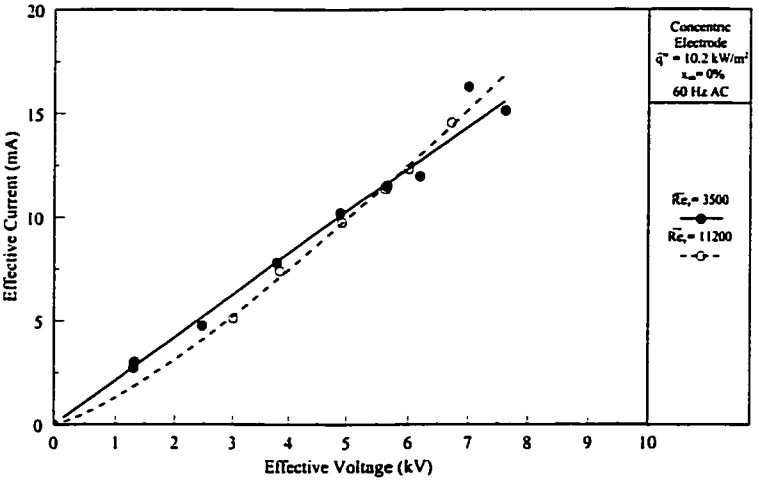

Figure 7.29: Effective Voltage - Current Characteristics for 60 Hz AC Power Supply.

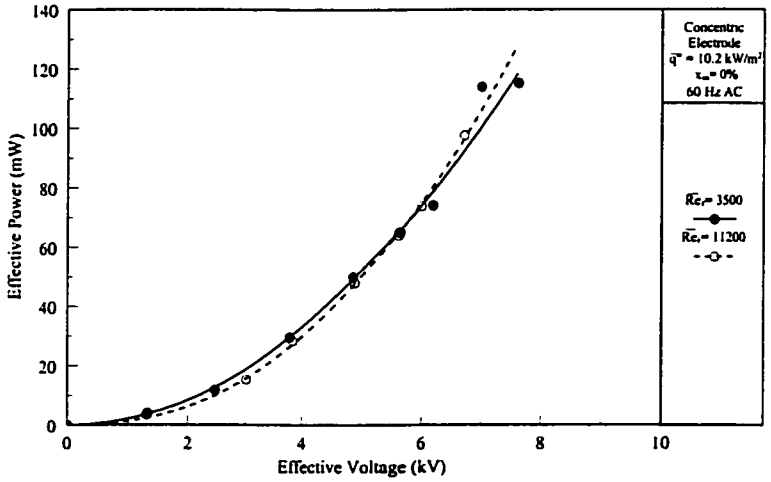

Figure 7.30: Effective Power Consumption vs Effective Voltage for 60 Hz AC Power Supply.

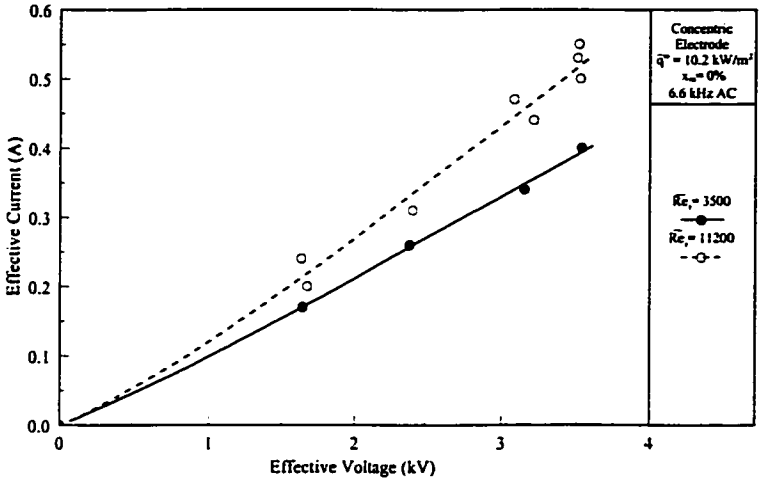

Figure 7.31: Effective Voltage - Current Characteristics for 6.6 kHz AC Power Supply.

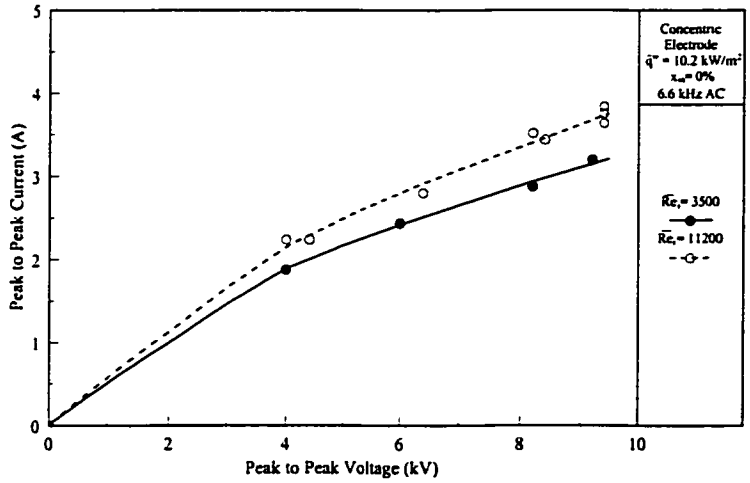

Figure 7.32: Peak to Peak Voltage - Current Characteristics for 6.6 kHz AC Power Supply.

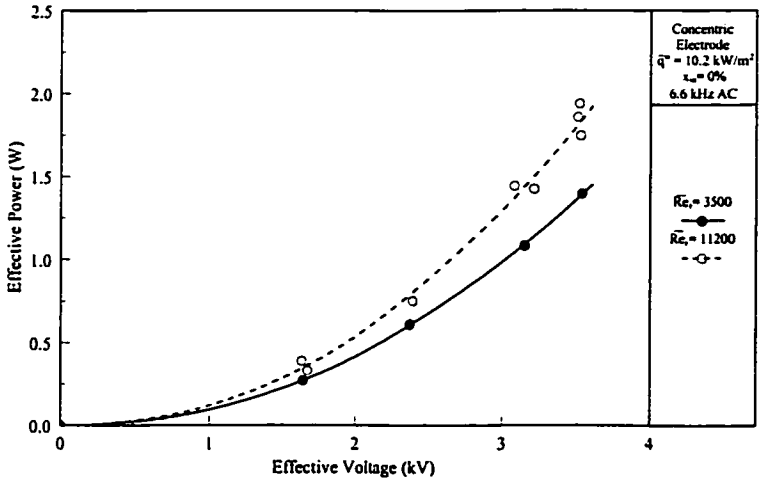

Figure 7.33: Effective Power Consumption vs Effective Voltage for 6.6 kHz AC Power Supply.

For each frequency, plots of the peak to peak, V_{pp}, and effective current voltage characteristics are shown with the effective power consumption of the EHD system. These Figures demonstrate the maximum EHD power consumption depends on the frequency of the applied voltage as the conductivity of HFC-134a increases with frequency. For the DC experiments, the maximum power was ~3 mW, while the two AC frequencies investigated, 60 Hz and 6.6 kHz, resulted in effective power requirements of ~0.1 W and 2 W, respectively. The power-voltage relationship is typical of a pure resistance behaviour and follows a square law form give as $P \propto V^2/R$, similar to Singh (1995) Although difficult to differentiate for the DC and low frequency AC experiments, the 6.6 kHz AC power-voltage characteristics clearly demonstrate the dependence of current flow on the mass flux of the refrigerant at a fixed heat flux and quality. The flow current increased with mass flux. This increase results from the lower average quality and void fraction of the refrigerant in the test section, as the electrical resistance of the liquid refrigerant is lower than the vapour refrigerant. Hence, the effective power consumption is lower at high test section void fractions since the liquid area contacting the electrode is smaller.

7.4 Summary

The evaporation results show the overall heat transfer coefficients may be increased by as much as 250% for an 8 kV DC applied voltage and approximately 300% for 24 kV (peak to peak) 60 Hz AC voltage in the concentric arrangement. The drawbacks are the power requirements of the voltage supply and the increase in pressure loss for the electrode arrangement. For the concentric electrode, the pressure drop across the heat exchanger increased 1.8 and 2.6 fold for the DC and 60 Hz AC at maximum heat transfer enhancement, respectively. The EHD power consumption was less than 3 mW for the DC experiments and

less than 0.2 W for the 60 Hz AC experiments. Locally, heat transfer coefficient enhancement in excess of 2000% has been observed. The results suggest under the experimental parameters investigated, enhancement increased with high electric fields and decreased with increased mass and heat fluxes. However, the primary mechanism of influence on both heat transfer and pressure drop is from the effect of the electric field distribution on the flow pattern.

The threshold for EHD flow was analyzed through dimensional analysis and it has been suggested the influences of EHD induced flow on a system become significant when the Dielectric Rayleigh number is of the same order of magnitude as the square of the liquid Reynolds number, $E_{t\varepsilon} \approx Re_l^2$. When the proposed dimensional criterion is satisfied, the EHD body forces can have a strong influence on the flow pattern within the channel as seen through the interpretation of the transient surface temperature, pressure drop and flow visualization results. A redistribution of the phases have been consequently deduced and the flow progression have been reconstructed to clearly show the effect of various flow configurations on both the heat transfer and the pressure loss of the system.

The next Chapter presents experimental results conducted for the eccentric geometry to provided evidence that a desired transition in flow regime may be achieved to positively influence heat transfer rates at significantly lower voltage levels and pressure drop penalties through the establishment of the appropriate electric field distribution .

Chapter 8

Eccentric Electrode Electrohydrodynamic Evaporator Experimental Results and Discussion

Based on the interdependence that exists between the observed flow regime and the electric field distribution, as demonstrated in the previous two chapters, the electric field distribution was determined for several alternative electrode configurations. The evaluation of the static electric field distribution was performed for various flow regimes, with the purpose of maximizing heat transfer rates by positioning the electrode eccentrically in the channel vertically offset ± 2.73 mm. The displacements were selected arbitrarily as the displacement of the electrode position is not expected to change the zero electric field heat transfer and pressure drop characteristics very much. However, it was expected that an electric field distribution of similar magnitude to the concentric case will occur initiating a phase migration at significantly lower voltage potentials. In addition, the interactions between phases were examined in a similar analysis to Chapter 7 by considering the effects of flow regime experimentally as they affect the average and local heat transfer coefficients, the overall pressure drop and the transient parameters.

8.1 The Effect of Electric Field Distribution on Flow Regimes in Eccentric Electrode Configuration

For the eccentric configuration, any liquid - vapour distribution is expected to result in a complex electric field distribution. For this reason, the numerical procedure developed

in Section 6.1 is required. For comparison purposes, the results of the validation conditions in Figures 6.8 and 6.13 for annular flow (t_L = 0.85 mm) at 25°C with a 8.0 kV voltage applied to the concentric electrode arrangement, are presented for the eccentric geometries in Figures 8.1 to 8.4 at 2.0 kV. As shown in Figures 8.1 to 8.4, the electric field distributions are no longer symmetric over any angular position, contrary to the results for the concentric channel.

Two plots are required to describe the established field strength distribution and the electric field vector direction, a field strength distribution plot and a plot of the voltage gradient vectors, as described in Chapter 6. Aside from the different orientation, the electric field distribution for the two electrode configurations is identical in annular flow. First, consider the lower electrode eccentric position, -2.73 mm below the tube centerline. Although the difference in the liquid and vapour electric field gradient are obvious from the plot of the voltage gradient in Figure 8.1, Figure 8.2 gives a global picture of the variation in electric field strength. In the liquid phase, the electric field strength ranges from approximately 300 kV/m to ~0 kV/m while in the vapour phase, a significant deviation in the field strength exists from 5,000 kV/m directly below the electrode and 1,000 kV/m above the electrode to ~200 kV/m at the top of the channel. Comparing these values to the concentric configuration in Chapter 6, the differences in field strength magnitudes for the two phases are approximately the same even with a four-fold decrease in applied voltage. Consequently, the magnitude of bulk and interfacial electric forces are expected to be of the same order of magnitude as the electric forces observed in the concentric arrangement.

For the complex distribution presented in the above figures, an accurate description of the change in the liquid and vapour orientation is extremely difficult. However, several qualitative observations are discernible. An order of magnitude difference in the field

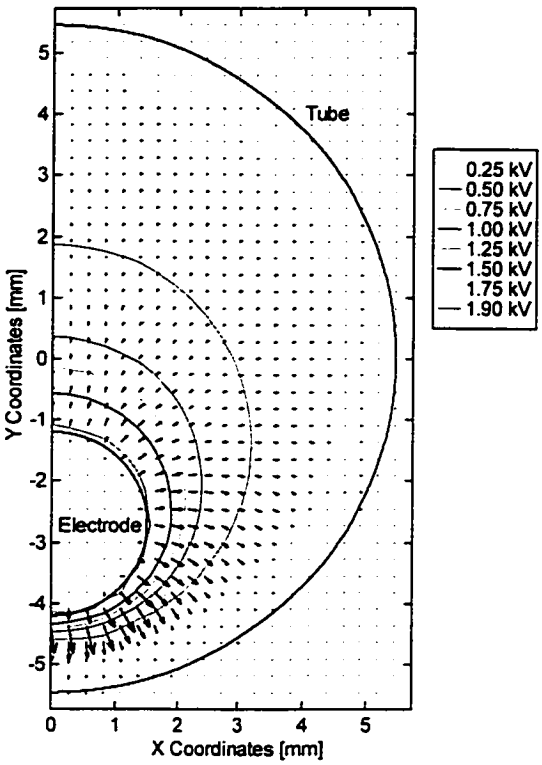

Figure 8.1: Voltage Contour and Gradient for Annular Flow, Liquid Thickness $t_L = 0.85\ mm$, (Electrode -2.73 mm from Centerline).

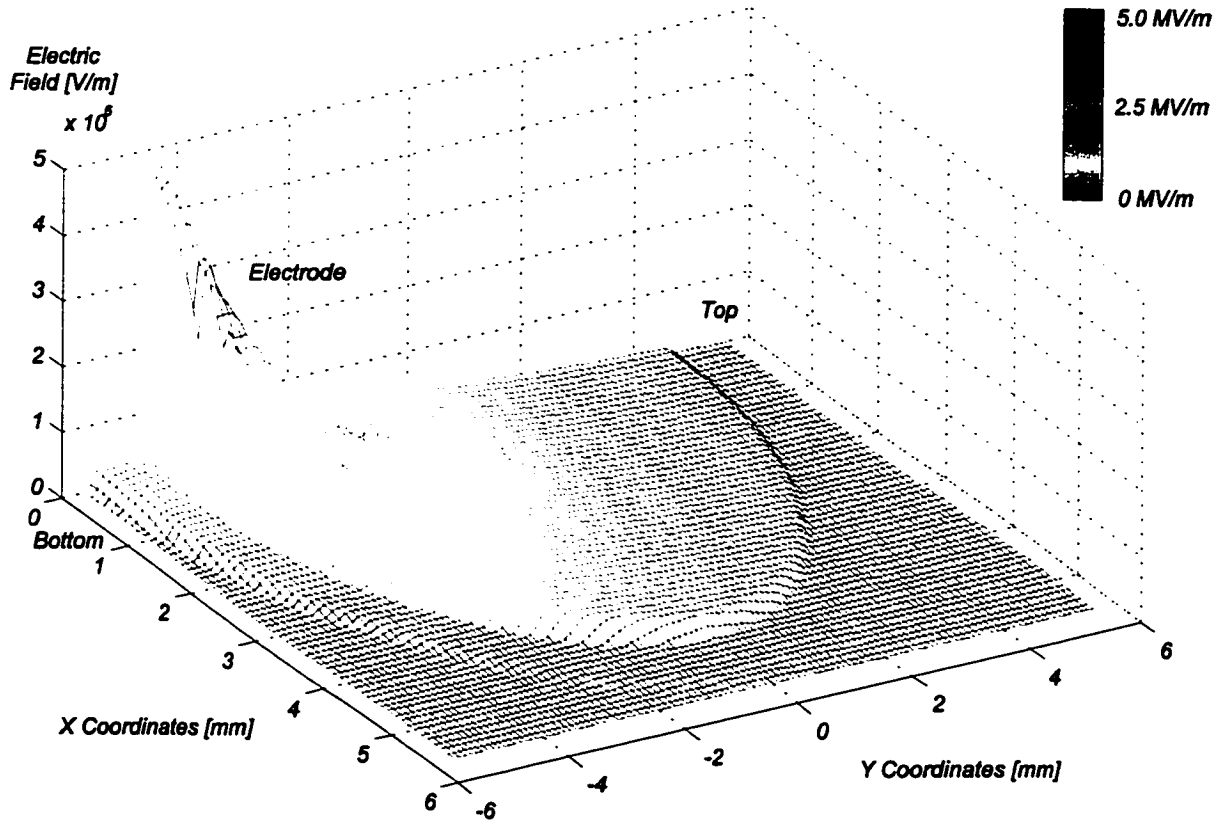

Figure 8.2: Electric Field Distribution of an Eccentric Electrode (-2.73 mm from Centerline) for Annular Flow, Liquid Thickness $t_L = 0.85\ mm$.

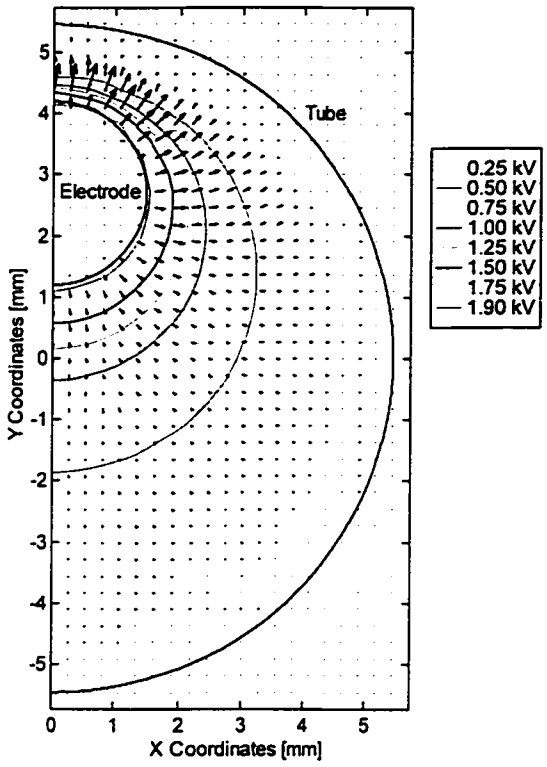

Figure 8.3: Voltage Contour and Gradient for Annular Flow, Liquid Thickness $t_L = 0.85$ *mm*, (Electrode +2.73 mm from Centerline).

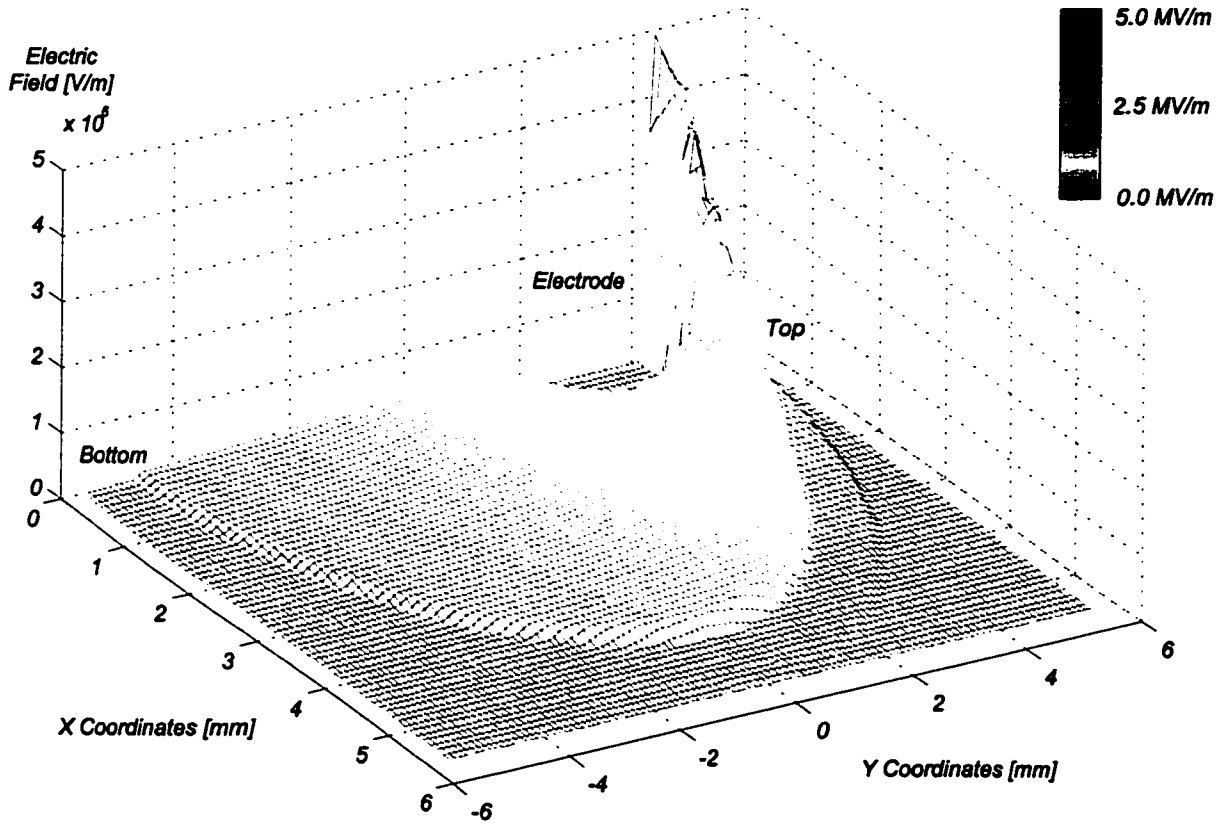

Figure 8.4: Electric Field Distribution of an Eccentric Electrode (+2.73 mm from Centerline) for Annular Flow, Liquid Thickness $t_L = 0.85$ *mm*.

strength may be observed at the liquid-vapour interface below the electrode. This nonuniformity would create an attractive force that draws the liquid, having higher permittivity, toward the region of higher electric field strength in the vapour. A similar effect is observed around the circumference of the liquid-vapour interface but the forces acting on the interface are expected to be smaller, due to the considerably lower strength in the vapour at higher vertical elevations. The net effect is an attractive force acting across the entire interface, pulling the liquid towards the electrode and consequently the lower half of the channel. By extracting liquid from the liquid annulus towards the electrode or into the vapour core in the form of droplet entrainment, the temperature gradient inside the annulus film is believed to increase to enhance interfacial vaporization and heat transfer.

The primary difference between the two eccentric configurations in the annular flow regime is the direction of the strongest interfacial electric force. For the upper eccentric electrode configuration, where the electrode is position +2.73 mm vertically from the centerline, the greatest forces are working with gravity to pull the liquid downwards, while the liquid at the bottom of the channel is attracted against gravity for the lower eccentric configuration. In general, both effects tend to attract the liquid away from the tube and into the vapour core, likely in the form of entrained droplets. However, due to the typical distribution in annular flow (*ie.*, dispersed vertically due to gravitational influences as discussed in Chapter 5), there is a greater potential for dryout of the upper surface when the electrode is positioned vertically upwards. Therefore, a reduction in heat transfer may be observed on the top of the channel in the upper eccentric position.

When the electric field is calculated for stratified flow, as with the concentric case, the radial distribution depends on the angular position. However, unlike the different categories at the different liquid levels in Chapter 6, the eccentric geometries have similar

electric field distributions, regardless of the amount of liquid in the system. Therefore, a qualitative assessment based upon the interaction between the electric field and possible flow reorientation can be explained though examination of one liquid level. For the lower eccentric configuration, a liquid level of $h_L = 8.19$ mm was selected as shown in Figures 8.5 and 8.6. A level of $h_L = 4.44$ mm was selected as shown in Figures 8.7 and 8.8, for the upper eccentric electrode placement. Appendix C presents three other liquid levels for each class of effects in Chapter 6 (below, in contact with and above the electrodes) for each eccentric configuration. The liquid levels presented in Appendix C illustrate similarity in electric field distributions of an eccentric electrode geometry.

When considering the lower electrode position, the electric field distribution is not very different from the single-phase case. The electric field strength is greatest in the vicinity of the electrode and decreases with increasing elevation. Further, the difference in field strength between the liquid and vapour phases slightly below and above the interface, Figure 8.6, is negligible. Consequently, there is unlikely to be a significant vertical force acting across the entire interface so that a flow regime transition is not expected as the bulk of the liquid resides within the most intense field region. The only exception to this distribution occurs when the liquid level is below the bottom surface of the electrode (see Figure C.7). For this range small range of liquid levels, the liquid is expected to be attracted upwards until it contacts the electrode. Upon the migration of liquid toward the electrode, the electric field distribution becomes similar to the distribution observed in Figure 8.6. As a result any further change in the flow pattern will likely be negligible.

Conversely, when the electrode is positioned +2.73 mm above the centerline, the impact of the electric field distribution is expected to influence phase migration significantly when the flow is originally stratified. In this electrode configuration, the liquid extraction

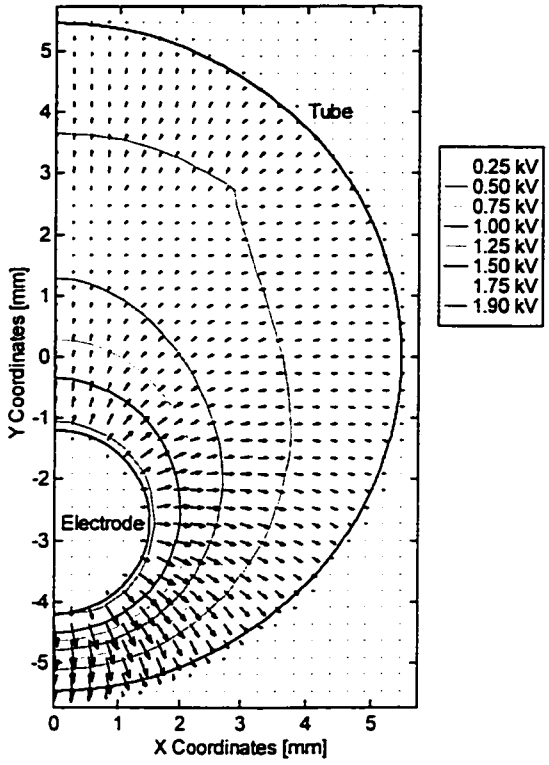

Figure 8.5: Voltage Contour and Gradient for Stratified Flow, Liquid Level $h_L = 8.19$ *mm*, (Electrode -2.73 mm from Centerline).

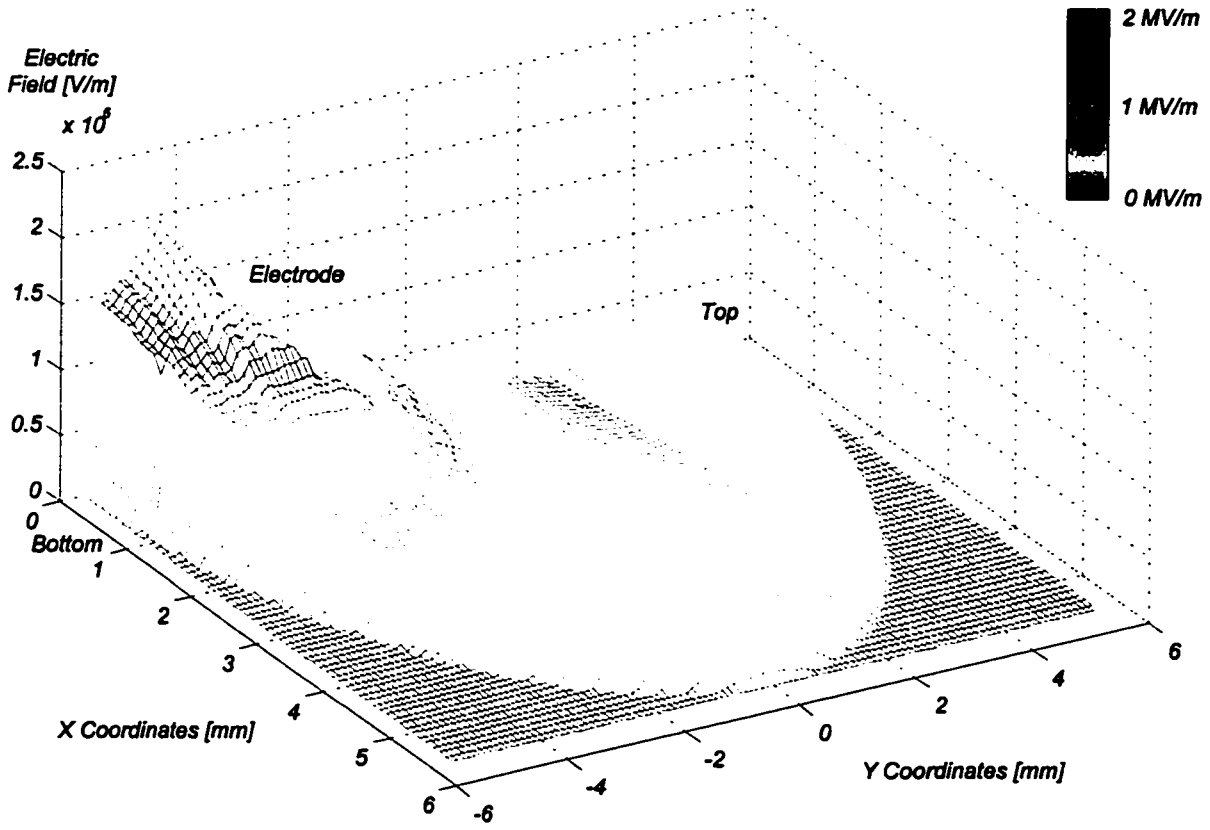

Figure 8.6: Electric Field Distribution of an Eccentric Electrode (-2.73 mm from Centerline) for Stratified Flow, Liquid Level $h_L = 8.19$ *mm*.

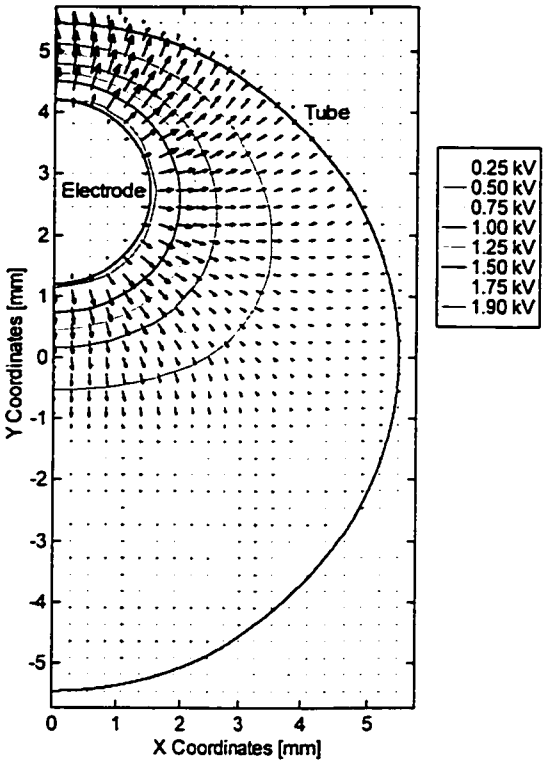

Figure 8.7: Voltage Contour and Gradient for Stratified Flow, Liquid Level $h_L = 4.44\ mm$, (Electrode +2.73 mm from Centerline).

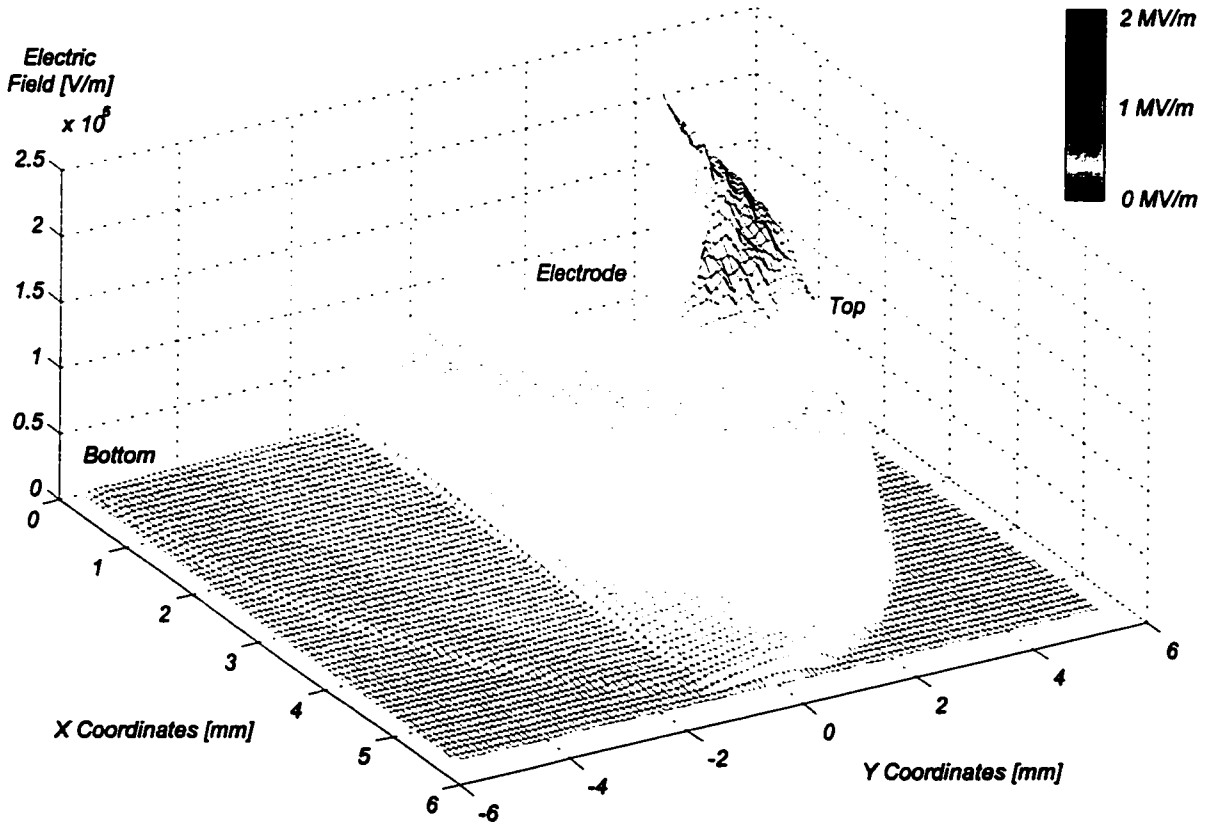

Figure 8.8: Electric Field Distribution of an Eccentric Electrode (+2.73 mm from Centerline) for Stratified Flow, Liquid Level $h_L = 4.44\ mm$.

influences observed in the concentric configuration at liquid levels below $h_L = 3.87$ mm are expected to influence the flow in the upper eccentric channel for liquid levels as high as $h_L = 6.23$ mm. These influences are discussed in Sections 6.2 and 6.3. By comparing Figures 8.6 and 6.15, the similarity of the interfacial electric field distribution becomes apparent. Although slightly lower in magnitude, the difference in electric field strength between the field slightly above and below the liquid-vapour interface is of the same order of magnitude as that developed in the concentric electrode channel. Accordingly, the self-propagating mechanisms inducing a flow pattern transition, discussed in Section 6.4, apply for the upper eccentric channel with a transition likely observed from stratified flow to intermittent or annular flow. Experimentally, both eccentric configurations have been explored to confirm these qualitative interpretations of the electric field distribution. They are the focus of discussion for the remainder of the chapter.

8.2 Heat Transfer and Pressure Drop Results

This section presents the parametric investigation of the eccentric electrode evaporator channels with and without EHD. The focus of the experimental results is a condensed version of Chapter 7 for the purpose of identifying the heat exchanger performance using the quasi-local method of determining the overall heat transfer coefficient.

Prior to establishing the influence of the electric field as it affects the flow pattern for the eccentric arrangements, the effect of displacing the electrode in the absence of the field is discussed. Figures 8.9 and 8.10 present the effect of moving the electrode vertically ±2.73 mm from the concentric case in Chapter 7 at different mass fluxes and inlet qualities. The observations for the eccentric geometries are similar to the heat transfer and pressure

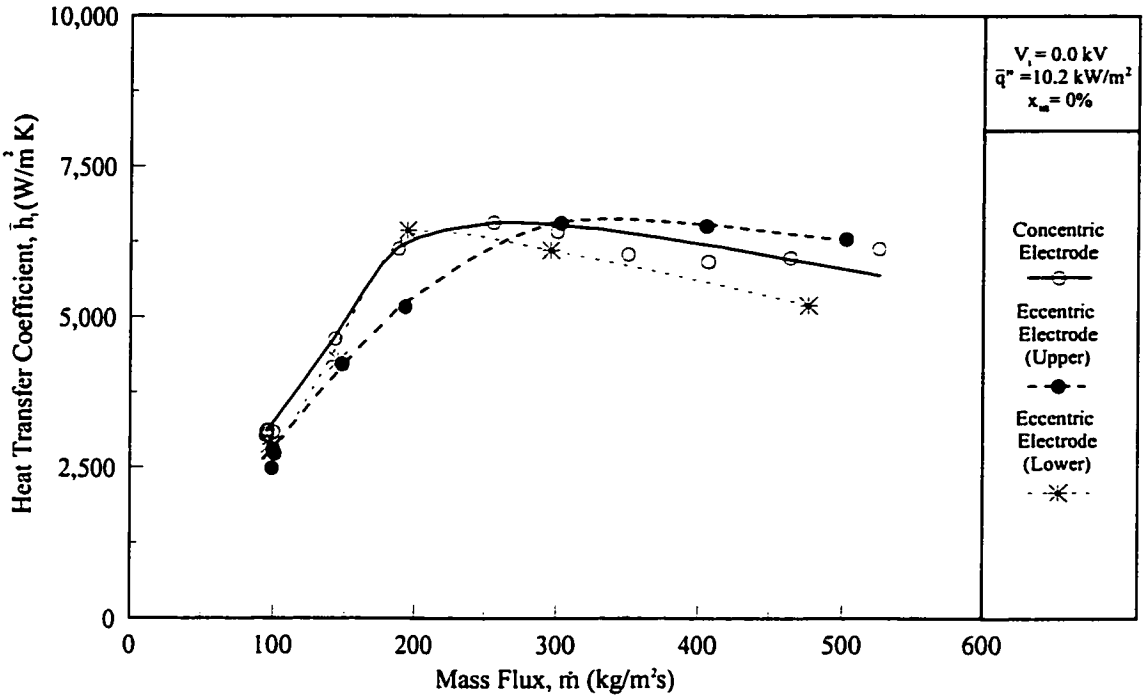

a) Heat Transfer Coefficient vs. Mass Flux

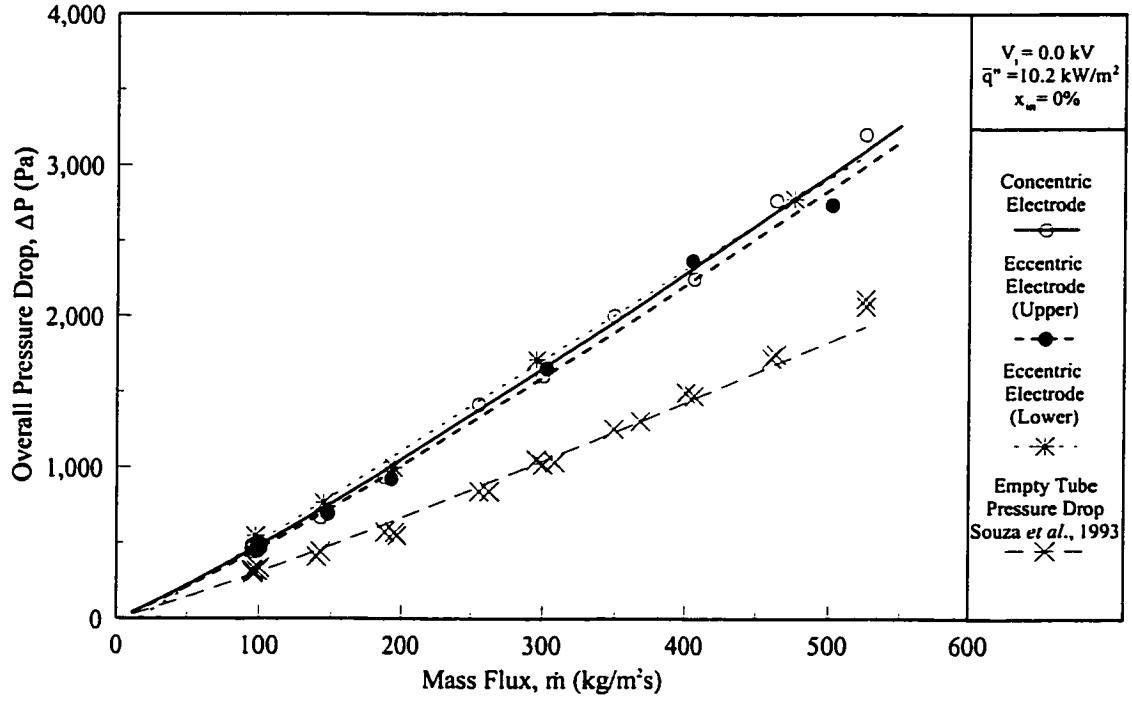

b) Overall Pressure Drop vs. Mass Flux

Figure 8.9: The Effect of Mass Flux on the a) Average Heat Transfer Coefficient and b) Overall Pressure Drop for different Electrode Configurations without the EHD Effect.

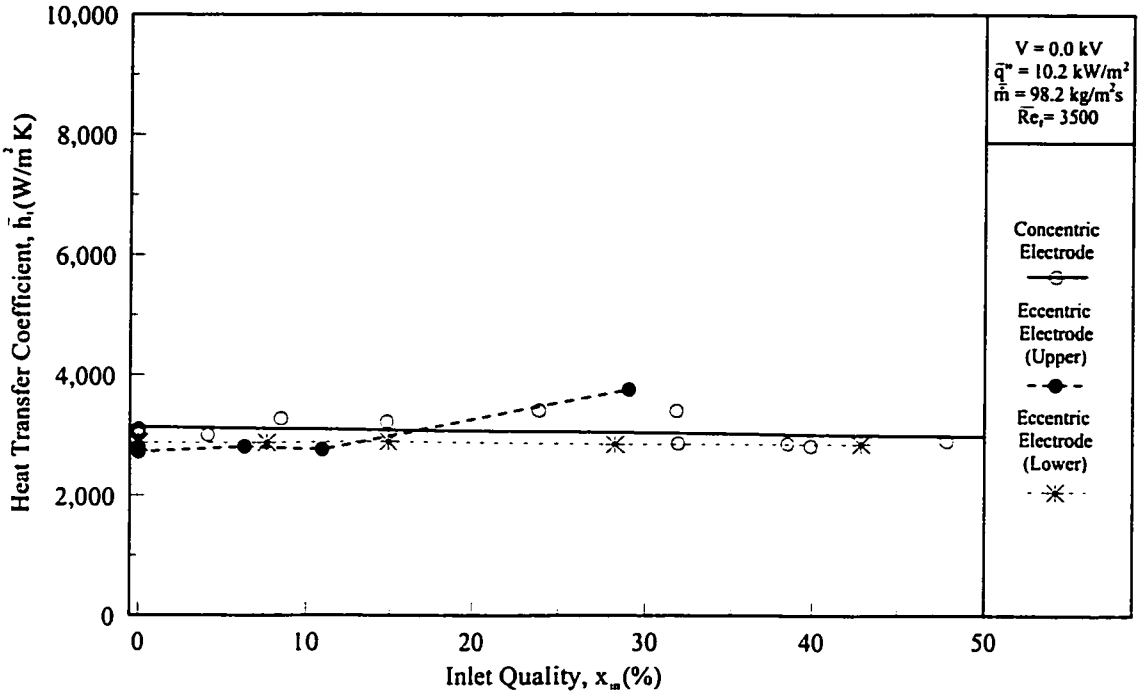

a) Heat Transfer Coefficient vs. Inlet Quality

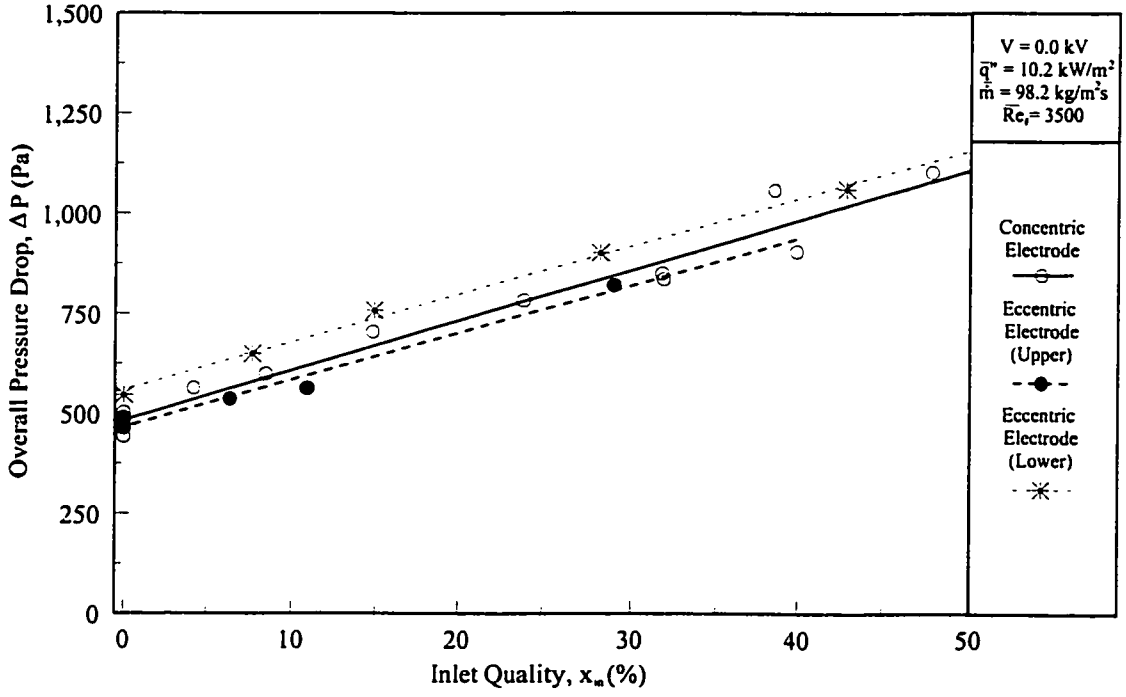

b) Overall Pressure Drop vs. Inlet Quality

Figure 8.10: The Effect of Inlet Quality on the a) Average Heat Transfer Coefficient and b) Overall Pressure Drop for different Electrode Configurations without the EHD Effect.

drop of the annular channel. The maximum difference in the heat transfer coefficient depends primarily on the mass flux while the difference pressure drop of the three designs depends more on the inlet quality. First, considering the influence of mass flux for relatively low mass flux levels, the heat transfer characteristics of the concentric and eccentric (lower) electrodes are essentially identical but the upper eccentric electrode placement results in lower rate of heat transfer. The reason for this difference is postulated to be the effect the electrode has in displacing the liquid that accumulates along the bottom of the channel due to the more dominant gravitational effects at lower mass flow rates as discussed in Chapter 5. Above approximately $\dot{m} \approx 250$ kg/m^{2}s, this trend changes and the concentric and upper eccentric electrode configurations converge while the lower electrode position heat transfer coefficients decrease.

Considering the effect of inlet quality, the scatter in the data does not distinguish any significant differences between the three electrode arrangements. However, the pressure drop reveals a definite trend in both the studies of mass flux and the inlet quality. Increasing the height of the electrode decreases the pressure drop. This is also believed to be due to buoyancy effects. As the electrode is raised vertically, the amount of liquid in contact with the electrode decreases. The decreasing volume of liquid in contact with the electrode subsequently deceases wall friction, reducing the pressure differential across the heat exchanger. In general, the difference in the performance of the heat exchanger without EHD were relatively invariant to the changes in electrode positioning. Therefore, the flow regimes encountered within the eccentric channels are similar to those encountered in the flow configurations presented in Chapter 5.

In the following subsections, the relevant flow and EHD parameters are explained in terms of their effect on the heat exchangers performance, by considering the overall

influences of the electrohydrodynamic forces on the channel. Both the local enhancement and suppression effects in addition to the transient parametric analysis of the experimental set of conditions investigated in Chapter 7 are repeated for the upper eccentric electrode configuration at increasing voltage potentials.

8.2.1 The Overall Influence of a DC Electric Field on Eccentric Electrode Configurations

The results of the eccentric electrode experiments are presented in Figures 8.11 to 8.15. The experimental results are shown in terms of both the average boiling heat transfer coefficient and the pressure drop as a function of the parametric values of applied voltage, mass flux and inlet quality. This section is only a brief overview of the EHD effect applied to eccentric channels because the underlying mechanisms responsible for inducing a reorientation of the flow patterns which increases both heat transfer and pressure drop, are similar to the concentric electrode arrangement as discussed in Chapter 7.

The distribution of the average refrigerant heat transfer coefficient for all three electrode positions is presented in Figure 8.11a at increasing levels of applied voltage. The conditions compared in Figure 8.11, are similar to the local and transient analysis presented in Section 7.2: Re_l = 3500, x_{in} = 0%, and q'' = 10.2 kW/m^2 for the annular channel. The effect of increasing the applied voltage increased heat transfer by 85% at the maximum voltage potential (V_i = 8.0 kV) for the concentric arrangement while the upper eccentric electrode position attained an overall enhancement of 60% over the zero electric field case at only V_i = 2.0 kV, a fourfold decrease in the required voltage with almost the same reduction in power consumption. However, applying the same voltage to the lower electrode had a negligible effect on the heat transfer characteristics at these conditions. The primary difference is attributed to the distribution of the electric field in the three geometries that was

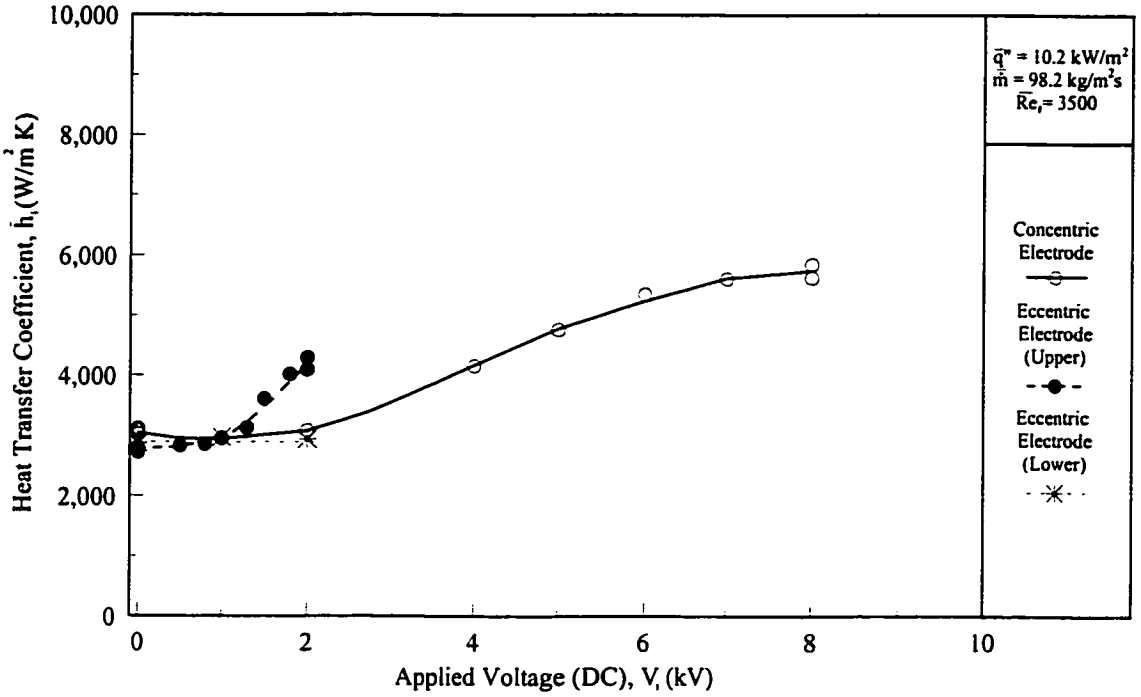

a) Heat Transfer Coefficient vs. Applied Voltage

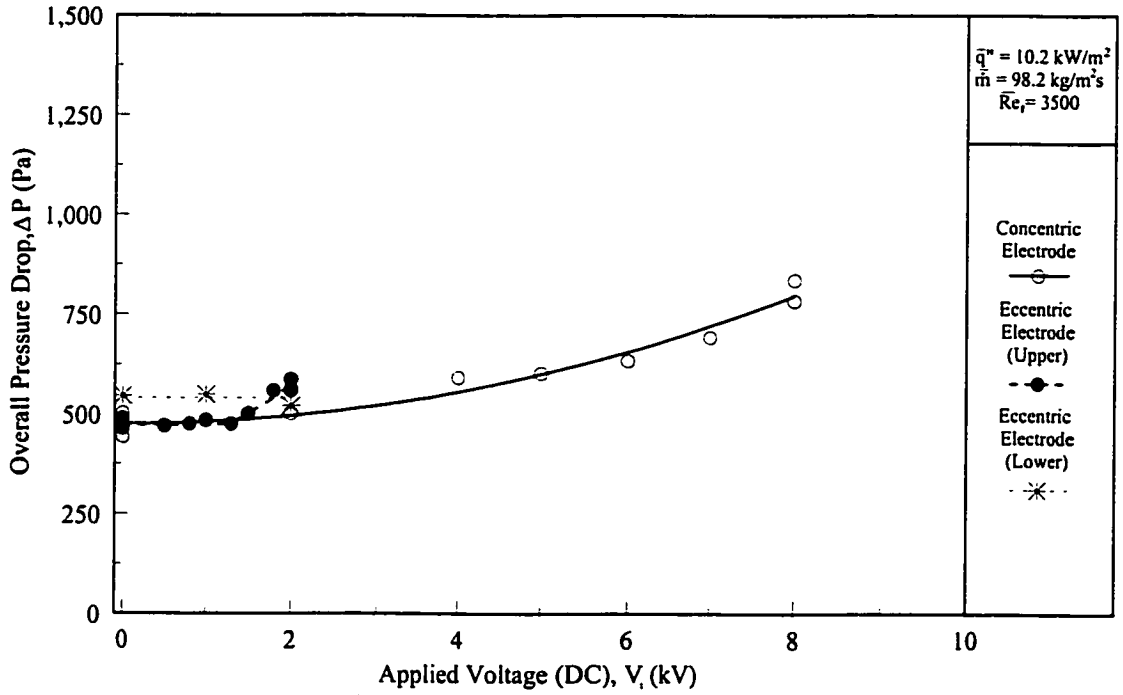

b) Overall Pressure Drop vs. Applied Voltage

Figure 8.11: The Effect of Applied Voltage on the a) Heat Transfer Coefficient and b) Overall Pressure Drop at a Fixed Mass, Flux Heat Flux and Inlet Quality for Different Electrode Configurations.

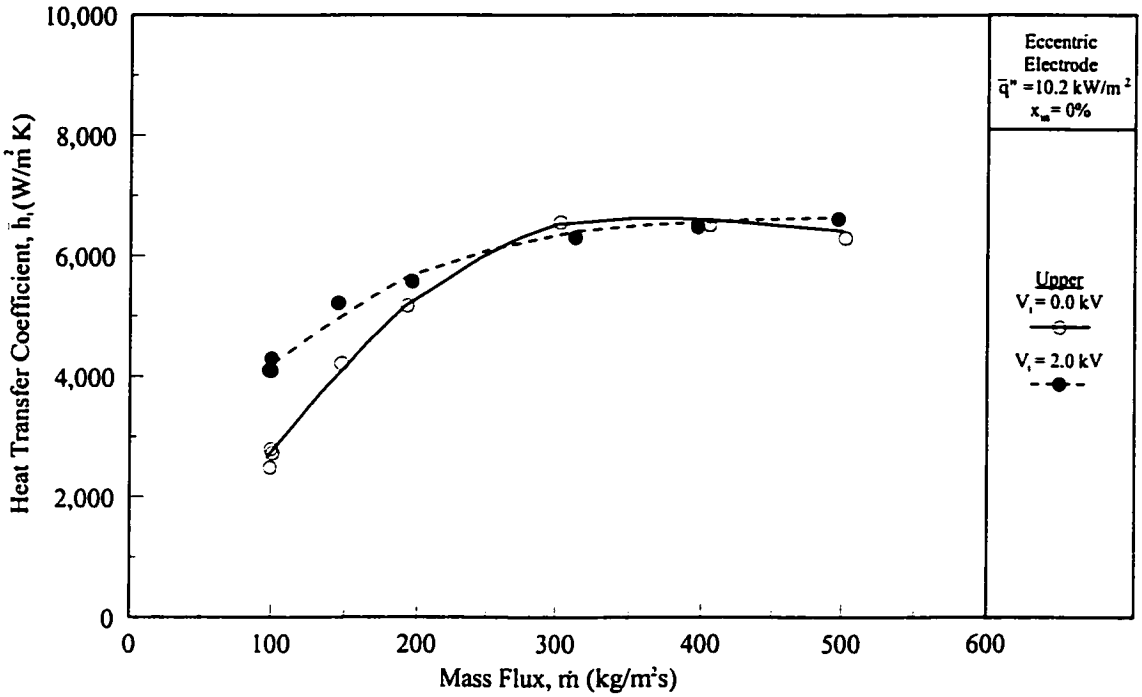

a) Heat Transfer Coefficient vs. Mass Flux

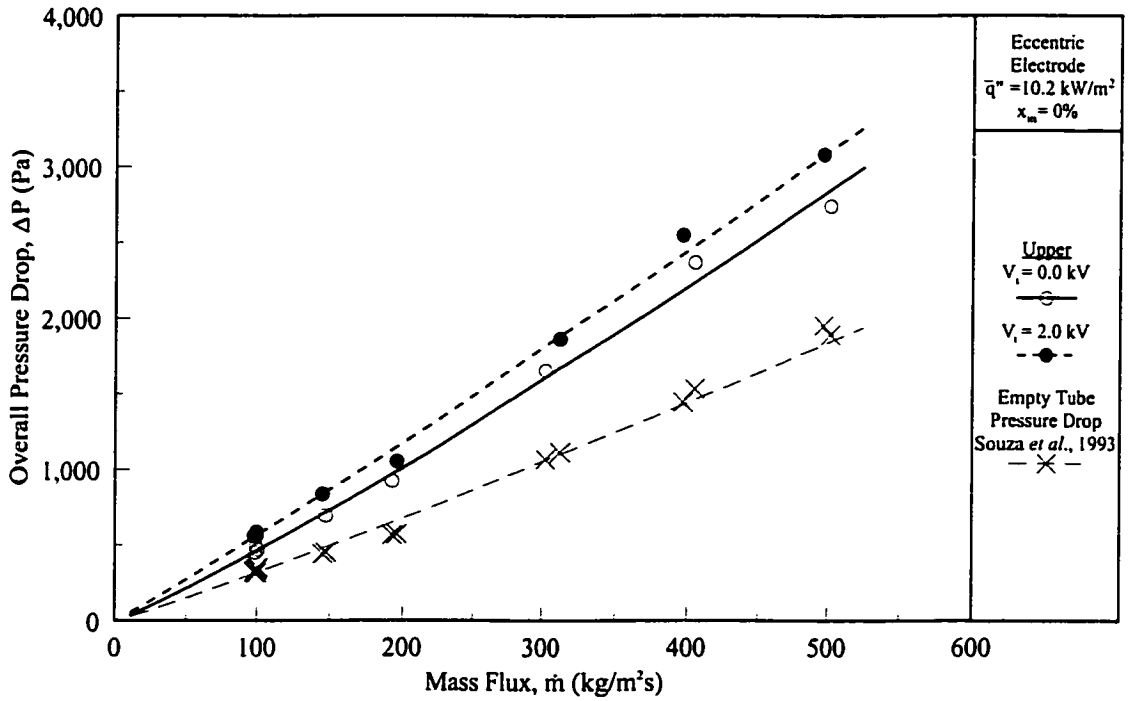

b) Overall Pressure Drop vs. Mass Flux

Figure 8.12: The Effect of Mass Flux on the a) Average Heat Transfer Coefficient and b) Overall Pressure Drop with and without the EHD Effect at a Fixed Heat Flux and Inlet Quality for the **Upper** Eccentric Electrode Configuration.

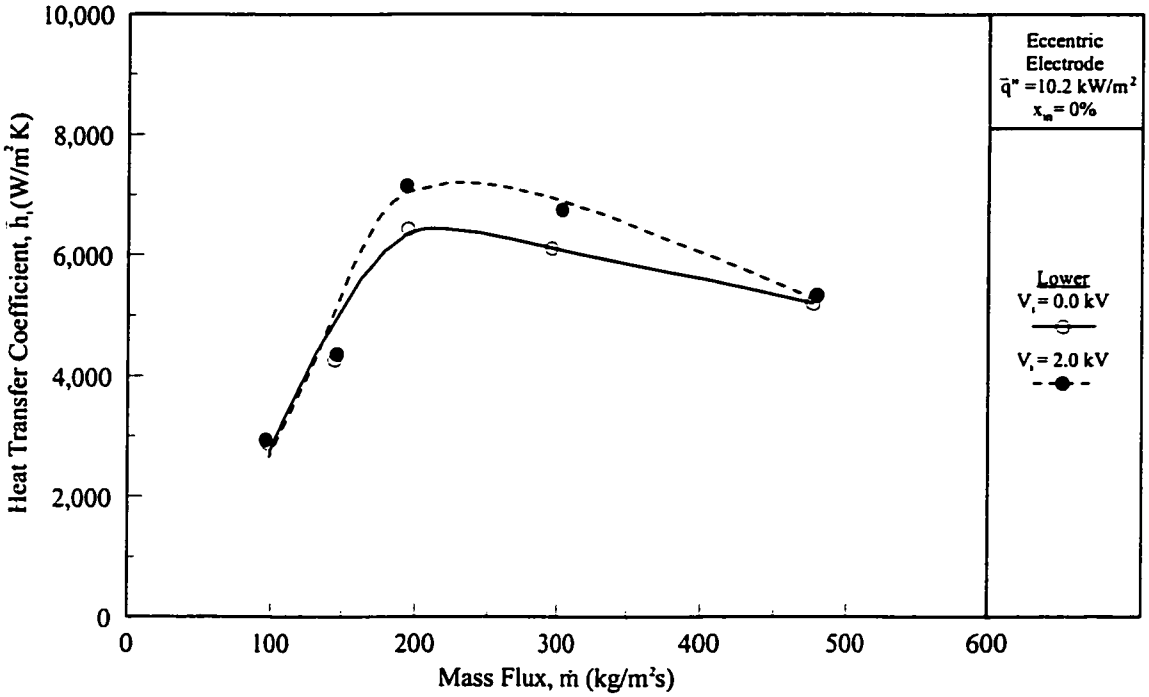

a) Heat Transfer Coefficient vs. Mass Flux

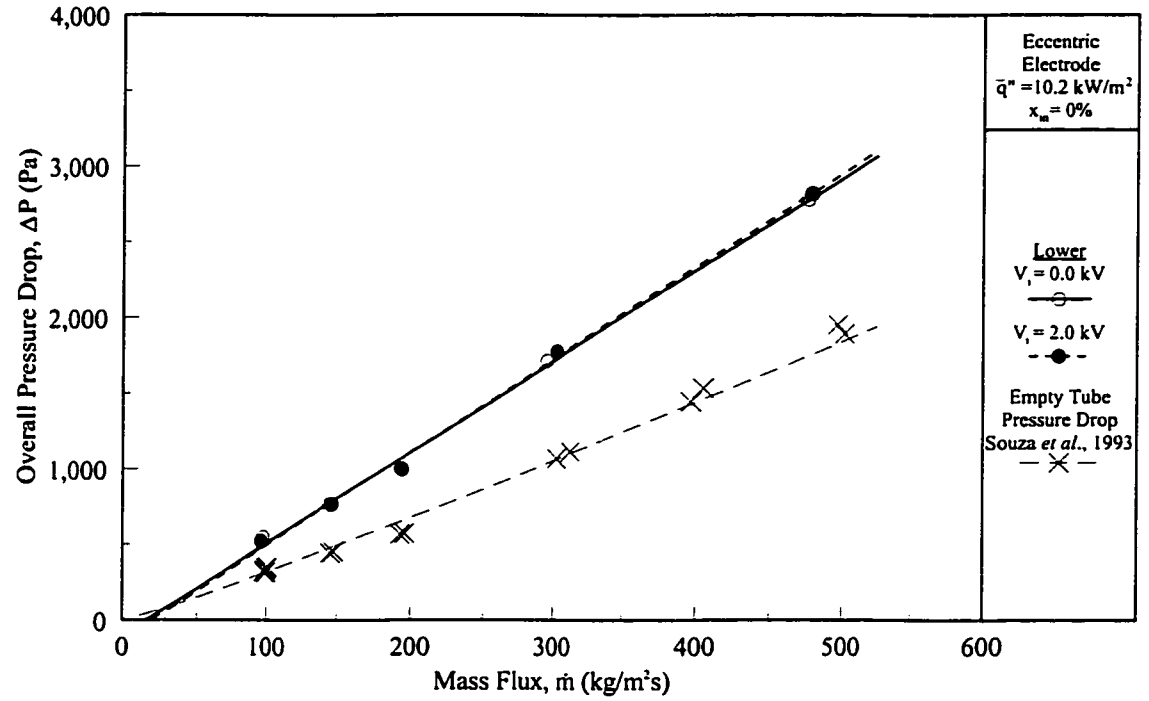

b) Overall Pressure Drop vs. Mass Flux

Figure 8.13: The Effect of Mass Flux on the a) Average Heat Transfer Coefficient and b) Overall Pressure Drop with and without the EHD Effect at a Fixed Heat Flux and Inlet Quality for the **Lower** Eccentric Electrode Configuration.

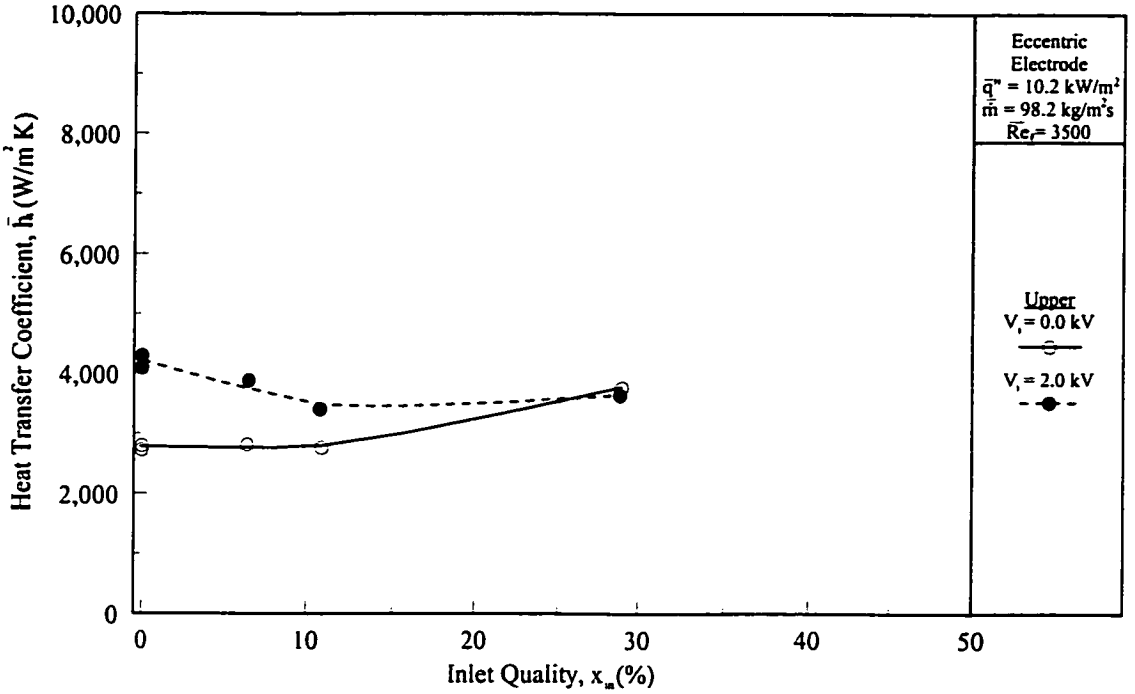

a) Heat Transfer Coefficient vs. Inlet Quality

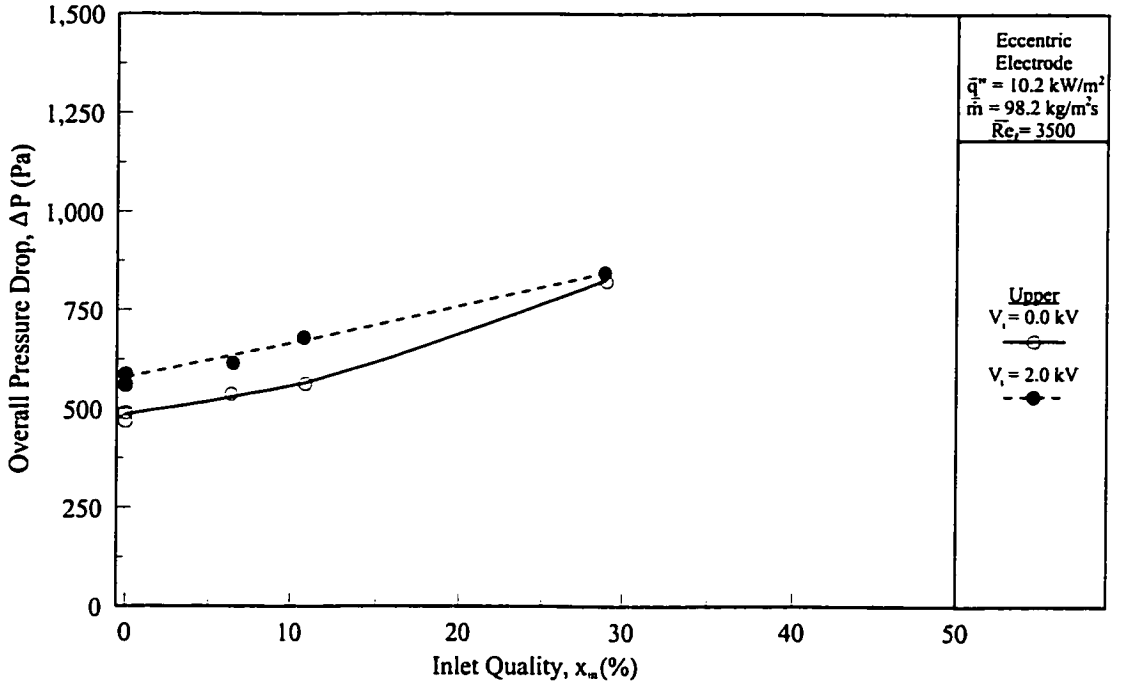

b) Overall Pressure Drop vs. Inlet Quality

Figure 8.14: The Effect of Inlet Quality on the a) Average Heat Transfer Coefficient and b) Overall Pressure Drop with and without the EHD Effect at a Fixed Heat Flux and Inlet Quality for the **Upper** Eccentric Electrode Configuration.

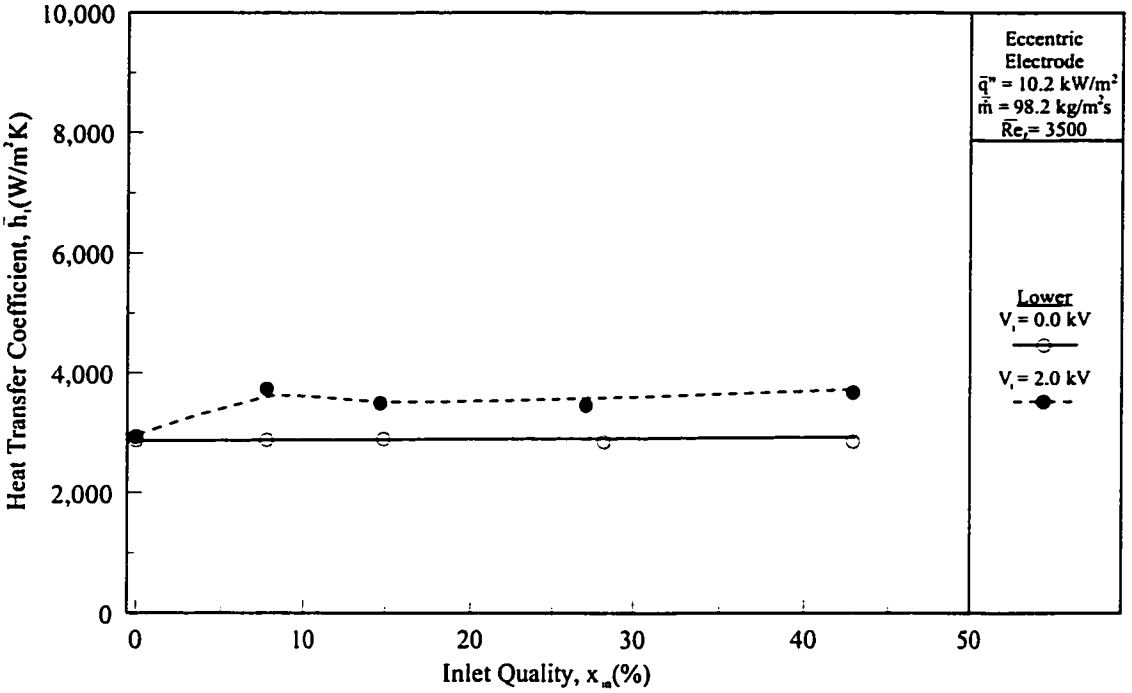

a) Heat Transfer Coefficient vs. Inlet Quality

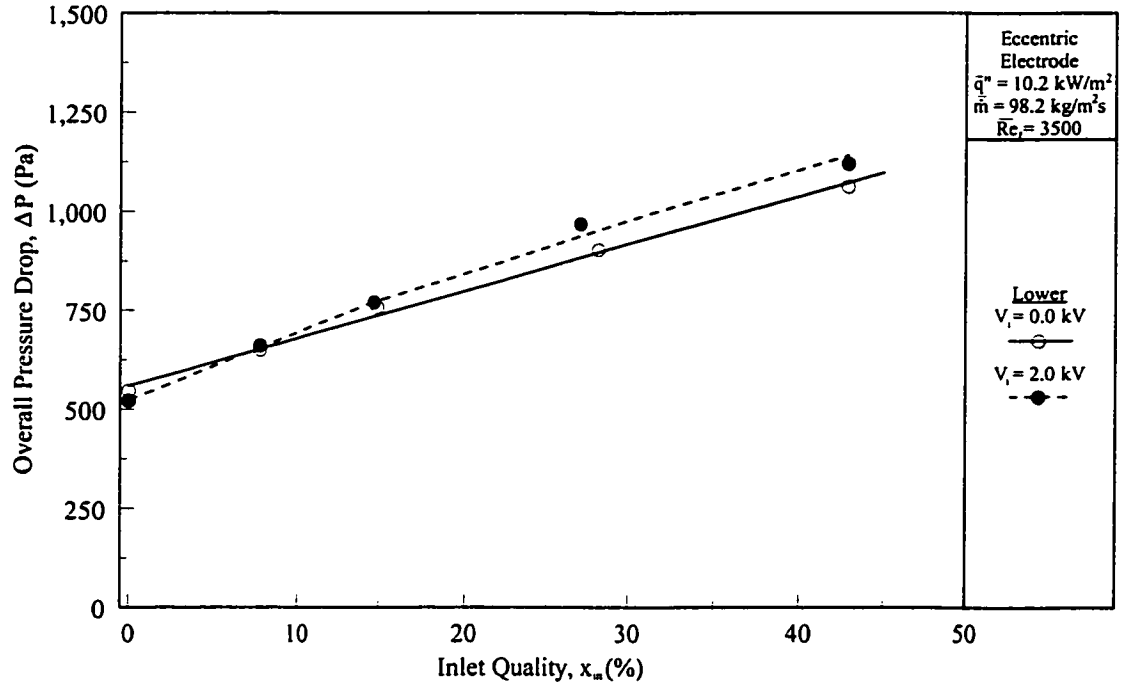

b) Overall Pressure Drop vs. Inlet Quality

Figure 8.15: The Effect of Inlet Quality on the a) Average Heat Transfer Coefficient and b) Overall Pressure Drop with and without the EHD Effect at a Fixed Heat Flux and Inlet Quality for the **Lower** Eccentric Electrode Configuration.

discussed in the previous section. As the strength of the interfacial jump in electric field strength in the upper eccentric configuration at V_i = 2.0 kV is essentially the same as the interfacial conditions observed in the concentric case at V_i = 8.0 kV in Chapter 7, comparable forces are expected to have developed. These forces induce a similar phase migration to that described in the detailed parametric analysis in Section 7.2.2. In order to qualitatively describe the effects of the electric field on heat transfer and pressure drop, the local and transient conditions in the annular geometry at different voltage levels are evaluated for the upper eccentric geometry in the following section.

The overall pressure drop associated with the three geometries is presented in Figure 8.11b. As shown, the pressure drop increases when the electrode is offset by +2.73 mm. This is almost identical to the pressure drop observed in the concentric case for an equivalent heat transfer augmentation (when $V_i \sim$ 6.0 kV), suggesting a similar flow pattern configuration may exist for these experiments regardless of the electrode position.

The final observation when considering the difference in the heat transfer and pressure drop characteristics is an increase in overall pressure drop when the electrode is vertically lowered. The differences in pressure drop may be due to buoyancy effects at this relatively low Froude number flow condition, resulting in a dominantly stratified flow which is subsequently displaced by the electrode in the lower position.

Figures 8.12a and 8.13a show the average heat transfer coefficients as a function of mass flux for a fixed heat flux and a zero inlet refrigerant quality at the upper and lower eccentric placements, respectively. The results with and without EHD effects (V_i = 2.0 kV) are presented. Similar to the observations in Chapter 7, the results for the upper electrode configuration indicate an increase in mass flux increases the heat transfer coefficient. Also the results show that the EHD effects can lead to upper heat transfer coefficients for the

range of qualities and heat fluxes tested at the upper electrode position. However, increasing the flow above approximately $\dot{m} \approx 250$ kg/m^{2}s results in a reduction of heat transfer when the electrode is positioned below the centerline. This is difficult to interpret for the current system but may be due to a reduction in flow circulation in the lower half of the channel because of the positioning of the electrode.

Generally, observations from the discussion of the annular geometry are qualitatively similar for eccentric channels: When the mass flux (Reynolds number) increases, the EHD forces must overcome the increasing momentum effects, existing surface tension and gravitational influences in order to induce phase migration or draw the liquid away from the wall to increase the temperature gradient in the liquid layer or promote dryout. Consequently, electrically induced heat transfer effects are reduced with increasing Reynolds number.

Figures 8.14a and 8.15a show the variation of average heat transfer coefficient with inlet quality at a fixed heat and mass flux, $q'' = 10.2$ kW/m^2 and $\dot{m} \approx 100$ kg/m^{2}s for the two eccentric geometries. Like the concentric electrode configuration, the effect of applying a voltage to the upper eccentric configuration is more dominant in lower quality regions ($x_{in} < 10\%$). The mechanisms affecting low quality regions may be due both to the electrohydrodynamic effects on the nucleation component (Pounder, 1980, Cheng and Chaddock, 1986, Ogata *et al.*, 1985, Kawahira *et al.*, 1990, Ogata and Yabe, 1993a, Eames and Sabir, 1997) and the redistribution of the flow pattern from stratified wavy flow to a more uniformly distributed flow. The effect of EHD on flow redistribution is based on the transient surface temperature measurements and high speed photography at the test section exit. This is discussed in the following section.

The effects of decreasing the electrode position -2.73 mm vertically (lower

eccentric), as shown in Figure 8.15a, is explained through an examination of the electric field distribution and the transient profiles of the surface temperature. Here, the positioning of the electrode displaces the liquid upward so a more uniform wall temperature is measured as the inlet quality increases. As suggested from the electric field distribution for annular flow in Section 8.1, the dielectrophoretic force tends to draw liquid toward the electrode, leaving less liquid in direct contact with the wall. At relatively low qualities, this decreases the annular film and the thermal boundary layer, thus increasing the heat transfer coefficient.

The primary drawback of EHD enhanced heat transfer is the pressure drop penalty which is also apparent in this type of electrode arrangement. Figures 8.11b to 8.15b show the total pressure drop of the test section as a function of applied voltage, mass flux and inlet quality for the above heat transfer characteristics. As with the concentric configuration, the electric field effect on the flow patterns may act to increase the momentum interaction, particularly from the enhancement of entrained droplets and bubbles in the respective phases. As described in Chapter 7, the pressure drop is increased by the effect of the electrohydrodynamic body force and by the subsequent reorientation of the liquid-vapour distribution into regimes with increased instability as liquid is drawn toward the upper portion of the tube against gravity. These influences are elucidated when the local and transient measurements are further studied.

8.2.2 The Local Influence of a DC Electric Field on the Upper Eccentric Electrode Configuration

The local and transient analysis are presented in this section for the conditions: Re_l = 3500, x_{in} = 0%, and q'' = 10.2 kW/m^2 at different DC voltage levels in the upper eccentric electrode configuration. This is the experimental quasi-local data (Figure 8.16), corresponding to the DC data in Figure 7.9 for the concentric electrode configuration.

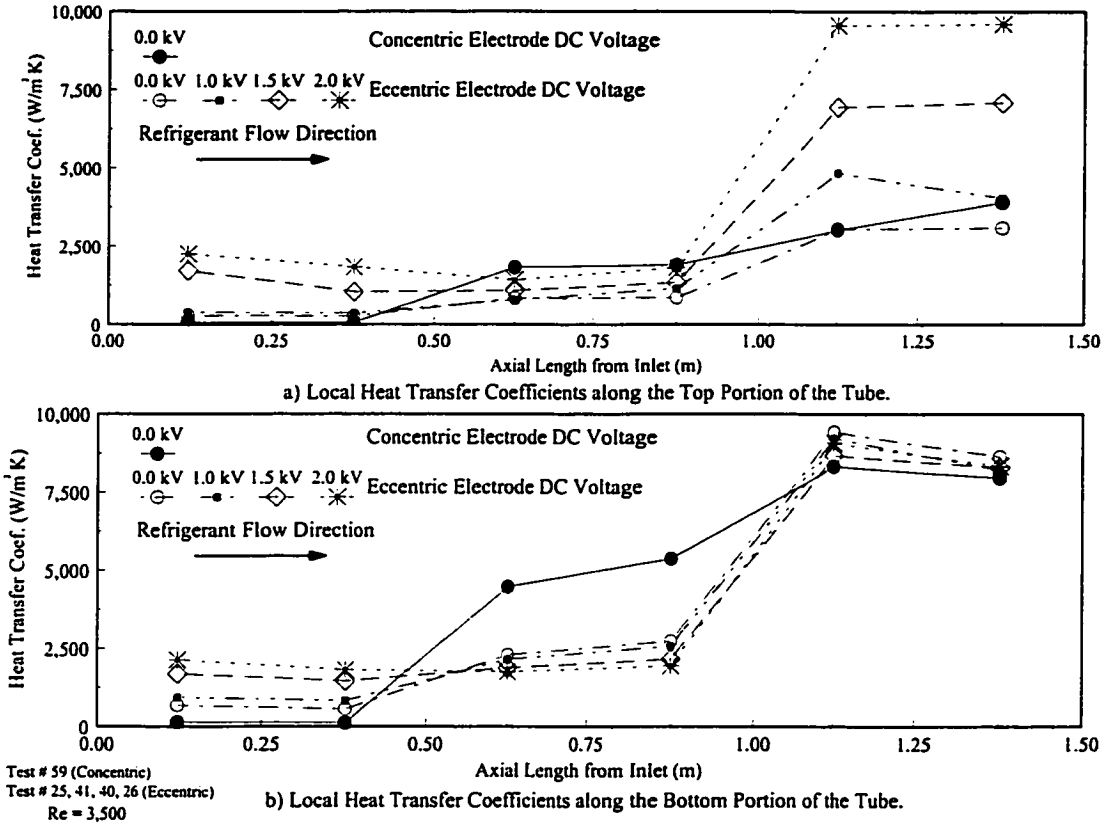

Figure 8.16: Quasi-Local Heat Transfer Coefficients with Increasing Applied DC Voltages for the **Upper** Eccentric Electrode Configuration.

Although the overall performance shows an enhancement of approximately 60%, locally the effect ranges from an enhancement as large as 800% to a suppression in heat transfer of 25% on the channel bottom with respect to the no EHD condition. The conditions in Figure 8.16, for the eccentric channel without EHD are consistent with the results from the concentric channel: The flow is predominantly stratified wavy which explains the significant difference in heat transfer coefficients from the top to the bottom. When the applied voltage is increased, there is an increase in local heat transfer on the upper half of the channel. Analogous to the annular channel, this is explained by considering the resultant forces acting on the liquid - vapour interface. In both the eccentric (upper) and concentric configurations, similar dielectrophoretic forces are introduced which create instabilities (protrusions) on the interface which significantly disturb the flow with larger, potentially

more frequent waves as EHD is applied. The vapour flowing over the protrusion accelerates, reducing the vapour pressure which in turn produces an larger upward force. The force generated causes the protrusion to grow unless the force is more than offset by the downward gravitational and surface tension forces. As the protrusion grows, the electric field distribution in the vapour phase increases (see Appendix C), which in turn increases the attractive force on the liquid, further accelerating the wave upwards. If the combined flow effect is significant, then a flow regime transition will occur, changing the stratified liquid to either intermittent or annular. In each case, both thinner liquid thickness on the bottom of the tube and a rewetting of the top are expected to increase the rate of heat transfer around the tube. However, the increase in heat transfer is only observed for the upper half of the channel, as seen in Figure 8.16b. When the voltage level is increased, there is actually a reduction in the heat transfer coefficient in the last three quarters of the channel. The mechanisms behind this suppression in heat transfer requires further investigation. Based on the given measurements, no conclusive influences can be derived to explain this phenomena. The flow regime transitions are revealed in greater detail by examining the transient local temperature measurements.

Wall Surface Temperature Profiles for the Upper Eccentric Electrode Placement With and Without EHD

Figure 8.17a shows the time averaged axial superheat temperature profile for the eccentric channel at the same flow conditions as the transient analysis of both the DC and AC experiments conducted for the concentric geometry. These are presented against the concentric 0 kV case, Test # 59 (Figure 7.10) for reference purposes. Figure 8.17b shows the corresponding standard deviation of the surface temperature fluctuations.

For the base case upper eccentric channel experiment (the zero electric field case)

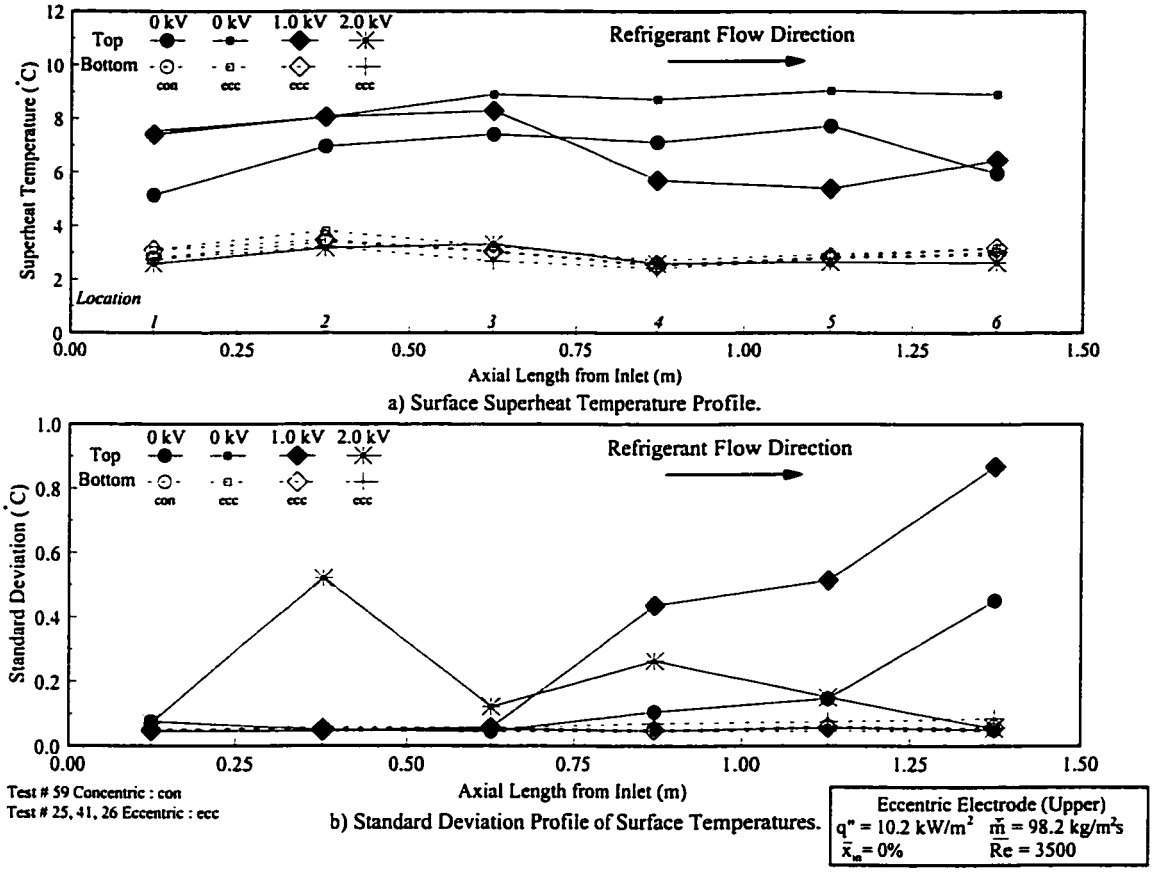

Figure 8.17: Time-Averaged Surface Superheat Temperature and Standard Deviation Profiles of the **Upper** Eccentric Electrode Configuration at Increasing Applied Voltage Levels.

Test #25, the flow entering the test section was a single-phase liquid at a temperature slightly below the saturation temperature, similar to Test #59 discussed in Chapter 7. When the flow reaches the first thermocouple station (location 1), Figure 8.17a indicates that the average temperature of the top surface is over 4°C higher than the bottom surface. Like the concentric channel, this difference in temperature indicates either a flow and/or thermal stratification inside the tube. Figures 8.18 a, b and c are typical time responses of the top and bottom thermocouples and the differential pressure transducer for Test #25. Note the similarity between Figure 8.18 and Figure 7.11. The temperature is almost identical at each thermocouple location. The top average surface temperature at these locations is slightly higher than that at the down downstream location and they are only 1°C to 2°C below the

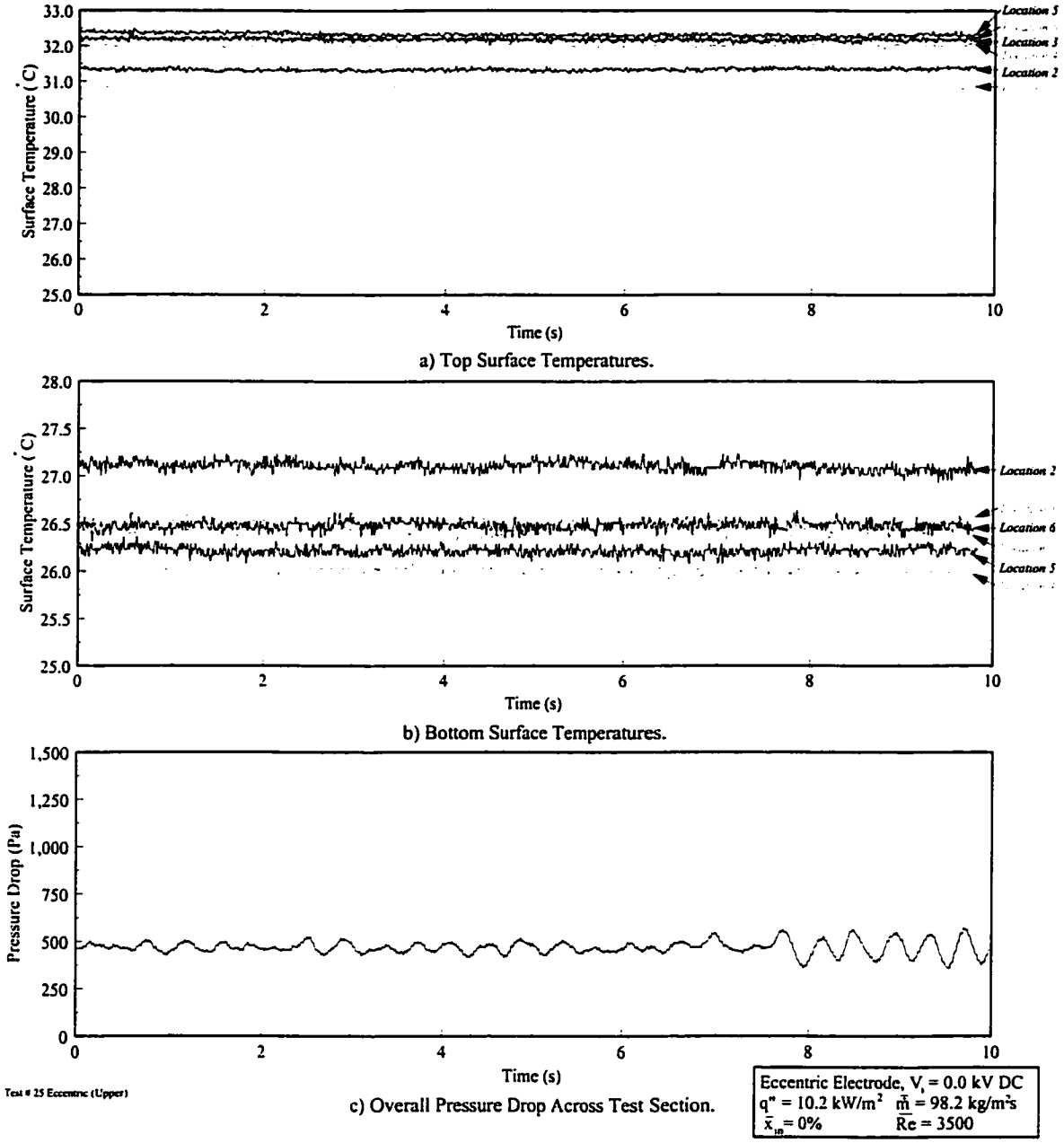

Figure 8.18: Time Trace of Surface Temperature and Pressure Drop of the **Upper** Eccentric Electrode Configuration without an Applied Voltage.

outside water temperature measurements. Conversely, the bottom surface temperatures are almost constant at approximately three degrees above the refrigerant temperature. Figure 7.10b shows that the standard deviation of the bottom measurements is negligible when the external noise is considered. Similar to the evaluation for most of the channel in Test #59, these transient temperature profiles suggest that the conditions can be attributed

to stratified flow. Again, the trend of increasing temperature on the upper surface is accredited to the counterflow configuration of the heat exchanger.

The primary difference between the experiment for this eccentric configuration, Figure 8.18, and the results for the concentric channel is the final surface temperature measurement at location 6, 12.5 cm upstream from the exit of the heated section. At this point, the concentric channel measurements of the top temperature varies by as much as 2°C between the extremes of location 1 and locations 2 to 5. The number of fluctuations in the temperature trace indicates the top surface is alternately dried and rewetted, presumably by the action of slug flow, droplet entrainment or the intermittent wetting due to climbing of liquid around the circumference of the tube. For the upper eccentric case, these fluctuations are no longer evident in Figure 8.18. The primary difference is believed to be due to either the lower electrode position displacing liquid to inducing a flow pattern transition or the location of the spacers in the concentric channel 'tripping' the flow regime transition. High speed video imaging at the viewing windows just upstream of the heated section confirmed that the flow regime was stratified wavy having a thickness $h_L \approx 2.7$ mm with a complete dryout on the top half of the channel.

Figure 8.18c presents the overall pressure drop variation across the heat exchanger. For this condition, the mean overall pressure drop is 470 Pa with a 30 Pa standard deviation. Compared to Test #59, the mean value is approximately the same as the concentric case while the standard deviation is half the value observed in Figure 7.11. This is consistent with the inferences made from the temperature traces that the dominant flow regime being stratified wavy. The flow transition observed in Test #59 no longer occurs for the upper electrode position, resulting in a lower overall pressure variation within the channel.

Based on the above observations, schematics of the flow pattern along the length of

the channel without an applied voltage can be reconstructed, as shown in the following section, to illustrate the process of flow regime transition inferred through the analysis of the flow pattern map, surface temperatures and pressure drop.

Figure 8.17a shows the time averaged axial superheat temperature profile for the same flow conditions considered in the previous section at two values of applied voltage 1.0 kV and 2.0 kV. The behaviour of the surface temperatures at locations 1 through 6 shows the application of an electric field tends to have a larger effect on the top surface temperatures than the bottom surface temperatures in terms of dynamic behaviour of the temperature traces. As observed for the concentric channel at each location, the average bottom superheat temperatures decreases slightly with applied voltage. The top surface temperatures do not indicate a clear trend aside from the increase in temperature variation as indicated from the standard deviation. Identical to the effect of increasing the applied voltage in the concentric channel, the interfacial electric force increases, thereby enhancing the momentum suction pressure effect and attracting the liquid towards the upper part of the channel. Further as interfacial waves grow larger, the nonuniformity of the electric field increases and more liquid is expected to be entrained in the form of droplets in the vapour core.

Figure 8.17b shows the standard deviation of the temperature at the bottom surface of the tube at locations 1 through 6 are roughly the same, regardless of the applied electric field potential. However, the standard deviation for the top locations show there is a large variance in the temperature of the top surface of the channel. The time traces of surface temperature are more instructive in determining the EHD effect on flow pattern. Figure 8.19 illustrates the time traces of temperature and pressure drop for an applied voltage of 1.0 kV (Test #41). Likewise, Figure 8.20 illustrates the time traces for an applied potential of

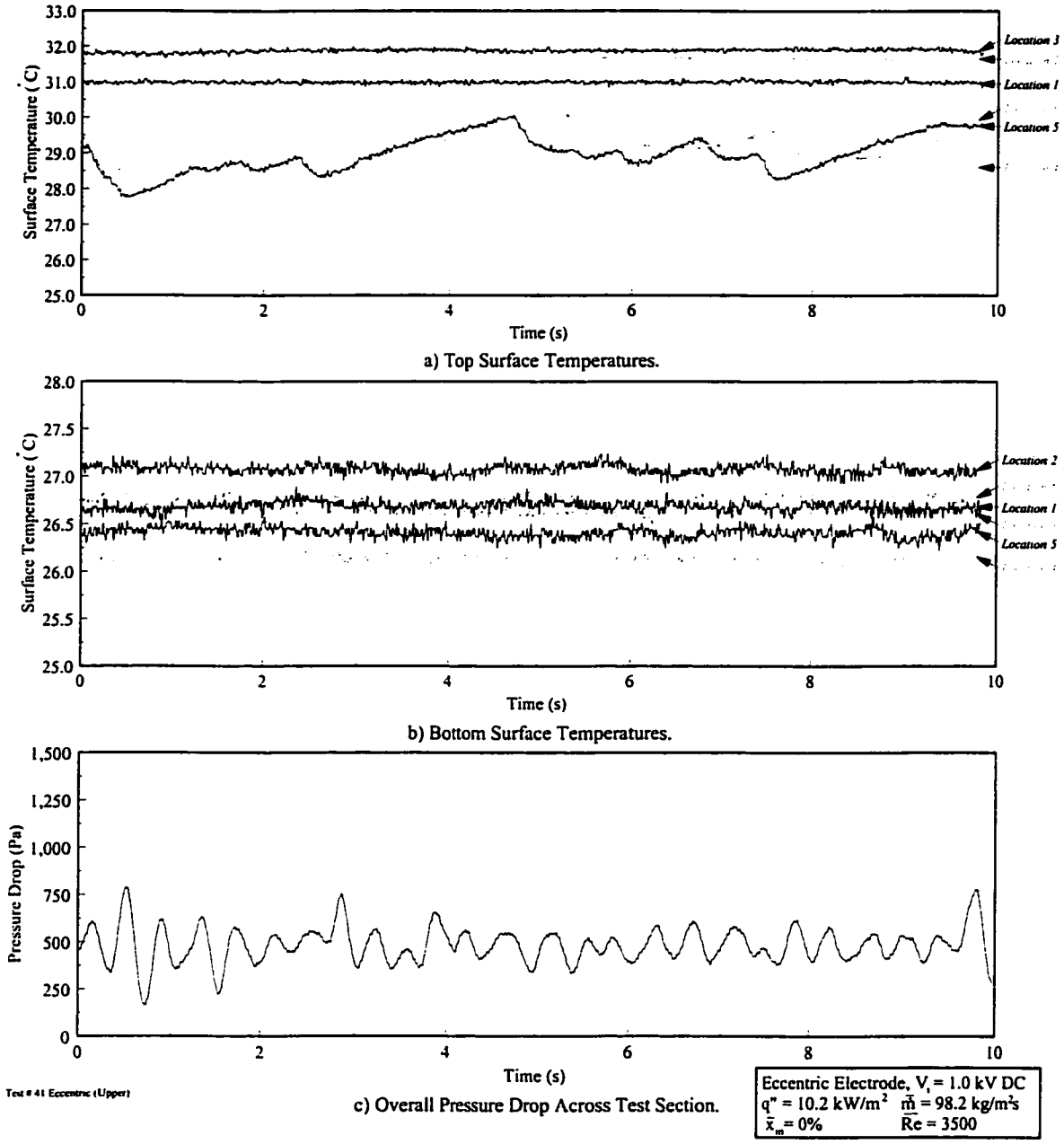

Figure 8.19: Time Trace of Surface Temperature and Pressure Drop of the **Upper** Eccentric Electrode Configuration at an Applied Voltage of V_i = 1.0 kV DC.

2.0 kV (Test #26). The deviation of the transient temperatures compared against these temperature trace in the absence of an electric field is obvious. Here, the fluctuating temperature in the concentric channel have manifested at the top axial locations 4 through 6 in Test #41 and at each location when the voltage is increased to 2.0 kV. The profile of these traces are similar with 5 ~ 10 fluctuations in the range of ~2°C, indicating the surface

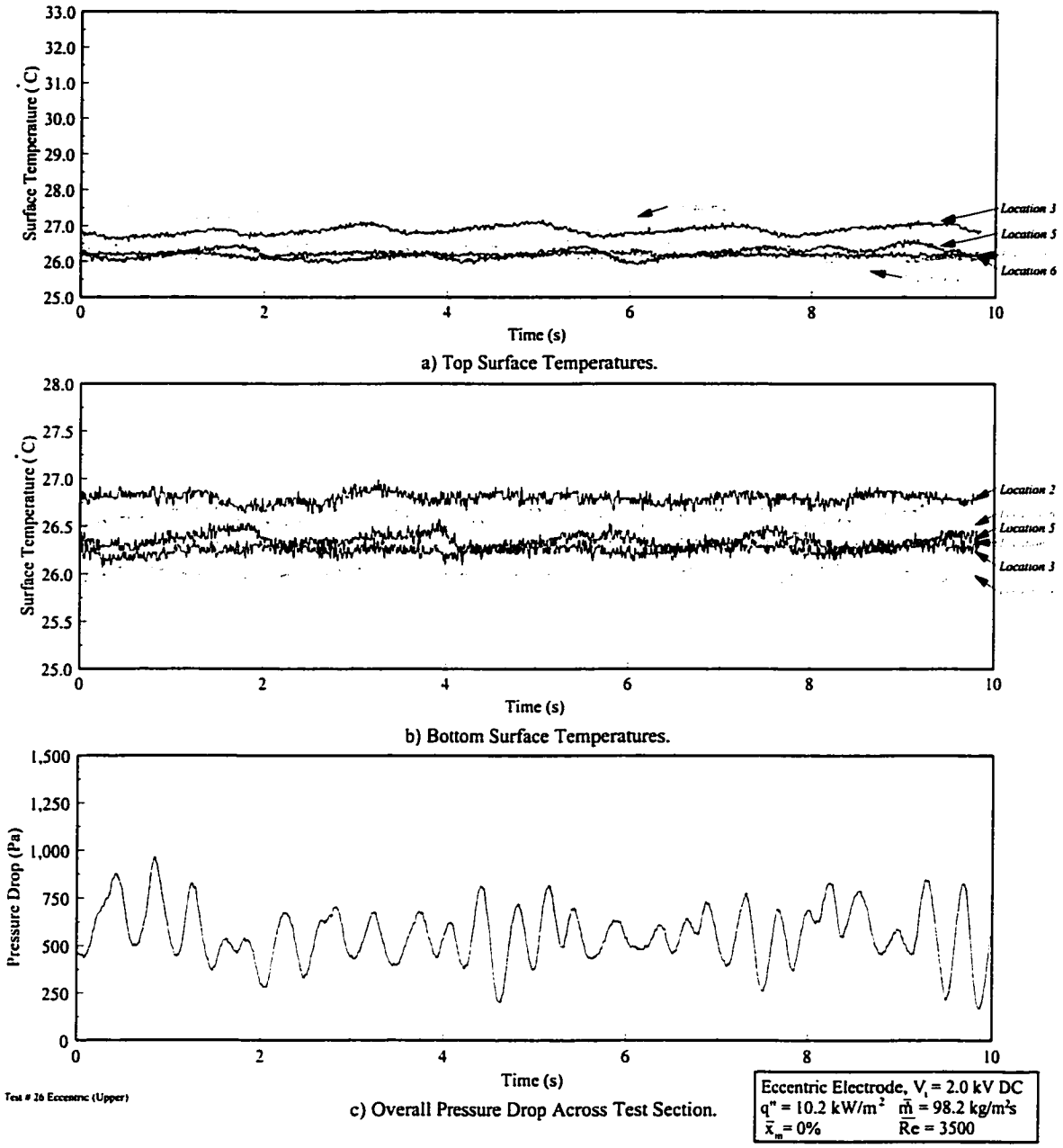

Figure 8.20: Time Trace of Surface Temperature and Pressure Drop of the **Upper** Eccentric Electrode Configuration at an Applied Voltage of V_i = 2.0 kV DC.

is alternately dried and rewetted. This drying and rewetting of the surface within the tube is attributed to the action of slug flow, significant droplet entrainment or the intermittent wetting due to climbing of liquid around the circumference of the tube. With the condition of a constant overall heat flux regardless of the applied voltage, the liquid must be taken from the previously stratified liquid layer. However, unlike the enhancement effect observed

by reducing the liquid layer thickness in the concentric channel, the local heat transfer coefficient data reveals that the magnitude of heat transfer actually decreased for reasons presently unknown.

The transient pressure drop traces, Figures 8.19c and 8.20c, exhibit similar fluctuation patterns to the pressure measurements observed at 8.0 kV in the concentric channel. Again, this is an indiction of the establishment of unstable flow patterns prone to increased momentum interaction, *ie.* slug flow or entrained droplet flow. Using the high speed video imaging system at the viewing windows just upstream of the heated section, this regime was identified as a slug type flow with a liquid film encircling the electrode. The schematics of the proposed flow pattern reconstruction in the absence of an electric field and at increasing DC applied voltage levels are presented in Figure 8.21. In summary, the interfacial dielectrophoretic forces created by the application of a voltage to the eccentric electrode may also cause several different flow regime transitions. However, the change of flow regime and subsequent augmentation in heat transfer rate is realized at significantly lower voltage levels with lower pressure drop penalties.

8.2.3 The Local Influence of a DC Electric Field on the Lower Eccentric Electrode Configuration

Local and transient analysis are presented in this section for the conditions: Re_l = 3500, x_{in} = 0%, and q'' = 10.2 kW/m^2 at different DC voltage levels in the lower eccentric electrode configuration. This is experimental quasi-local data, Figure 8.22, corresponding to the condition investigated in the previous section. Figure 8.22 clearly shows the different heat transfer characteristics between the two electrode geometries as discussed in Section 8.2. However, the effect of voltage for these conditions is negligible, because the electric field distribution that develops is stratified flow as demonstrated in the

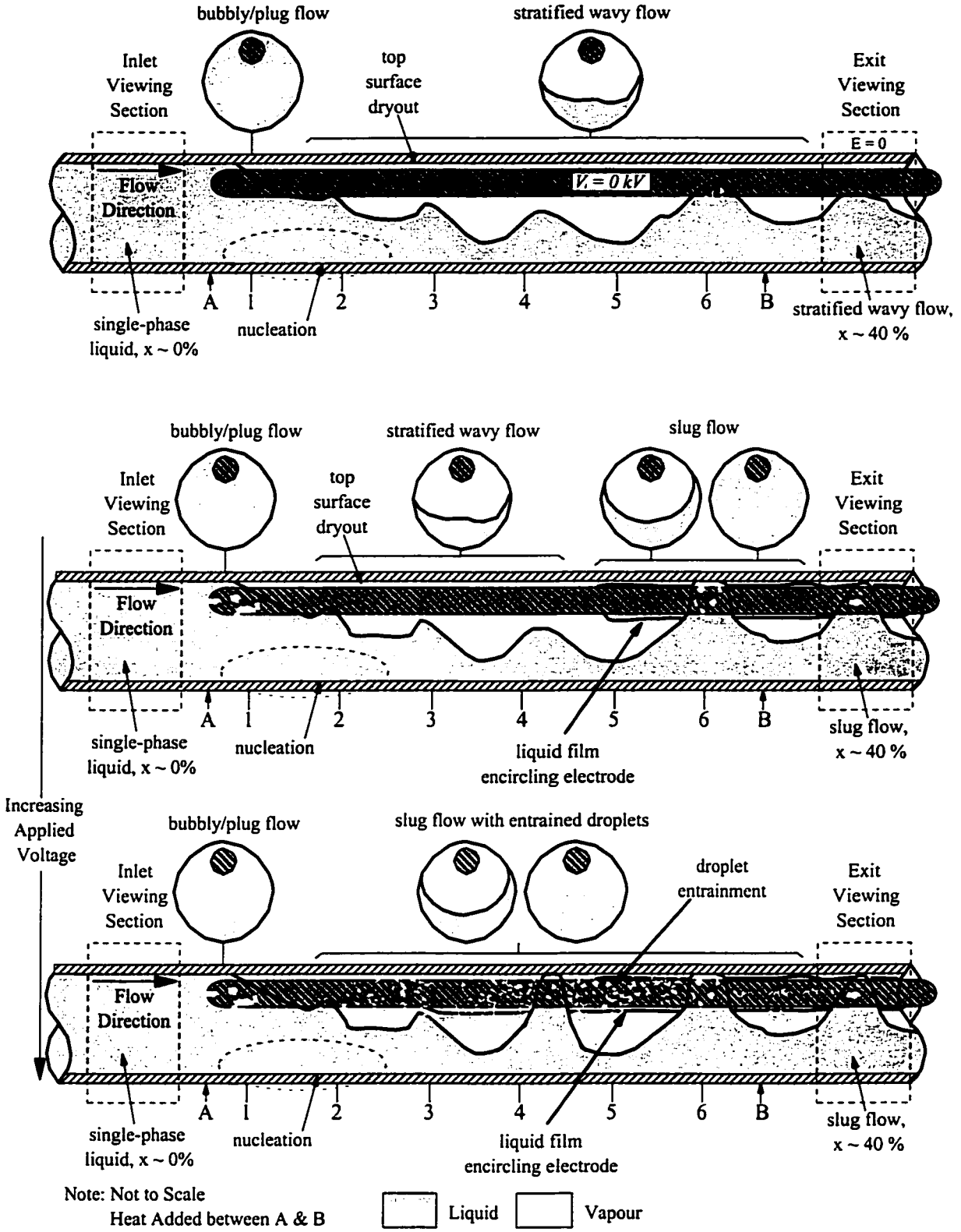

Figure 8.21: Proposed Reconstructed Flow Pattern from Surface Temperature and Pressure Drop Traces and Inlet and Outlet Flow Regime Observations for Upper Eccentric Geometry with and without EHD ($\dot{m}$ = 100 kg/m²s, q'' = 10.2 kW/m² & x_{in} = 0%).

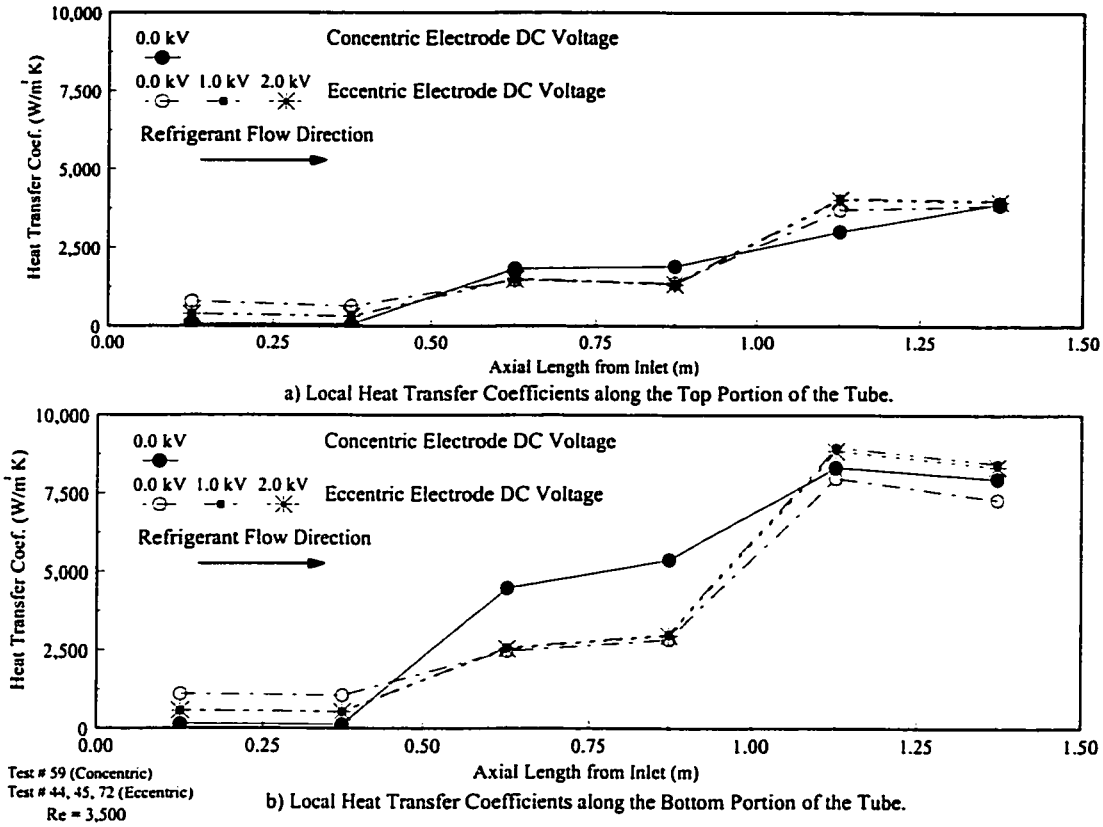

Figure 8.22: Quasi-Local Heat Transfer Coefficients with Increasing Applied DC Voltages for the **Lower** Eccentric Electrode Configuration.

finite element analysis in Section 8.1. As the electric field decreases significantly with elevation, the interfacial jump in the electric field strength is reduced, thereby decreasing the interfacial EHD forces. The negligible impact of the EHD effect is also apparent in the plot of time averaged axial superheat temperature and the corresponding standard deviation profiles for the lower eccentric electric configuration (Figure 8.23).

8.3 Current and Voltage Characteristics

The current and voltage characteristics for the eccentric electrode configuration channel were not detectable with the present measurement system because of the extremely low current levels. At the maximum applied voltage (V_i = 2.0 kV), the current level was below 0.2 μA which is less than 0.4 mW of consumed power.

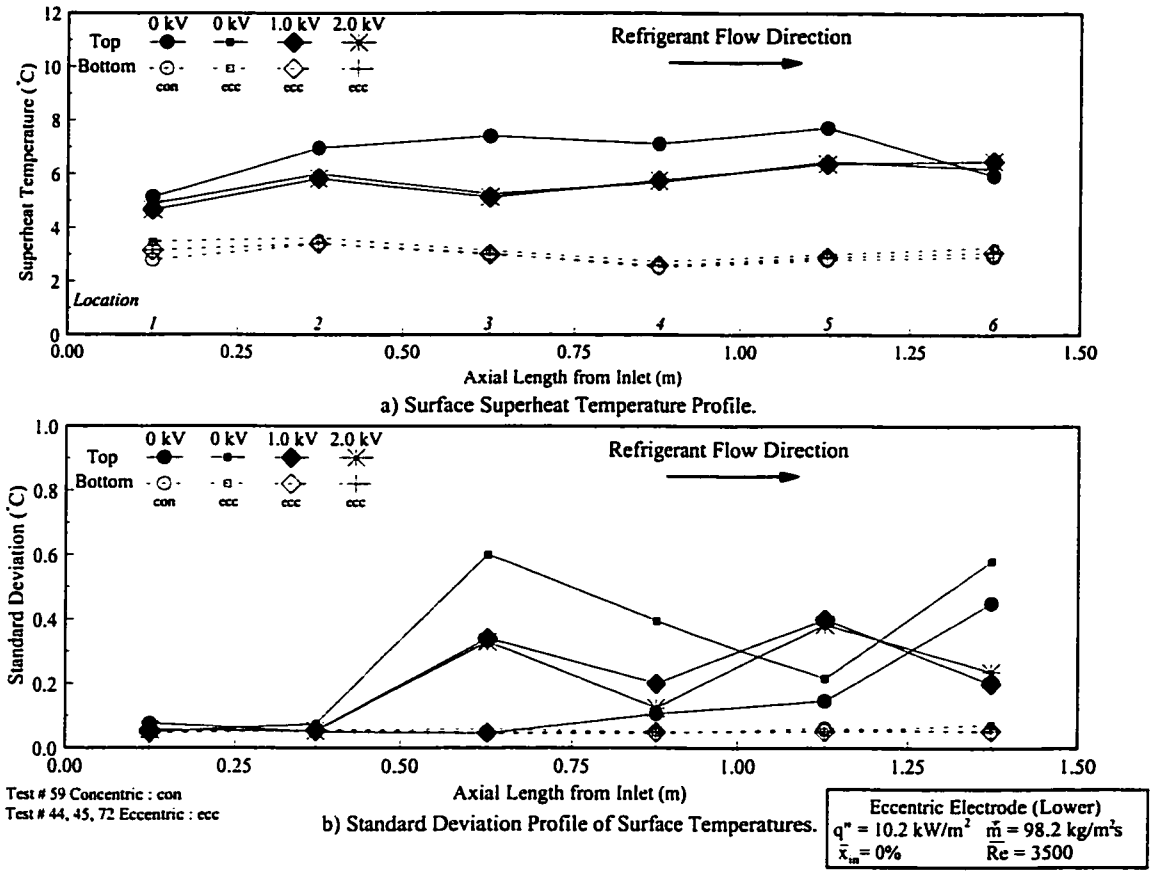

Figure 8.23: Time-Averaged Surface Superheat Temperature and Standard Deviation Profiles of the **Lower** Eccentric Electrode Configuration at Increasing Applied Voltage Levels.

8.4 Summary

The experiments conducted for the eccentric geometry have provided evidence that through the establishment of an appropriate electric field distribution, a desired change in flow regime will occur which is able to positively influence heat transfer rates at significantly lower voltage levels and pressure drop penalties. These results were predicted through the interpretation of the finite element results of the electric field distribution for the arrangement under investigation. The experiment has demonstrated that when the electrode was positioned eccentrically +2.73 mm from the centerline, a 160% enhancement in heat transfer coefficient was observed under the application of a 2.0 kV DC voltage while the

pressure drop increase was only 1.2 fold. Locally, heat transfer coefficient enhancement in excess of 800% has been observed. These results indicate heat transfer enhancement increased with high electric fields and decreased with increased mass and heat fluxes for the given experimental conditions.

Chapter 9

Conclusions

The fundamental goal of this investigation has been accomplished; the initiation of a methodology in the development of the EHD technique as applied to heat transfer in two-phase systems. This investigation has shown that electric body forces may lead to a reduction in the thermal boundary layer, increased convection, boiling activity, interfacial area, interfacial instabilities or phase migration, that can result in a redistribution of the flow regime and, as a consequence, an augmentation in heat transfer rates. Accordingly, in an effort to aid in the prediction of heat transfer coefficients in EHD two-phase convective boiling systems, a mechanistic model to determining flow regime transition due to the influence of the electric field has been developed.

To accomplish this a finite element analysis was performed to determine the electric field distribution for a concentric electrode and two eccentric electrode configurations in two phases having different liquid-vapour distributions and interfacial geometries. These results, coupled with analytical calculations for several symmetric flow regimes, revealed qualitative evidence regarding the redistribution of phases and provided an understanding of the forces acting on the interface. The interfacial electric forces were subsequently introduced into a modified flow pattern map to account for the electric field effect on the transition boundaries between stratified and annular or intermittent flows. Combining this flow pattern map and electric field analysis with the experimental overall and local parametric study, the axial

flow patterns progression was reconstructed to explain the pressure drop increase and heat transfer augmentation observed. In general it was found that when the flow redistribution wet parts of the channel that were previously dry (*i.e.*, changed stratified flow to annular) or thinned the thermal boundary layer by extracting liquid in contact with the tube, vaporization enhancement occurred.

To establish how and when EHD may influence a forced convective flow, a dimensional analysis was performed. Through this analysis it was shown that the electrohydrodynamic forces become significant when the ratio of the Dielectric Electric Rayleigh number is of the same order of magnitude as the square of the liquid Reynolds number, $E_{tc} \sim Re^2$. The aforementioned flow boiling experiments have provided evidence that when the proposed dimensionless criterion is satisfied, EHD body forces have a strong influence on the liquid-phase and consequently the flow pattern within the channel. This flow redistribution is the primary mechanism affecting the increase in pressure drop and the augmentation or even suppression of heat transfer. If anything, this dissertation has shown the importance of determining the flow regime if accurate methods of estimating flow boiling heat transfer rates are to be developed for EHD enhanced convective boiling.

To summarize, the experimental investigation produced the following results through which the above conclusions were drawn and future research areas, outlined in the following chapter, identified:

a) The Concentric Electrode Configuration in the Presence of AC and DC Electric Fields

- The evaporation results show that the overall heat transfer coefficients may be increased by as much as 250% for an 8 kV DC applied voltage and approximately 300% for 24 kV (peak to peak) 60 Hz AC voltage in the concentric arrangement.

- The drawbacks are the power requirements of the voltage supply and the increase in pressure loss for the electrode arrangement. For the concentric electrode, the pressure drop across the heat exchanger increased 1.8 and 2.6 fold for the DC and 60 Hz AC at maximum heat transfer enhancement, respectively. The pressure drop increased due to the establishment of unstable flow patterns. These fluctuating flow patterns tend to increase momentum interaction and hence pressure losses along the length of the tube, as well as increase the wall surface contact as the liquid is attracted to the electrode. The EHD power consumption was less than 3 mW for the DC experiments and less than 0.2 W for the 60 Hz AC experiments.

- Locally, heat transfer coefficient enhancement in excess of 2000% has been observed. However, it was also shown that the liquid extraction phenomena induced by imposing an electric field may result in premature dryout of the heat transfer surface and subsequently a reduction in heat transfer. The maximum quasi-local reduction in heat transfer coefficients was approximately 50%.

- The results suggest that under the experimental parameters investigated, enhancement increased with high electric fields and decreased with increased mass and heat fluxes. However, the primary mechanism of influence on both heat transfer and pressure drop is the effect of the electric field distribution on the flow pattern.

- Both low and high frequency AC voltages were investigated in order to verify the dimensional analysis prediction that the dominant force was dielectrophoretic. For the high frequency experiments, the flow pattern transition and heat transfer coefficient results coincided with those observed for the DC fields. This can be attributed to the fact that a high frequency AC field prevented the accumulation of a surface charge density on the liquid-vapour interface.

- Through the application of a low frequency (60 Hz) AC electric field, an entrained-droplet oscillatory flow regime developed, unique to any encountered in previous investigations. At the outlet of the test section the flow fluctuation occurred at approximately twice the frequency of the applied voltage as observed from the flow developed. The interaction and interfacial area of this phase was extremely high, which, when coupled with the increased turbulent mixing created by the oscillatory motion of the flow, proved to lead to significant enhancements in heat transfer coefficient when applied under the appropriate conditions.

b) The Eccentric Electrode Configurations in the Presence of a DC Electric Field

- The experiments conducted for the eccentric geometry have provided evidence that through the establishment of an appropriate electric field distribution, a desired change in flow regime will occur which is able to positively influence heat transfer rates at significantly lower voltage levels and pressure drop penalties. These results were predicted through the interpretation of the finite element results of the electric field distribution for the arrangement under investigation.

- The experiment has demonstrated that when the electrode was positioned eccentrically +2.73 mm from the centerline, a 160% enhancement in heat transfer coefficient was observed under the application of a 2.0 kV DC voltage. When compared to the voltage required to achieve a similar augmentation in heat transfer for the same conditions in the concentric electrode channel, positioning the electrode eccentrically required a 300% lower applied voltage.

- The pressure drop increase for this amount of enhancement was only 1.2 fold above eccentric (upper) base case, $V_i = 0.0$ kV. However, compared to the pressure drop for the concentric electrode without an applied voltage at identical conditions, the increase in pressure drop is only 1.16 fold, due to the effect of electrode position on pressure drop.

- Locally, heat transfer coefficient enhancement in excess of 800% have been observed.

- These results indicate heat transfer enhancement increased with high electric fields and decreased with increased mass and heat fluxes for the given experimental conditions.

Chapter 10

Recommendations For Future Work

During the course of the present investigation several new research areas have been identified that should be explored. Further research is needed in all aspects of EHD-coupled two-phase flow processes. Several issues brought to light in previous investigations have been addressed in this dissertation, however considerable work remains. The following items are recommended for future research:

- It is suggested that the Kattan *et al.* (1998c) methodology in predicting heat transfer rates be pursued. The development of a flow pattern map is a first step. At this stage of development, a data bank of investigations should be compiled and mechanistic models developed based on flow patterns.

- Further, adiabatic flow pattern visualization experiments should be performed with a conductive transparent channel to confirm the flow pattern map over a greater range of qualities. This may lead to a mechanistic approach to predict the transition criterion to mist flow or dryout of the heat transfer surface. Further, it is recommended that additional experiments be initiated at different electrode and tube diameters to determine the diameter ratio effect of flow pattern transition holds.

- As local heat transfer rates have a strong effect on the flow regime, it is suggested that a study be initiated to confirm the proposed diabatic flow pattern progression in convective flow boiling. A real-time neutron radiography (RTNR) technique of void fraction measurement and flow pattern reconstruction should be employed to reconstruct the flow regime during vaporization.

- More work is required in order to understand the effects of an alternating current in the flow regime. Particularly the oscillating regime encountered in this investigation. The frequency effects should be investigated in the range of 10 Hz to 1000 Hz.

- EHD investigations in the future should develop a method of measuring the electrical properties of refrigerants of known purities. In particular the dielectric constant and electrical conductivity due to the highly sensitive nature of these properties to impurities.

- Further experiments in EHD flow vaporization with different fluids and fluids with impurities are required to determine the effects of dielectric constant and conductivity on heat transfer performance and flow pattern transition as well as to confirm the proposed dimensionless criterion.

- Long term influences must be investigated to ensure that a continuous application of an electric field does not affect thermal or electrical fluid properties.

- The concept of electrohydrodynamic pumping should be coupled with EHD heat transfer augmentation investigations to reduce or eliminate pressure drop penalties.

- Experiments combining the upper eccentric geometry with AC applied voltages should be performed to realize the potential to apply higher voltages without electrical breakdown. This should result in considerably higher interfacial forces, and will likely result in a similar oscillatory flow pattern to that observed in the concentric experiments. With optimization of the electrode eccentricity and applied voltage frequency, significant enhancement should be observed over all ranges of conditions.

As EHD applied to two-phase systems has proven to be an effective tool in heat transfer augmentation and commercialization seems to be a certainty in the near future, manufacturability and feasibility studies should be conducted. As opposed to the addition of an electrode/spacer design to an existing commercial heat exchange channel, investigations should consider making the electrode geometry an integral part of a channel. Designing a heat exchanger that takes into consideration the electric field distribution required to influence the flow configuration towards regimes which are prone to higher heat transfer rates and making the electrode an integral part of the channel will likely lead to considerable heat transfer augmentation with potentially lower pressure losses by adding a pumping effect.

Nomenclature

Symbol	Description	Unit (SI)
a	speed of sound	m/s
A	area	m^2
A	Helmholtz free energy per unit mass	J/kg
A_L	area occupied by liquid	m^2
A_V	area occupied by vapour	m^2
B	magnetic flux density	N/A·m
B	parameter in Chisholm (1973) equation	–
C	capacitance	pF
C	friction factor coefficient	–
C	Lockhart & Martinelli constant	–
C_p	specific heat at constant pressure	kJ/kg·K
C_2	constant in Taitel and Dukler analysis	–
d, D	diameter or distance	m
d_b	bubble departure size	m
$dP, \Delta P$	pressure differential or drop	Pa
D	coefficient of molecular diffusion	$C \cdot m^2/s$
D	dielectric flux density (electric displacement)	C/m^2
D_h	hydraulic diameter	m
D_e	electrode diameter	m
D_i	tube inner diameter	m
D_j	shell water jacket inside diameter	m
D_L	liquid hydraulic diameter	m
D_o	outside annulus diameter	m
D_V	vapour hydraulic diameter	m
E	electric field strength	V/m
E	equation in the Friedel (1979) correlation	–
E_ℓ	EHD Rayleigh number	–

E_t	tangential electric field strength	V/m
f	frequency	Hz
f	friction factor	–
f_{eB}'''	electric body force per unit volume	N/m^3
f_g	gravitational force per unit area	N/m^2
f_I	interfacial friction factor	–
f_L	liquid friction factor	–
f_V	vapour friction factor	–
f''_e	interfacial electric force	N/m^2
f''_{ec}	conductive interfacial force per unit area	N/m^2
f''_{ed}	dielectric interfacial electric force per unit area	N/m^2
F	equation in the Friedel (1979) correlation	–
F	force	N
F	forced convection correction factor in Chen (1966)	–
F_B	body force	N/m^3
F_{KF}	parameter in Klimenko-Fyodorov map	–
g	acceleration due to gravity	m/s^2
G	mass flux	$kg/m^2 \cdot s$
h	heat transfer coefficient	$W/m^2 \cdot K$
h_i	liquid level above bottom of electrode	m
h_L	stratified liquid level	m
H	equation in the Friedel (1979) correlation	–
H	magnetic field strength	A/m
i	enthalpy	kJ/kg
i_{fv}	latent heat of vaporization	kJ/kg
I	current	A
I_e	direct electric heating preheater current	A
I_i	electrohydrodynamic current	A
j	superficial velocity	m/s
J	current density	A/m^2
k	thermal conductivity	$W/m \cdot K$
K	parameter in Taitel & Dukler Map	–
L	length	m
m	friction factor coefficient	–
$\dot{m}$	mass flow rate	kg/s
M	molecular mass	kg

n	friction factor coefficient	–
n	ion number density	m^{-3}
N_g	Loshmidt number	m^{-3}
P, p	pressure	Pa
P_{ATM}	atmospheric pressure	Pa
P_R	test section refrigerant inlet pressure	Pa
P_{SAT}	saturated refrigerant pressure	Pa
q	heat	W
q''	heat flux	W/m^2
q_{eB}'''	EHD energy generation rate per unit volume	W/m^3
Q	quantity of heat transferred	W
Q_{EHD}	EHD power consumption	W
$\dot{Q}$	volumetric flow rate	m^3/s
$\dot{Q}_R$	volumetric flow rate of single-phase subcooled refrigerant	m^3/s
$\dot{Q}_W$	volumetric flow rate of test section water	m^3/s
$\dot{Q}_{W\text{-}COND}$	volumetric flow rate of condenser water	m^3/s
$\dot{Q}_{W\text{-}PRE}$	volumetric flow rate of preheater water	m^3/s
r	radius or radial distance	m
R	electrical resistance	Ω
R_I	interfacial radius	m
Re_{lo}	Reynold's number with all flow as liquid	–
Fr_{lo}	Froude number with all flow as liquid	–
s	distance	m
S	suppression factor in Chen (1966)	–
S	surface area	m^2
S_I	interfacial perimeter	m
S_L	wetted liquid perimeter	m
S_V	wetted vapour perimeter	m
t	thickness	m
t	time	s
t_l, t_L	liquid annular film thickness	m
t_v	vapour annular film thickness	m
T	parameter in Taitel & Dukler Map	–
T	temperature	°C
$T_{R\text{-}COND\text{-}o}$	refrigerant condenser outlet temperature	°C
$T_{R\text{-}i}$	refrigerant test section inlet temperature	°C

$T_{R\text{-}o}$	refrigerant test section outlet/condenser inlet temperature	°C
$T_{R\text{-}Sub}$	refrigerant inlet temperature (subcooled)	°C
T_{SAT}	saturated refrigerant temperature	°C
$T_{W\text{-}COND\text{-}i}$	condensing water inlet temperature	°C
$T_{W\text{-}COND\text{-}o}$	condensing water outlet temperature	°C
$T_{W\text{-}i}$	test section heating water inlet temperature	°C
$T_{W\text{-}o}$	test section heating water outlet temperature	°C
$T_{W\text{-}PRE\text{-}i}$	preheater inlet water temperature	°C
$T_{W\text{-}PRE\text{-}o}$	preheater outlet water temperature	°C
$Tn_{W\text{-}b}$	test section axial top water temperature at location n	°C
$Tn_{W\text{-}t}$	test section axial bottom water temperature at location n	°C
$Tn_{S\text{-}b}$	test section axial bottom surface temperature at location n	°C
$Tn_{S\text{-}t}$	test section axial top surface temperature at location n	°C
u	velocity	m/s
u_l , u_L	liquid velocity	m/s
u_v , u_V	vapour velocity	m/s
U	overall heat transfer coefficient	$W/m^2 \cdot K$
U_L	superficial liquid velocity	m/s
U_o	reference velocity	m/s
U_V	superficial vapour velocity	m/s
v	velocity	m/s
V	voltage	V
V_e , V_i	voltage applied to electrode	V
V_l	interfacial voltage	V
V_o	voltage of tube	V
$\dot{V}$	volumetric flow rate	m^3/s
W	work	J
x	vapour quality	–
x , X	spacial co-ordinate	m
X_h	parameter in Hashizume map	–
y , Y	spacial co-ordinate	m
Y_h	parameter in Hashizume map	–
z	spacial co-ordinate	m

Greek

α	polarizability	–
α	thermal diffusivity	m^2/s
α	void fraction	–
β	volumetric thermal expansion constant	K^{-1}
γ	pressure drop ratio ($\nabla P/\nabla P_{E=0}$)	–
γ	density ratio	–
Γ	parameter in Chisholm (1973) correlation	–
ε	dielectric permittivity	N/V^2
ε_L	dielectric constant of liquid phase	–
ε_o	dielectric permittivity of free space	N/V^2
ε_s	dielectric constant ($\varepsilon/\varepsilon_0$)	–
ε_V	dielectric constant of vapour phase	–
η	heat transfer enhancement factor h/h_0	–
θ	temperature ratio	–
λ	charge density per unit length	$C/m^3/m$
λ	parameter in Hashizume map	–
μ	dynamic viscosity	kg/m·s
μ	ion mobility	$m^2/V{\cdot}s$
μ	permeability	N/A^2
μ_L	liquid dynamic viscosity	kg/m·s
μ_V	vapour dynamic viscosity	kg/m·s
ν	kinematic viscosity	m^2/s
ρ	mass density	kg/m^3
ρ	electrical resistivity	Ω·m
ρ_{ei}	charge density	C/m^3
ρ_L	liquid density	kg/m^3
ρ_V	vapour density	kg/m^3
ρ_+	positive charge density	C/m^3
ρ_-	negative charge density	C/m3
σ	surface tension	N/m
σ_e	electrical conductivity	S/m
σ_e	surface charge density	C/m^2
τ_σ	electrical charge relaxation time	s
τ_I	interfacial shear stress	Pa
τ_{OL}	liquid wall shear stress	Pa

τ_{ov}	vapour wall shear stress	Pa
φ	electric potential	V
φ_1	incident electric field angle	rad
φ_2	electric field angle exiting interface	rad
Φ_L^2	liquid two-phase multiplier	–
Φ_v^2	vapour two-phase multiplier	–
ψ'	parameter in Hashizume map	–

Dimensionless Numbers

b_{La}	Laplace Constant	$\left(\frac{\sigma_l}{(\rho_l - \rho_v) g D}\right)^{1/2}$
Bo	boiling number	$\frac{q}{Gi_{fv}}$
Co	convection number	$\left(\frac{1-x}{x}\right)^{0.8}\left(\frac{\rho_v}{\rho_l}\right)^{0.5}$
E_{kc}	conductive Rayleigh number	$\frac{I_0 L^3}{\rho_0 \nu^2 \mu_c A}$
$E_{kε}$	dielectric Rayleigh number	$\frac{\varepsilon_0 E_0^2 T_0 (\partial \varepsilon_s / \partial T)_\rho L^2}{2\rho_0 \nu^2}$
F	modified Froude number	$\frac{xG}{\sqrt{\rho_v[(\rho_L - \rho_v) D_o g]}}$
F_e	modified electric Froude number	$\frac{xG}{\sqrt{\rho_v[(\rho_L - \rho_v) D_o g - f_e'']}}$
Fr_l	liquid Froude number	$\frac{u_l^2}{gD_o}$
Fr_v	vapour Froude number	$\frac{u_v^2}{gD_o}$
M	Mach number	$\frac{u}{a}$

Nu	Nusselt number	$\frac{hD}{k}$
Pr	Prandtl number	$\frac{\mu C_p}{k}$
Re	Reynolds number	$\frac{GD}{\mu}$
Re_{Dh}	hydraulic Reynolds number	$\frac{GD_{Dh}}{\mu}$
Re_L	liquid Reynolds number	$\frac{D_L u_L \rho_L}{\mu_L}$
Re_V	vapour Reynolds number	$\frac{D_V u_V \rho_V}{\mu_V}$
S	slip ratio	$\frac{u_v}{u_l}$
We_L	liquid Weber number	$\frac{\rho_L u_L^2 D_o^2}{\sigma_L}$
X	Martinelli parameter	$\frac{(dp_f/dz)_L}{(dp_f/dz)_V}$

Abbreviations

AC	alternate current
DC	direct current
EHD	electrohydrodynamics
I.D.	inner diameter
N/A	not applicable or not available
O.D.	outer diameter

Subscripts

0	vacuum or reference
φ	phase
acc	acceleration component

avg	average
ATM	atmospheric
b	boiling, bottom or bulk
B	bottom or nucleate boiling
Bi	onset of nucleate boiling
BD	bubble detachment
c	cold or conductive
COND	condenser
d	dielectric
e	electrical or electrode
ef	effective
eq	thermodynamic equilibrium
f	free charges or frictional component
fc	forced convection
h	hot or hydrodynamic
H	homogeneous
i	inlet or inner
l, L	liquid
lm	log mean
LO	total flow is assumed to be liquid
m	mean
mac	macroscopic
mic	microscopic
n	normal
N	negative charge
o	only, outer or outlet
pool	pool boiling
pp	peak to peak
P	positive charge
PRE	preheater
R	refrigerant
s, S	surface
s, SAT	saturation state
sp	single-phase
ss	stainless steel
sup	wall superheat

SUB	subcooled
t	tangent or top or turbulent
tp	two-phase
tt	liquid and vapour phases are turbulent
T	constant temperature or total
v, V	vapour
VO	total flow is assumed to be vapour
w, W	water
x	local

References

Abdul-Razzak, A., Shoukri, M., and Chang, J.S., 1994, "Measurement of Two-Phase Refrigerant Liquid-Vapour Mass Flow Rate," *ASHRAE Research Report (722-TRP)*.

Abdul-Razzak, A., Shoukri, M., and Chang, J.S., 1995, "Characteristics of Refrigerant R-134a Liquid Vapor Two-Phase Flow in a Horizontal Pipe," *ASHRAE Trans.*, Vol. 101, Pt. 1, pp. 953-964.

Assael, M.J., Nagasaka, Y., Nieto de Castro, C.A., Perkins, R.A., Ström, K., Vogel, E., and Wakeham, W.A., 1995, "Status of the Round Robin on the Transport Properties of R-134a," *Int. J. Thermophysics*, Vol. 16, No. 1, pp. 63-78.

Ashmann, G., and Kronig, R., 1951, "The Influence of Electric Fields in the Convective Heat Transfer in Liquids," *Appl. Sci. Res.*, Vol. A2 (1950), pp. 235-244, erratum in Vol. A3 (1951), pp. 85-88.

ASHRAE Handbook: Fundamentals - SI Edition, 1997, "Thermophysical Properties of Refrigerants," *ASHRAE Inc.*, Chapter 19.

ASTM D 924 - 92, 1999, *Annual Book of ASTM Standards*, "Standard Test Method for Dissipation Factor (or Power Factor) and Relative Permittivity (Dielectric Constant) of Electrical Insulating Liquids," Section 10.3, pp. 54-60.

Atten, P., McCluskey, A.M.J., and Lahjomri, A.C., 1987, "The Electrohydrodynamic Origin of Turbulence in Electrostatic Precipitators," *IEEE Trans. Ind. Appl.*, IA-23, pp. 705-711.

Baker, O., 1954, "Design of Pipe Lines for Simultaneous Flow of Oil and Gas," *Oil and Gas J.*, July, pp. 26.

Barao, T., Nieto de Castro, C.A., Mardolcar, U.V., Okambawa, R., and St-Arnaud, J.M., 1995, "Dielectric Constant, Dielectric Viral Coefficients, and Dipole Moments of 1,1,1,2-Tetrafluoroethane," *J. Chem. Eng. Data*, Vol. 40, pp. 1242-1248.

Barao, T., Mardolcar, U.V., and Nieto de Castro, C.A., 1996, "The Dielectric Constant of Liquid HFC 134a and HCFC 142b," *Int. J. Thermophysics*, Vol. 17, No. 3, pp. 573-585.

Baroczy, C.J., 1966, "A Systematic Correlation for Two-Phase Pressure Drop," *Chem. Eng. Prog. Symp. Ser.*, Vol. 62/64, pp. 232-249.

Berghmans, J., 1976, "Electrostatic Fields and the Maximum Heat Flux," *Int. J. Heat Mass Transfer*, Vol. 19, pp. 791-797.

Bergles, A.E., Nirmalan, V., Junkhan, G.H., and Webb, R.L., 1983, "Bibliography on Augmentation of Convective Heat and Mass Transfer II," Heat Transfer Laboratory Report HTL-31, ISU-ERI-Ames-84221, Iowa State University, December.

Bergles, A.E., 1988, "Some Perspectives on Enhanced Heat Transfer - Second-Generation Heat Transfer Technology," *Trans. ASME*, Vol. 110, pp. 1082-1096.

Bergles, A.E., Jensen, M.K., Somerscales, E.F.C., and Manglik, R.M., 1991, "Literature Review of Heat Transfer Enhancement Technology for Heat Exchangers in Gas Fired Applications," GRI 91-0146, Gas Research Institute, Chicago, Illinois.

Bjorge, R.W., Hall, G.R., and Rohsenow, W.M., 1982, "Correlation of Forced Convection Boiling Heat Transfer Data," *Int. J. Heat Mass Transfer*, Vol. 25, No. 6, pp. 753-757.

Blasius, H., 1913, "Das Ahnlichkeitsgesetz bei Reibungsvorgangan in Flussigkeiten," *Mitteilungen uber Forschungs Arbeiten Ingenieur Wesens*, No. 134.

Bologa, M.K., Kozhukhar, I.A., Mardarskiy, O.I., and Shkilev, V.D., 1980, "Heat Transfer and Hydrodynamics of Electrohydrodynamic Heat Pipes," *Heat Transfer-Soviet Research*, Vol. 12, pp. 173-191.

Bologa, R.W., Korovkin, V.P., and Savin, I.K., 1995, "Mechanism of Condensation Heat Transfer Enhancement in an Electric Field and the Role of Capillary Processes," *Int. J. Heat Mass Transfer*, Vol. 38, No. 1, pp. 175-182.

Bonjour, E., Verdier, J. and Weil, L., 1962, "Electroconvection Effects on Heat Transfer," Chem. Eng. Progress, Vol. 58, No. 7, pp. 63-66.

Bottcher, C.J.F., 1952, *Theory of Electric Polarization*, Elsevier Co., New York.

Briggs, D.E., and Young, E.H., 1969, "Modified Wilson Plot Techniques for Obtaining Heat Transfer Correlations for Shell and Tube Heat Exchangers," *Chem. Eng. Prog. Symp. Ser.*, Vol. 65, No. 92, pp. 35-45.

Brocilo, D., 1997, Private Communication.

Brunner, K., and Chang, J.S., 1980, "Flow Regime Transition Under Electric Fields in Horizontal Two-Phase Flow," *Proc. 15th IEEE Ind. Appl. Soc. Conf.*, pp. 1042-1047.

Bryan, J.E., and Seyed-Yagoobi, J., 1997, "Influence of Flow Regime, Heat Flux, and Mass Flux on Electrohydrodynamically Enhanced Convective Boiling," *ASME Heat Transfer Division (Publication)*, HTD-351, pp. 187-196.

Bryan, J.E., 1998, "Fundamental Study of Electrohydrodynamically Enhanced Convective and Nucleate Boiling Heat Transfer," PhD Thesis, Texas A&M University, United States.

Butterworth, D., 1972, "A Visual Study in Horizontal Air-Water Flow," Rept. AERE-M2556, UKAEA, Harwell.

Carey, V., 1992, *Liquid-Vapor Phase-Change Phenomena: An Introduction to the Thermophysics of Vaporization and Condensation Processes in Heat Transfer Equipment*, Hemisphere Publishing, New York.

Chang, J.S., and Tran, F., 1980, "Numerical Analysis of Transient Natural Convection of Gas in a Horizontal Cylindrical Annulus Under a DC Electric Field,"*ASME Heat Transfer Division (Publication)*, HTD-16, pp. 51-59.

Chang, J.S., 1984, "Impact of Electromagnetic Field and Pulse on the Boiling of Conducting and Nonconducting Fluids," *Proc. 1984 Int. Electromagnetic Compatibility Conf.*, D.S. Bern *et al.* ed., Tech. Univ. Wroclaw Press, Poland, pp. 719-730.

Chang, J.S., 1989a, "Electrohydrodynamic Control of Fluid Flow and Heat Transfer," *Cham. Eng.*, Japan (Kagaku Kogaku), Vol. 53, pp. 100-103.

Chang, J.S., 1989b, "Stratified Gas-Liquid Two-Phase Electrohydrodynamics in Horizontal Pipe Flow," *IEEE Trans. Ind. Appl.*, Vol. 25, No. 2, pp. 241-247.

Chang, J.S., and Maezono, I., 1989, "The Effects of Electrohydrodynamic Flow on a Corona Torch," *J. of Electrostatics*, Vol. 23, pp. 323-330.

Chang, J.S., Myint, T.A., Wu, M.W., Galichi, D., and Brodowicz, K., 1991, "Development of Non-Intrusive Capacitance Transducer Techniques for Void Fraction, Velocity and Flow Regime Measurements in Two-Phase Gas-Powder Flow," *Proc. Int. Conf. Multi-Phase Flow*, 91-Tsukuba, G. Matsui, and A. Serizawa, ed., Vol. 2, pp. 265-269.

Chang, J.S., and Watson, A., 1994, "Electromagnetic Hydrodynamics," *IEEE Trans. Dielectric. and Elec. Insu.*, Vol. 1, No. 5, pp. 871-895.

Chang, J.S., 1998, "Two-Phase Flow In Electrohydrodynamics," Part V, *Electrohdyrodynamics*, International Centre for Mechanical Sciences Courses and Lectures- No. 380, A. Castellanos, ed., Springer Wein, New York.

Chen, J.C., 1966, "A Correlation for Boiling Heat Transfer to Saturated Fluids in Convective Flow," *Ind. Eng. Chem., Process Design and Development*, Vol. 5, No. 3, pp. 322-329.

Cheng, K.J., and Chaddock, J.B., 1986, "Maximum Size of Bubbles During Nucleate Boiling in an Electric Field," *Int. J. Heat Fluid Flow*, Vol. 7, No. 4, pp. 278-282.

Cheung, K.H., Ohadi, M.M., and Dessiatoun, S., 1995, "Compound Enhancement of Boiling Heat Transfer of R-134a in a Tube Bundle," *ASHRAE Trans.*, Vol. 101, Pt. 1, pp. 1009-1019.

Chisholm, D., 1973, "Pressure Gradients Due to Friction During the Flow of Evaporating Two-Phase Mixtures in Smooth Tubes and Channels," *Int. J. Heat Mass Trans.*, Vol. 16, pp. 347-358.

Choe, W.G., Weinberg, L., and Weisman, J., 1978, "Observation and Correlation of Flow Pattern Transition in Horizontal Cocurrent Gas-Liquid Flow," *Two-Phase Transport and Reactor Safety*, T.N. Veziroğlu, and S. Kakaç, ed., Hemisphere, Washington, pp. 1357-1393.

Choi, H.Y., 1968, "Electrohydrodynamic Condensation Heat Transfer," *ASME J. Heat Transfer*, Vol. Vol. 90, No. 1, pp. 98-102.

Chu, B.T., 1959, "Thermodynamics of Electrically Conducting Fluids," *Phys. Fluids*, Vol. 2, No. 5, pp. 473-484.

Chubb, L.W., 1916, "Improvements Relating to Methods and Apparatus for Heating Liquids," U.K. Patent No. 100796.

Collier, J.G., and Thome, J.R., 1994, *Convective Boiling and Condensation*, 3rd ed., Oxford University Press, Oxford.

Cooper, P., 1992, "Practical Design Aspects of EHD Heat Transfer Enhancement in Evaporators," *ASHRAE Trans.*, Vol. 98, Pt. 2, pp. 445-454.

Cotton, J.S., Abdul-Razzak, A., Shoukri, M., and Richter, M., 1996, "Pressure Drop During Two-Phase Flow of Refrigerant R-134a in a Horizontal Pipe," *CSME Symp.*, Hamilton, Pt. 1, pp. 34-41.

Cotton, J.S., Brocilo, D., Shoukri, M., Smith-Pollard, T., and Chang, J.S., 1998a, "Mechanisms of Electrohydrodynamic Flow Boiling Heat Transfer in Coaxial Flow Channels of Dielectric Refrigerant R-134a," *Annual Report of 1998 Conf. Elec. Insu. and Dielectric Phenomena, CEIDP*, Vol. 1, pp. 178-181.

Cotton, J.S., Shoukri, M., Chang, J.S., and Smith-Pollard, T., 1998b, "A Study of Convective Boiling Electrohydrodynamic (EHD) Heat Transfer in a Horizontal Flow Channel," *17th Multi-Phase Flow Symp.*, Tokyo, pp. 93-95.

Cross, J.D., and Wang, C.R., 1991, "Interfacial Instability -- A New Approach to Transient EHD Motion with Unipolar Injection," *IEEE Trans. Elec. Insu.*, Vol. 26, No. 4, pp. 641-646.

Damianidis, C., Karayiannis, T.G., Al-Dadah, R.K., James, R.W., Collins, M.W., and Allen, P.H.G., 1992, "EHD Boiling Enhancement in Shell-and-Tube Evaporators and its Application in Refrigeration Plants," *ASHRAE Trans.*, Vol. 98, Pt. 2, pp. 462-472.

Darabi, J., Salehi, M., Saeedi, M.H., and Ohadi, M.M., 1995, "Review of Available Correlations for Prediction of Flow Boiling Heat Transfer in Smooth and Augmented Tubes," *ASHRAE Trans.*, Vol. 101, Pt. 1, pp. 965-975.

Davidson, W.F., Hardie, P.H., and Humphreys, C.G.R., 1943, "Studies of Heat Transmission through Boiler Tubing at Pressures from 500 to 3300 pounds," *Trans. ASME*, Vol. 65, pp. 553-591.

Dittus, F.W., and Boelter, L.M., 1930, *University of California (Berkeley) Publications on Engineering*, Vol. 2, pp. 443.

Dodkoski, A.B., and Bologa, M.K., 1981, "Vapor Film Condensation Heat Transfer and Hydrodynamics under the Influence of an Electric Field, *Int. J. Heat Mass Trans.*, Vol. 24. No. 5, pp. 811-819.

Dupont Technical Information, 1993, "Thermodynamic Properties of HFC-134a (1,1,1,2-Tetrafluoroethane)," T-134a-SI.

Duffin, W.J., 1973, *Electricity and Magnetism*, McGraw-Hill, Toronto.

Eames, I.W., and Sabir, H.M., 1997, "Potential Benefits of Electrohydrodynamic Enhancement of Two-Phase Heat Transfer in the Design of Refrigerant Systems," *Appl. Thermal Eng.*, Vol. 17, No. 1, pp. 79-92.

Felici, N., and Lacroix, J.C., 1978, "Electroconvection in Insulating Liquids With Special Reference to Uni- and Bi-polar Injection," *J. Electrostatics*, Vol. 5, pp. 135-144.

Fellows, B.R., Richard, R.G., and Shankland, I.R., 1991, "Electrical Characterization of Alternative Refrigerants," *XVIIth Int. Cong. of Refrig.*, Paper No. 45, Montreal, Canada, pp. 98-402.

Fernández, J.L., and Poulter, R., 1987, "Radial Mass Flow in Electrohydrodynamically-Enhanced Forced Heat Transfer in Tubes," *Int. J. Heat Mass Transfer*, Vol. 30, No. 10, pp. 2125-2136.

Filonenko, G.K., 1954, "Hydraulic Resistance in Pipes," (in Russian) Teploénergetika 1, No. 4., pp. 40-44.

Friedel, L., 1979, "Improved Friction Pressure Drop Correlations for Horizontal and Vertical Two-Phase Flow," *European Two-Phase Flow Group Meeting*, Italy, Paper E2.

Fujino, T., Yokoyama, Y., and Mori, Y.H., 1989, "Augmentation of Laminar Forced Convective Heat Transfer by the Application of a Transverse Electric Field," *ASME J. Heat Transfer*, Vol. 111, pp. 345-351.

Garton, C.G., and Krasucki, Z., 1964, "Bubbles in Insulating Liquids: Stability in an Electric Field," *Proc. Roy. Soc.* A, London, Vol. 280, pp. 211-226.

Govan, A.H., Hewitt, G.F., Owen, D.G., and Bott, T.R., 1988, "An Improved CHF Modelling Code," *Proc. 2nd U.K. Conf. Heat Transfer*, Institute of Mechanical Engineers, London, Vol. 1, pp. 33-48.

Gungor, K.E., and Winterton, R.H.S., 1986, "A General Correlation for Flow Boiling in Tubes and Annuli," *Int. J. Heat Mass Transfer*, Vol. 29, No. 3, pp. 351-358.

Gungor, K.E., and Winterton, R.H.S., 1987, "Simplified General Correlation for Saturated Flow Boiling and Comparisons of Correlations With Data," *Can. J. Chem. Eng.*, Vol. 65, No. 1, pp. 148-156.

Gurova, A.N., Barao, T., Nieto de Castro, C.A., and Mardolcar, U.V., 1994, "The Thermal Conductivity and Dielectric Constant of HCFC-141b, HCFC-123, HCFC-142b, and HFC-134a," *High Temp.-High Pres.*, Vol. 26, pp. 25-34.

Ha, S., and Bergles, A.E., 1992, "Heat Transfer Characteristics of Horizontal In-tube Evaporator," Heat Transfer Laboratory Report HTL-10, Rensselaer Polytechnic Institute, New York.

Haidra, M., and Atten, P., 1985, "Role of EHD Motion in the Electrical Conduction of Liquid in a Blade Plane Geometry," *IEEE Trans. Ind. Appl.*, Vol. 21, pp. 709-714.

Hashizume, K., 1983, "Flow Pattern and Void Fraction of Refrigerant Two-Phase Flow in a Horizontal Pipe," *Bulletin of JSME*, Vol. 26, No. 219, pp. 1597-1602.

He, W., and Chang, J.S., 1995, "EHD Enhanced Mass Transfer Operations and Chemical Reactions," Chapter 24, *Handbook of Electrostatic Processes*, J.S. Chang, A.J. Kelly, and J.M. Crowley, ed., Marcal Dekker, Inc., New York, pp. 527-554.

Hewitt, G.F., and Hall-Taylor, N.S., 1970, *Annular Two-Phase Flow*, Pergamon Press, Oxford.

Hewitt, G.F., 1978, "Critical Heat Flux in Flow Boiling," *Proc. 6th Int. Heat Transfer Conf.*, Toronto, Keynote Lecture, Vol. 6, pp. 143-172.

Hewitt, G.F., 1982, "Liquid-Gas Systems," Chapter 2, *Handbook of Multiphase Systems*, G. Hetsroni, ed., McGraw-Hill, New York.

Husain, A., and Weisman, J., 1978, "Applicability of Homogeneous Flow Model to Two-Phase Pressure Drop in a Straight Pipe and Across Area Changes," *Chem. Eng. Prog. Symp. Ser.*, Vol. 74, pp. 205-214.

Johnson, R.L., 1968, "Effect of an Electric Field on Boiling Heat Transfer," *AIAAJ*, Vol. 6, August, pp. 1456-1460.

Jones, T.B., and Schaeffer, R.C., 1976, "Electrohydrodynamically Coupled Minimum Film Boiling in Dielectric Fluids," *AIAAJ*, Vol. 14, pp. 1759-1765.

Jones, T.B., 1978, "Electrohydrodynamically Enhanced Heat Transfer in Liquids - A Review," *Advances in Heat Transfer*, Vol. 14, pp. 107-148.

Joos, F.M., and Snaddon, R.W.L., 1985, "A Study of Flow Boiling Heat Transfer with Refrigerant Mixtures," *Int. J. Heat Mass Transfer*, Vol. 32, No. 9, pp. 1751-1764.

Jung, D.S., McLinden, M., Radermacher, R., and Didion, D., 1989, "A Study of Flow Boiling Heat Transfer with Refrigerant Mixtures," *Int. J. Heat Mass Transfer*, Vol. 32, No. 9, pp. 1751-1764.

Kandlikar, S.G., 1983, "An Improved Correlation for Predicting Two-Phase Flow Boiling Heat Transfer Coefficients in Horizontal and Vertical Tubes," *Heat Exchangers for Two-Phase Flow Applications*, ASME, New York.

Kandlikar, S.G., 1990, "A General Correlation for Saturated Two-Phase Flow Boiling Heat Transfer Inside Horizontal and Vertical Tubes," *ASME J. Heat Transfer*, Vol. 112, pp. 219-228.

Kao, K.C., 1961, "Some Electromechanical Effects on Dielectrics," *British J. Appl. Phys.*, Vol. 12, November, pp. 629-632.

Kattan, N., 1996, "Contribution to the Heat Transfer Analysis of Substitute Refrigerants in Evaporator Tubes with Smooth or Enhanced Tube Surfaces," Ph.D. Thesis, N° 1498, École Polytechnique Fédérale De Lausanne, Lausanne, Switzerland.

Kattan, N., Thome, J.R., and Favrat, D., 1998a, "Flow Boiling in Horizontal Tubes: Part 1 - Development of a Diabatic Two-Phase Flow Pattern Map," *ASME J. Heat Transfer*, Vol. 120, February, pp. 140-147.

Kattan, N., Thome, J.R., and Favrat, D., 1998b, "Flow Boiling in Horizontal Tubes: Part 2- New Heat Transfer Data for Five Refrigerants," *ASME J. Heat Transfer*, Vol. 120, February, pp. 148-155.

Kattan, N., Thome, J.R., and Favrat, D., 1998c, "Flow Boiling in Horizontal Tubes: Part 3-Development of a New Heat Transfer Model Based on Flow Pattern," *ASME J. Heat Transfer*, Vol. 120, February, pp. 156-165.

Kawahira, H., Yoshiaki, K., Yokoyama, T., and Ogata, J., 1990, "The Effect of an Electric Field on Boiling Heat Transfer of Refrigerant-11- Boiling on a Single Tube," *IEEE Trans. Ind. Appl.*, Vol. 26, No. 2, pp. 359-365.

Kip, A.F., 1969, *Fundamentals of Electricity and Magnetism*, 2nd ed., McGraw-Hill, New York.

Klimenko, V.V., 1990, "A Generalized Correlation for Two-Phase Forced Flow Heat Transfer," Second Assessment, *Int. J. Heat Mass Transfer*, Vol. 33, pp. 2073-2088.

Klimenko, V.V., and Fyodorov, M., 1990, "Prediction of Heat Transfer for Two-Phase Forced Flow in Channels of Different Orientation," *Proc. 9th Int. Heat Trans. Conf.*, Vol. 5, pp. 65-70.

Kline, S.J., and McClintock, F.A.,1953, "Describing Uncertainties in Single Sample Experiments," *Mech. Eng.*, pp. 3-8.

Kutateladze, S.S., 1961, "Boiling Heat Transfer," *Int. J. Heat Mass Transfer*, Vol. 31, pp. 541-552.

Laudau, L.D., and Lifshitz, E.M., 1963, *Electrodynamics of Continuous Media*, Pergamon, New York.

Langevin, P., 1905, "Magnétisme et théorie des électrons," (Magnetism and the theory of electrons) *Ann. Chim. Phys.*, Vol. 5, No. 8, pp. 70-127.

Lightstone, L., Osamusali, S.I., and Chang, J.S., 1991, "Gas-Liquid Two-Phase Flow in Symmetrically Divided Horizontal Tubes," *AIChE J.*, Vol. 37, No. 1, pp. 111-122.

Lockhart, R.W., and Martinelli, R.C., 1949, "Proposed Correlation of Data for Isothermal Two-Phase, Two Component Flow in Pipes," *Chem. Eng. Progress*, Vol. 45, No. 1, pp. 39-48.

Lovenguth, R., and Hanesian, D., 1971, "Boiling Heat Transfer in the Presence on Nonuniform, Direct Current Electric Fields," *Ind. Eng. Chem. Fundam.*, Vol. 10, No. 4, pp. 570-576.

Lui, Z., and Winterton, R.H.S., 1991, "A General Correlation for Saturated and Subcooled Flow Boiling in Tubes and Annuli Based on a Nucleate Pool Boiling," *Int. J. Heat and Mass Transfer*, Vol. 34, pp. 2759-2765.

Martinelli, R.C., and Nelson, B., 1948, "Prediction of Pressure Drop During Forced Circulation Boiling Water," *Trans. ASME*, Vol. 70, pp. 695-702.

McAdams, W.H., Woods, W.K., Heroman, J.R., L.C.,1942, "Vaporization Inside Horizontal Tubes, II-Benzene-Oil Mixtures," *Trans. ASME*, Vol. 64, p. 193-200.

McAllister, I.W., 1989, "The Dielectric Strength of 1,1,1,2-$C_2H_2F_4$ (Arcton-34a)," *J. Phys. D: Appl. Phys.*, Letter to the Editor, Vol. 22, pp. 1783-1784.

McFadden, P.W., and Grassmann, P., 1962, "The Relation Between Bubble Frequency and Diameter During Nucleate Pool Boiling," *Int. J. Heat Mass Transfer*, Vol. 5, pp.169-173.

Melcher, J.R., 1961, "EHD and MHD Surface Waves and Instabilities," *Phys. Fluids*, Vol. 4, pp. 1348-1354.

Melcher, J.R., 1963, *Field-Coupled Surface Waves: A Comparative Study of Surface-Coupled Electrohydrodynamic and Magnetohydrodynamic Systems*, M.I.T. Press, Cambridge, Massachusetts.

Melcher, J.R., 1976, "Electric Fields and Forces in Semi-Insulating Liquids," *J. Electrostatics*, No. 2, pp. 121-132.

Melcher, J.R., 1981, *Continuum Electromechanics*, M.I.T. Press, Cambridge, Massachusetts.

Meyer, C.W., and Morrison, G., 1991, "Dipole Moments of Seven Partially Halogenated Ethene Refrigerants," *J. Phys. Chem.*, Vol. 95, pp. 3860-3866.

Moody, L.F., 1944, "Friction Factors for Pipe Flow," *Trans. ASME*, Vol. 66, November, pp. 671-684.

Norris, C., 1998, "Electrohydrodynamic (EHD) Effects on Convective Boiling In Horizontal Tubes," M. Eng. Thesis, McMaster University, Hamilton, Ontario, Canada.

Norris, C., Cotton, J.S., Shoukri, M., Chang, J.S., and Smith-Pollard, T., 1999, "Electrohydrodynamic Effects on Flow Redistribution and Convective Boiling in Horizontal Concentric Tubes," *ASHRAE Trans.*, Vol. 105, Pt. 1, pp. 222-236.

Ogata, S., Tan, K., Nishijima, K., and Chang, J.S., 1985, "Development of Improved Bubble Disruption and Dispersion Technique by an Applied Electric Field Method," *AIChE J.*, Vol. 31, No. 1, pp. 62-69.

Ogata, J., and Yabe, A., 1991, "Augmentation of Nucleate Boiling Heat Transfer by Applying Electric Fields: EHD Behaviour of Boiling Bubble," *Proc. ASME/JSME Thermal Eng. Joint Conf.*, Book No. I0309C, pp. 41-46.

Ogata, J., Iwafuji, Y., Shimada, Y., and Yamazaki, T., 1992, "Boiling Heat Transfer Enhancement In Tube-Bundle Evaporators Utilizing Electric Field Effects," *ASHRAE Trans.*, Vol. 98, Pt. 2, pp. 435-444.

Ogata, J., and Yabe, A., 1993a, "Augmentation of Boiling Heat Transfer by Utilizing the EHD Effect - EHD Behaviour of Boiling Bubbles and Heat Transfer Characteristics," *Int. J. Heat Mass Transfer*, Vol. 36, No. 3, pp. 783-791.

Ogata, J., and Yabe, A., 1993b, "Basic Study on the Enhancement of Nucleate Boiling Heat Transfer by Applying Electric Fields," *Int. J. Heat Mass Transfer*, Vol. 36, No. 3, pp. 775-782.

Ohadi, M.M., 1991, "Heat Transfer Enhancement in Heat Exchangers," *ASHRAE J.*, December, pp. 42-50.

Ohadi, M.M., Nelson, D.A., and Zia, S., 1991b, "Heat Transfer Enhancement of Laminar and Turbulent Pipe Flow via Corona Discharge," *Int. J. Heat Mass Transfer*, Vol. 34, No. 4/5, pp. 1175-1187.

Ohadi, M.M., Papar, R.A., Ng, T.L., Faani, M.A., and Radermacher, R., 1992, "EHD Enhancement of Shell Side Boiling Heat Transfer Coefficients of R-123/Oil Mixture," *ASHRAE Trans.*, Vol. 98, Pt. 2, pp. 427-434.

Ohadi, M.M., Dessiatoun, S., Singh, A., and Faani, M.A., 1993a, "EHD-Enhancement of In-tube Boiling of Alternative Refrigerant/Refrigerant Mixtures," *ATRI Final Report*, Project No. ARTI-MCLR 655-51700, August.

Ohadi, M.M., Dessiatoun, S., Singh, A., and Faani, M.A., 1993b, "EHD-Enhancement of In-tube Boiling of Alternative Refrigerant/Refrigerant Mixtures," *EHD Consortium Quarterly Reports*, No. 1, (September 1993), No. 2 (December 1993), No. 3, (March 1994).

Ohadi, M.M., Dessiatoun, S., Singh, A., Cheung, K., and Salehi, M., 1995a, "EHD-Enhancement of Boiling/Condensation Heat Transfer of Alternative Refrigerants," *Presented to U.S. Department of Energy and the EHD Consortium Members*, January, Chicago, Illinois.

Ohadi, M.M., Salehi, M., Dessiatoun, S., and Singh, A., 1995b, "EHD-Enhanced Pool Boiling of R-123 in a Parallel Configuration - Application to Compact Heat Exchangers," *4th ASME/JSME Thermal Eng. Joint Conf.*, Vol. 2, pp. 225-232.

Osamusali, S.I., and Chang, J.S., 1987, "Regime-4 Code for Prediction of Flow Regime Transition in a Horizontal Pipe, Annulus and Bundle Flow Under Gas-Liquid Two-Phase Flow," *Proc. 8th Annual Can. Nucl. Soc. Conf.*, Saint John, N.B., pp. 125-133.

Osamusali, S.I., 1988, "Study of Gas-Liquid Two-Phase Flow Pattern Transitions in Horizontal Pipe, Annulus and Nuclear Fuel Type Rod Bundle Flow Systems," Ph.D. Thesis, McMaster University, Hamilton, Canada.

Osamusali, S.I., and Chang, J.S., 1988, "Two Phase Flow Regime Transition in a Horizontal Pipe and Annulus Flow Under Gas-Liquid Two-Phase Flow," *Fundamentals of Gas-Liquid Flows*, ASME Winter Annual Meeting, Vol. 72, pp. 63-69.

Panofsky, W., and Phillips, M., 1962, *Classical Electricity and Magnetism*, 2nd ed., Addison-Wesley, Pub. Co., Reading, Massachusetts.

Peters, J.M.H., Sproston, J.L., and Walker, G., 1980a, "Preliminary Observations on Bulk Electroconvection in Electrically Stressed Liquid Insulants, Part I: Experimental Investigation," *J. of Electrostatics*, Vol. 8, pp. 139-152.

Peters, J.M.H., Sproston, J.L., and Walker, G., 1980b, "Preliminary Observations on Bulk Electroconvection in Electrically Stressed Liquid Insulants, Part II : Theoretical Investigation," *J. of Electrostatics*, Vol. 9, pp. 1-14.

Petukhov, B.S., and Popov, V.N., 1963, "Theoretical Calculation of Heat Exchange and Frictional Resistance in Turbulent Flow in Tubes of Incompressible Fluids with Variable Physical Properties," *High Temperature*, Vol. 1, No. 1, pp. 69-83.

Pohl, H., 1951, "The Motion and Precipitation of Suspensoids in Divergent Electric Fields," *J. Appl. Phys.*, Vol. 22, No. 7, pp. 869-871.

Pounder, C., 1980, "Charge Carrying Particles From Leidenfrost Boiling," *J. Electrostatics*, Vol. 9, pp. 159-182.

Prandtl, L., 1944, "*Führer durch die Strömungslehre*" (*Guide to Flow Theory*) Vieweg und Sohn, Braunschweig.

Richard, R.G., 2000, Private Communication, June 14, 2000.

Rohsenow, W.M., Harnett, J.P., and Ganic, E.N., 1985, *Handbook of Heat Transfer Fundamentals*, 2nd ed., McGraw-Hill, New York.

Salehi, M., Ohadi, M.M., and Dessiatoun, S., 1995, "EHD-Enhanced Convective Boiling of R-134a in Grooved Channels - Application to Compact Heat Exchangers," *ASME J. Heat Transfer*, Vol. 119, pp. 805-809.

Salehi, M., Ohadi, M.M., and Dessiatoun, S., 1996, "The Applicability of the EHD Technique for Convective Boiling of Refrigerant Blends-Experiments with R-404A," *ASHRAE Trans.*, Vol. 102, Part 1, pp. 839-844.

Schneider, J.M., and Watson, P.K., 1970, "Electrohydrodynamic Stability of Space-Charge-Limited Currents in Dielectric Liquids, I. Theoretical Study," *Phys. Fluids*, Vol. 13, No. 8, pp. 1948-1954.

Seyed-Yagoobi, J., Hardesty, J.T., Raghupathi, P., and Bryan, J.E., 1997, "Experimental Study of Electrohydrodynamically Augmented Pool Boiling Heat Transfer on Smooth and Enhanced Tubes," *J. Electrostatics*, Vol. 40/41, pp. 597-602.

Seyed-Yagoobi, J., and Bryan, J.E., 1999, "Enhancement of Heat Transfer and Mass Transport in Single-Phase and Two-Phase Flows with Electrohydrodynamics," *Advances in Heat Transfer*, Vol. 33, pp. 95-186.

Shah, M.M., 1976, "A New Correlation for Heat Transfer During Boiling Flow Through Pipes, *ASHRAE Trans.*, Vol. 82, Pt. 2, pp. 66-86.

Shah, M.M., 1982, "Chart Correlation for Saturated Boiling Heat Transfer: Equations and Further Study," *ASHRAE Trans.*, Vol. 88, Pt. 1, pp. 185-196.

Shoukri, M., and Abdul-Razzak, A., 1996 "Flow Regime Identification of R-134a Liquid- Vapor Flow in Horizontal Pipe," Presented by : J.S. Cotton, *ASHRAE Winter Meeting*, Seminar 26.

Singh, A., Kumar A., Dessiatoun, S., Faani, M.A., Ohadi, M.M., and Ansari, A.A., 1993, "Compound EHD-Enhanced Pool-Boiling of R-123 in a Liquid-to-Refrigerant Heat Exchanger," *ASME J. Heat Transfer*, Paper No. 93-WA/HT-40, New Orleans.

Singh, A., Ohadi, M.M., Dessiatoun, S., and Chu, W., 1994, "In-tube Boiling Heat Transfer Enhancement of R-123 Using the EHD Technique," *ASHRAE Trans.*, Vol. 100, Pt. 2, pp. 818-825.

Singh, A., 1995, "Electrohydrodynamic (EHD) Enhancement of In-Tube Boiling and Condensation of Alternative (Non-CFC) Refrigerants," Ph.D. Thesis, University of Maryland, Maryland, United States.

Singh, A., Ohadi, M.M., Dessiatoun, S., Salehi, M., and Chu, W., 1995, "In-tube Boiling Enhancement of R-134a Utilizing the Electric Field Effect," *4th ASME/JSME Thermal Eng. Joint Conf.*, Vol. 2, pp. 215-223.

Souza, A.L., Chato, J.C., Wattelet, J.P., and Christoffersen, B.R., 1993, "Pressure Drop During Two-Phase Flow of Pure Refrigerants and Refrigerant-Oil Mixtures in Horizontal Smooth Tubes," *ASME Heat Transfer Division (Publication)*, HTD-243, pp. 35-41.

Spedding, P.L., and Nguyen, V.T., 1980, "Regime Maps for Air Water Two-Phase Flow," *Chem. Eng. Sci.*, Vol. 35, pp. 779-793.

Steiner, D., and Taborek, J., 1992, "Flow Boiling Heat Transfer in Vertical Tubes Correlated by an Asymptotic Model," *Heat Transfer Eng.*, Vol. B, No. 2, pp. 43-69.

Steiner, D., 1993, "Heat Transfer to Boiling Saturated Liquids," *VDI-Wärmeatlas (VDI Heat Atlas)*, Verein Deutscher Ingenieure, ed. VDI-Gessellschaft Verfahrenstechnik und Chemieingenieurwesen (GCV), Düsseldorf, Germany, (Translator: J.W. Fullarton) pp. .

Stratton, J.A., 1941, *Electromagnetic Theory*, McGraw-Hill, New York.

Stuetzer, O.M., 1959, "Ion drag pressure generation," *J. Appl. Phys.*, Vol. 30, pp.984-994.

Stuetzer, O.M., 1963a, "Pressure Analysis of Conduction in Liquids," *Phys. Fluids*, Vol. 6, pp. 190-194.

Stuetzer, O.M., 1963b, "Gas Bubbles in a Charged Liquid," *J. Appl. Phys.*,Vol. 34, pp. 958-963.

Taitel, Y., and Dukler, A.E., 1976, "A Model for Predicting Flow Regime Transition in Horizontal and Near Horizontal Gas-Liquid Flow," *AIChE J.*, Vol. 22, pp. 47-55.

Taitel, Y., 1990, "Flow Pattern Transition in Two-Phase Flow," *9th Int. Heat Trans. Conf.*, Jerusalem pp. 237-254.

Tritton, D.J., 1977, *Physical Fluid Dynamics*, Van Nostrand Reinhold Company, New York, pp. 135-161.

Unal, H.C., 1986, "Prediction on Nucleate Boiling Heat Transfer Coefficients for Binary Mixtures," *Int. J. Heat Mass Transfer*, Vol. 29, No. 4, pp. 637-640.

Velkoff, H.R. and Miller, J.H., 1965, "Condensation of Vapor on a Vertical Plate with a Transverse Electrostatic Field," *ASME J. Heat Transfer*, Vol. 87, pp. 197-201.

Webb, R.L., 1980, "Special Surface Geometries for Heat Transfer Augmentation," Chapter 7, *Developments in Heat Exchanger Technology-I*, D. Chisholm, ed., Applied Science Publishers, London.

Webb, R.L., and Bergles, A.E., 1983, "Heat Transfer Enhancement: Second Generation Technology," *Mech. Eng.*, Vol. 105, pp. 60-67.

Webb, R.L., Bergles, A.E., and Junkhan, G.H., 1983, "Bibliography of U.S. Patents on Augmentation of Convective Heat and Mass Transfer," Heat Transfer Laboratory Report HTL-32, ISU-ERI-Ames-81070, Iowa State University, December.

Webb, R.L., 1987, "Enhancement of Single-Phase Heat Transfer," Chapter 17, *Handbook of Single -Phase Heat Transfer*, S. Kakac, R.K. Shah, and W. Aung, ed., Hemisphere Publishing Corp., Washington, D.C., pp. 287-324.

Webb, R.L., 1994, *Principles of Enhanced Heat Transfer*, John Wiley & Sons, Inc., New York.

Weisman, J., 1979, "Flow Pattern Identification in Concurrent Vapour-Liquid Flow," *Proc. Japan-US Seminar Two Phase Flow Dynamics*, Inter-University Seminar House, Kansai, Japan.

Whalley, P.B., 1990, *Boiling, Condensation and Gas-Liquid Flow*, Clarendon Press, Oxford.

Wilson, E.E., 1915, "A Basis for Rational Design of Heat Transfer Apparatus," *Trans. ASME*, Vol. 37, pp. 47-70.

Yabe, A., Kikuchi, K., Taketani, T., Mori, Y., and Hijikata, K., 1982, "Augmentation of Condensation Heat Transfer by Applying Non-Uniform Electric Fields," *Proc. of 7th Int. Heat Transfer Conf.*, Vol. 5, pp. 189-194.

Yabe, A., Kikuchi, K., Taketani, T., Mori, Y., and Hijikata, K., 1982, "Augmentation of Condensation Heat Transfer by Applying Non-Uniform Electric Fields," *Heat Transfer*, Hemisphere, Vol. 5, pp. 189-194.

Yabe, A., Mori, Y., and Hijikata, K., 1987a, "Heat Transfer Enhancement Techniques Utilizing Electric Fields," *Heat Transfer in High Technology and Power Engineering*, W.J. Yang, and Y. Mori, ed., Hemisphere, Washington, D.C., pp. 394-405.

Yabe, A., Taketani, T., Kikuchi, K., Mori, Y., and Hijikata, K., 1987b, "Augmentation of Condensation Heat Transfer Around Vertical Cooled Tubes Provided with Helical Wire Electrodes by Applying Non-Uniform Electric Fields," *Int. Heat Transfer Science and Technology*, B.X. Wang, ed., Hemisphere, Washington, D.C., pp. 812-819.

Yabe, A., Taketani, T., Maki, H., Takahashi, K., and Nakadai, Y., 1992, "Experimental Study of Electrohydrodynamically (EHD) Enhanced Evaporator For Non-Azeotropic Mixtures," *ASHRAE Trans.*, Vol. 98, Pt. 2, pp. 455-461.

Yabe, A., 1995, "Heat Engineering," Chapter 25, *Handbook of Electrostatic Processes*, J.S. Chang, A.J. Kelly, and J.M. Crowley, ed., Marcal Dekker, Inc., New York, pp. 555-580.

Yamashita, K., Kumagai, M., and Sekita, S., 1991, "Heat Transfer Characteristics on an EHD Condenser," *ASME/JSME Thermal Eng. Proc.*, Vol. 3, pp. 61-67.

Yamashita, K., and Yabe, A., 1995, "EHD Enhancement of Falling Film Evaporation Heat Transfer and Durability of EHD Heat Exchangers," *4th ASME/JSME Thermal Eng. Joint Conf.*, Vol. 4 pp. 253-260.

Yokoyama, T., Yamazaki, T., Kubo, Y., Ogata, J., Kawada, A., Ooki, Y., 1987, "Effect on an Electric Field on Boiling Heat Transfer of Fluorocarbon R-11," *International Centre for Heat and Mass Transfer in Refrigeration and Cryogenics*, J. Bouguard, and N. Afgan, ed., Hemisphere Publishing, pp. 140-151.

Appendix A

Electrical and Transport Properties of HFC-134a

Appendix A describes the transport and electrical property data and correlations of HFC-134a used throughout the thesis. The inclusion of this section avoids any confusion regarding the calculation of the various thermodynamic properties in the dissertation. Several researchers suggest that large discrepancies exist in the transport properties of HFC-134a between the results reported by various authors. This has subsequently resulted in an international project coordinated by the Subcommittee on Transport Properties of Commission 1.2 of the International Union of Pure and Applied Chemistry (Assael *et al.*, 1995). Although the thermodynamic transport properties have been reviewed in the committee's Round Robin study, little effort has been initiated to elucidate the discrepancies and the lack of data with respect to the electrical properties of HFC-134a. This appendix includes new measurements of the specific dielectric constant for HFC-134a, obtained from the test section described in Chapter 4. The experimental data obtained is compared with other results available in the literature in order to select the appropriate correlation.

Transport Properties

Two principal property tables are available for HFC-134a in the open literature: *ASHRAE Fundamentals* (1997) and *Dupont* (1993). A comparison has been made between

the two data sets. The difference in the correlated saturation temperature is within -0.03°C and -0.04°C. The *ASHRAE* data is adopted in this study as their sources openly meet the international standards required by the ASME. In order to minimize the regression errors encountered during data reduction, all relevant properties have been correlated for the range of refrigerant temperatures measured in this study (10°C to 40°C). Table A.1 lists the correlated transport property equations.

Table A.1: Transport Property Correlations.

Property	State	Correlation	R^2
Pressure	Saturated	$P_s = -184.53+474.73\exp(\frac{T_s}{42.96})$	0.9999968
Density - *f(T)*	Liquid (Subcooled)	$\rho_l = 1290.68 - 2.317\ T^{1.1173}$	0.999979
Specific Heat - *f(T)*	Liquid (Subcooled)	$C_{p_l} = 1.1527 + 0.1824\exp(\frac{T}{62.569})$	0.9999528
Viscosity - *f(T)*	Liquid (Subcooled)	$\mu_l = 18.382 + 268.55\exp(-\frac{T}{77.425})$	0.9999945
Thermal Cond. - *f(T)*	Liquid (Subcooled)	$k_l = 93.443 - 0.4648\ T^{0.99816}$	0.9999426
Density - *f(P)*	Liquid (Saturated)	$\rho_{ls}^{0.5} = 38.378 - 0.1414P^{0.5}$	0.9999959
	Vapour (Saturated)	$\rho_{vs} = -371.336 + 372.316\exp(\frac{P}{8230.56})$	0.9999995
Specific Heat - *f(P)*	Liquid (Saturated)	$C_{p_{ls}}^{\ 2} = 1.5364 + \frac{0.004820P}{\ln(P)}$	0.9999293
	Vapour (Saturated)	$\ln(C_{p_{vs}}) = -0.304973 + 0.0018896\ P^{0.5}\ln(P)$	0.9999316
Viscosity - *f(P)*	Liquid (Saturated)	$\mu_{ls}^{0.5} = 33.299 - 2.87848\ \ln(P)$	0.9999916
	Vapour (Saturated)	$\mu_{vs}^{0.5} = 2.9554 + 0.02081\ P^{0.5}$	0.9999128
Thermal Cond. - *f(P)*	Liquid (Saturated)	$k_{ls}^{-1} = 0.008661 + 2.117E\text{-}5\ P^{0.5}\ln(P)$	0.9999232
	Vapour (Saturated)	$k_{vs}^{-1} = 0.17917 - 0.01662\ \ln(P)$	0.9999789
Units: T (°C), P (kPa), ρ (kg/m^3), c_p (kJ/kgK), ν (μPas), *k* (mW/mK)			

Electrical Properties

In the present investigation, an accurate measurement of the electrical properties of HFC-134a is essential to the understanding of the EHD phenomena. Several researchers in the past decade have explored the electrical properties of these refrigerants. However, the range is not extensive and some discrepancies remain. The following section will compare the most relevant studies with the measurements of this experiment and outline the electrical properties used in the present study.

A technical limitation of the electrohydrodynamic technique is the limiting voltage gradient of the fluid, termed the dielectric strength, at which appreciable current flow (*or breakdown*) occurs and the dielectric fails. The following two studies assess the breakdown voltage. McAllister (1989) measured the breakdown voltage in the pressure range of 10 to 70 kPa at 20°C in a parallel-plate uniform electric field using a highly stabilized DC voltage. At a pressure of 69.1 kPa, the average breakdown value was 35.653 ± 0.016 kV for a 14mm gap or 25.47 kV/cm. Fellows *et al.* (1991) applied ASTM standard methods for gaseous measurements of dielectric strength and found that the breakdown voltage for HFC-134a at 101.325 kPa (21.1°C) with a 25.4 mm gap sphere to plate arrangement was 6.6 kV (26.0 kV/cm). In the present investigation, arcing occurred at applied voltages of approximately 10 kV for the annular gap tested (3.9 mm) in the liquid and vapour states. This corresponds to a breakdown voltage slightly below Fellows *et al.* (1991). However, arcing occasionally occurred as low as 9 kV during phase change experiments which is believed to be the result of the flow regime within the annular gap. Therefore, the maximum applied DC voltage was established at 8 kV to prevent arcing in the present investigation.

Several recent investigations have focussed on accurate measurements of the relative permittivity (specific dielectric constant) for HFC-134a as a function of temperature and pressure. In Fellows *et al.* (1991), the specific dielectric constant was determined for nineteen fluorocarbons using ASTM D 924 - 82b, *A-C Loss Characteristics and Relative Permittivity (Dielectric Constant) of Electrical Insulating Liquids*. The specific dielectric constant for HFC-134a was 9.51, but the publication does not mention the temperature and pressure. Both Gurova *et al.* (1994) and Barao *et al.* (1996) presented measurements of the liquid specific dielectric constant along the saturation line between 200 and 300K using a three-terminal capacitance method, reporting an accuracy of 0.1%. The results obtained in the Gurova *et al.* study were fitted to polynomial functions in temperature and density as shown in Equation (A.1). The Barao *et al.* (1996) results relevant to the range of saturation temperatures encountered within this investigation are summarized in Table A.2.

$$\varepsilon_l = \sum_{i=0}^{3} c_i T^i \quad , \quad \varepsilon_l = \sum_{i=0}^{3} d_i \rho^i \qquad \text{(A.1) a,b}$$

where

$c_0 = 11.3597 \pm 0.0104$ $\quad$ $d_0 = -203.655 \pm 0.011$
$c_1 = -83.5 \pm 1.7$ E-3 $\quad$ $d_1 = 51.7 \pm 3.3$ E-2
$c_2 = 30 \pm 1$ E-5 $\quad$ $d_2 = 43.00 \pm 0.25$ E-4
$c_3 = -26 \pm 1$ E-7 $\quad$ $d_3 = 1.27 \pm 0.06$ E-7

with T in °C and ρ in kg/m^3. (Note: Gurova *et al.* (1994) stated that T was in K)

Table A.2: Saturated Liquid Specific Dielectric Constant (Barao *et al.*, 1996).

Temperature (°C)	Dielectric Constant (Sat)
14.85	10.270
24.85	9.4551
31.85	9.0099
34.85	8.6770

Barao *et al.* (1995) extended the saturation data by measuring the specific dielectric constant for subcooled liquid HFC-134a between 205K and 308K in increments of 1 MPa from slightly above the saturation pressure to 20 MPa. These experiments were performed

in a modification of the same cell used to measure the saturation data in some of the previously mentioned studies. Again, the results relevant to the conditions within this investigation are summarized in Table A.3.

Table A.3: Subcooled Liquid Specific Dielectric Constant (Barao *et al.*, 1995).

Temperature (°C)	Pressure (kPa)	Density (kg/m^3)	Dielectric Constant
13.20	1110	1252.92	10.306
13.20	660	1250.76	10.281
24.29	1600	1214.93	9.5120
24.29	700	1209.66	9.4583
30.19	1100	1188.88	9.0299
35.01	1520	1172.09	8.7199
35.01	950	1167.91	8.6813

When comparing the three referenced studies, the specific dielectric constant is almost invariant with respect to pressure. For example, at a liquid temperature of 24.29°C the Gurova *et al.* (1994) correlation for the saturation line (P_{SAT} = 651.07 kPa) produced a value of specific dielectric constant of 9.4712, while the Barao *et al.* (1995) study produced values for the specific dielectric constant of 9.4583 and 9.5120 at the same temperature with subcooled pressures corresponding to 700 kPa and 1600 kPa, respectively. Similar results were found with the Barao *et al.* (1996) measurement of the saturation specific dielectric constant, which was 9.4551 at a temperature of 24.85°C (P_{SAT} = 662.04 kPa).

The liquid specific dielectric constant for HCF-134a was measured in the EHD test facility shown in Figure 4.1 at various temperatures. Capacitance measurements were made across the annular gap over the length of the test section under vacuum conditions, C_S (<3 torr), and with the sample of liquid refrigerant, C_T, using a Boonton Capacitance Meter - Model 72B with the manufacturer's suggested accuracy being ±0.5% full scale. The test section was assumed to be two capacitors in parallel, the delrin spacers and the refrigerant, respectively as shown in Figure A.1.

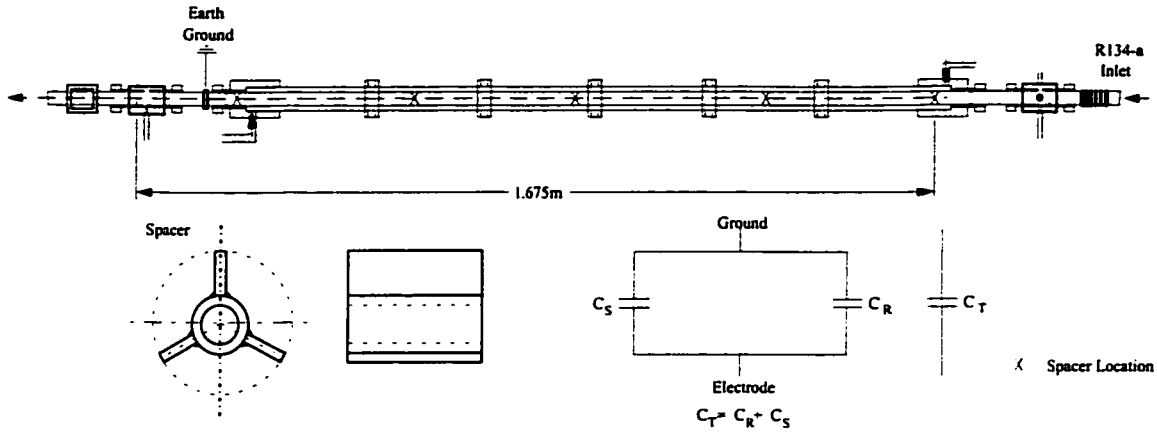

Figure A.1: Specific Dielectric Constant Test Section Measurement Arrangement.

The effective refrigerant capacitance was determined by measuring the capacitance under vacuum conditions with only the spacers and measuring the capacitance of the refrigerant and spacers together in parallel. The difference between these capacitances was interpreted as the effective refrigerant capacitance:

$$C_R = C_T - C_S \tag{A.2}$$

The assumption of a definite charge existing on the electrode with the effective refrigerant capacitance in Equation (A.2) permits the direct application of Gauss law. Therefore a relationship between the specific dielectric constant and capacitance can be established across the test section:

$$\frac{C_R}{L} = \frac{2\pi\varepsilon_0\varepsilon_l}{\ln\,(b/a)} \tag{A.3}$$

where the length of the coaxial cylinders L = 1.675 m, and b = 10.92 mm and a = 3.18 mm are the outer and inner diameters of the annulus, respectively. Measurements were taken at twelve temperatures slightly above the saturation point. These are summarized in Table A.4.

Figure A.2 compares the liquid state specific dielectric constant of HFC-134a as a function of temperature for both of the present measurements and the four experimental studies previously reviewed. As shown, the measured values deviate slightly from Gurova's

correlation (Equation A.1). The maximum difference between Gurova's correlation and the measured data was only $\Delta\varepsilon \sim 0.15$ even though these experiments were below the saturation line and did not conform to a standard measurement technique. Therefore, the Gurova *et al.* (1994) correlation (Equation A.1) was used for the liquid specific dielectric constant along the saturation line because of the agreement with experimental measurements.

Table A.4: Specific Dielectric Constant Measurements.

Refrigerant Temperature (°C)	Total System Capacitance, C_T, (pF)	Refrigerant Capacitance, C_R, (pF)	Dielectric Constant
17.9	840	759	10.06
18.9	837	756	10.02
19.3	834	753	9.98
21.4	811	730	9.68
21.6	814	733	9.72
22.6	807	726	9.63
23.7	799	718	9.52
24.3	796	715	9.48
25.1	792	711	9.43
25.4	787	706	9.36
25.8	784	703	9.32
25.9	782	701	9.29

(The vacuum capacitance C_S measured was 81 pF)

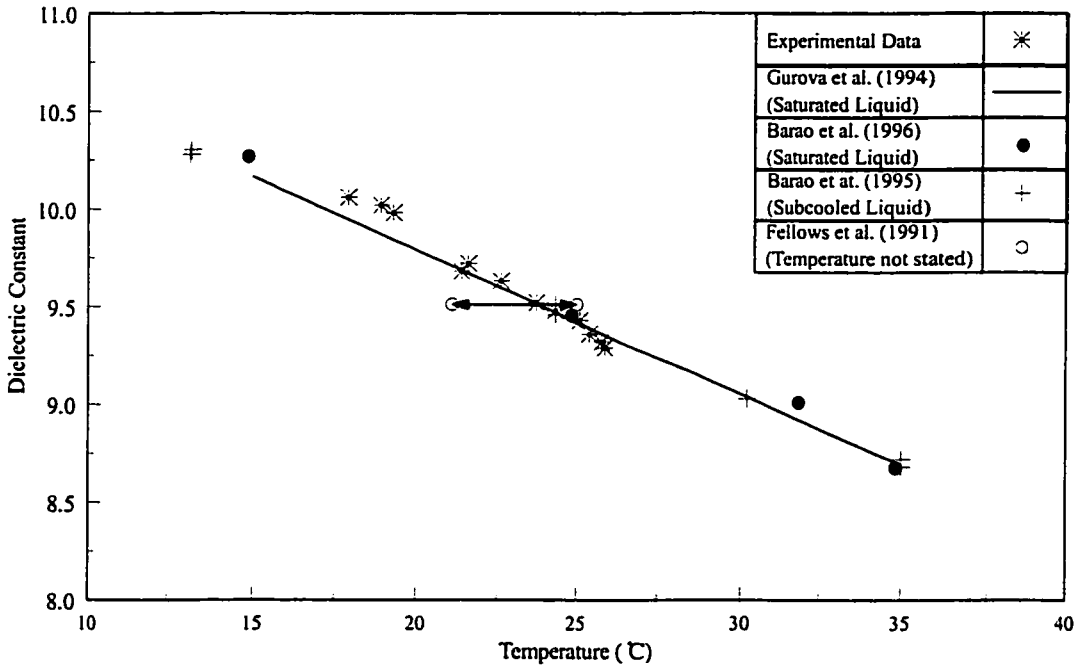

Figure A.2: Specific Dielectric Constant of HFC-134a in the Liquid Phase as a Function of Temperature.

The measurement of gaseous specific dielectric constant for refrigerant HFC-134a appears in two previous studies (Meyer and Morrison, 1991 and Barao *et al.*, 1995). These are reproduced in Figure A.3 as a function of pressure. However, both studies focussed on measurements below the saturation pressure representing the superheated vapour specific dielectric constant. In the Meyer and Morrison's investigation, the temperature range was between 35°C and 140°C for modest pressure range, below 210 kPa. Due to the limited range of temperatures investigated in this study, only their vapour specific dielectric constant for the lowest temperature (35.85°C) are included in Figure A.3. The data from Barao *et al.* (1995) for three temperatures (25.00°C, 35.05°C, and 50.00°C) are shown in Figure A.3. This data was linearly extrapolated to the saturation pressure to give an indication of the saturated vapour specific dielectric constant. By linear regression of these extrapolated values, Figure A.3 shows the approximate range of the saturated vapour specific dielectric constant for the temperature range of the present study ($20.0°C < T_{SAT} < 26.0°C$) being

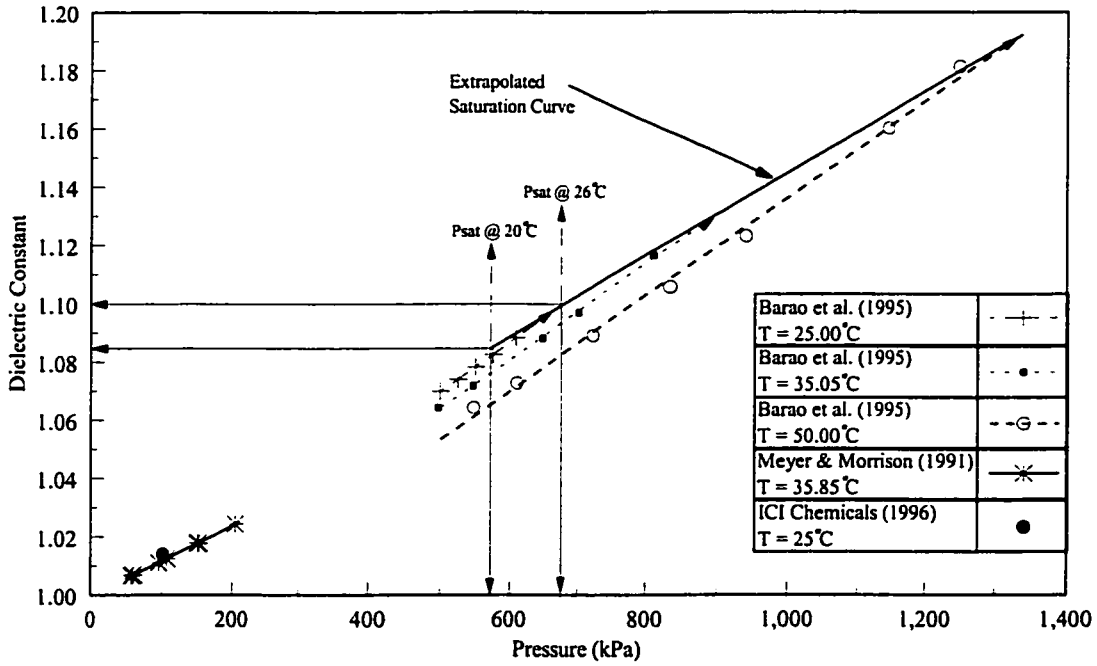

Figure A.3: Specific Dielectric Constant of HFC-134a in the Vapour Phase as a Function of Pressure.

between 1.085 and 1.100. With such a small difference, the average value of $\varepsilon_v = 1.09$ has been selected to represent the saturated vapour specific dielectric constant throughout the thesis.

In addition to dielectric measurements, Fellows *et al.* (1991) measured the AC dissipation and conductivity and DC resistivity for the same nineteen fluorocarbons. Table A.5 presents a comparison of several DC resistivity values measured by Fellows *et al.* (1991) against the values recommended by ASHRAE. All measurements were observed in the liquid state at ambient temperatures.

Table A.5: Resistivity Data of Several Common Refrigerants

Refrigerant		Resistivity DC (MΩ×m)	Resistivity DC (MΩ×m)
Fluid No.	Name	ASHRAE (1997)	Fellows *et al.* (1991)
11	Trichlorofluoromethane	63680	4098.75
12	Dichlorodifluoromethane	53900	17400
114	Dichlorotetrafluoroethane	66470	2.13×10^7
134a	1,1,1,2-tetrafluoroethane	n/a	660.40

Table A.5 suggests considerable discrepancies between these two references. Based on a private conversation with Robert G. Richard, one to the co-authors of the Fellows *et al.* (1991) paper, this discrepancy was likely due to impurity ion in the samples measured. Although the purities were reported to be 99+%, a small excess of ions in the sample could have had a considerable influence the refrigerant conductivity (Richard, 2000).

Consequently, an accurate measure of the charge relaxation time is not possible. In order to give a range for the charge relaxation time, Equation (3.27) has been evaluated at both 660.4 MΩ·m (the value for HFC-134a in Fellows *et al.*, 1991) and 50,000 MΩ·m (the order of magnitude of the three refrigerants reported by ASHRAE, 1997). The range of charge relaxation for HFC-134a is expected to be within:

$$0.05\ s < \tau_\sigma < 4\ s$$

Inferences regarding the effect of an alternating current on the flow based the range of τ_σ, are inappropriate due to the strong dependence of frequency on conductivity. Fellows *et al.* (1991) reported a two order of magnitude increase in electrical conductivity of HFC-134a (1.77 MΩ·m) when a 1 kHz AC voltage was applied. By applying Fellows' measurement of the AC electrical conductivity, free charges should be unlikely to accumulate at a threshold electric field alternating frequency of $f \sim 5$ to 10 kHz (*ie.* $f > 1/\tau_\sigma$).

The influence of thermophysical properties, with respect to temperature and applied DC voltage on the EHD dimensionless numbers for both a saturated liquid and vapour in a concentric channel are presented for HFC-134a in Figures A.4 to A.7. The conductive and dielectric Rayleigh numbers are calculated by:

$$E_{t\sigma} = \frac{I_0 L^3}{\rho_0 \nu^2 \mu_e A} \tag{A.4}$$

$$E_{t\varepsilon} = \frac{\varepsilon_0 E_0^2 T_0 (\partial \varepsilon_s / \partial T)_\rho \, L^2}{2\rho_0 \, \nu^2} \tag{A.5}$$

Implicit to the above equations are that:

- the reference electric field is taken to be the electrode surface
- the conductivity data of refrigerant liquid HFC-134a is questionable and the vapour conductivities are not available from literature so the free charge density within the fluid is assumed to be equal to the total charge injected by the electrodes (*i.e.*, $I_0 = dQ_0/dt$).
- the current flux is taken to be the total current over the surface area of the electrode, assuming uniform charge injection, for the range of measured values in Chapter 7
- the thermophysical data is calculated at the reference temperature according to Table A.1
- the reference length is the annular gap of the concentric electrodes (3.9 mm)
- the gradient of the specific dielectric constant is approximated as the slope of the Gurova *et al.* (1996) correlation in Equation (A.1a) $\partial \varepsilon_s / \partial T = 0.074$

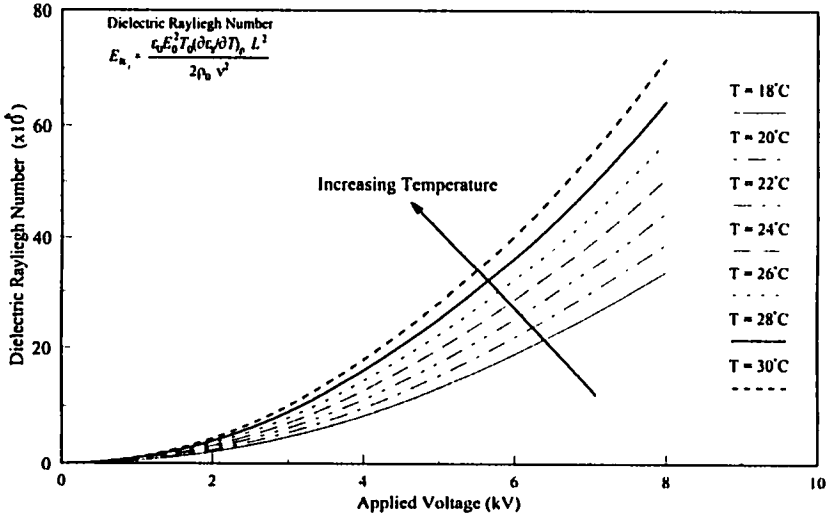

Figure A.4: The Effect of Applied Voltage on the Liquid Dielectric Rayleigh Number $E_{tc\text{-}l}$ at Different Temperatures.

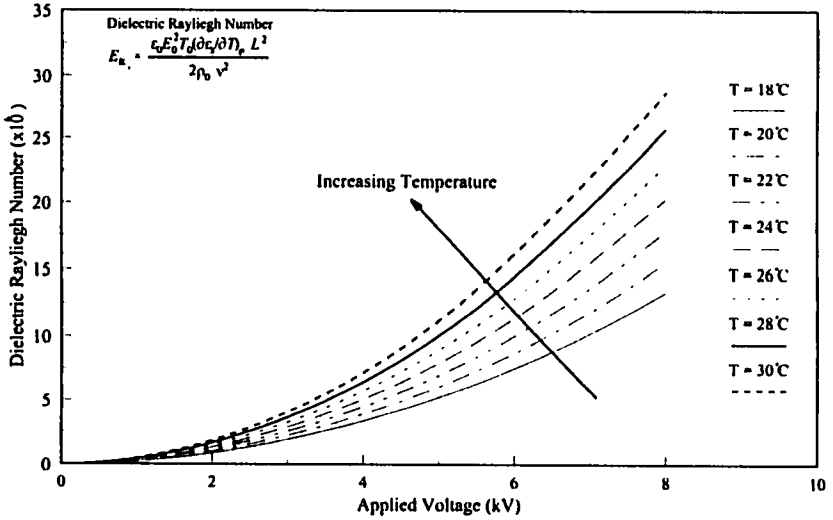

Figure A.5: The Effect of Applied Voltage on the Vapour Dielectric Rayleigh Number $E_{tc\text{-}v}$ at Different Temperatures.

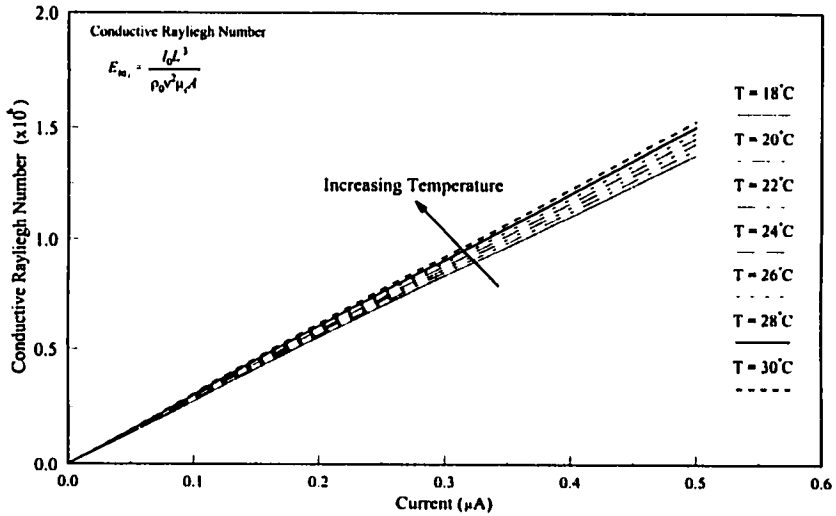

Figure A.6: The Effect of Applied Voltage on the Liquid Conductive Rayleigh Number $E_{t\sigma\text{-}l}$ at Different Temperatures.

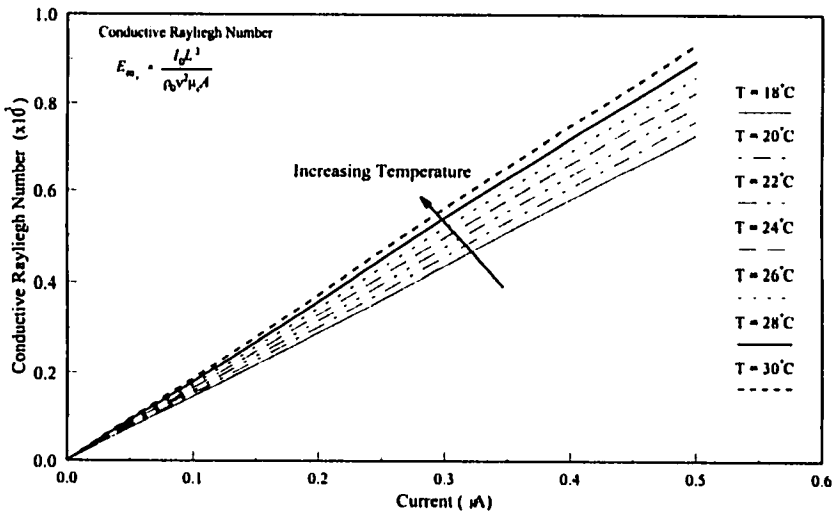

Figure A.7: The Effect of Applied Voltage on the Vapour Conductive Rayleigh Number $E_{t\sigma\text{-}v}$ at Different Temperatures.

- the liquid ion mobility is approximated according to the formulas relating mobility to the viscosity as suggested by Melcher (1981), $\mu_{0+} \approx 1.5 \times 10^{-11}/\mu_l$; $\mu_{0-} \approx 3.0 \times 10^{-11}/\mu_l$ ions in highly insulating liquids.

- the vapour ion mobility approximated according to the Langevin correlation (Langevin, 1975):

$$\mu_{\pm} = 0.5105 \frac{1}{\sqrt{N_g 4\pi\varepsilon_0(\varepsilon_s - 1)}} \left(1 + \frac{m_g}{m_{\pm}}\right)^{1/2} \qquad \text{(A.6)}$$

assuming the mass ratio $m_g/m_{\pm} \sim 1$ and the vapour specific dielectric constant is $\varepsilon_s = 1.09$, the resultant ion mobility of the vapour phase is of the order $\mu_{\pm} \sim 10^{-3}$ which is in the typical range for heavy molecules (Melcher, 1981).

Figures A.4 to A.7 suggest both the conductive and dielectric contributions are expected to increase with increasing temperatures and applied voltages (current levels) for both liquid and vapour phases. By comparing the effect of the electric body forces on the individual phases, both components of the body force are stronger in the liquid phase than the vapour phase, consequently the liquid will be the phase most affected by an electric field in a two phase medium.

Appendix B

Experimental Data Analysis

Both the analysis of the experimental data used to determine the refrigerant heat transfer coefficients and the error associated with the experimental arrangement, are presented in this appendix. The methods employed in developing a correlation for the shell-side heat transfer coefficient for the electrohydrodynamic heat exchanger shown in Figure 4.2 are discussed. Next, a comparison of the three calculation procedures for measuring the heat transfer coefficient is made and finally the measurement uncertainty is summarized.

The experiments for determining the water side heat transfer coefficient involved heating refrigerant HFC-134a (without phase change) by water in an annular heat exchanger for the range of conditions in Table 4.2. The experiments conducted for the Wilson Plot analysis did not involve EHD. As discussed in Chapter 4, the heat transfer analysis followed the modified Wilson Plot technique proposed by Briggs and Young (1969) which was later extended by Kattan (1996) using the Dittus-Boelter (1930) and/or the Petukhov-Popov (1963) correlations for either the shell or tube side heat transfer coefficients. Although the range of water side Reynolds numbers were within the typical laminar-turbulent transitional range for pipe flow, the present heat transfer analysis employs a turbulent correlation for both the tube and shell side of the heat exchanger. The reason for a turbulent correlation is the presumption that both the inlet conditions and turbulence enhancing objects along the

test section (the spacers and thermocouple wires on the tube and shell side, respectively) would prevent the flow from becoming laminar once tripped to the turbulent state. The three procedures of analysis are: *i)* the Dittus-Boelter equation for the tube and shell side, *ii)* the Petukhov-Popov equations for both sides and, *iii)* the Dittus-Boelter equation for the tube with the Petukhov-Popov equation on the shell side. The following discussion of these procedures follows the presentation by Kattan (1996).

Procedure 1: Shell: Dittus-Boelter – Tube: Dittus-Boelter

The inside *'i'* (tube) and outside *'o'* (shell) correlations take the form:

$$Nu_{D_{hi}} = \frac{h_i D_{hi}}{k_i} = C_i \, Re_i^{\,a} \, Pr_i^{0.4} \tag{B.1}$$

$$Nu_{D_{ho}} = \frac{h_o D_{ho}}{k_o} = C_o \, Re_o^{\,b} \, Pr_o^{0.3} \tag{B.2}$$

where Re and Pr are the Reynolds (using the hydraulic diameter) and Prandtl numbers, respectively. D_h is the annulus hydraulic diameters defined by:

$$D_{hi} = D_i - D_e \tag{B.3}$$

$$D_{ho} = D_j - D_o \tag{B.4}$$

for the inside and outside annuli, respectively.

Introducing Equations (B.1) to (B.4) into the overall heat transfer coefficient, U_o given in Equation (4.10), the following expression is obtained:

$$\frac{1}{U_o} = \frac{1}{C_o Re_o^{\,b} Pr_o^{0.3} (k_o / D_{ho})} + R_w + \frac{D_o / D_i}{C_i Re_i^{\,a} Pr_i^{0.4} (k_i / D_{hi})} \tag{B.5}$$

where R_w has been substituted to represent the thermal resistance of the wall. There is no general solution to Equation (B.5) due to the number of unknowns (C_o, C_i, a and b). However, in order to solve this equation, Briggs and Young (1969) employed the relationship presented by Wilson (1915) that $h \propto V^{0.8}$ on the tube side. Consequently, $a = 0.8$

and the remaining unknowns are determined by successive linear regressions.

First, rearranging Equation (B.5) into the Tube-Side Wilson Plot relationship:

$$\left(\frac{1}{U_o} - R_w\right)\left(Re_o^{\,b} Pr_o^{0.3}(k_o/D_{ho})\right) = \frac{1}{C_o} + \frac{1}{C_i}\left(\frac{Re_o^{\,b} Pr_o^{0.3}(k_o/D_{ho})}{Re_i^{\,a} Pr_i^{0.4}(k_i/D_{hi})}\right)\left(\frac{D_o}{D_i}\right) \qquad \text{(B.6)}$$

Equation (B.6) takes the form $y_1 = n + mx_1$, with $n = 1/C_o$ intercept and $m = 1/C_i$ slope, where y_1 and x_1 are used to represent the left and right hand side terms, respectively. Rearranging for the Shell-Side relationship:

$$\left(\frac{1}{U_o} - R_w - \frac{D_o / D_i}{C_i Re_i^{\,a} Pr_i^{0.4}(k_i/D_{hi})}\right)\left(Pr_o^{0.3}(k_o/D_{ho})\right) = \frac{1}{C_o Re_o^{\,b}} \qquad \text{(B.7)}$$

Next, substituting y_2 for the left hand side of Equation (B.7) and taking the natural logarithm gives:

$$\ln(1/y_2) = b\,\ln(Re_o) + \ln(C_o) \qquad \text{(B.8)}$$

The successive regression is initiated by guessing the exponent b in Equation (B.6) and plotting the Tube-Side relationship to solve for C_i and C_o. The leading constants are then used in Equation (B.8) to solve for b which is used in Equation (B.6) until the coefficients converge. The final form of the Tube and Shell Wilson Plots are presented in Figures B.1 and B.2, respectively. The unknown coefficients resulting the regression are $b = 0.816$, $C_i = 0.0283$ and $C_o = 0.0207$.

Procedure 2: Shell: Petukhov-Popov -- Tube: Petukhov-Popov

The inside *'i'* (tube) and outside *'o'* (shell) correlations are:

$$Nu_{D_{hi}} = \frac{h_i D_{hi}}{k_i} = C_i Nu_i = C_i \frac{(f_i/8)\,Re_i Pr_i}{1.07 + 12.7\,(f_i/8)^{1/2}\,(Pr_i^{2/3} - 1)} \qquad \text{(B.9)}$$

$$Nu_{D_{ho}} = \frac{h_o D_{ho}}{k_o} = C_o Nu_o = C_o \frac{(f_o/8)\,Re_o Pr_o}{1.07 + 12.7\,(f_o/8)^{1/2}\,(Pr_o^{2/3} - 1)} \qquad \text{(B.10)}$$

where the friction factor for the inside f_i and outside f_o are calculated according to the

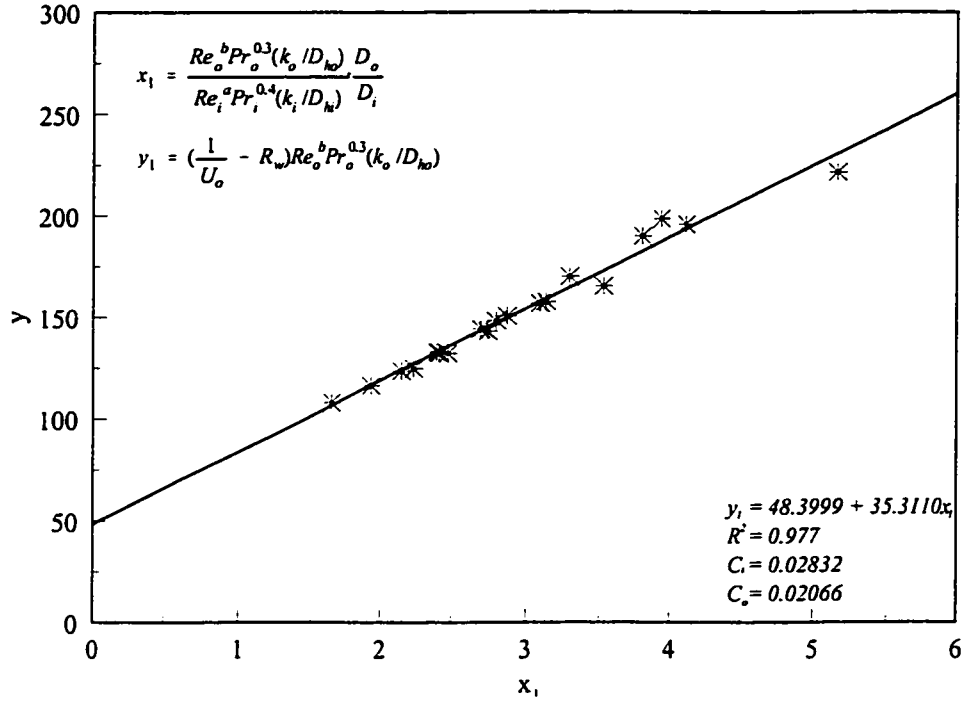

Figure B.1: Tube Side Wilson Plot Applying the Dittus-Boelter Equation for both Shell and Tube Side Heat Transfer Coefficients.

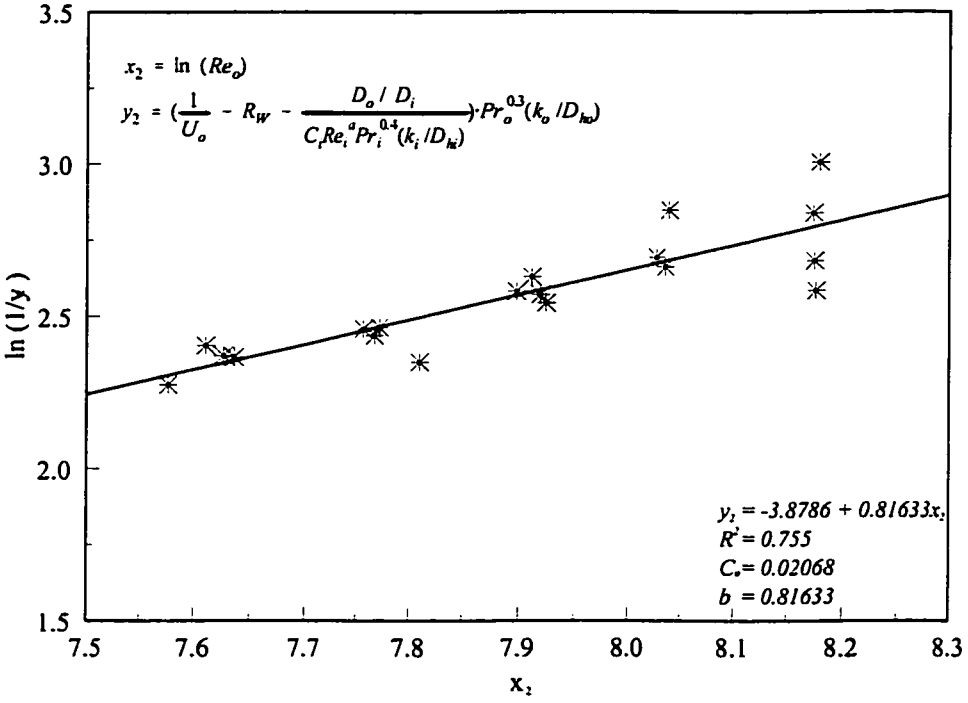

Figure B.2: Shell Side Wilson Plot Applying the Dittus-Boelter Equation for both Shell and Tube Side Heat Transfer Coefficients.

Filonenko (1954) correlation in Equation (4.9), as suggested by Kattan (1996). The form of Equations (B.9) and (B.10) is almost identical to the correlation for single-phase flow in a tube (i.e. Nu_i, Nu_o). The only difference between these correlations is the leading constant. Substituting Equations (B.9) and (B.10) into Equation (4.10) gives:

$$\frac{1}{U_o} = \frac{1}{C_o Nu_o(k_o / D_{ho})} + R_w + \frac{D_o / D_i}{C_i Nu_i(k_i / D_{hi})} \tag{B.11}$$

Rearranging Equation (B.11):

$$\left(\frac{1}{U_o} - R_w\right) Nu_o(k_o / D_{ho}) = \frac{1}{C_o} + \frac{1}{C_i}\left(\frac{Nu_o(k_o / D_{ho})}{Nu_i(k_i / D_{hi})}\right)\frac{D_o}{D_i} \tag{B.12}$$

By plotting Equation (B.12) in Figure B.3, the leading constants are given without iteration through the direct evaluation of the slope and intercept. For the test data collected, the leading constants are $C_i = 1.14$ and $C_o = 0.814$

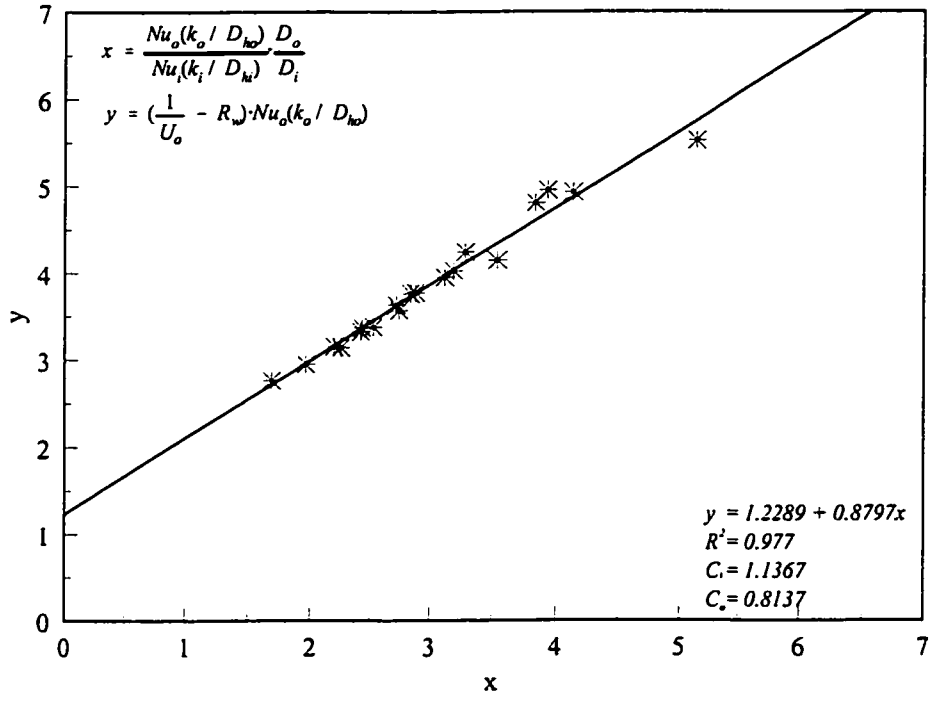

Figure B.3: Wilson Plot Applying the Petukhov-Popov Correlation for both Shell and Tube Side Heat Transfer Coefficients.

Procedure 3: Shell: Petukhov-Popov -- Tube: Dittus-Boelter

The inside *'i'* (tube) and outside *'o'* (shell) correlations take the form:

$$Nu_{D_{hi}} = \frac{h_i D_{hi}}{k_i} = C_i \, Re_i^{\,a} \, Pr_i^{0.4} \tag{B.13}$$

$$Nu_{D_{ho}} = \frac{h_o D_{ho}}{k_o} = C_o \, Nu_o = C_o \frac{(f_o/8)\, Re_o Pr_o}{1.07 + 12.7\,(f_o/8)^{1/2}\,(Pr_o^{2/3} - 1)} \tag{B.14}$$

Substituting Equations (B.13) and (B.14) into Equation (4.10) gives:

$$\frac{1}{U_o} = \frac{1}{C_o Nu_o (k_o / D_{ho})} + R_w + \frac{D_o / D_i}{C_i \, Re_i^{\,a} \, Pr_i^{0.4} (k_i / D_{hi})} \tag{B.15}$$

Rearranging Equation (B.15) into the Tube-Side and Shell-side format as shown in Procedure 1 gives:

$$\left(\frac{1}{U_o} - R_w\right)\left(\frac{k_i}{D_{hi}}\right)\left(\frac{D_i}{D_o}\right) \cdot Re_i^{\,a} \, Pr_i^{0.4} = \frac{1}{C_i} + \frac{1}{C_o}\left(\frac{Re_i^{\,a} \, Pr_i^{0.4} \cdot (k_i / D_{hi})}{Nu_o (k_o / D_{ho})}\right)\frac{D_i}{D_o} \tag{B.16}$$

$$\left(\frac{1}{U_o} - R_w - \frac{1}{C_o Nu_o (k_o / D_{ho})}\right) \cdot \frac{D_i}{D_o} \cdot Pr_i^{0.4} \cdot \frac{k_i}{D_{hi}} = \frac{1}{C_i \, Re_i^{\,a}} \tag{B.17}$$

respectively. Again, substituting y_2 for the left hand side of Equation (B.17), the shell-side equation, and taking the natural logarithm gives:

$$\ln(1/y_2) = a \ln(Re_i) + \ln(C_i) \tag{B.18}$$

The regression is initiated by guessing the exponent a in Equation (B.16) and plotting the Tube-Side relationship to solve for C_i and C_o. The leading constants are used in Equation (B.18) to solve for a which is substituted in Equation (B.16) until the coefficients converge. The final form of the Tube and Shell Wilson Plots are presented in Figures B.4 and B.5, respectively. The unknown coefficients from the regression are $a = 0.816$, $C_i = 0.0247$ and $C_o = 0.802$.

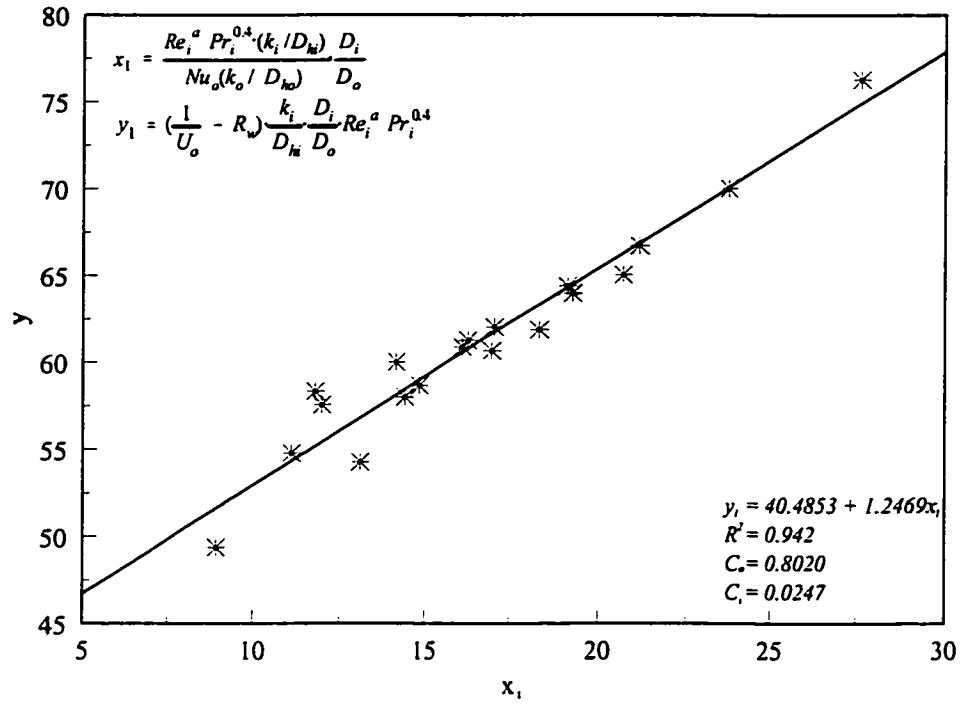

Figure B.4: Tube Side Wilson Plot Applying the Dittus-Boelter Equation to the Tube Side and the Petukhov-Popov Equation to the Shell Side Heat Transfer Coefficients.

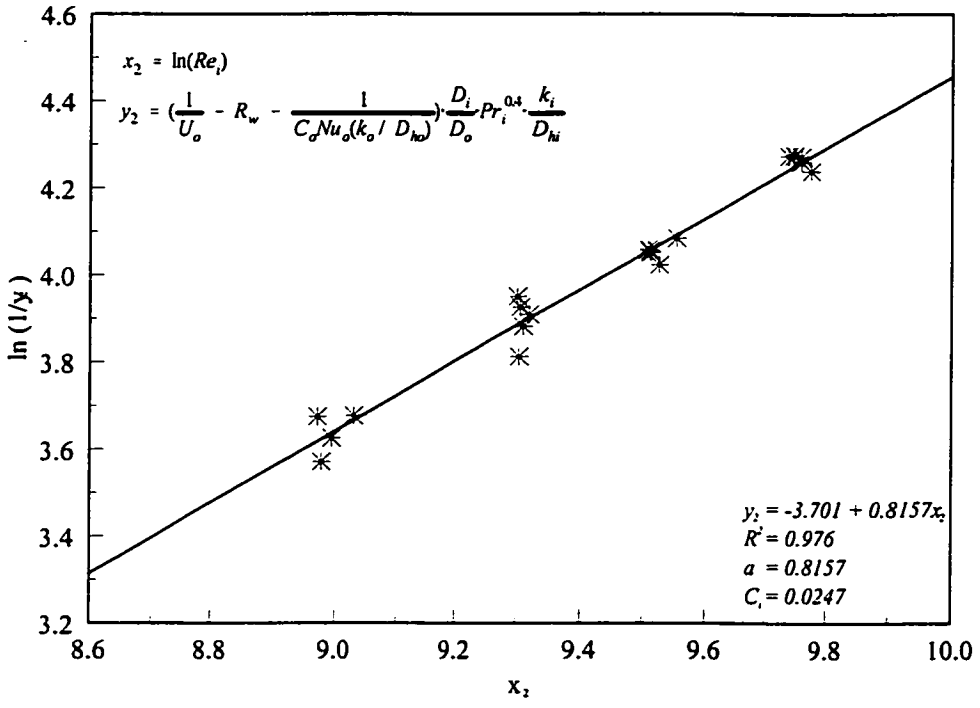

Figure B.5: Shell Side Wilson Plot Applying the Dittus-Boelter Equation to the Tube Side and the Petukhov-Popov Equation to the Shell Side Heat Transfer Coefficients.

Figure B.6 shows a comparison of the three shell-side heat transfer coefficient correlations for the test data. The agreement between the three correlations is very good, deviating by approximately 1.0% at low Reynolds numbers to approximately 4.0% at the maximum Reynolds number tested *(Re~4000)*. Each of these correlations are acceptable to describe the experimental results. However, based on both the ease of determining the correlation and the goodness of fit with respect to the measured data, $R^2 = 0.977$, the Petukhov-Popov correlation from Procedure 2 is used to predict the shell-side heat transfer coefficient. The correlation is:

$$Nu_{D_{ho}} = \frac{h_o D_{ho}}{k_o} = 0.81 Nu_o = 0.81 \frac{(f_o/2)\, Re_o Pr_o}{1 + 12.7\,(f_o/2)^{1/2}\,(Pr_o^{2/3} - 1)} \qquad \text{(B.19)}$$

for the water flow through the test section jacket which is introduced into Equation (4.10) to determine the refrigerant heat transfer coefficient.

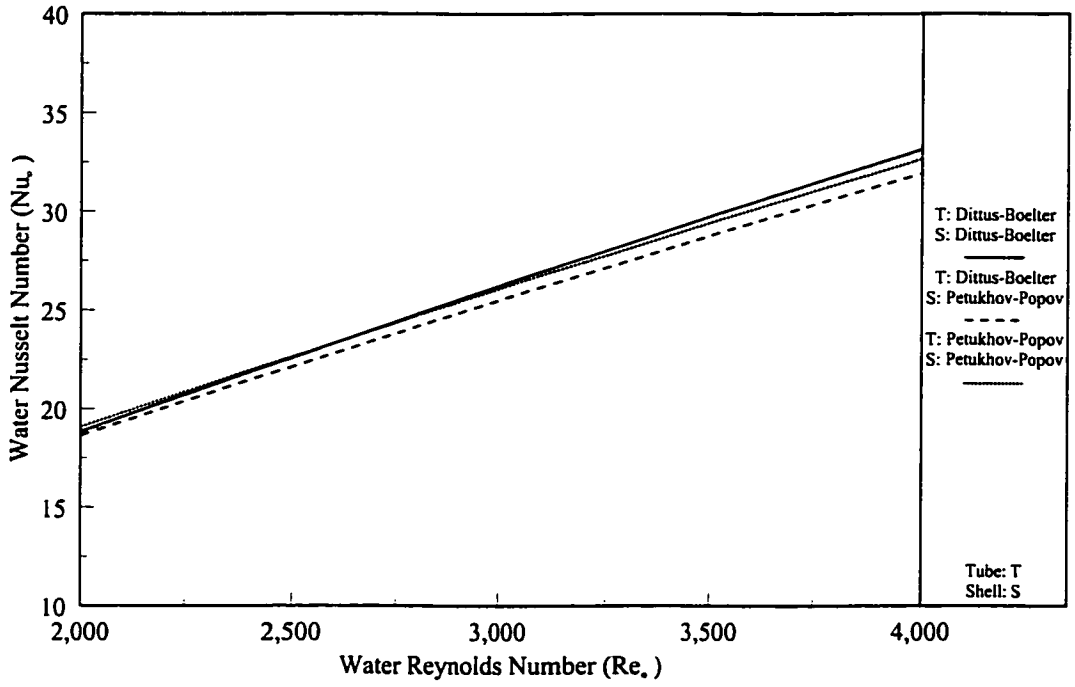

Figure B.6: Comparison of the Shell-Side Heat Transfer Coefficient Correlations obtained through the Modified Wilson Plot Technique.

Figures B.7 and B.8 present a comparison of the three methods used to determine the heat transfer coefficient These are: *i)* the Wilson Technique using the Petukhov-Popov correlation (Equation B.19) and the Dittus-Boelter correlation for the water jacket, *ii)* a standard forced convection calculation assuming heat transfer is axially and circumferentially uniform along the cylinder using the average of the wall surface temperatures and *iii)* a quasi local calculation of heat transfer coefficients by assuming the top and bottom surface temperature measurements represent distinct halves of the channel

Figure B.7 shows the three procedures are consistent, deviating by only ±15% at a heat flux of 20.4 kW/m^2 with an inlet quality of 0% over the entire range of mass fluxes tested. For these experiments, an inspection of the flow pattern map in Figure 5.9 shows the dominant flow regime is annular. Consequently, the heat transfer coefficient is expected to be almost constant around the circumference of the tube, which explain the agreement between the various techniques. However, the agreement is poor when the predominant flow pattern along the length of the channel is stratified, as the conditions associated with Figure B.8 dictate. Under stratified flow conditions the heat transfer coefficient, is considerably lower at the surface in contact with the vapour compared to the liquid. From Chapter 7, the wall temperature difference exceeds 8°C (between the top and bottom thermocouple) at various axial locations depending on the parameters under investigation. So by assuming a constant heat transfer coefficient around the tube, the first two methods under-predict the actual heat transfer coefficient. Although, inaccurate in the assumption that exactly half the tube is at the top measured temperature and exactly half at the bottom temperature, the quasi-local method provides a weighted average value of the heat transfer coefficient. This is believed to be a more accurate representation of the heat transfer

coefficient as much as the non-uniformities associated with a nonlinear axial heat flux and flow stratification are considered. Accordingly, this method of determining the refrigerant heat transfer coefficient has been used in the present investigation.

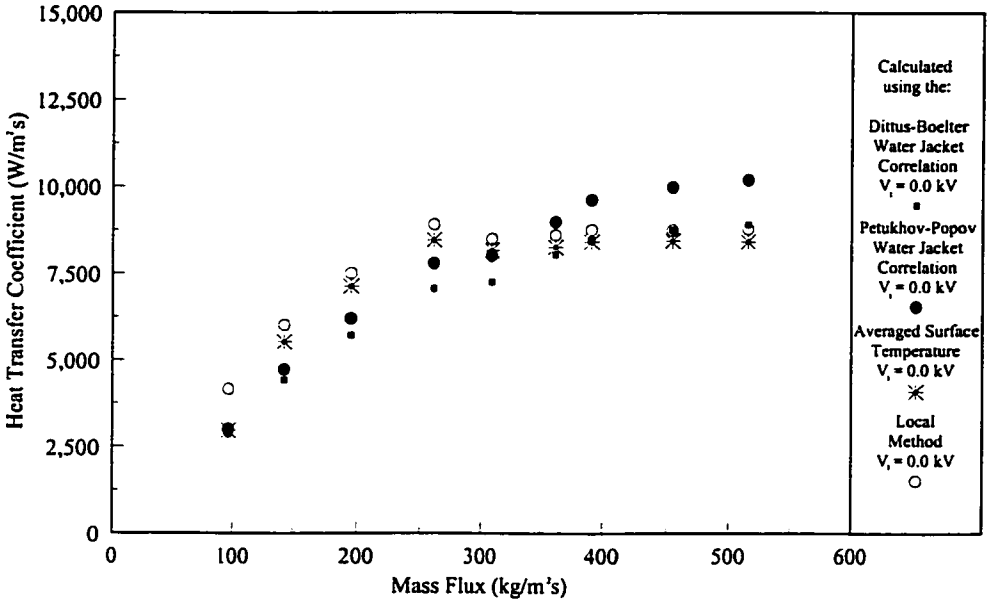

Figure B.7: A Comparison of the Various Methods Employed in Determining the Refrigerant Heat Transfer Coefficient at Different Mass Fluxes for a Heat Flux of 20.4 kW/m2 and an Inlet Quality of 0%.

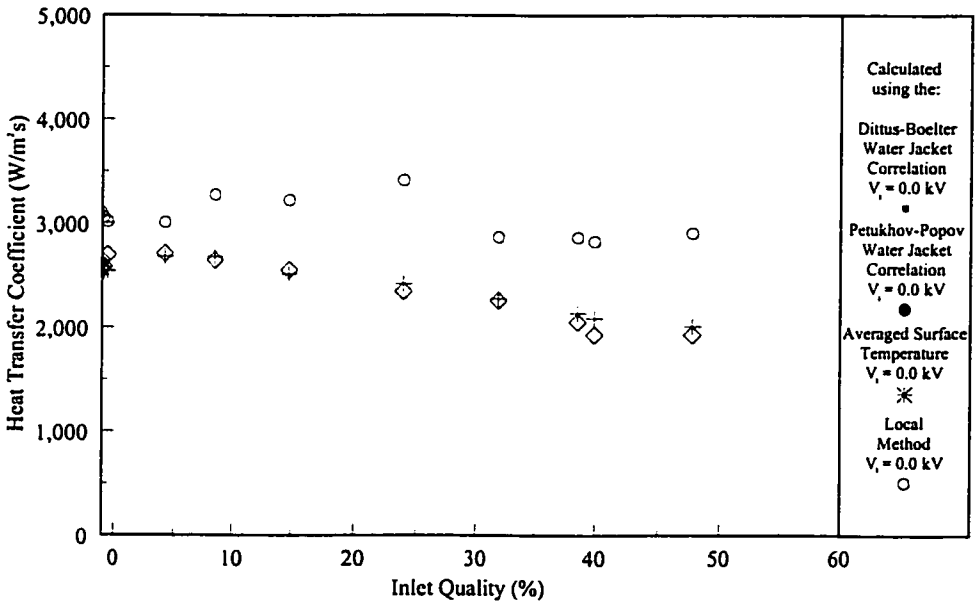

Figure B.8: A Comparison of the Various Methods Employed in Determining the Refrigerant Heat Transfer Coefficient at Different Qualities Mass Fluxes for a Heat Flux 10.3 kW/m^2 and a Reynolds Number of 3500.

Error Analysis

The different measurement devices and their associated measurement errors described in Chapter 4 are itemized in Table B.1. For the purposes of uncertainty calculation, each measurement is denoted x_n and the uncertainty in the measurement w_n. The result of a calculation using these measurements is denoted R and the uncertainty in the calculated result is denoted w_R. The uncertainty w_R is calculated using the method of Kline and McClintock (1953) (root mean sum square method) using the following equation:

$$w_R^2 = \sqrt{\sum_{i=1}^{n}\left(\frac{\partial R}{\partial x_i}w_i\right)^2} \tag{B.20}$$

Table B.1: Measurement Error for Different Devices

Parameter (Make, Type)	Error
Temperature (calibrated) (type-T, OMEGA thermocouple)	±0.1 °C
Refrigerant Mass Flow Rate (FTB-101, OMEGA turbine flow meter)	0.0313 ± 0.0002 kg/s (low) 0.1428 ± 0.0007 kg/s (high)
Refrigerant Mass Flow Rate (FTB-502, OMEGA turbine flow meter)	0.00810 ± 0.00004 kg/s (low) 0.0183 ± 0.0001 kg/s (high)
Condensing Water Flow Rate (F.& P. Rotameter)	3.07 ± 0.06 l/min (3.07 l/min meter) 10.2 ± 0.2 l/min (10.2 l/min meter)
Heating Water Mass Flow Rates (FTB-101, OMEGA turbine flow meter)	0.03744 ± 0.0002 kg/s (low) 0.09871 ± 0.0005 kg/s (high)
Pressure Drop (8.618 kPa, Validyne Transducer)	71.5 ± 0.1 Pa (low) 7639 ± 8 Pa (high)
Refrigerant Pressure Heise Pressure sensor	620 ± 1 kPa (low) 680 ± 1 kPa (low)
Applied Voltage - DC (EHD) (EL30R1.5, Glassman DC power supply)	2.0 ± 0.2 kV 8.0 ± 0.3 kV
DC Current (EHD)	0.5 ± 0.1 μA

The maximum experimental uncertainties are summarized in Table B.2.

Table B.2: Error in Governing Parameters

Parameter	Maximum Percentage Error
Heat Flux (W/m^2)	±10%
Reynolds Number	±3%
Quality	±6%
Heat Transfer Coefficient (W/m^2K)	±14%
Nusselt Number	±15%
Modified Froude Number	±9%
Martinelli Parameter	±14%

Appendix C

Electric Field Analysis and Results

FINITE ELEMENT ANALYSIS OF ELECTRIC FIELD

I) Preprocessing

i) Governing Equation for the FEA Analysis

The Poisson equation:

$$\varepsilon \nabla^2 V = -\rho_e \tag{C.1}$$

and for a charge-free region, as in the present situation the Laplace equation can be written:

$$\varepsilon \nabla^2 V = 0 \tag{C.2}$$

The boundary conditions for the following case are:

$V = V_1$ at $r = R_1$
$V = 10$ kV at $r = 1.58$ mm

$V = V_2$ at $r = R_2$
$V = 0$ at $r = 5.46$ mm

$$\begin{aligned} E_{n_1} &= E_{n_2} \\ \varepsilon_1 E_{1_t} &= \varepsilon_2 E_{2_t} \end{aligned} \tag{C.3}$$

ii) Derivation of Stiffness Matrix and Force Vector

From the governing equations, assuming that the interface is charge-free, the functional governing equation has the following form:

$$F(V) = \iint \left\{ \frac{\varepsilon}{2} \left[\left(\frac{\partial V}{\partial x} \right)^2 + \left(\frac{\partial V}{\partial y} \right)^2 \right] \right\} dx\, dy = 0 \tag{C.4}$$

If the domain of interest is divided into discrete triangles, then vector V within the triangle

can be expressed as a function of nodal values V_k and shape function N_k where (k = 1, 2, 3)

$$= V_1 N_1 + V_2 N_2 + V_3 N_3 \qquad V_1, V_2, V_3 \text{ ... nodal values, } N_1, N_2, N_3 \text{ .. shape functions}$$

$$\begin{aligned} V_1 &= N_1 + N_2 x_1 + N_3 y_1 \quad x_1, y_1 \quad \text{coordinates of node 1} \\ V_2 &= N_1 + N_2 x_2 + N_3 y_2 \quad x_2, y_2 \quad \text{coordinates of node 2} \\ V_3 &= N_1 + N_2 x_3 + N_3 y_3 \quad x_3, y_3 \quad \text{coordinates of node 3} \end{aligned} \tag{C.5}$$

$$D = \begin{vmatrix} 1 & x_1 & y_1 \\ 1 & x_2 & y_2 \\ 1 & x_3 & y_3 \end{vmatrix} = (x_2 y_3 - x_3 y_2) - (x_1 y_3 - x_3 y_1) + (x_1 y_2 - x_2 y_1) \tag{C.6}$$

$$Area = 0.5 * |D| \tag{C.7}$$

$$N_1 = \frac{a_1 + b_1 x + c_1 y}{D} \quad \text{where} \quad a_1 = x_2 y_3 - x_3 y_2;\ b_1 = y_2 - y_3;\ c_1 = x_3 - x_2$$

$$N_2 = \frac{a_2 + b_2 x + c_2 y}{D} \qquad a_2 = x_3 y_1 - x_1 y_3;\ b_2 = y_3 - y_1;\ c_2 = x_1 - x_3 \tag{C.8}$$

$$N_3 = \frac{a_3 + b_3 x + c_3 y}{D} \qquad a_3 = x_1 y_2 - x_2 y_1;\ b_3 = y_1 - y_2;\ c_3 = x_2 - x_1$$

$$V = V_1 N_1 + V_2 N_2 + V_3 N_3 \tag{C.9}$$

$$\begin{aligned} \frac{\partial V}{\partial x} &= V_1 \frac{\partial N_1}{\partial x} + V_2 \frac{\partial N_2}{\partial x} + V_3 \frac{\partial N_3}{\partial x} = \frac{V_1 b_1 + V_2 b_2 + V_3 b_3}{2 \times \text{Area}} \\ \frac{\partial V}{\partial y} &= V_1 \frac{\partial N_1}{\partial y} + V_2 \frac{\partial N_2}{\partial y} + V_3 \frac{\partial N_3}{\partial y} = \frac{V_1 c_1 + V_2 c_2 + V_3 c_3}{2 \times \text{Area}} \end{aligned} \tag{C.10}$$

Substituting the above expressions into the governing equation:

$$\begin{aligned} F(V) &= \iint \left\{ \frac{\varepsilon}{2} \left[\left(\frac{\partial V}{\partial x} \right)^2 + \left(\frac{\partial V}{\partial y} \right)^2 \right] \right\} dx\, dy \\ &= \iint \left\{ \frac{\varepsilon}{8\ \text{Area}^2} \left[(V_1 b_1 + V_2 b_2 + V_3 b_3)^2 + (V_1 c_1 + V_2 c_2 + V_3 c_3)^2 \right] \right\} dx\, dy \end{aligned} \tag{C.11}$$

Minimizing the governing equation with respect to V_1, V_2, V_3 and solving gives

$$\frac{\partial F(V)}{\partial V_1} = \iint \left\{ \frac{\varepsilon}{4\,\text{Area}^2} \left[(V_1 b_1 + V_2 b_2 + V_3 b_3)\, b_1 + (V_1 c_1 + V_2 c_2 + V_3 c_3)\, c_1 \right] \right\} dx\, dy$$

$$= \frac{\varepsilon}{4\,\text{Area}} \left[(V_1 b_1 + V_2 b_2 + V_3 b_3)\, b_1 + (V_1 c_1 + V_2 c_2 + V_3 c_3)\, c_1 \right] \tag{C.12}$$

$$\frac{\partial F(V)}{\partial V_2} = \iint \left\{ \frac{\varepsilon}{4\,\text{Area}^2} \left[(V_1 b_1 + V_2 b_2 + V_3 b_3)\, b_2 + (V_1 c_1 + V_2 c_2 + V_3 c_3)\, c_2 \right] \right\} dx\, dy$$

$$= \frac{\varepsilon}{4\,\text{Area}} \left[(V_1 b_1 + V_2 b_2 + V_3 b_3)\, b_2 + (V_1 c_1 + V_2 c_2 + V_3 c_3)\, c_2 \right] \tag{C.13}$$

$$\frac{\partial F(V)}{\partial V_3} = \iint \left\{ \frac{\varepsilon}{4\,\text{Area}^2} \left[(V_1 b_1 + V_2 b_2 + V_3 b_3)\, b_3 + (V_1 c_1 + V_2 c_2 + V_3 c_3)\, c_3 \right] \right\} dx\, dy$$

$$= \frac{\varepsilon}{4\,\text{Area}} \left[(V_1 b_1 + V_2 b_2 + V_3 b_3)\, b_3 + (V_1 c_1 + V_2 c_2 + V_3 c_3)\, c_3 \right] \tag{C.14}$$

In the matrix form:

$$\frac{\partial F(V)}{\partial V} = 0$$

$$\begin{bmatrix} \frac{\partial F(V)}{\partial V_1} \\ \frac{\partial F(V)}{\partial V_2} \\ \frac{\partial F(V)}{\partial V_3} \end{bmatrix} = \begin{bmatrix} S_{11} & S_{12} & S_{13} \\ S_{21} & S_{22} & S_{23} \\ S_{31} & S_{32} & S_{33} \end{bmatrix} \begin{bmatrix} V_1 \\ V_2 \\ V_3 \end{bmatrix} = 0 \tag{C.15}$$

where

$$S_{11} = \frac{\varepsilon}{4\,\text{AREA}} (b_1^2 + c_1^2), \quad S_{12} = \frac{\varepsilon}{4\,\text{AREA}} (b_1 b_2 + c_1 c_2), \quad S_{13} = \frac{\varepsilon}{4\,\text{AREA}} (b_1 b_3 + c_1 c_3)$$

(C.16)

$$S_{21} = \frac{\varepsilon}{4\,AREA}(b_2 b_1 + c_2 c_1), \quad S_{22} = \frac{\varepsilon}{4\,AREA}(b_2^2 + c_2^2), \quad S_{23} = \frac{\varepsilon}{4\,AREA}(b_2 b_3 + c_2 c_3)$$

(C.17)

$$S_{31} = \frac{\varepsilon}{4\,AREA}(b_3 b_1 + c_3 c_1), \quad S_{32} = \frac{\varepsilon}{4\,AREA}(b_3 b_2 + c_3 c_2), \quad S_{33} = \frac{\varepsilon}{4\,AREA}(b_3^2 + c_3^2)$$

(C.18)

Finally, the electric field distribution was calculated using the numerical voltage distribution values according to:

$$E = \nabla V \tag{C.19}$$

As discussed in Chapter 6, two plots are required to describe the established field strength distribution and the electric field vector direction, a field strength distribution plot and a plot of the voltage gradient. Figures D.1 to D.18 present these plots for three addition levels of stratification at each electrode position investigated experimentally. The liquid levels are distinguished with respect to the electrode contact (below the electrode, in contact with the electrode and above the electrode).

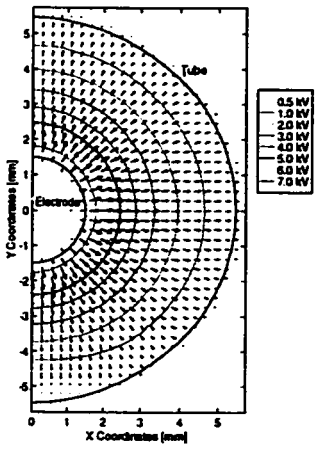

Figure C.1: Voltage Contour and Gradient for Stratified Flow, Liquid Level $h_L = 0.68$ *mm*, (Concentric Electrodes)

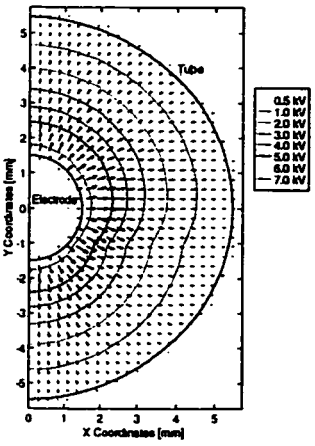

Figure C.2: Voltage Contour and Gradient for Stratified Flow, Liquid Level $h_L = 4.44$ *mm*, (Concentric Electrodes)

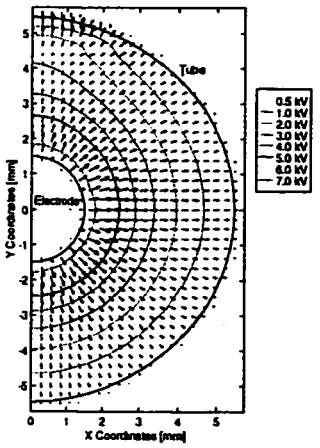

Figure C.3: Voltage Contour and Gradient for Stratified Flow, Liquid Level $h_L = 10.24$ *mm*, (Concentric Electrodes)

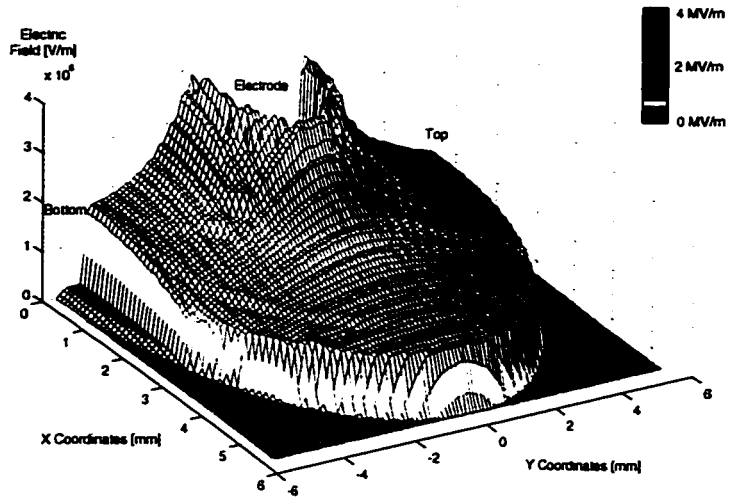

Figure C.4: Electric Field Distribution of Concentric Electrodes for Stratified Flow, $h_L = 0.68$ *mm*.

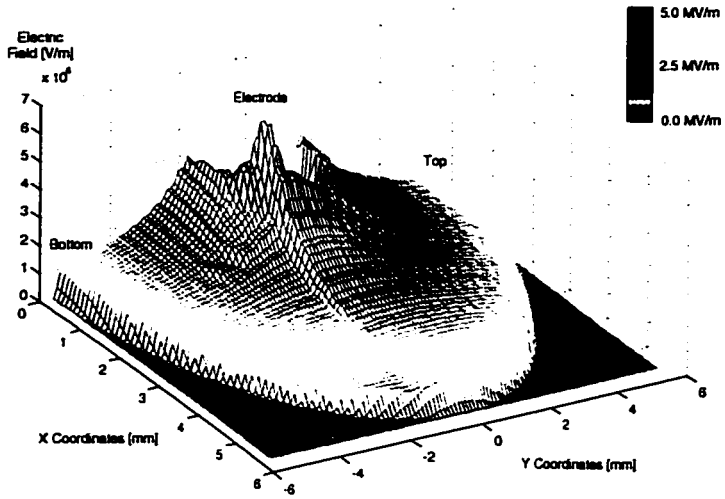

Figure C.5: Electric Field Distribution of Concentric Electrodes for Stratified Flow, $h_L = 4.44$ *mm*.

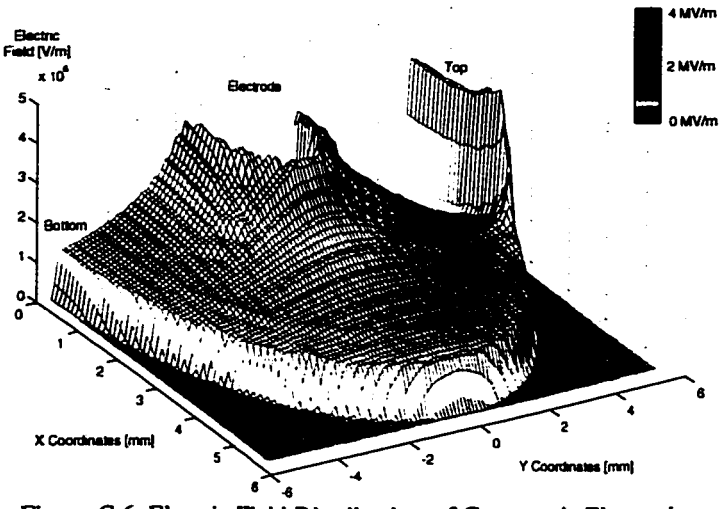

Figure C.6: Electric Field Distribution of Concentric Electrodes for Stratified Flow, $h_L = 10.24$ *mm*.

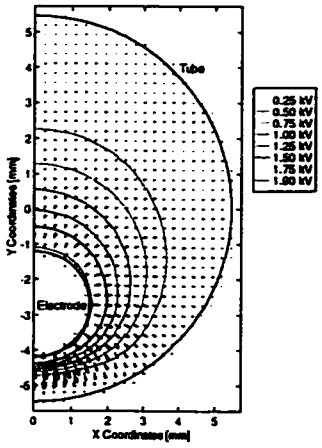

Figure C.7: Voltage Contour and Gradient for Stratified Flow, Liquid Level $h_L = 0.68$ *mm*, (Electrode -2.73 mm from Centerline).

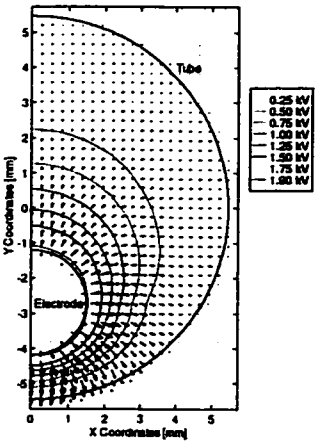

Figure C.8: Voltage Contour and Gradient for Stratified Flow, Liquid Level $h_L = 2.73$ *mm*, (Electrode -2.73 mm from Centerline).

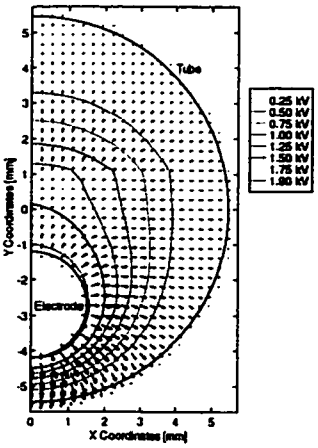

Figure C.9: Voltage Contour and Gradient for Stratified Flow, Liquid Level $h_L = 6.48$ *mm*, (Electrode -2.73 mm from Centerline).

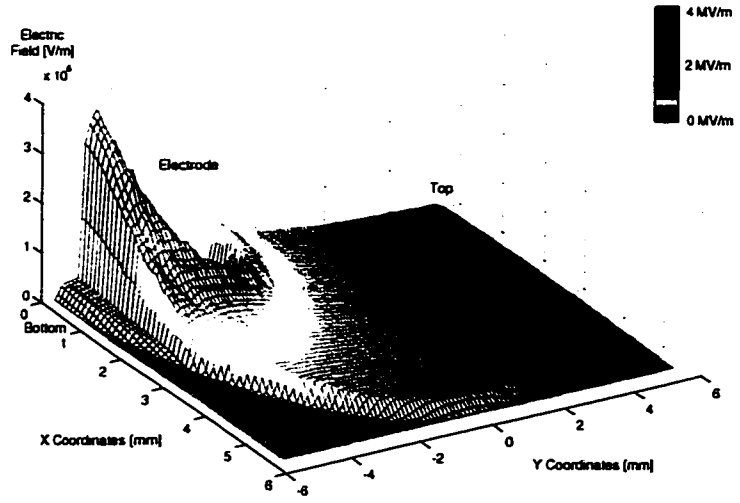

Figure C.10: Electric Field Distribution of an Eccentric Electrode (-2.73 mm from Centerline) for Stratified Flow, $h_L = 0.68$ *mm*.

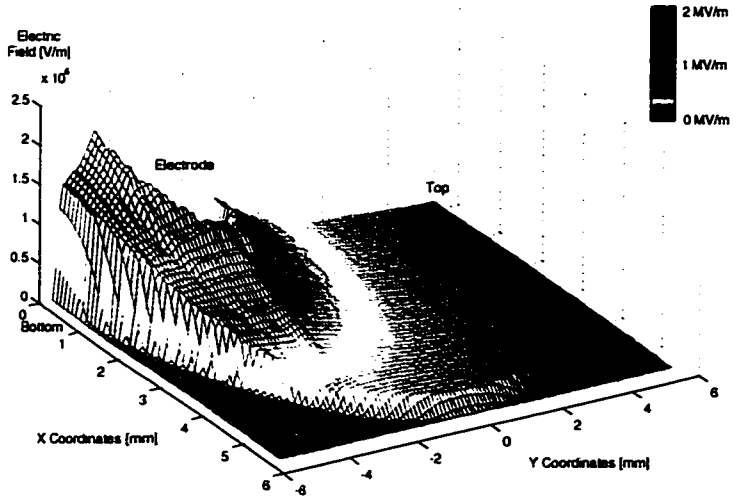

Figure C.11: Electric Field Distribution of an Eccentric Electrode (-2.73 mm from Centerline) for Stratified Flow, $h_L = 2.73$ *mm*.

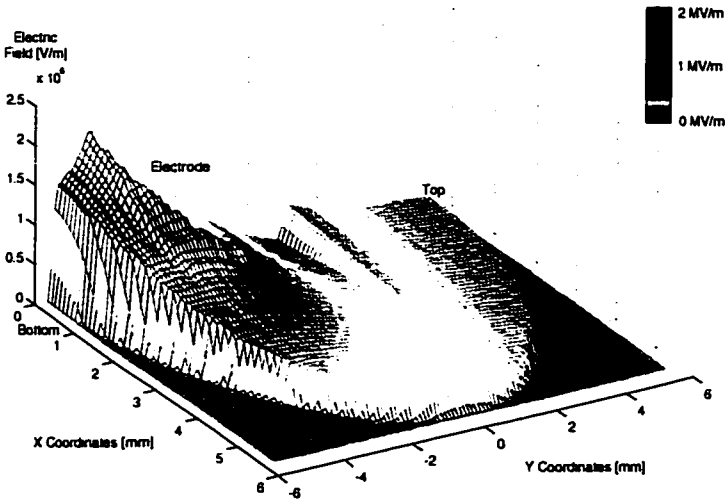

Figure C.12: Electric Field Distribution of an Eccentric Electrode (-2.73 mm from Centerline) for Stratified Flow, $h_L = 6.48$ *mm*.

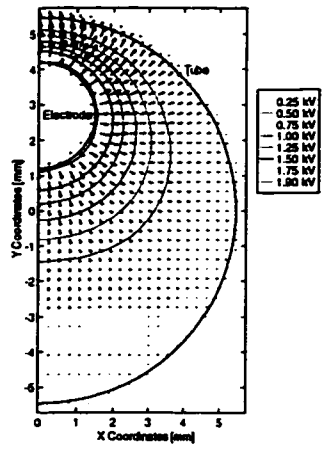

Figure C.13: Voltage Contour and Gradient for Stratified Flow, Liquid Level h_L = *2.73 mm*, (Electrode +2.73 mm from Centerline).

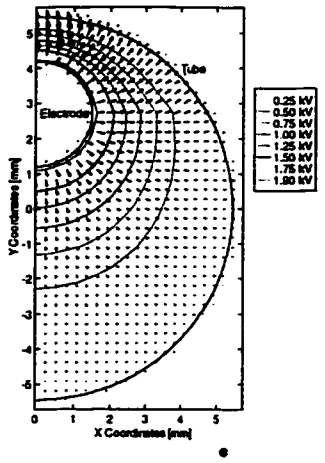

Figure C.14: Voltage Contour and Gradient for Stratified Flow, Liquid Level h_L = *8.19 mm*, (Electrode +2.73 mm from Centerline).

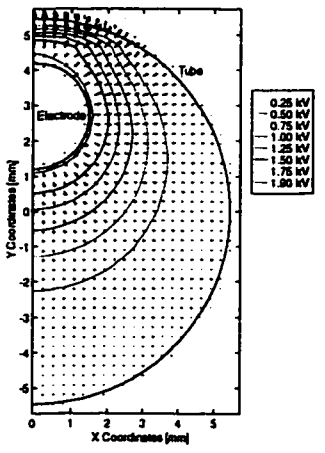

Figure C.15: Voltage Contour and Gradient for Stratified Flow, Liquid Level h_L = *10.24 mm*, (Electrode +2.73 mm from Centerline).

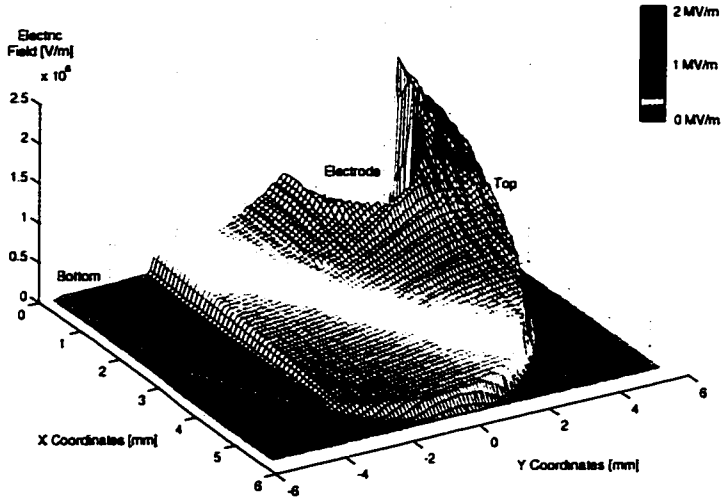

Figure C.16: Electric Field Distribution of an Eccentric Electrode (+2.73 mm from Centerline) for Stratified Flow, h_L = *2.73 mm*.

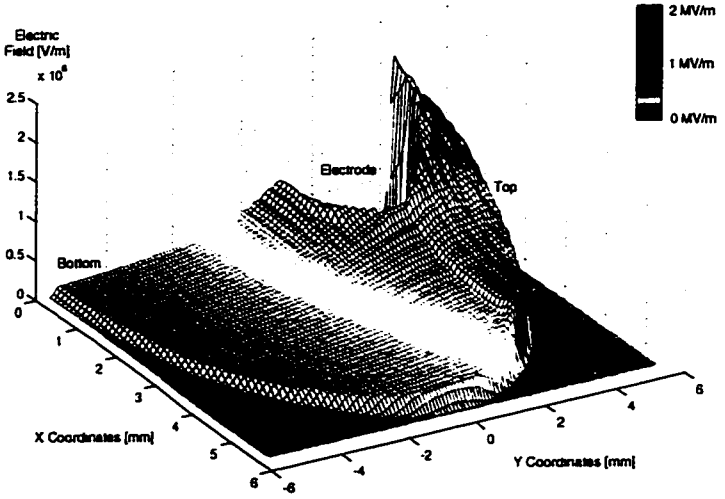

Figure C.17: Electric Field Distribution of an Eccentric Electrode (+2.73 mm from Centerline) for Stratified Flow, h_L = *8.19 mm*.

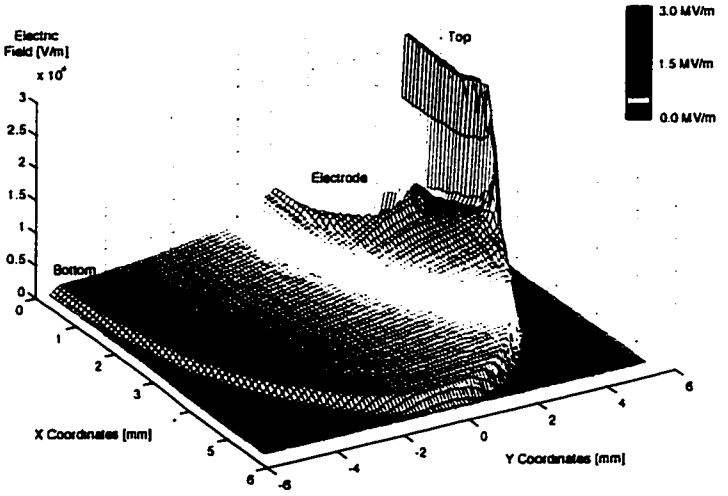

Figure C.18: Electric Field Distribution of an Eccentric Electrode (+2.73 mm from Centerline) for Stratified Flow, h_L = *10.24 mm*.

Appendix D

Evaluation of Effective Current, Voltage and Power

The power associated with the AC current and voltage requires an evaluation of their *effective* values I_{eff} and V_{eff}, respectively. These effective values are the equivalent DC current and voltages that give the same heating in a resistance as the average heating AC currents. The effective value of an AC current is determined by letting the AC current through a resistance R be written as $i = I_0 \sin \omega t$. The average power dissipation in the resistance will then be:

$$P = i^2 R = I_0^2 \sin^2 \omega t \qquad AC \tag{D.1}$$

where $\sin^2 \omega t$ means the average value of $\sin^2 \omega t$. The power dissipation in the case of a steady current (I), is

$$P = I^2 R \qquad DC \tag{D.2}$$

If the average power in the DC case is made equal to the DC power then the current (I) will be the effective values of the AC current I_{eff}. Thus

$$I_{eff}^2 R = I_0^2 R \, \overline{\sin^2 \omega t} = I_0 R \, \frac{\int_0^t \sin^2 \omega t \, dt}{t} \tag{D.3}$$

which yields

$$I_{eff}^2 = \frac{I_0^2}{2} \qquad or \qquad I_{eff} = \frac{1}{\sqrt{2}} I_0 \tag{D.4}$$

The same argument for voltage gives

$$V_{eff} = \frac{1}{\sqrt{2}} V_0 \tag{D.5}$$

In the following example, the waveform was sinusoidal and the effective value was the root-mean-square (rms) value. A similar argument is used for the general function of current and voltage for the power supplies in this experiments. In general, where *I=f(t) and V = g(t)*, for these experiments the effective values are:

$$I_{eff} = \sqrt{\frac{\sum_{j=0}^{N} f_j(t)^2}{N}} \quad and \quad V_{eff} = \sqrt{\frac{\sum_{j=0}^{N} g_j(t)^2}{N}} \tag{D.6}$$

where N is the number of discrete current and voltage measurements over one cycle. Finally, the power was determined by multiplying these effective values:

$$P_{eff} = I_{eff} \times V_{eff} \tag{D.7}$$